TU Delft

Delft University of Technology

Luminous Glass

A Study on the Optics Governing Luminescent Solar Concentrators and Optimization of Luminescent Materials through Combinatorial Gradient Sputter Deposition

Merkx, E.P.J.

DOI
10.4233/uuid:01c293b2-ed2c-480e-a997-aec9d4dc04a1

Publication date
2020

Document Version
Final published version

Citation (APA)
Merkx, E. P. J. (2020). *Luminous Glass: A Study on the Optics Governing Luminescent Solar Concentrators and Optimization of Luminescent Materials through Combinatorial Gradient Sputter Deposition*. [Dissertation (TU Delft), Delft University of Technology]. https://doi.org/10.4233/uuid:01c293b2-ed2c-480e-a997-aec9d4dc04a1

Important note
To cite this publication, please use the final published version (if applicable).
Please check the document version above.

Copyright
Other than for strictly personal use, it is not permitted to download, forward or distribute the text or part of it, without the consent of the author(s) and/or copyright holder(s), unless the work is under an open content license such as Creative Commons.

Takedown policy
Please contact us and provide details if you believe this document breaches copyrights.
We will remove access to the work immediately and investigate your claim.

This work is downloaded from Delft University of Technology.
For technical reasons the number of authors shown on this cover page is limited to a maximum of 10.

Luminous Glass

A Study on the Optics Governing Luminescent Solar Concentrators and Optimization of Luminescent Materials through Combinatorial Gradient Sputter Deposition

Luminous Glass

A Study on the Optics Governing Luminescent Solar Concentrators and Optimization of Luminescent Materials through Combinatorial Gradient Sputter Deposition

Dissertation

for the purpose of obtaining the degree of doctor
at Delft University of Technology
by the authority of the Rector Magnificus Prof. dr. ir. T.H.J.J. van der Hagen,
chair of the Board for Doctorates
to be defended publicly on
Monday 14 December 2020 at 15:00 o'clock

by

Evert Pieter Jan MERKX

Master of Science in Applied Physics,
Delft University of Technology, Delft, the Netherlands,
born in Oostvoorne, the Netherlands.

This dissertation has been approved by the promotors.

Composition of the doctoral committee:

Rector Magnificus,	chairperson
Prof. dr. P. Dorenbos,	Delft University of Technology, promotor
Dr. E. van der Kolk,	Delft University of Technology, promotor
Independent members:	
Prof. dr. L.D.A. Siebbeles,	Delft University of Technology
Prof. dr. W.G.J.H.M. van Sark,	Utrecht University
Prof. dr. D. Poelman,	Ghent University, Belgium
Dr. C. de Mello Donegá,	Utrecht University
Dr. A. Jung,	PHYSEE BV, the Netherlands
Prof. dr. E.H. Brück,	Delft University of Technology, reserve member







This research was funded by The Netherlands Organization for Scientific Research (NWO/OCW), as part of the Frontiers of Nanoscience program (NF16NFS01) and as part of the LumiCon project (15024).

Keywords:	Luminescence, Combinatorial science, Solar concentration, Simulation
Printed by:	Ipskamp Printing
Front & back:	An abstract representation of rays of light traveling through a gradient thin-film – Marocha Arredondo

Copyright © 2020, E.P.J. Merkx

Casimir PhD Series, Delft-Leiden 2020-30
ISBN 978-90-8593-456-1

An electronic copy of this dissertation is available at
`http://repository.tudelft.nl/`.

Contents

Acronyms **xiii**

Symbols **xv**

In Short **xvii**

1 Introduction **1**

1.1 Motivation 3

1.2 A Crash Course in Luminescence 6

1.2.1 Luminescence in Organic Dyes 6

1.2.2 Luminescence in Quantum Dots 9

1.2.3 Luminescence in Rare-Earth Ions 11

1.2.4 Hybrid Combinations 14

1.3 Approach 15

1.4 Thin-Film Deposition Using Sputter Coating 17

1.4.1 Sputtering Conductive Materials 17

1.4.2 Sputtering Insulating Materials 20

1.4.3 Forming Nitrides and Oxides from Metallic Targets . . . 22

1.5 Outline 22

References 25

2 The State-of-the-Art of Luminescent Solar Concentrators **33**

2.1 Principle of Operation 35

2.1.1 Absorption of Light 35

2.1.2 Emission within the LSC 36

2.1.3 Effects of Self-Absorption 37
2.1.4 Influence of the Waveguide 38
2.1.5 Conversion of Concentrated Light to Electricity 38
2.2 Calculating LSC Performance 39
2.2.1 Figures of Merit 39
2.2.2 Upper Bound for LSC Efficiency 40
2.3 State-of-the-art LSC Materials 43
2.3.1 Measures for the Visual Performance of LSC Materials . . 43
2.3.2 Evaluating the Performance of State-of-the-Art LSCs . . . 45
2.3.3 Dye-Based Luminescent Solar Concentrators 46
2.3.4 Rare-Earth-Based Luminescent Solar Concentrators . . . 48
2.3.5 Quantum-Dot- And Doped Quantum-Dot-Based Luminescent Solar Concentrators 49
2.4 Tm^{2+}-Doped Halide Luminescent Solar Concentrators 54
2.5 Conclusion 57
References 58

3 Rapid Optimization of Large-Scale Luminescent Solar Concentrators: Evaluation For Adoption in the Built Environment 65
3.1 Introduction 67
3.2 Multiple-Generation Light Transport 69
3.3 Monte Carlo Simulation 73
3.4 Model Verification 75
3.5 LSC Optimization Results 80
3.6 Expected BIPV Efficiencies 83
3.7 Conclusions 87
3.8 Appendix: Positive Self-Absorption in MGLT 88
References 88

4 A Method for the Detailed Characterization of Co-Sputtered Inorganic Luminescent Material Libraries 93
4.1 Introduction 95
4.2 Results and Discussion 96
4.2.1 Library Creation and Method for Characterization 96
4.2.2 Luminescent Alkali-Halide Library 100

4.3 Conclusion . . . 106
4.4 Experimental Procedures . . . 107
4.5 Appendix: Comparison XY-Scanner and Conventional Photoluminescence Setup . . . 110
4.6 Appendix: Additional Characterization of NaI:Eu^{2+} and NaBr:Eu^{2+} 111
References . . . 112

5 Functionalizing Window Coatings with Luminescence Centers by Combinatorial Sputtering of Scatter-Free Amorphous SiAlON:Eu^{2+} Thin-Film Composition Libraries 115
5.1 Introduction . . . 117
5.2 Experimental . . . 118
5.3 Results and Discussion . . . 120
5.3.1 Fabrication of the Library . . . 120
5.3.2 Index of Refraction and Absorption . . . 122
5.3.3 Luminescent Properties . . . 124
5.3.4 Luminescent Quantum Efficiency . . . 127
5.4 Conclusion . . . 129
5.5 Acknowledgements . . . 129
5.6 Appendix: X-Ray Diffraction Data . . . 130
5.7 Appendix: Fitting Transmission Spectra . . . 130
5.8 Appendix: Fitting Emission Spectra . . . 133
5.9 Appendix: Ternary Diagrams of Optical Data . . . 134
References . . . 135

6 Modeling and Optimization of UV Absorbing Photovoltaic Windows Using a Thin-Film AlN:Eu^{3+} Luminescence Library 139
6.1 Introduction . . . 141
6.2 Experimental . . . 144
6.3 Results and Discussion . . . 146
6.4 Conclusion . . . 154
6.5 Acknowledgements . . . 155
6.6 Appendix: Thermal Treatments . . . 156
6.7 Appendix: X-Ray Diffraction . . . 157
6.8 Appendix: Determination of the Complex Index of Refraction . 157

6.9 Appendix: Idealized Luminescence Optimization 158
References 160

7 The Potential of Transparent Sputtered NaI:Tm^{2+}, $CaBr_2$:Tm^{2+}, and CaI_2:Tm^{2+} Thin-Films as Luminescent Solar Concentrators 163
7.1 Introduction 165
7.2 Methods 168
7.2.1 Library Synthesis 168
7.2.2 Luminescence 170
7.2.3 Tm Concentration 171
7.2.4 Transmission 171
7.2.5 Photoluminescent Decay 172
7.3 Results and Discussion 172
7.3.1 Local Luminescence 172
7.3.2 Thickness and Index of Refraction 175
7.3.3 Photoluminescent Quantum Yield 176
7.3.4 Absorption of Thulium 181
7.3.5 Prognosis for a Luminescent Solar Concentrator 183
7.4 Conclusion 188
7.5 Acknowledgements 189
7.6 Appendix: Relation Mean Decay Time and Photoluminescent Quantum Yield 190
7.7 Appendix: Determining the Molar Absorption Coefficient of Rare-Earth-Doped Thin-Films in Wide-Bandgap Insulators 192
References 195

Summary and Conclusions 199
Results Presented in this Thesis 199
Significance for Science and Society 204

Samenvatting en Conclusies 207
Resultaten van dit Proefschrift 207
Belang voor de Wetenschap en de Samenleving 213

Acknowledgments 217

Publications **221**
Refereed Journal Papers 221
Conference Contributions 222
Other Publications 223

About the Author **225**

Acronyms

BIPV	Building-integrated photovoltaic
CIE	Commission Internationale de l'Éclairage (International Commission on Illumination)
CT	Charge transfer
DFT	Density-functional theory
EDX	Energy-dispersive X-ray spectroscopy
FWHM	Full-width half-maximum
LED	Light-emitting diode
LSC	Luminescent solar concentrator
MC	Monte Carlo
MGLT	Multiple-generation light transport
NC	Nanocrystal
NIR	Near-infrared
PDMS	Polydimethylsiloxane

PMMA	Poly(methyl methacrylate)
PMT	Photomultiplier tube
PV	Photovoltaic
QD	Colloidal quantum dot
SEM	Scanning electron microscopy
UV	Ultraviolet
VRBE	Vacuum-referred binding energy
XRD	X-ray diffraction

Symbols

α	the absorption coefficient for the Napierian Beer-Lambert law: $I(d) = I_0 e^{-\alpha d}$. When the decadic absorption coefficient ($I(d) = I_0 10^{-\alpha_{\text{decadic}} d}$) is used, this is indicated in the text. [cm^{-1}]
c	dopant concentration at.%
CCT	correlated color temperature [K]
d	thickness [nm, μm, or mm]
ε	atomic absorption coefficient [$\text{cm}^{-1}\text{at.}\%^{-1}$]
EQE	external quantum efficiency [%]
η_{abs}	the fraction of incident light that the luminophores contained within the LSC are able to absorb [%]
η_{opt}	optical efficiency of an LSC: ratio photons incident on the front of the LSC, the the amount of photons concentrated at the perimeter [%]
η_{Power}	power efficiency of an LSC: the ratio of incident to concentrated power [%]
η_{QY}	photoluminescent quantum yield: ratio of absorbed photons by a luminescent ion to the amount of emitted photons [%]
η_{SA}	the self-absorption efficiency [%]
η_{trap}	trapping efficiency of an LSC [%]

η_{WG}	the waveguiding efficiency [%]
Γ	concentration factor: area-corrected improvement in power output from an LSC over directly exposing PV cells to light
I	intensity of light [a.u.]
k	the imaginary part of the complex index of refraction, also called the extinction coefficient
λ	wavelength [nm]
n	the real part of the complex index of refraction
R	reflection [%]
R_a	color rendering index
$S_{AM1.5}$	AM1.5g solar spectrum [photons $nm^{-1} m^{-2}$]
T	transmission of light through a medium [%]
τ	photoluminescent decay time [ms or μs or ns]
X	X-tristimulus value
Y	Y-tristimulus value, luminance
Z	Z-tristimulus value

In Short

A luminescent solar concentrator (LSC) is a concept from the 1970s that can find novel application as an electricity-generating window. An LSC converts sunlight to light of a different color by a process called luminescence. This light is transported to the edges of the LSC, where photovoltaic cells convert this incoming light to electricity. Since only a small part of the incoming sunlight is absorbed, most sunlight will still illuminate the rooms behind the LSC-window. Turning buildings and offices into nearly zero-energy buildings (nZEBs) is unlikely to happen by using electricity from rooftop photovoltaics (PVs) alone. Turning the envelope of a building, especially the large amount of glass used as windowpanes or facades, into a source of electricity by using LSCs can go a long way towards making these nZEBs a reality. Why then is not every window already an LSC? As will be explained in Chapter 2 and Chapter 3, current LSCs can be efficient at converting sunlight, but suffer from strong coloring, or are not compatible with large-scale industrial processes.

To solve the issue of coloring, one solution is to dope halides, such as table salt, with rare-earth elements, specifically divalent Thulium (Tm^{2+}). This combination absorbs the entire visible spectrum. Another strategy is to dope insulating nitride or oxynitride materials with divalent or trivalent Europium (Eu^{2+} or Eu^{3+}). Eu^{2+} or Eu^{3+} are strong absorbers of ultraviolet light.

In this thesis, optimizing the luminescent properties of these rare-earth-doped materials is researched using combinatorial synthesis methodology and a novel, fast but detailed characterization setup. The combinatorial synthesis methodology implies that a continuum of rare-earth-doped compositions is deposited on a single $5 \times 5\,cm^2$ piece of glass. This composition spread is equivalent to many hundreds of individual samples. The novel characterization setup can

characterize the luminescence and other optical properties of these compositions in a matter of minutes.

In Chapter 4, this technique is used to form and analyze solid solutions of Eu^{2+}-doped halides. The broad-band Eu^{2+}-emission is sensitively susceptible to its local environment, unlike the infrared line-emitter Tm^{2+}. Researching such solid solutions is of great importance for Tm^{2+}-doped halide LSCs. A solid solution can combine the luminescent properties of its constituents, potentially yielding *uniform* absorption of the entire visible spectrum, which would make an LSC-window only dimming, without coloring the incident light. Unfortunately, while these halide materials solve the problem of coloring, they are very sensitive to water and are not used in large scale industrial production.

This is why the focus is shifted in Chapter 5 to materials composed of silicon (Si), aluminum (Al), oxygen (O) and nitrogen (N): the SiAlON material family. These SiAlONs are chemically stable, scratch-resistant and, because of their likeness to amorphous glass, do not scatter light. These SiAlONs are sputtered on a large-scale by industrial glass manufacturers.

Next to fabricating all these materials and characterizing their luminescence, it is also important to predict how they would behave if they were applied as large-scale LSCs. This is done through modeling all optical processes that occur within an LSC, presented in Chapter 3 and Chapter 6. In Chapter 3, a new way of modeling the optical processes within an LSC is presented. The industry-standard is ray-tracing, which can get slow when an LSC absorbs more light, or becomes larger in size. The model presented in Chapter 3 calculates all efficiency steps in an LSC in the same amount of time, regardless of the LSC's size or transparency. In Chapter 6, we use all these methodologies—fast synthesis and characterization of luminescent thin-films, and modeling of light transport through an LSC—to simulate how efficient an LSC based on $AlN:Eu^{3+},O^{2-}$ would be. Such an LSC would be transparent in the visible spectrum, as it only absorbs ultraviolet light. $AlN:Eu^{3+},O^{2-}$ emits red luminescence. Therefore, $AlN:Eu^{3+},O^{2-}$ will not parasitically absorb the emission that makes its way to the LSC's edges. The methodology to predict the performance of an LSC used in Chapter 6 is not specific to $AlN:Eu^{3+},O^{2-}$, but applicable to all combinatorially synthesized luminescent thin-films.

As mentioned before, halide-type materials doped with Tm^{2+} have been often suggested as promising materials for LSCs. In the final chapter, Chapter 7,

sputtered thin-films of NaI, $CaBr_2$, and CaI_2 doped with Tm^{2+} have therefore been evaluated on their performance as LSC; both in terms of simulated optical efficiency, as well as in terms of aesthetic appeal. Our Tm^{2+}-based thin-film LSCs absorb the entire visible spectrum and emit a line of near-infrared radiation centered at 1140 nm. Chapter 7 demonstrates the universality of the techniques presented in Chapters 5 and 6. These techniques are adapted to take hygroscopic nature of the halides into account. The chapter does forgo on fully taking industrial compatibility into account: halides are not often sputtered, and the water-sensitivity will be a hurdle for implementation on window glass. By combining theory and modeling, we see that 10 µm thick films which transmit 80 % of the visible spectrum would be able to achieve optical efficiencies of 0.71 %. This efficiency already compares favorably to the maximally achievable optical efficiency of 3.5 % at those transmission constraints. Further research will have to show whether the photoluminescent quantum yield of the sputtered thin-films can be increased to achieve unity photon conversion.

— 1 —

Introduction

This chapter gives the motivation for this research. It establishes that luminescent solar concentrators (LSCs) are a feasible solution for integrating photovoltaics in the built environment as electricity-generating windows. A part of the working principle of an LSC is presented via a crash course in luminescence. In that section, the three major luminescence systems and their hybrid combinations used in LSCs are treated. The absorbing and emitting states of rare-earth-doped phosphors can be tuned such that there is no overlap between the two. Rare-earth-doped phosphors are therefore worth studying for LSCs applications. These phosphors can be directly deposited onto window glass using sputter deposition, as is also used in large-scale industrial applications. As an added benefit, sputter deposition enables the fabrication of a continuous composition spread: analogous to hundreds of samples on a single substrate. Analysis techniques of luminescent composition spreads are traditionally rudimentary. A large part of this thesis therefore focuses on developing more advanced techniques to characterize these luminescent composition spreads in detail, with regards to their local composition, luminescence, and refractive index. After a short account on the operating principle of thin-film deposition using reactive magnetron sputter coating, the research goals and outline of thesis are presented.

Parts of this chapter are adapted from: E.P.J. Merkx and E. van der Kolk, "Luminescent Solar Concentrators," in *Indoor Photovoltaics*, edited by M. Freunek. (Wiley-Scrivener, 2020) Chap. 6

1.1 Motivation

The makeup of produced electricity around the world is expected to move towards electricity generated from renewable sources, and especially to electricity generated by photovoltaics (PV) [1]. This expectation can partly be explained by increasing regulations, such as the Paris Agreement [2]. The International Energy Agency reports that renewable energy sources such as PV will be the main instrument for complying with the Paris Agreement [1]. The other part of this expectation can be explained by the ever higher efficiencies of PV, and therefore the benefit for local energy production by e.g. consumers or office spaces. PV has become sufficiently cheap, in cost per Watt, to install at home or in the office for the climate-change-aware consumer, architect, or government. To illustrate the cost perspective: in 1957, a MWh of PV electricity on a sunny day would cost $300 000. In today's US dollars, this price has now fallen to just $20 [3, p.8]. And as illustration for the efficiency: in the 1980s, the highest efficiency silicon (Si) PVs had efficiencies of 16 % to 20 % [4]. Now these Si PVs are inching ever closer to the Shockley-Queisser limit of 32 %, with top-efficiencies now exceeding 26 % [5, 6]. Even with these impressive improvements in cost and efficiencies, a critical concern is that standalone PV takes up space that cannot be used for anything else. A shortage of installation sites might therefore become an issue for these PV modules [7]. A solution to that problem is to make PV part of the built environment, which would immediately bring energy supply and demand to the same place. Making PV part of the built environment can either be done by using building-attached PV, which implies covering the walls and roofs of a building with PV, or by seamlessly integrating PV with construction materials, so-called building-integrated photovoltaics (BIPVs). An area of research in the field of BIPVs focuses on transferring the working principle of conventional PV to windows. One strategy is to use conventional PV with small holes cut out of the cell, and laminating this onto window glass. While these aperture-type solar cells yield high efficiencies[1], they are not aesthetically pleasing. Another strategy is to use thin-film solar cells, that by nature of their thickness are semi-transparent, or to use semi-transparent dye-sensitized solar cells [7]. However,

[1] The efficiency of such aperture-type solar cells is a function of their transmittance and therefore cannot be expressed as a single number.

these technologies still suffer from stability issues and heavy coloring. Furthermore, due to these technologies being electrode-based, large-scale transparency is difficult to attain. All of these factors hinder public acceptance of this type of BIPV.

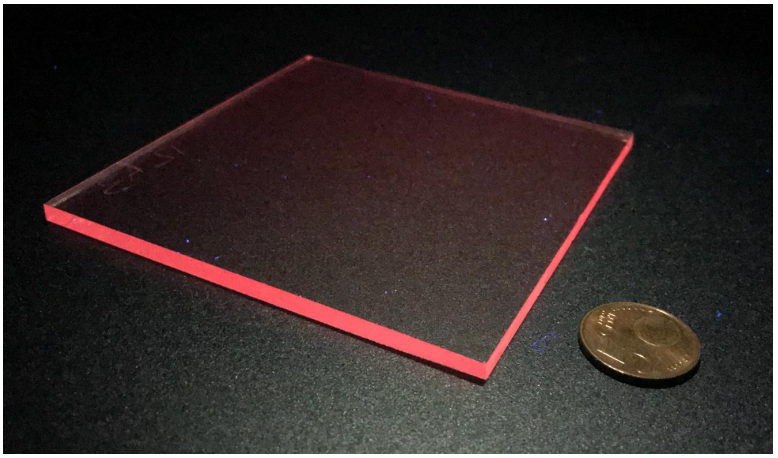


Figure 1.1: Example of a thin-film LSC. Depicted here is a SiAlON:Sm^{2+},Sm^{3+} LSC made as a demonstrator of thin-film LSCs. This LSC consists out of a glass waveguide, coated with a thin-film of SiAlON:Sm^{2+},Sm^{3+}. Ultraviolet light illuminates the film from above, which is converted to red light by Sm^{2+}. This red light is (mostly) waveguided to the perimeter of the glass. Hence the name luminescent solar concentrator, as the luminescence from the large surface of the thin-film is concentrated at the perimeter of the glass.

A luminescent solar concentrator (LSC) can be a cheap and much simpler alternative technology to realize electricity generating windows. LSCs, as illustrated in Figure 1.1, were first studied in the 1970s [8–10] as a cost-saving alternative to lens-based solar concentrators. In those days, silicon PV was still prohibitively expensive, and therefore increasing the amount of sunlight a small cell could receive was seen as greatly beneficial [8, 11]. The advantage of the LSC over lens-based concentrators in these original studies was that an LSC is able to absorb both direct and diffuse light. Therefore, LSCs would not need costly solar-tracking systems to stay pointed towards the sun, as lenses do. Today, the value of LSCs lies more in their potential as a BIPV window [12, 13].

As will be explained in extensive detail in Chapter 2, an LSC functions by (partially) absorbing direct and indirect sunlight with a luminescent coating on, or embedded in, a transparent glassy plate. The luminescent coating converts

this absorbed light to a longer wavelength and re-emits this light in all directions. Much like light would in an optical fiber, this converted light can then travel through the plate, which functions as a waveguide. Upon reaching the perimeter of the waveguide, this converted light will be absorbed by PV cells. These PV cells then convert this concentrated light to electricity.

Since the 1970s, research on LSCs has come a long way. The first LSCs were made using luminescent dyes that typically suffer from strong self-absorption: an overlap between the absorption and the emission of the luminescent material. This means that these dye-based LSCs cannot be scaled up to large areas, since luminescence generated by light incident on the center of a large dye-based LSC is unlikely to reach the perimeter of the LSC. Later on, LSCs started to be fabricated out of luminescent colloidal quantum dots (QDs) [14]. In the first studies, these QDs also suffered from strong self-absorption, lost their luminescent abilities when dissolved in a plastic waveguide, and were made out of either toxic cadmium (Cd) or lead (Pb) [14, 15]. Results from recent research have shown that some of these problems can be mitigated. The self-absorption in LSCs based on QDs has been overcome by specifically designing QDs to have no overlapping absorption and emission. The toxicity problem has been overcome by switching to materials like aluminum (Al), copper (Cu), indium (In), and zinc (Zn) [16, 17]. The loss of luminescence has been mostly overcome by placing a protective shell around the dot that isolates the dots from the surrounding plastic. The main hurdles that these QD-based LSCs still face is that QDs still are difficult to dissolve in a plastic matrix without coagulation, that they do not exhibit uniform absorption over the visible spectrum, which would give a colorless appearance, and that industrial large-scale lamination of a QD layer on window glass is not yet available [15]. Therefore, it is still necessary to find a luminescent material that (in no particular order of importance)

- is colorless due to absorption of only ultraviolet light, or due to absorption of the entire visible spectrum,
- has no overlap between its emission and its absorption,
- luminesces brightly,
- can be directly coated on window glass, using industry-compatible methods,

- does not scatter incident light,
- is non-toxic,
- is chemically stable,
- is scratch-resistant,
- is cost-efficient.

To see how an LSC operates and what material choices are considered, it is necessary to understand how different materials generate luminescence. To this end, the following section will expand upon the working principle behind luminescence.

1.2 A Crash Course in Luminescence

Luminescent centers, often also called luminophores, absorb light of various wavelengths, as described by their characteristic absorption spectrum. This absorbed light gets converted to a different energy, yielding the emission of the luminescent center. When the absorption and emission happen between the same electronic states, the difference between the absorbed and the emitted wavelength (and therefore energy) is referred to as the 'Stokes shift'. This conversion of light from one wavelength to another occurs with an efficiency known as the (photoluminescent) quantum yield η_{QY}, defined as

$$\eta_{QY} = \frac{\#\text{photons in}}{\#\text{photons out}} \tag{1.1}$$

Three different types of luminescent materials that are of particular relevance to LSCs—organic dyes, colloidal quantum dots, and rare-earth ions—will be treated in the following sections. In these sections, we will give a short overview of the working principle of the luminophore in question, together with an explanation of some frequently used terminology.

1.2.1 Luminescence in Organic Dyes

A large family of luminescent solar concentrators is based on luminescent dyes. This can be explained by their high quantum yields, as well as by their high solubility in waveguide matrices, such as poly(methyl methacrylate) (PMMA) [18]

and polycarbonates [19]. These factors make that luminescent dyes can easily be turned into prototype LSCs.

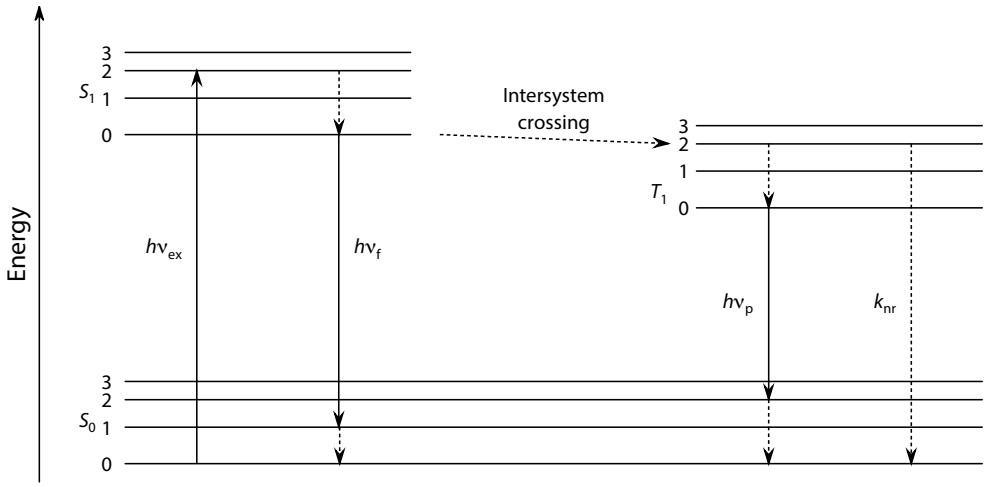


Figure 1.2: A simplified Jablonski diagram of luminescence processes in dyes. A photon with energy $h\nu_{\mathrm{ex}}$ excites the system from the S_0 level. The system relaxes (non-radiatively, indicated by a dashed arrow) either (efficiently) from $S_1 \rightarrow S_0$ under emission of a photon with lower energy $h\nu_f$ (fluorescence), or the system moves to the excited triplet state T_1 through intersystem crossing. From the T_1 excited level, the system either relaxes through non-radiative relaxation k_{nr}, or through emission of a photon with energy (phosphorescence). Non-radiative transitions to the ground state are not excluded for the excited singlet states, but less likely than for the triplet states.

These dyes are π-conjugated organic molecules: molecules with a chain of carbon atoms having alternating single and double bonds, causing the p-orbitals of the carbon atoms to overlap. This leads to a system of delocalized π-electrons, above and below the planar conjugated chain. As shown in Figure 1.2, absorption in these dyes is caused by a promotion of the molecule from the singlet ground state S_0 to an excited state S_1 through absorption of a photon with sufficient energy. Subsequent luminescence is a result of relaxation of the molecule to the lowest S_1 excited state, followed by emission of a photon, leading the system to fall back to a higher S_0 state, which in turn is followed by non-radiative relaxation to the S_0 ground state. A more in-depth explanation of dye luminescence can be found in Ref. [20], or, for a briefer overview of the underlying concepts, Ref. [21]. For dyes specific for LSCs, an overview can be found in the review by Debije and Verbunt [13].

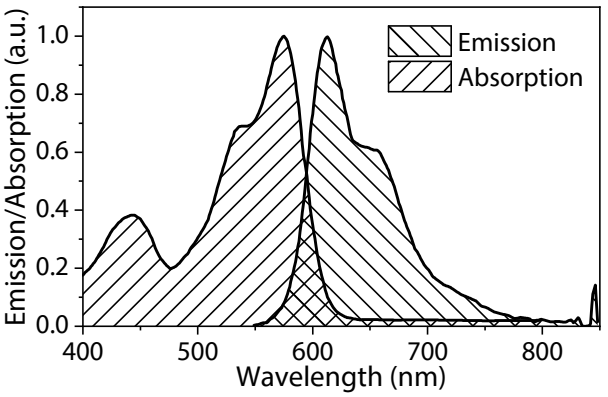


Figure 1.3: Normalized absorption and emission for BASF Lumogen F Red 305 [19]. The mirror image from absorption to higher lying singlet states and subsequent fluorescence is clearly visible. The cross-hatched area shows the overlap between absorption and emission. The area of this overlap should not be seen as a "self-absorption percentage" as both curves are normalized.

An interesting property of the $S_0 \leftrightarrow S_1$ interplay is that the excitation spectrum mirrors the emission spectrum, as displayed for the popular LSC dye BASF Lumogen F Red 305 in Figure 1.3. In organic dyes, the shape of the absorption and emission spectra, and the Stokes shift between them, is mainly governed by the chain length and the number of π-electrons in the conjugated plane of the molecule.

The mirror image of the absorption and emission is an immediate disadvantage of dyes for LSC use. As will be further explored in Section 2.1, having an overlap between absorption and emission can be detrimental to LSC performance when scaling up the LSC to dimensions spanning near a square meter. Absorption is only followed by emission if the quantum yield of the luminophore is sufficiently high. Therefore, if the dye is able to absorb its own emission, the LSC's overall performance will decrease when the LSC increases in size, since a larger LSC leads to more absorption taking place (and therefore also to absorption of its own emission).[2]

Next to the limitation of self-absorption, dyes are also known to only have

[2]The impact of an overlap between absorption and emission is the product of distance and absorption. If light has to travel a long distance to the edges of the LSC, but only has a small chance of being absorbed per distance, the overall absorption during light transport will be the same as when the light only has to travel a short distance, but with a high chance of being absorbed per distance.

limited absorption ranges, causing a single dye to never be able to absorb the entire solar spectrum. Being unable to absorb the entire solar spectrum not only reduces the total achievable efficiency of an LSC, but will also reduce applicability due to (bright) coloring decreasing aesthetic appeal. A strategy to overcome this limitation is, of course, to combine multiple dyes. This can be done by either having multiple LSCs stacked on top of each other [13, 22, 23], akin to tandem solar cells, or by mixing all dyes together in a single waveguide [13, 24]. The absorption range of a dye can be altered by changing the conjugated chain. However, when increasing the chain length for moving the absorption to the infrared, the solubility of the dye in a matrix material decreases [25]. A lower energy between transitions also makes it easier for the dye to fall back non-radiatively from its excited state, leading to a decreased quantum yield when moving the emission to the near-infrared.

1.2.2 Luminescence in Quantum Dots

Colloidal quantum dots, in the luminescence community often abbreviated to quantum dots (QDs), are nanocrystals (NCs) of semiconductor material so small in size that their optical properties are dictated by quantum confinement effects, rather than by their bulk material properties. Because of these effects, QDs are often likened to artificial atoms, since, to a very good degree, the effects observed in QDs can be described with the same equations as the hydrogen atom (see e.g. Refs. [26, 27]). In QDs made of a single material, changing the diameter of the QD directly influences its optical properties. By altering the diameter of the QD, the emission wavelength can be changed. A larger diameter QD leads to a smaller bandgap and therefore a more redshifted emission. Literature often features images of vials of QDs, where each vial contains a solution of QDs with a specific diameter, showing that the emission wavelength is tunable over the entire visible spectrum.

A disadvantage of QDs composed of single materials such as CdSe of PbS are their negligible Stokes shifts, causing the QD-LSC to suffer greatly from losses due to self-absorption. Furthermore, due to the size of a quantum dot (typically only a few nanometers in diameter), there is a large surface-to-volume ratio. This means that there are many surface atoms, leading to a large fraction of the QD

having unsaturated bonds. Such unsaturated bonds can lead to channels for non-radiative recombination, thereby reducing the quantum yield of the QD [28].

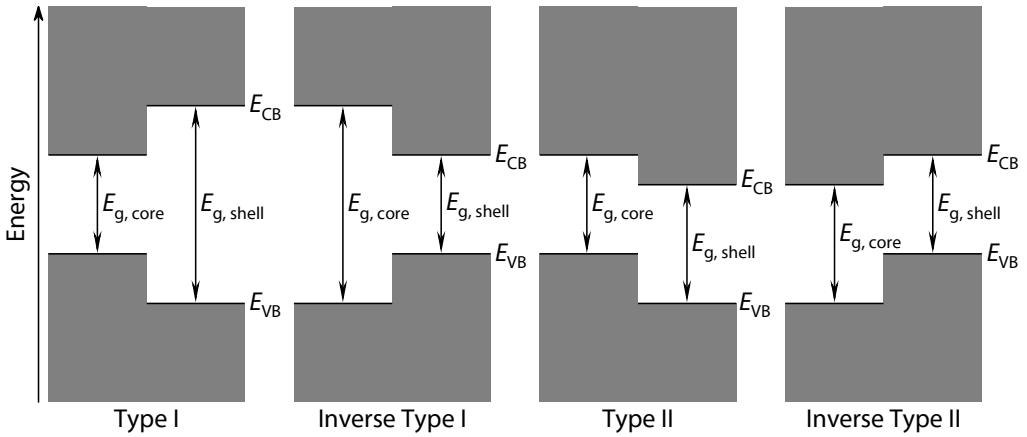


Figure 1.4: The different types of core/shell quantum dots [29].

Enabling a larger energy shift between absorption and emission in QDs can be achieved by separating the absorption from the emission, by fabricating core/shell heteronanocrystals. In these core/shell QDs, the shell (made from a different material than the core) serves as an sensitizer, transferring its absorbed energy to the core, as seen in Figure 1.4. The core functions as activator, eventually emitting the absorbed energy as luminescence [25, 29]. Here, the absorption wavelength is determined by the shell thickness, in much the same way as the luminescence is governed by the diameter of the core. Adding a shell to the emitting core of the quantum dot solves the problem the core dots have of unsaturated bonds at the surface. However, depending on the core/shell configuration chosen, it introduces a different set of problems. With the addition of a shell, the QD grows in size, increasing the likelihood of light scattering and therefore a drop in efficiency of the LSC. the e of Type I core/shell QDs, the shell can still trap the charge carriers or have them leak to the surface, leading to reduced quantum yields [30]. In the case of Type II core/shell QDs, the hole and the electron are spatially separated. While this does give the advantage of tuning the emission further to the infrared (avoiding self-absorption) than was possible with just the core or shell material, it does also mean that it will take some time for the spatially separated hole and electron to recombine radiatively.

This increased radiative recombination time can make it possible for faster non-radiative quenching processes to dominate the luminescence, again leading to lower quantum yields [28].

1.2.3 Luminescence in Rare-Earth Ions

Inorganic hosts doped with rare-earth ions[3] known as phosphors, are widely used in various optical applications, such as laser materials, (LED) phosphors, bank-note security, and luminescent markers in the field of biomedics [32–34]. In the field of photovoltaics, various combinations of rare-earth materials doped in a great variety of hosts are used. These compounds find use as either up- or downconversion materials (with $NaYF_4$ doped with Yb^{3+} and Er^{3+} as the most prominent class for upconversion) [35–38] to improve solar cell efficiency; and in LSCs, as will be elaborated on in this thesis.

A remarkable feature of the rare-earth ions in compounds is their (partially) filled 4f-shell. What makes these 4f-electrons remarkable, is that because of the completely filled $5s^2 5p^6$-shells surrounding them, their intra-orbital transitions are well-shielded from the influence of their environment. For this reason, regardless of what host these ions are placed within, they will have (to a great degree) the same 4f-energy levels [39, 40]. The intensity (and altogether presence) of transitions, and therefore emissions, from these f-levels is dependent on the local symmetry and available phonon-modes of the host.

Intra-f absorption is strongly forbidden by the parity selection rule, but not fully excluded due to mixing with opposite parity states [33, p.26]. Therefore, absorption transitions between the f-states are generally extremely weak. To become interesting for LSC applications, the much stronger (parity-allowed) absorbing f-d transitions have to be considered. 4f→5d absorption is typically 10^2 to 10^4 times stronger than 4f→4f absorption.

The 5d-orbitals of a rare-earth are much more extended in space than the 4f-orbitals. Hence, the 5d-orbitals do not have the same degree of shielding by the outer filled $5s^2$- and $5p^2$-shells. This means that the energy difference of

[3] Rare-earths are the lanthanides, the elements with atomic numbers 57 to 71, from lanthanum (La) through lutetium (Lu), often depicted as its own row underneath the periodic table, combined with Scandium (Sc) and Yttrium (Y). 'Rare' earth is a misnomer. While the rare-earths in nature are difficult to separate, and are typically not found in clusters of pure elements, they are quite abundant in the Earth's crust [31].

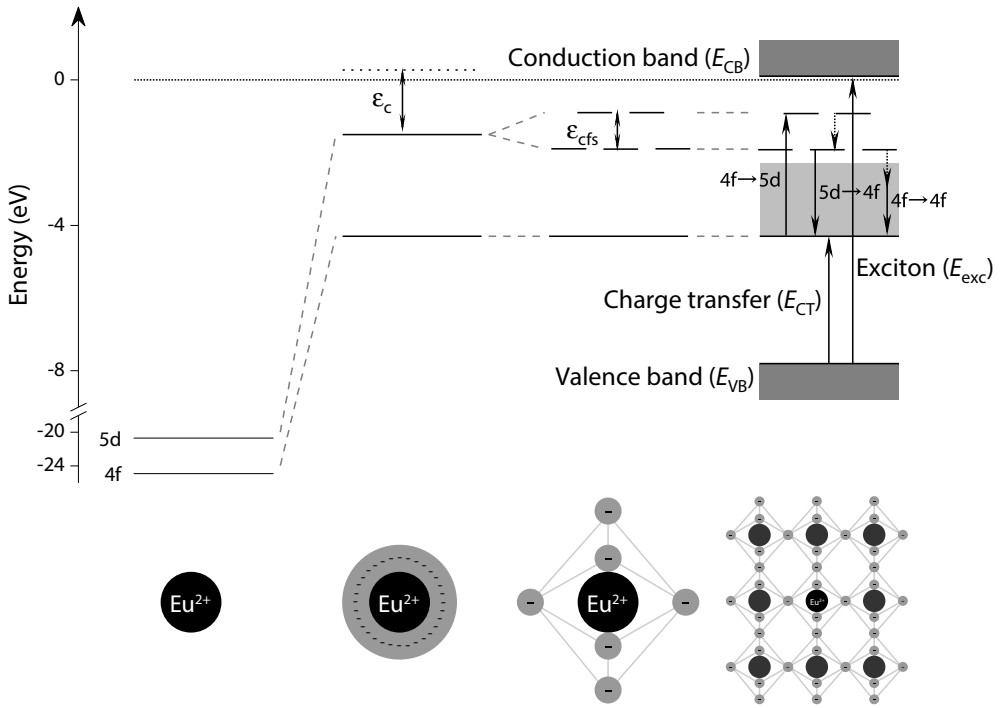


Figure 1.5: The development of the binding energy of an electron in a state of a divalent europium cation when it is incorporated in a host, relative to the vacuum level (at 0 eV). First, there is the free cation, with the electron's binding energy well below the vacuum level. Surrounding the cation with a spherically symmetrical field of negative ions leads to a shifting of the energy levels altogether, the chemical shift, and the centroid shift ε_c of the 5d-level. Transitioning from this field to negative ligands splits the 5d-levels,[4] yielding the crystal field splitting ε_{cfs}. Expanding the surrounding ligands to a crystal adds the valence and conduction bands. In this last frame, the various types of possible transitions are also shown. The many 4f-levels are indicated as a light gray area above the ground state.

the excited 5d-level with the 4f-ground state is strongly dependent on the host material. Therefore, it is possible to engineer the absorption range of a rare-earth-based LSC by changing the host material. The energy of the 5d-levels compared to that of a free ion, is mainly altered by the host in two ways: by ligand anion type, and by the structure of the host crystal, as illustrated in Figure 1.5.

We can liken incorporating the cation in a host to surrounding the cation by a

[4]Because of spin-orbit (LS) coupling (not displayed in Figure 1.5), the 5d-levels are already split, covering a small energy range. LS coupling is around half as intense as the splitting caused by the crystal field. In terms of overall influence on the energy w.r.t. the vacuum level, a general rule-of-thumb is: chemical shift> ε_c > ε_{cfs} > LS coupling.

spherically symmetrical field with negative charge. The negative charge screens the charge of our cation. The screening lifts the binding energy levels of the cation's states closer to the vacuum level. This effect is called the 'chemical shift' and affects both the 4f- and 5d-levels. The intensity of this effect depends on the type of ligand anion and follows what is called the nephelauxetic[5] sequence. The nephelauxetic sequence is, in order of raising the level closer to the vacuum level at 0 eV: F, oxides, Cl, Br, N, I, S, Se, Te. The shift in binding energy of the 5d-levels is on average smaller than that of the 4f-levels. To correct for this, the centroid shift ε_c is introduced. For ε_c the nephelauxetic sequence is also followed, with the difference between 4f- and 5d-energy being highest for fluoride ligands (i.e. low ε_c) and lowest for telluride ligands (i.e. high ε_c).

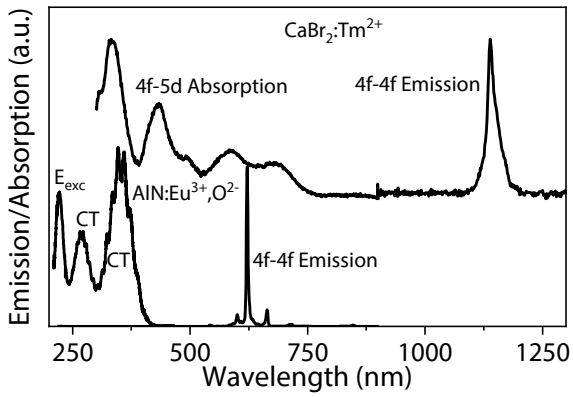


Figure 1.6: Optical transitions in $CaBr_2:Tm^{2+}$ (top) and $AlN:Eu^{3+},O^{2-}$(bottom). $CaBr_2:Tm^{2+}$ displays a very broad 4f-5d absorption region, spanning the entire visible spectrum, followed by 4f-4f emission at 1140 nm. $AlN:Eu^{3+}$ shows two other types of absorption: Exciton (E_{exc}) and two charge transfer (CT) transitions. These are followed by a series of 4f-4f emissions, centered around 622 nm.

In reality, the host we place the cation in is not a spherically symmetrical field, but rather has a certain type of (local) structure to the position of the cation and its ligands: the coordinating polyhedron. The energies of the 5d-levels are affected through their orbitals by the local structure of the host.[6] Depending on the coordinating polyhedron, the 5d-levels are split into different components at different energies. This is called the 'crystal field splitting'. In practice, these

[5] Greek for "cloud expanding".

[6] In principle, this also affects the 4f-levels. However, the influence of the structure of the surrounding crystal on them is ~ 50× weaker than for the 5d-levels.

splitting effects mean that rare-earths can have absorption ranging from just UV absorption, to covering the entire visible spectrum. The splitting of the 5d-levels can be observed by exciting the luminescent material at different wavelengths, illustrated for $CaBr_2$:Tm^{2+} in Figure 1.6.

Next to excitation from a 4f → 5d transition, photoluminescence in rare-earths can also be generated through the allowed charge transfer excitation or host-lattice excitation (formation of an exciton), seen for AlN:Eu^{3+},O^{2-} in Figure 1.6. In a charge transfer excitation, an electron from the ligands L surrounding the rare-earth cation is excited to the 4f-level of the rare-earth ($4f^n L^q \rightarrow 4f^{n+1} L^{q-1}$). Following this transition, the system relaxes back, but leaves an excited $4f^n$ state behind. This excited 4f-state can radiatively emit: $4f^{n+1} L^{q-1} \rightarrow (4f^n)^* L^q \rightarrow 4f^n L^q + h\nu$.

Host-lattice excitation is a special type of excitation where an electron from the host is excited across the bandgap. The electron and hole can travel through the lattice in a correlated motion and can transfer their energy to the rare-earth ion. This energy transfer leaves the rare-earth ion in an excited state, which again can lead to emission from the rare-earth.

Quantum yields are to a great degree determined by interaction with the host through the host's vibrational frequencies. The hosts that most rare-earths are doped in have vibrational frequencies of less than 4–5 times the energy difference of the radiative relaxation [33, Section 4.2]. This leads to only very little energy being lost to lattice vibrations. With little energy lost to lattice vibrations, all the remaining energy can be used for the generation of luminescence, and therefore leading to a high quantum yield.

1.2.4 Hybrid Combinations

All luminescence processes described in the previous sections concern a single family of luminophores. The processes involved all require transfer of energy from one state to another, which does not have to be confined to only one family of materials. Often combinations of two techniques are seen. For instance, rare-earths can be combined with dyes to form an organometallic compound. In such compounds, the dye is responsible for absorption, but will transfer its energy to the rare-earth, which is in turn responsible for the emission. An example of this is Eu^{3+} complexed with central organic ligand thenoyl trifluoroacetone

(TTA) and synergetic organic ligand triphenyl phosphine oxide (TPPO), yielding $Eu(TTA)_3(TPPO)_2$. In $Eu(TTA)_3(TPPO)_2$, the organic ligand groups ('antenna groups') are responsible for absorption. The ligands then transfer their absorbed energy to the complexed Eu^{3+} [41]. Similarly, one can dope QDs with transition-metal [42] or rare-earth ions [43]. Here, the semi-conductor host absorbs energy, which it transfers to the doped cation. As the shift from absorption to emission is now governed by the dopant in stead of the QD, a large, structure-independent shift is possible.

1.3 Approach

Most research on LSCs focuses on photoluminescent organic dyes or colloidal quantum dots, as will become evident in Section 2.3.3 and Section 2.3.5. Rare-earth-doped solids can also be of great interest to LSC research because of the great tunabilty of their absorbing states, their narrow line emissions which are (to a first order) independent from the absorptive states, and their high achievable quantum yields. Hence, the research described in this thesis mainly focuses on luminescence generated by embedding ions from the lanthanide family of elements, specifically Eu^{2+}, Eu^{3+}, and Tm^{2+} in inorganic transparent solids.

However, virtually infinite combinations of elements that comprise the host of a phosphor exist. This set of materials under consideration gets even larger since a modest variation in concentration of the dopant already profoundly influences the luminescent properties of the phosphor. While many efforts have been made to simulate and predict the luminescent behavior of such rare-earth-doped solids, either by using density functional theory [45, 46], or by using empirical methods [47–50], most research on phosphors still relies on traditional guided trial-and-error. This trial-and-error entails starting out with a known phosphor, or a known structure, and slowly varying the composition, stoichiometry, dopants, and processing conditions to reach an optimum [33, 51]. As one can imagine, if no high-throughput synthesis and screening are available, this can be a laborious process. To aid in collecting data on material properties and therefore to help in optimizing a material for a desired property, it is imperative to be able

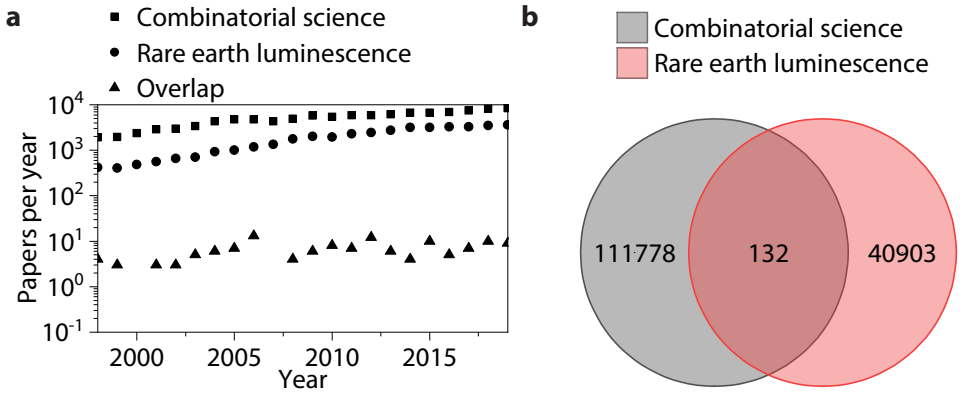


Figure 1.7: Overview of research output in rare-earth luminescence and combinatorial materials science. **a**. Article output per year in either combinatorial science, or in rare-earth luminescence since 1998 until 2020, according to Scopus [44]. Output in the fields of medicine, the social sciences, and mathematics were excluded from this search. Note the logarithmic scale used. Per year, the overlap does not exceed 20 articles. **b**. Cumulative overlap of the fields of combinatorial materials science and rare-earth luminescence since 1998 until 2020. This thesis is responsible for 3 of the 132 articles in the area of overlap.

to quickly explore a material family[7]. This is exactly what combinatorial science intends to do. As can be seen in Figure 1.7, combinatorial research applied to rapidly produce and process large quantities of materials, referred to as a 'materials library', or 'library' for short, is not often used in the field of rare-earth luminescence. This can for a large part be explained by a lack of rapid characterization methods. The characterization of luminescence libraries fabricated through combinatorial means is often limited to (color-filtered) charge-coupled device (CCD) photography of a library under UV illumination [54–62] and other rudimentary characterization methods. In Chapters 4 to 6, a much more detailed characterization technique will be presented, that can quickly characterize the luminescence and optical properties of such libraries with no loss of detail.

For the application of combinatorial research, rare-earth-doped phosphors

[7] 'Material family' as used in this thesis and most combinational science literature (e.g. Ref. [52], or explained in more detail in Ref. [53]) entails the broad set of compounds that have certain properties in common. This can mean for instance for the 'family of nitrides' that all materials under study have nitrogen as their primary anion. The definition of 'family' can also be more narrow, such as in the case of the SiAlON-family of materials, encountered in Chapter 5. Here 'family' denotes all compounds that contain the elements Si, Al, O, and N, as main constituents, with possibly dopants added.

have another benefit over dyes and quantum dots: they can be synthesized using combinatorial sputter deposition. It is therefore possible to synthesize these phosphors on a substrate employing a continuous composition spread [63]. The desired material library is deposited on a substrate from two or more spatially separated and chemically distinct sputtering sources that are operating simultaneously, in either a reactive or a non-reactive atmosphere. In doing so, a thin-film with an inherent composition and dopant-concentration gradient is produced. The ability to be sputtered also makes these phosphors immediately of interest to LSCs. Sputter deposition is already extensively used in the glass industry for applying anti-reflection layers, and scratch-resistant coatings to window glass. This means that if a sputter-deposited rare-earth-doped phosphor is viable as an LSC material, it can quickly be upscaled to be included in industrial processes.

1.4 Thin-Film Deposition Using Sputter Coating

Sputter deposition is a widely used technique for the fabrication of high-quality thin-films. While often and ever more frequently used for the fabrication of conductive electrical contacts or specialized coatings in glass [64–66], the technique is not often employed in the field of rare-earth luminescence.

In the following paragraphs, a short qualitative description of the sputtering process is given. A more detailed explanation on the mechanics of sputter deposition can be found in the book edited by Ohring [67], especially in the fourth and in the fifth chapter, or in the thesis written by Cornelius [68], or, for the reader in a rush, in the chapter written by Depla et al. [69].

1.4.1 Sputtering Conductive Materials

The basics of sputtering are simple: a small quantity of gas is let into a chamber at high vacuum. In this thesis, this implies increasing the pressure of a chamber with a typical base pressure below 1.3×10^{-4} Pa to 0.4 Pa by introducing argon (Ar) gas. As seen in Figure 1.8a, when applying a voltage difference between a cathode and an anode in the vacuum chamber, the Ar is ionized. The cathode is covered by a so-called target material, i.e. the material we want to sputter, while the role of anode is fulfilled by the substrate carrier on the other side of the vacuum chamber and the shielding around the target. The electrons will be

accelerated to the anode, while the Ar^+ is accelerated to our target material. As seen in Figure 1.8b, the Ar^+ will bombard the target material and sputter off the target material, hence the name of the technique. Atoms of target material are ejected from the target bulk due to elastic momentum transfer, resulting in a plume of atoms of target material moving away from our target. By placing a substrate, in this thesis typically some type of glass or MgF_2, in this plume, a thin-film of target material will start to grow on the substrate. As the ionized Ar hits the target, its impact can free electrons from the target, which are called secondary electrons. These electrons in turn can have such energy that they ionize neutral Ar in the vacuum chamber. The electrons from the newly ionized argon can in turn ionize other neutral argon, and so on, causing that a much increased current can be measured. At this point, the plasma starts generating a glow due to the recombination of electrons with ions, and the discharge becomes self-sustaining. The self-sustaining avalanche of electrons is called the 'Townsend avalanche'. The sputtering process is schematically shown in Figure 1.8. Since this process involves a cathode and an anode, with the current only flowing in one direction, this type of sputtering is also referred to as 'diode sputtering'. Hence, the plasma can be characterized with a typical IV diode-characteristic, which will be made use of in Section 1.4.2.

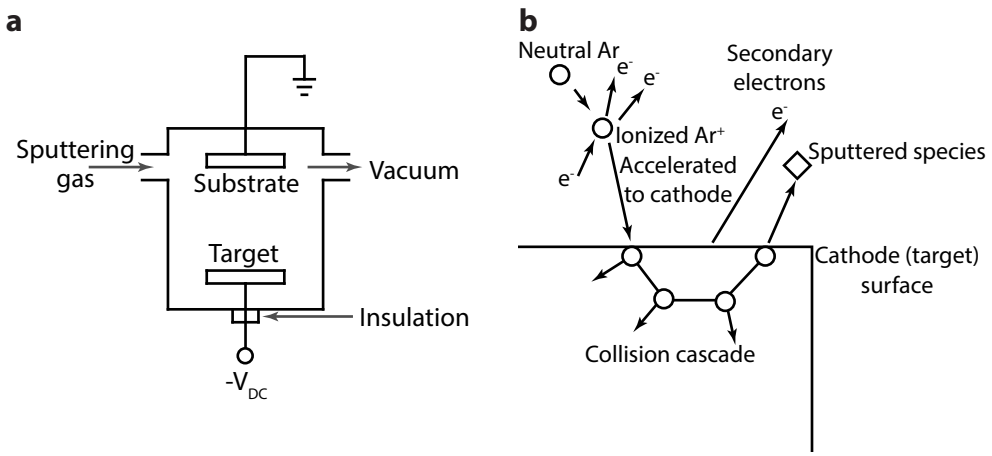


Figure 1.8: Schematic overview of diode sputtering. **a**. Schematic depiction of a DC sputtering system. Note that everything not connected to the target is grounded. **b**. Processes leading to sputtering of a target with argon as sputter gas. Ar has sufficient energy to traverse a large distance within the target. Only collisions from close to the surface of the target will lead to sputtering. Figure adapted from Ohring [67].

To see how effectively a material will sputter, several analytical, empirical and Monte Carlo methods are available, reviewed in [65, Chapter 1]. The effectiveness of sputtering is expressed by the sputter yield

$$Y = \frac{\#\text{ ejected particles}}{\#\text{ incident particles}}. \tag{1.2}$$

A simple model for this is given by Mahan and Vantomme [70] as

$$Y(E) = \frac{1}{4}\frac{E}{U_s \ln(\gamma E/U_s)}\frac{R_{\mathrm{pr}}}{R_{\mathrm{pp}}}, \tag{1.3}$$

with

$$\gamma = \frac{4m_1 m_2}{(m_1 + m_2)^2}. \tag{1.4}$$

Here E is the incident energy of the sputtering species (e.g. Ar) with mass m_1, U_s is the surface binding energy and the ratio $\frac{R_{\mathrm{pr}}}{R_{\mathrm{pp}}}$ is the ratio between the range of the 'recoiled' sputtered species with mass m_2 (R_{pr}, a few tenths of a nanometer) to the range of the sputtering 'projectile' species upon incidence on the target (R_{pp}, a few nanometers). This ratio gives the probability that the sputtered species are close enough to the target surface to escape. Finally, the term 1/4 is the average probability that the sputtered target species are moving toward the surface.

The most important term in eq. (1.3) is the reciprocal of the surface binding energy $1/U_s$. U_s is the sum of the enthalpy of vaporization ΔH_{vap} and enthalpy of fusion ΔH_{fus} for that specific material divided by the Avogadro constant N_{A}: $U_s = (\Delta H_{\mathrm{vap}} + \Delta H_{\mathrm{fus}})/N_{\mathrm{A}}$. For the rare-earths Eu and Tm the sum of those enthalpies amounts to $185\,\mathrm{kJ\,mol^{-1}}$ and $208\,\mathrm{kJ\,mol^{-1}}$, whereas for host elements Al and Si this is $304\,\mathrm{kJ\,mol^{-1}}$ and $409\,\mathrm{kJ\,mol^{-1}}$, respectively [71, 72]. $1/U_s$, which approximately scales with the sputtering yield Y, thus differs by about a factor 2 between the rare-earth dopant and the host elements. In practice, this means that even at low sputtering powers, the sputter yield for Tm and Eu is still too high to achieve 'dopant levels' of a few percent at the substrate. This is why in the rest of this thesis, Tm and Eu targets are masked with patterns of concentric holes to reduce the deposition rate[8].

[8] A bit of terminology: *sputter yield* is the amount of sputtered atoms of every incident atom, *deposition rate* quantifies the growth of a thin-film on the substrate per unit of time. In this thesis, attention is payed to the distinction. In a lot of literature however, these terms will be used interchangeably.

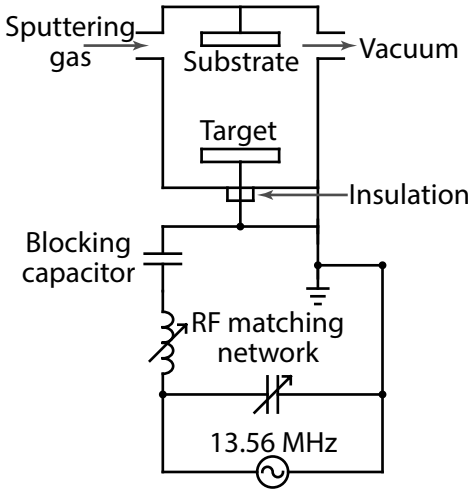


Figure 1.9: Schematic depiction of a sputtering chamber with RF sputtering. Before the blocking capacitor, a matching network is required to minimize reflections of the incident power.

1.4.2 Sputtering Insulating Materials

The discussion from the previous section involves the simplest configuration for sputtering: direct current (DC) sputtering. When attempting to sputter insulating materials, much of the voltage drop required to create and sustain a plasma occurs across the insulating target itself. Therefore, the surface of the target is already quite close to the ground potential and no plasma can be struck. This problem of high resistivity of an insulating material can be overcome by applying a high-frequency oscillating voltage on the to-be sputtered insulator, in much the same way as one would transfer voltage across a dielectric-filled capacitor [67, p. 5.2.4]. At frequencies above 1 MHz, electrons in the plasma acquire enough energy to ionize the Ar gas to form the required Ar^+ for sputtering.[9] The radio frequency (RF) is also sufficiently high that electrons will rapidly oscillate, due to their small mass. This is contrary to the ionized argon which will be less affected by the oscillating field, due to its much higher mass. Therefore, Ar^+ will only 'feel' the time-averaged field, and will therefore move towards the nearest cathode (our target material).

With an oscillating applied voltage, how exactly do we have a cathode? This is an added benefit of the low mobility of the positive ions. By placing a blocking capacitor between the target and the power supply (see Figure 1.9), no net current

[9] Practically all sputter coaters operate their radio frequency sources at 13.56 MHz, as this frequency is not reserved for telecommunications.

is allowed to flow. Because of the high mobility of the electrons, the positive half of an RF voltage sweep will yield a large electron current, which the lower mobility Ar^+ ions will never be able to compensate in terms of charge. As a result, the target 'self-biases' to a negative voltage, as can be seen in Figure 1.10. This self-biasing limits the electron current, and thereby equalizes the electron and Ar^+ current to the target. Therefore, averaged over time, no net current flows, satisfying the requirement put in place by our blocking capacitor. Since the target is now self-biased to a negative voltage, the target is now also the cathode we desire for sputtering.

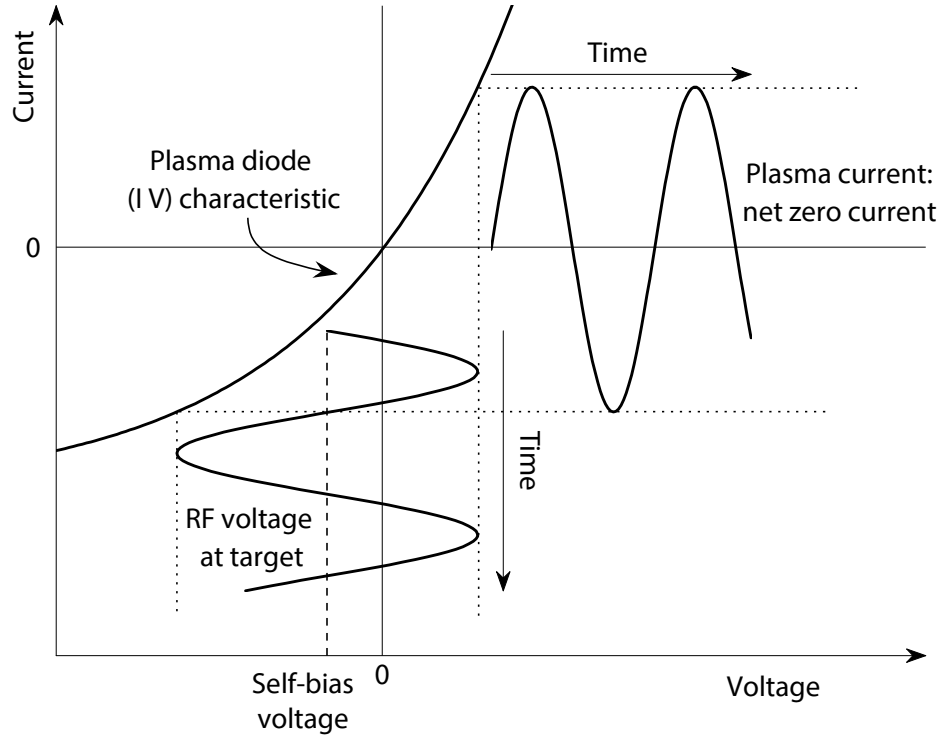


Figure 1.10: Self-bias of the target cathode. Because of the blocking capacitor (see Figure 1.9), no net current is allowed to flow. The diode characteristic of the plasma can be used to connect the current and the voltage. Therefore, when seeing what voltage goes paired with no net sinusoidal current (the dotted lines), we see that a negative self-biasing (indicated by the dashed line) of the target voltage occurs.

Even though RF sputtering makes it possible to sputter nearly any solid material, one should take practical considerations into account. Because of the

oscillating field, ion currents are never as high as with DC sputtering at equal powers. As a rule of thumb, a film grown by RF sputtering a conducting target will have only half of the deposition rate compared to a DC process at equal applied power.

1.4.3 Forming Nitrides and Oxides from Metallic Targets

One way to deposit nitride or oxide thin-films is to just begin with the nitride or oxide as starting material. This comes with many caveats:

- Atoms in a compound are more strongly bound than they are in elements. Therefore, U_s is significantly higher than for elemental materials. This leads to a much decreased sputtering yield, as per Equation (1.3).
- The different masses of the constituents can lead to one constituent being more scattered in the sputtering chamber than the other, leading to substoichiometric thin-films.
- The amount of flexibility is quite low. Many targets would be required to transition from a metal to an oxide, to an oxinitride, to a nitride.

Therefore, it is very desirable to sputter in a reactive atmosphere. In such a reactive atmosphere, Ar is still present to do the legwork for the sputtering of a metallic target. However, next to Ar being present, partial pressures of O_2 and N_2 can be introduced for the formation of oxidized and nitrided thin-films, as will be used in Chapter 5 and Chapter 6.

1.5 Outline

As has been mentioned in Section 1.3, this thesis mainly concerns the development and understanding of luminescent inorganic thin-films doped with rare-earth elements for use as luminescent solar concentrators. In order to further the LSC field, first a thorough understanding of the principle of operation of an LSC is needed, combined with a critical overview of the state-of-the-art. Therefore, in Chapter 2, a quantitative description of all separate optical processes that occur within an an LSC can be found. This chapter furthermore shows the state-of-the-art of LSCs in terms of optical efficiencies. Data from recent literature, in which

all properties necessary to simulate an LSC, i.e., absorption, emission, and quantum yield, has been presented is gathered. These data are used to calculate the expected performance in terms of coloring and optical efficiency of realistically sized LSCs, for 20 % visible light absorption.

In most literature (e.g. [73–77]), as well as in Chapter 2, the Monte Carlo (MC) raytracing approach is used to calculate the output of an LSC. The MC approach offers a very insightful and straightforward way of simulating LSCs. A disadvantage of MC is that it is a statistical approach. As the LSC of interest grows larger in size, or becomes more absorbing, the duration of the simulation will increase drastic the the case of a larger LSC, more rays will have to be simulated to obtain sufficient statistics to come to a satisfactor the For this reason, Chapter 3 presents a semi-analytical model that calculates the efficiency of an LSC with a constant simulation duration, regardless of LSC size or absorption strength. Like MC, this model can quantify what optical process within the LSC is responsible for the loss of efficiency. The chapter concludes with what can be expected in terms of power output from optimized LSCs used as BIPV.

The synthesis of luminescent thin-films is carried out by employing the combinatorial approach of continuous composition spreads using sputter deposition. This approach to the synthesis of luminescent materials requires a new way to semi-automatically characterize the luminescent properties, complex index of refraction, and composition of these gradient thin-films.

In Chapter 4, the foundation is laid for the combinatorial synthesis and characterization methods used throughout the rest of this thesis. In this chapter, the formation of a solid solution from two halide constituents is realized. The ability to form solid solutions during sputtering can be an essential step towards attaining the desired uniform absorption for LSCs made of glass, coated with halide thin-films. NaI and NaBr are therefore combinatorially sputtered and doped with Eu^{2+}. Here Eu^{2+} is used, as its emission wavelength is directly influenced by the surrounding host. The luminescence coming from Eu^{2+} therefore immediately shows if a solid solution that obeys Vegard's law has indeed formed. A novel setup, called the *xy*-scanner, is built and used to quickly process the many compositions present on the gradient-sputtered luminescent thin-film. This setup excites the thin-film using a focused wavelength-tunable laser and locally resolves the luminescence in terms of excitation, emission and photoluminescent decay. This local luminescence data is combined with local composition data

and therefore yields the influence the host and dopant-concentration have on the luminescence.

LSCs based on halides doped with divalent thulium show promising properties, such as a lack of self-absorption and absorption of the entire visible spectrum [78]. Yet, most halides are, unfortunately, hygroscopic and not sputtered by industry. The SiAlON-material family solves many of these issues, as it is a stable, scratch-resistant family of materials that is already routinely sputtered, in its undoped form, in the glass industry. In Chapter 5 the gradient deposition and analysis technique is employed to study a large library of previously unexplored SiAlON:Eu^{2+} compounds. Here, the *xy*-scanner is extended to also locally resolve the film's thickness, index of refraction and absorption coefficient. The effects that altering the ratio of Al to Si, and increasing the doping concentration of Eu, has on the quantum yield and emission of Eu^{2+} is studied on a single substrate. In this chapter, the host compound and dopant constitute three different materials. Ternary phase diagrams are therefore used to express the influence the composition has on emission, quantum yield, and index of refraction.

To mitigate the problem of parasitic self-absorption in an LSC, while retaining a window that is transparent to visible light, UV-light-absorbing and visible-light-emitting materials can be used. Consequently, in Chapter 6, the techniques presented in Chapter 4 are used on an AlN:Eu^{3+},O^{2-} concentration library. AlN:Eu^{3+},O^{2-} is known to be a strong UV-absorber and red-emitter. The exact absorption strength, and the influence dopant concentration has on the quantum yield were however unknown. In this chapter, all properties relevant for the optimization of an LSC are extracted from an AlN:Eu^{3+},O^{2-} thin-film library, where the Eu concentration varies. By combining the data of the local composition with the luminescence and optical properties of the gradient thin-film, the potential of AlN:Eu^{3+},O^{2-} as a UV-absorbing and red-emitting LSC is modeled. The techniques and applied model presented in this chapter are not specific to AlN:Eu^{3+},O^{2-}, but can be used for any sputtered luminescent thin-film that does not show self-absorption.

Finally, in Chapter 7, the techniques explored in Chapter 4 and Chapter 6 are combined and applied to a set of halide materials doped with Tm^{2+}. As already explored in Chapter 2, halide LSCs doped with Tm^{2+} can absorb the entire visible spectrum and emit in the near-infrared (NIR) without parasitic self-absorption. In this chapter this system is studied in detail, and the potential for use as LSC

is modeled.

References

[1]IEA, *Global Energy & CO_2 Status Report 2019*, 2019.

[2]United Nations Framework Convention on Climate Change, *Paris Agreement*, 2015.

[3]G. F. Nemet, *How Solar Energy Became Cheap: A Model for Low-Carbon Innovation* (Routledge, Abingdon, Oxon; New York, NY : Routledge, 2019., May 2019).

[4]National Renewable Energy Laboratory, *Best Research-Cell Efficiency Chart*, 2020.

[5]K. Yoshikawa, H. Kawasaki, W. Yoshida, T. Irie, K. Konishi, K. Nakano, T. Uto, D. Adachi, M. Kanematsu, H. Uzu, and K. Yamamoto, "Silicon heterojunction solar cell with interdigitated back contacts for a photoconversion efficiency over 26%," Nature Energy **2**, 17032 (2017).

[6]M. A. Green, E. D. Dunlop, J. Hohl-Ebinger, M. Yoshita, N. Kopidakis, and A. W. Ho-Baillie, "Solar cell efficiency tables (Version 55)," Progress in Photovoltaics: Research and Applications **28**, 3–15 (2020).

[7]M. Saifullah, J. Gwak, and J. H. Yun, "Comprehensive review on material requirements, present status, and future prospects for building-integrated semitransparent photovoltaics (BISTPV)," Journal of Materials Chemistry A **4**, 8512–8540 (2016).

[8]W. H. Weber and J. Lambe, "Luminescent greenhouse collector for solar radiation.," Applied Optics **15**, 2299–2300 (1976).

[9]J. S. Batchelder, A. H. Zewail, and T. Cole, "Luminescent solar concentrators 2: Experimental and theoretical analysis of their possible efficiencies," Applied Optics **20**, 3733 (1981).

[10]V. Wittwer, W. Stahl, and A. Goetzberger, "Fluorescent planar concentrators," Solar Energy Materials **11**, 187–197 (1984).

[11]M. A. Green, "How Did Solar Cells Get So Cheap?" Joule **3**, 631–633 (2019).

[12]B. Norton, P. C. Eames, T. K. Mallick, M. J. Huang, S. J. McCormack, J. D. Mondol, and Y. G. Yohanis, "Enhancing the performance of building integrated photovoltaics," Solar Energy **85**, 1629–1664 (2011).

[13]M. G. Debije and P. P. C. Verbunt, "Thirty Years of Luminescent Solar Concentrator Research: Solar Energy for the Built Environment," Advanced Energy Materials **2**, 12–35 (2012).

[14]K. Barnham, J. L. Marques, J. Hassard, and P. O'Brien, "Quantum-dot concentrator and thermodynamic model for the global redshift," Applied Physics Letters **76**, 1197–1199 (2000).

[15]M. Rafiee, S. Chandra, H. Ahmed, and S. J. McCormack, "An overview of various configurations of Luminescent Solar Concentrators for photovoltaic applications," Optical Materials **91**, 212–227 (2019).

[16]W. Chen, J. Li, P. Liu, H. Liu, J. Xia, S. Li, D. Wang, D. Wu, W. Lu, X. W. Sun, and K. Wang, "Heavy Metal Free Nanocrystals with Near Infrared Emission Applying in Luminescent Solar Concentrator," Solar RRL **1**, 1700041 (2017).

[17]M. R. Bergren, N. S. Makarov, K. Ramasamy, A. Jackson, R. Guglielmetti, and H. McDaniel, "High-Performance $CuInS_2$ Quantum Dot Laminated Glass Luminescent Solar Concentrators for Windows," ACS Energy Letters **3**, 520–525 (2018).

[18]A. P. Green and A. R. Buckley, "Solid state concentration quenching of organic fluorophores in PMMA," Physical Chemistry Chemical Physics **17**, 1435–1440 (2015).

[19]L. Desmet, A. J. M. Ras, D. K. G. de Boer, and M. G. Debije, "Monocrystalline silicon photovoltaic luminescent solar concentrator with 4.2% power conversion efficiency," Optics Letters **37**, 3087–3089 (2012).

[20]F. P. Schäfer, *Dye Lasers*, edited by F. P. Schäfer, 3rd ed., Topics in Applied Physics (Springer Berlin Heidelberg, Berlin, Heidelberg, 1989), p. 228.

[21]K. G. Fleming, "Fluorescence Theory," in *Encyclopedia of spectroscopy and spectrometry* (2010), pp. 628–634.

[22]L. H. Slooff, E. E. Bende, A. R. Burgers, T. Budel, M. Pravettoni, R. P. Kenny, E. D. Dunlop, and A. Büchtemann, "A luminescent solar concentrator with 7.1% power conversion efficiency," physica status solidi (RRL) - Rapid Research Letters **2**, 257–259 (2008).

[23]K. Wu, H. Li, and V. I. Klimov, "Tandem luminescent solar concentrators based on engineered quantum dots," Nature Photonics **12**, 105–110 (2018).

[24]C. Tummeltshammer, M. Portnoi, S. A. Mitchell, A.-T. Lee, A. J. Kenyon, A. B. Tabor, and I. Papakonstantinou, "On the ability of Förster resonance energy transfer to enhance luminescent solar concentrator efficiency," Nano Energy **32**, 263–270 (2017).

[25]F. Meinardi, F. Bruni, and S. Brovelli, "Luminescent solar concentrators for building-integrated photovoltaics," Nature Reviews Materials **2**, 17072 (2017).

[26]D. J. Norris and M. G. Bawendi, "Measurement and assignment of the size-dependent optical spectrum in CdSe quantum dots," Physical Review B **53**, 16338–16346 (1996).

[27]C. Delerue and M. Lannoo, *Nanostructures - Theory and Modeling*, 1st ed., NanoScience and Technology (Springer Berlin Heidelberg, Berlin, Heidelberg, 2004).

[28]P. Moraitis, R. Schropp, and W. van Sark, "Nanoparticles for Luminescent Solar Concentrators - A review," Optical Materials **84**, 636–645 (2018).

[29]D. Vasudevan, R. R. Gaddam, A. Trinchi, and I. Cole, "Core-shell quantum dots: Properties and applications," Journal of Alloys and Compounds **636**, 395–404 (2015).

[30]A. R. AbouElhamd, K. A. Al-Sallal, and A. Hassan, "Review of core/shell quantum dots technology integrated into building's glazing," Energies **12**, 10.3390/en12061058 (2019).

[31]G. B. Haxel, J. B. Hedrick, and G. J. Orris, "Rare Earth Elements - Critical Resources for High Technology," United States Geological Survey. USGS Fact Sheet: 087-02, edited by P. H. Stauffer II and J. W. Hendley, 1–11 (2002).

[32]J.-C. G. Bünzli, "Lanthanide Photonics: Shaping the Nanoworld," Trends in Chemistry, 1–13 (2019).

[33]G. Blasse and B. C. Grabmaier, *Luminescent Materials*, Vol. 148, 3743 (1941), pp. 118–119.

[34]B. Henderson and G. F. Imbusch, *Optical Spectroscopy of Inorganic Solids* (Oxford University Press, New York, 1989).

[35]W. G. van Sark, J. de Wild, J. K. Rath, A. Meijerink, and R. E. Schropp, "Upconversion in solar cells," Nanoscale Research Letters **8**, 81 (2013).

[36]C. Ronda, *Luminescence: From Theory to Applications*, edited by C. Ronda (WILEY-VCH Verlag GmbH & Co. KGaA, Weinheim, 2008).

[37]X. Huang, S. Han, W. Huang, and X. Liu, "Enhancing solar cell efficiency: the search for luminescent materials as spectral converters," Chemical Society Reviews **42**, 173–201 (2013).

[38]B. M. van der Ende, L. Aarts, and A. Meijerink, "Lanthanide ions as spectral converters for solar cells," Physical Chemistry Chemical Physics **11**, 11081 (2009).

[39]G. H. Dieke, H. M. Crosswhite, and B. Dunn, "Emission Spectra of the Doubly and Triply Ionized Rare Earths*," Journal of the Optical Society of America **51**, 820 (1961).

[40]C.-G. Ma, M. Brik, D.-X. Liu, B. Feng, Y. Tian, and A. Suchocki, "Energy level schemes of f^N electronic configurations for the di-, tri-, and tetravalent lanthanides and actinides in a free state," Journal of Luminescence **170**, 369–374 (2016).

[41]T. Wang, J. Zhang, W. Ma, Y. Luo, L. Wang, Z. Hu, W. Wu, X. Wang, G. Zou, and Q. Zhang, "Luminescent solar concentrator employing rare earth complex with zero self-absorption loss," Solar Energy **85**, 2571–2579 (2011).

[42]C. S. Erickson, L. R. Bradshaw, S. McDowall, J. D. Gilbertson, D. R. Gamelin, and D. L. Patrick, "Zero-Reabsorption Doped-Nanocrystal Luminescent Solar Concentrators," ACS Nano **8**, 3461–3467 (2014).

[43]R. Martín-Rodríguez, R. Geitenbeek, and A. Meijerink, "Incorporation and Luminescence of Yb^{3+} in CdSe Nanocrystals," Journal of the American Chemical Society **135**, 13668–13671 (2013).

[44]Exact search term used for overlap: ((TITLE-ABS-KEY (luminescence OR phosphorescence OR luminescent OR phosphorescent) AND (rare?earth OR rare AND earth OR lanthanid* OR (la%% OR ce%% OR pr%% OR nd%% OR pm%% OR sm%% OR eu%% OR gd%% OR tb%% OR dy%% OR ho%% OR er%% OR tm%% OR yb%%))) AND (TITLE-ABS-KEY (combinatorial OR high?throughput OR librar*))) AND (LIMIT-TO (SUBJAREA , "ENGI") OR LIMIT-TO (SUBJAREA , "ENER") OR LIMIT-TO (SUBJAREA , "CHEM") OR LIMIT-TO (SUBJAREA , "PHYS") OR LIMIT-TO (SUBJAREA , "MATE") OR LIMIT-TO (SUBJAREA , "CENG")).

[45]G. Kresse and J. Furthmüller, "Efficient iterative schemes for ab initio total-energy calculations using a plane-wave basis set," Physical Review B **54**, 11169–11186 (1996).

[46]G. Kresse and D. Joubert, "From ultrasoft pseudopotentials to the projector augmented-wave method," Physical Review B **59**, 1758–1775 (1999).

[47]P. Dorenbos, "Energy of the first $4f^7 \leftrightarrow 4f^6 5d$ transition of Eu^{2+} in inorganic compounds," Journal of Luminescence **104**, 239–260 (2003).

[48]P. Dorenbos, "Systematic behaviour in trivalent lanthanide charge transfer energies," Journal of Physics: Condensed Matter **15**, 8417–8434 (2003).

[49]P. Dorenbos, "The $4f^n \leftrightarrow 4f^{n-1} 5d$ transitions of the trivalent lanthanides in halogenides and chalcogenides," Journal of Luminescence **91**, 91–106 (2000).

[50]P. Dorenbos, "The 5d level positions of the trivalent lanthanides in inorganic compounds," Journal of Luminescence **91**, 155–176 (2000).

[51]T. X. Sun, "Combinatorial Synthesis of Display Phosphors," in *Combinatorial materials synthesis*, edited by X.-D. Xiang and I. Takeuchi, 1st ed. (CRC Press, Aug. 2003) Chap. 6.

[52]X. .-D. Xiang, X. Sun, G. Briceno, Y. Lou, K.-A. Wang, H. Chang, W. G. Wallace-Freedman, S.-W. Chen, and P. G. Schultz, "A Combinatorial Approach to Materials Discovery," Science **268**, 1738–1740 (1995).

[53]M. Lippmaa, H. Koinuma, and M. Kawasaki, "Parallel Synthesis of Artificially Designed Lattices and Devices," in *Combinatorial materials synthesis*, edited by X.-D. Xiang and I. Takeuchi, 1st ed. (CRC Press, Aug. 2003) Chap. 5.

[54]W. H. Weinberg, E. Danielson, J. H. Golden, E. W. McFarland, C. M. Reaves, and X. D. Wu, "A combinatorial approach to the discovery and optimization of luminescent materials," Nature **389**, 944–948 (1997).

[55]E. Danielson, M. Devenney, D. M. Giaquinta, J. H. Golden, R. C. Haushalter, E. W. McFarland, D. M. Poojary, C. M. Reaves, W. H. Weinberg, X. D. Wu, C. M. R. Damodara M. Poojary, W. H. Weinberg, and X. D. Wu, "A Rare-Earth Phosphor Containing One-Dimensional Chains Identified Through Combinatorial Methods," Science **279**, 837–839 (1998).

[56]X.-D. Sun, C. Gao, J. Wang, and X.-D. Xiang, "Identification and optimization of advanced phosphors using combinatorial libraries," Applied Physics Letters **70**, 3353–3355 (1997).

[57]Q. Wei, J. Wan, G. Liu, Z. Zhou, H. Yang, J. Wang, and Q. Liu, "Combinatorial Optimization of La, Ce-co-Doped Pyrosilicate Phosphors as Potential Scintillator Materials," ACS Combinatorial Science **17**, 217–223 (2015).

[58]R. Takahashi, H. Kubota, M. Murakami, Y. Yamamoto, Y. Matsumoto, and H. Koinuma, "Design of Combinatorial Shadow Masks for Complete Ternary-Phase Diagramming of Solid State Materials," Journal of Combinatorial Chemistry **6**, 50–53 (2004).

[59]B. Lee, S. Lee, H. G. Jeong, and K.-S. Sohn, "Solid-State Combinatorial Screening of $(Sr,Ca,Ba,Mg)_2Si_5N_8:Eu^{2+}$ Phosphors," ACS Combinatorial Science **13**, 154–158 (2011).

[60]L. Chen, Y. Fu, G. Zhang, J. Bao, and C. Gao, "Optimization of Pr^{3+}, Tb^{3+}, and Sm^{3+} Co-Doped $(Y_{0.65}Gd_{0.35})BO_3:Eu^{3+}_{0.05}$ VUV Phosphors through Combinatorial Approach," Journal of Combinatorial Chemistry **10**, 401–404 (2008).

[61]T.-S. Chan, Y.-M. Liu, and R.-S. Liu, "Combinatorial Search for Green and Blue Phosphors of High Thermal Stabilities under UV Excitation Based on the $K(Sr_{1-x-y})PO_4:Tb_x^{3+}Eu_y^{2+}$ System," Journal of Combinatorial Chemistry **10**, 847–850 (2008).

[62]S. Frost, S. Guérin, B. E. Hayden, J.-P. Soulié, and C. Vian, "High-Throughput Synthesis and Characterization of Eu Doped $Ba_xSr_{2-x}SiO_4$ Thin Film Phosphors," ACS Combinatorial Science, acscombsci.8b00045 (2018).

[63]R. Bruce van Dover and L. Schneemeyer, "The Continuous Composition Spread Approach," in *Combinatorial materials synthesis*, edited by X.-D. Xiang and I. Takeuchi, 1st ed. (CRC Press, Aug. 2003) Chap. 3.

[64]S. M. Rossnagel, "Sputter deposition for semiconductor manufacturing," IBM Journal of Research and Development **43**, 163–179 (1999).

[65]D. Depla and S. Mahieu, *Reactive Sputter Deposition*, edited by D. Depla and S. Mahieu, Vol. 109, Springer Series in Materials Science (Springer Berlin Heidelberg, Berlin, Heidelberg, 2008).

[66]J. E. Greene, "Review Article: Tracing the recorded history of thin-film sputter deposition: From the 1800s to 2017," Journal of Vacuum Science & Technology A: Vacuum, Surfaces, and Films **35**, 05C204 (2017).

[67]M. Ohring, *Materials Science of Thin Films* (2001).

[68]S. Cornelius, "Charge transport limits and electrical dopant activation in transparent conductive (Al,Ga):ZnO and Nb:TiO_2 thin films prepared by reactive magnetron sputtering," Doctoral dissertation (2014), p. 225.

[69]D. Depla, S. Mahieu, and J. Greene, "Sputter Deposition Processes," in *Handbook of Deposition Technologies for Films and Coatings*, Third Edition (Elsevier, 2010), pp. 253–296.

[70]J. E. Mahan and A. Vantomme, "A simplified collisional model of sputtering in the linear cascade regime," Journal of Vacuum Science & Technology A: Vacuum, Surfaces, and Films **15**, 1976–1989 (1997).

[71]J. A. Dean, *Lange's Handbook of Chemistry* (McGraw-Hill Professional, Oct. 1998).

[72]Y. Zhang, J. R. G. Evans, and S. Yang, "Corrected Values for Boiling Points and Enthalpies of Vaporization of Elements in Handbooks," Journal of Chemical & Engineering Data **56**, 328–337 (2011).

[73]M. Carrascosa, S. Unamuno, and F. Agullo-Lopez, "Monte Carlo simulation of the performance of PMMA luminescent solar collectors.," Applied optics **22**, 3236 (1983).

[74]D. Şahin, B. Ilan, and D. F. Kelley, "Monte-Carlo simulations of light propagation in luminescent solar concentrators based on semiconductor nanoparticles," Journal of Applied Physics **110**, 033108 (2011).

[75]S. R. Wilton, M. R. Fetterman, J. J. Low, G. You, Z. Jiang, and J. Xu, "Monte Carlo study of PbSe quantum dots as the fluorescent material in luminescent solar concentrators," Optics Express **22**, A35 (2014).

[76]V. I. Klimov, T. A. Baker, J. Lim, K. A. Velizhanin, and H. McDaniel, "Quality Factor of Luminescent Solar Concentrators and Practical Concentration Limits Attainable with Semiconductor Quantum Dots," ACS Photonics, acsphotonics.6b00307 (2016).

[77]F. Meinardi, Q. A. Akkerman, F. Bruni, S. Park, M. Mauri, Z. Dang, L. Manna, and S. Brovelli, "Doped Halide Perovskite Nanocrystals for Reabsorption-Free Luminescent Solar Concentrators," ACS Energy Letters **2**, 2368–2377 (2017).

[78]O. M. ten Kate, K. W. Krämer, and E. van der Kolk, "Efficient luminescent solar concentrators based on self-absorption free, Tm^{2+} doped halides," Solar Energy Materials and Solar Cells **140**, 115–120 (2015).

— 2 —

The State-of-the-Art of Luminescent Solar Concentrators

This chapter explicates the working principle behind luminescent solar concentrators (LSCs). An overview of the optical properties of 28 state-of-the-art LSCs is presented. These LSCs are evaluated with regards to their performance for building-integrated purposes. Simulations show that non-toxic quantum-dot-based LSCs can already attain an optical efficiency of more than 2.8 %, without compromising on color rendering properties. Next to these state-of-the-art LSCs, a new development in the form of thulium-doped halides is highlighted. These halides are able to absorb the entire visible spectrum without coloration, and could be scaled to efficient LSCs of virtually and size thanks to their lack of self-absorption.

Parts of this chapter have been published as: E.P.J. Merkx and E. van der Kolk, "Luminescent Solar Concentrators," in *Indoor Photovoltaics*, edited by M. Freunek. (Wiley-Scrivener, 2020) Chap. 6

2.1 Principle of Operation

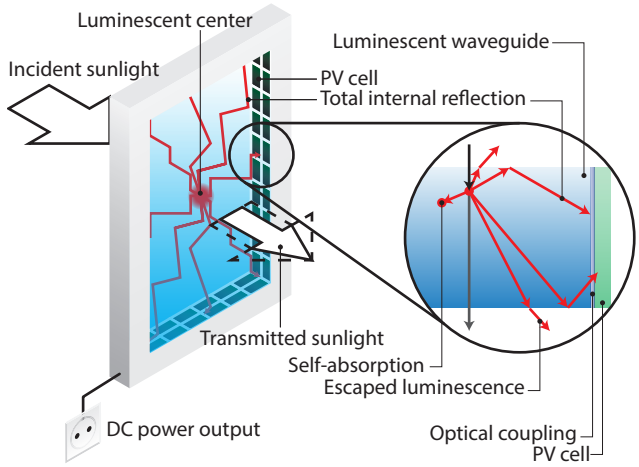


Figure 2.1: Schematic of the working of a single-layer LSC. Other configurations are also possible. For instance, (laminated) films on a waveguide (e.g., glass or polycarbonate); or tandem configurations, where two LSCs are stacked on top of each other.

The workings of a luminescent solar concentrator (LSC) are schematically summarized in Figure 2.1. In brief, an LSC works by concentrating direct and diffuse incident light absorbed at the face of a luminescent waveguide onto photovoltaic cells located at the sides of the waveguide. The concentration of light occurs because luminescent centers absorb the incident light and convert the light to a longer wavelength. The waveguide then guides the generated luminescence to the sides, through total internal reflection. A more in-depth explanation can be found in the following sections.

2.1.1 Absorption of Light

At its core, an LSC is nothing more than a luminescent material embedded in, or placed on top of, a waveguide. For an LSC to function, it needs to be exposed to a source of light. An LSC works with both direct and diffuse light. Dependent on the refractive index of the material used to build the LSC, light will be refracted into it. For an LSC made of a single slab of PMMA, 96 % of light incident normal to the surface of the LSC will be refracted into the LSC. Light incident at different angles will have lower efficiencies in accordance with the Fresnel laws, as will be explained in Chapter 3. The light that has been refracted into the LSC can

now be absorbed by the luminescent particles within. Of course, not all refracted light will be absorbed. The amount of absorption is dependent on both (i) the physical properties of the luminescent particles, and (ii) design considerations of the LSC. For use as a building-integrated photovoltaic window, LSCs that absorbs ultraviolet (UV) light can have up to 100 % absorption. By contrast, LSCs that absorb visible light (up to a specific color, or the entire visible spectrum) should have lower absorption, to still provide sufficient light for the environment behind the window. In a study by Vossen et al. [1], it was shown that 25 % absorption is the limit for red-tinted LSC BIPV windows. All things remaining equal, an LSC that absorbs 25 % of the visible spectrum will always outperform an LSC that absorbs 100 % of the UV, just because sunlight has substantially more photons in the visible spectrum than in the UV. All light refracted into the LSC and not absorbed will be refracted out the back of the LSC and illuminate the area behind it.

2.1.2 Emission within the LSC

The light absorbed by the luminescent particles will be converted to emission characteristic for the luminescent particle in question. Usually, especially with experimental materials, this conversion does not happen with 100 % efficiency. Part of the absorbed light will excite the available phonon modes in the LSC, eventually only generating heat. The absorbed light that 'survived' conversion will now be emitted isotropically within the LSC[1]. This separation of absorption and emission is precisely what makes an LSC independent of the direction and type of incident light, as the direction of the emitted photons is randomized independently of their origin. As happened with the light incident on the LSC, the light emitted by the luminescent particles can be refracted out of the LSC's faces. Again, this happens in accordance with the Fresnel laws. The light that is refracted out is said to "be in the escape cone". The light that is not refracted out of the LSC will remain 'trapped' within the waveguide by total internal reflection (TIR) and will start traveling through the LSC, much like light coupled into an optical fiber would. The percentage of converted photons trapped within the

[1] As with everything, exceptions to this generalization exist. A subclass of LSC materials feature non-isotropic emission with e.g., specially oriented nanorods, that are optimized to couple the emitted light to the sides of the LSC, promoting total internal reflection, and therefore overall efficiency [2, 3].

LSC is referred to as the trapping efficiency η_{trap}. For a single-slab PMMA LSC, η_{trap} amounts to approximately 75 %.

2.1.3 Effects of Self-Absorption

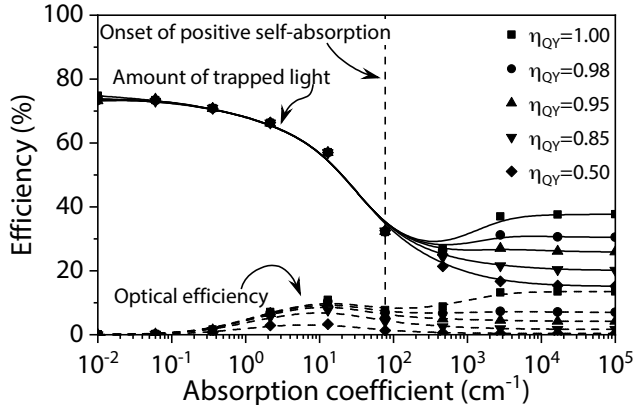


Figure 2.2: Theoretical efficiencies of a Red305 LSC with varying absorption coefficient and quantum yield, as will be presented in more detail in Chapter 3. At a sufficiently high quantum yield, the trapping of light can increase due to recapture of light in the escape cone. This recaptured light can then partake in the total internal reflection process. The optical efficiency rises, since with an increasing absorption coefficient the absorption of incident sunlight rises.

The description from the previous paragraphs is a complete overview for LSCs without any overlap between their absorption and emission spectra. However, if the used luminophore has such an overlap, the emitted light traveling through the LSC can be reabsorbed in a process known as 'parasitic self-absorption'. As can be seen in Figure 2.2 for BASF Lumogen F Red305, one of the best-known LSC materials, a high degree of self-absorption can occur. Parasitic self-absorption is a problem, as it results in a photon that was traveling to the LSC perimeter by TIR becoming reabsorbed by the luminescent particles. The photon then might get quenched (non-unity η_{QY}) or get re-emitted, but in such a direction that it is lost in the escape cone. It should, however, be noted that self-absorption does not always have to be detrimental to the overall efficiency of an LSC. As shown in Figure 2.2, if a material has a sufficiently high η_{QY}, paired with a sufficiently high absorption, self-absorption can bolster the overall LSC efficiency. This effect was first shown theoretically in Chapter 3 and

then experimentally by Krumer et al. [4]. If the absorption is sufficiently high, light originally emitted in the escape cone will be reabsorbed and subsequently re-emitted with a high probability of not ending up in the escape cone again, thereby contributing to the overall LSC efficiency.

2.1.4 Influence of the Waveguide

Even in luminophores that have no overlapping absorption and emission, another limiting factor for the light transport efficiency is the waveguide itself [5, 6]. Scattering of light during TIR leads to losses in efficiency. This scattering can happen either at the surface of the waveguide due to surface roughness, or within the waveguide due to defects in the LSC itself. This scattering leads to a randomization of the traveling direction of the formerly waveguided light, which may result in the light being scattered into the escape cone[2]. For LSCs larger than 1 m^2, such as LSC-based windows, the eventual device efficiency can differ by a factor 10, based on the choice of waveguide. As shown in Ref. [8], normal window glass (soda-lime) has a too high an absorption in the red to near infrared spectrum relevant to LSCs to be of practical use in windows. Other materials, such as N-BK7 glass, fluorinated PMMA, or TIREXtreme make for a much more viable non-absorbing waveguide. For IPV applications, the absorption from the waveguide will not impact performance much, given the short distances emitted light has to travel.

2.1.5 Conversion of Concentrated Light to Electricity

When the TIR light reaches the perimeter of the LSC, most conventional LSC designs dictate that the light will be coupled out of the waveguide, mediated by a form of optical coupling, to finally be converted into electricity by a photovoltaic cell. Most often, off-the-shelf Si PV cells are used in LSC research [9], since most contemporary LSCs output yellow to red light. In this range, Si PV cells have excellent performance. However, off-the-shelf photovoltaics are to an increasing degree optimized to absorb the solar spectrum, and so are LSCs. LSCs try to convert this sunlight outside of their absorption range, i.e., out of the visible range, and into the red to NIR, where Si PV cells start to lose performance.

[2] Sufficient scattering might lead to an increase in LSC performance [7]. A high degree of scattering does also mean that the LSC will appear hazy, defeating its use as a window-like PV.

One strategy to overcome the spectral mismatch between LSC output and Si input is to use high efficiency III-V PV cells, such as GaAs [10] or InGaP [11, 12]. Using these better-matched cells can greatly enhance the LSC efficiency, typically by a factor 2–3 (see Chapter 3). Another approach would be to latch on to the recent developments in wavelength-tunable PV, by using perovskite-based solar cells or by tuning the bandgap of CIGS cells, that have better absorption characteristics in the LSC output region [13].

2.2 Calculating LSC Performance

With the qualitative description of the previous section in mind, an LSC can be modeled in much the same way as one would model a PV module: through ray-tracing. As such, some LSC articles even extend upon conventional PV modeling software or principles. This ray-tracing approach will be treated in Section 3.3. A more analytic approach that follows the same paradigm of tracing the separate optical steps is described in Section 2.2.2. This analytic approach yields the maximal possible output for an LSC with a simple geometry. A more detailed approach, suitable for LSCs of any geometry is described using a quick semi-analytic approach in Chapter 3. Next to the methods presented here, LSCs can also be described through entropic models, as described extensively in Ref. [14].

2.2.1 Figures of Merit

Before we start with how an LSC can be calculated in full, we first have to define what it exactly is that we want to calculate. The goal of an LSC is to convert light incident on its faces to light radiating from its sides. This concentration of light is quantified by what in literature is referred to as the 'optical efficiency'

$$\eta_{\text{opt}} = \frac{\#\text{photons in}}{\#\text{photons out at edges}} = \frac{\int S_{\text{in}}(\lambda)\ \mathrm{d}\lambda}{\int S_{\text{edges}}(\lambda)\ \mathrm{d}\lambda}\,. \tag{2.1}$$

η_{opt} is sometimes also referred to as the 'LSC luminescence efficiency' $\eta^{\text{PL,LSC}}$ [15], and sometimes, confusingly, the 'external quantum efficiency' [11], although the external quantum efficiency can also refer to all light emitted from the LSC (i.e. both from the faces and the sides).

Here it should be noted that η_{opt} is not concerned with the origin of the photons or whether their wavelengths are useful for further conversion by a

photovoltaic cell. This is where the PV, or power efficiency comes in:

$$\eta_{\text{Power}} = \frac{I_{\text{sc}} V_{\text{oc}} FF}{P_{\text{in}}} \,. \tag{2.2}$$

Here, I_{sc} is the short-circuit current, V_{oc} the open-circuit voltage and FF the filling factor of the LSC waveguide combined with photovoltaic cells while exposed to a light source (such as the sun, an LED, or tube lighting) with power P_{in}.

In LSC literature, the optical efficiency is preferred over the power efficiency. The power efficiency is too dependent on the performance of the optical coupling and on the types of PV cells used and therefore does not say much about the performance of the LSC itself.

To quantify whether using an LSC is more efficient than directly exposing the attached PV cells to the light source, another figure of merit is introduced: the concentration factor

$$\Gamma = \frac{G\eta_{\text{Power}}}{\eta_{\text{PV}}} \,, \tag{2.3}$$

where $G = \frac{A_{\text{LSC}}}{A_{\text{PV}}}$ is the geometric gain (the ratio of the face area of the LSC to that of the attached PV cells) and η_{PV} the efficiency of the used PV cells.

At the time of writing, the top-performing single-crystal Si PV cells have $\eta_{\text{PV}} = 26.7\,\%$ [16, 17].

If we assume a window measuring $1 \times 1 \times 0.05\,\text{m}^3$, this would mean that for an LSC with PV cells all around the window frame, $A_{\text{PV}} = 0.2\,\text{m}^2$. The LSC itself covers the entire window, measuring at $A_{\text{LSC}} = 1\,\text{m}^2$. For an LSC to make sense, $\Gamma \gg 1$. Therefore, $\eta_{\text{Power}} \gg 5.3\,\%$ for it to make sense to install an LSC, as opposed to exposing the PV cells directly to the incident sunlight.

2.2.2 Upper Bound for LSC Efficiency

In its most essential form, the behavior of an LSC can be summarized as

$$\eta_{\text{opt}} = (1 - R)\,\eta_{\text{abs}}\eta_{\text{QY}}\eta_{\text{trap}}\eta_{\text{SA}}\eta_{\text{WG}}. \tag{2.4}$$

Here, R is the amount of reflection from the LSC face, η_{abs} is the fraction of light that the luminophores contained within the LSC are able to absorb, η_{QY} is the quantum yield of the used luminophores, η_{trap} is the fraction of light emitted outside the escape cone and η_{SA} and η_{WG} are factors to take the self-absorption and waveguiding (scattering) efficiency respectively into account.

An upper bound for this optical efficiency, which does not take self-absorption into account, is given by

$$\eta_{\text{opt}} = \frac{\int [1 - R(\lambda)] \overbrace{S(\lambda)[1 - \exp(-\varepsilon(\lambda) c d)]}^{\eta_{\text{abs}}} \eta_{\text{QY}} \overbrace{\sqrt{1 - \frac{1}{n_{\text{LSC}}^2}}}^{\eta_{\text{trap}}} \mathrm{d}\lambda}{\int S(\lambda)\, d\lambda}. \tag{2.5}$$

Here, the first braced term is the Beer-Lambert law as a function of the molar attenuation coefficient $\varepsilon(\lambda)$ of the luminophore at concentration c, for an LSC of thickness d, for a light source with spectrum (expressed in amount of photons) $S(\lambda)$. $S(\lambda)$ is usually taken to be the AM1.5g spectrum, when discussing LSCs for solar (outdoor) applications. The term in the second brace is η_{trap} written out using Snell's law for a refractive index of n_{LSC}, for an LSC surrounded by air at both faces.

We now have all the ingredients needed to see what a hypothetical LSC should be capable of in order to be more effective than directly exposing the perimeter's PV cells to sunlight. As we saw in Section 2.2.1, for a $1 \times 1 \times 0.05\,\text{m}^3$ LSC with a perimeter of Si solar cells, we want $\eta_{\text{Power}} \gg 5.3\,\%$. To accomplish this, we can define two types of LSC that would not cause artificial color blindness[3], shown in Figure 2.3a. One type absorbs uniformly until 400 nm: a UV-absorbing LSC that leaves the visible spectrum unaltered. The other absorbs uniformly until 780 nm, thereby also dimming the visible light that enters a building. Both LSCs feature no self-absorption (as we cannot account for that yet) by emitting a 20 nm full-width half-maximum Gaussian centered at 900 nm. These hypothetical LSCs furthermore have $n = 1.49$ (PMMA), yielding $(1 - R) = 0.96$ for light at normal incidence and $\eta_{\text{trap}} = 0.75$.

Calculating the power efficiency for such an LSC works in much the same way as one would calculate the theoretical efficiency for a solar cell. The theoretical power efficiency for a solar cell is found by integrating the external quantum efficiency $EQE(\lambda)$ of the PV cell multiplied by the spectrum of light incident on the PV cell. In our case, that is the edge-emission spectrum of our LSC $\Phi_{\text{em}}(\lambda)$ in terms of photons per second. All these photons will get an energy equal to the

[3]Color blindness induced by an external source, such as a window that only transmits red light.

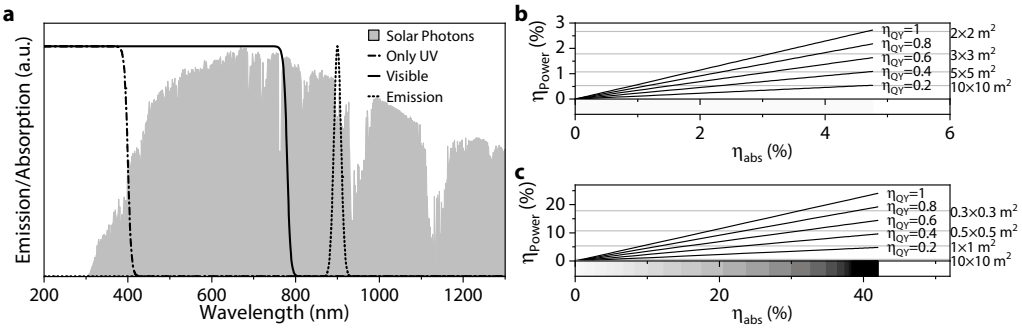


Figure 2.3: Power efficiencies for two hypothetical LSCs without self-absorption. **a:** Absorption spectra for two LSCs, one absorbing only UV light (until 400 nm), one absorbing UV and all visible light (until 780 nm), both emitting at 900 nm. Behind these spectra are normalized photon counts for AM1.5g. **b, c:** Power efficiencies for the UV- (panel b) and visible- (panel c) absorbing LSC. Grey reference lines are placed indicating at what surface area these square LSCs would exceed $\Gamma = 1$. Below the graphs is an indication of the perceived brightness of light passing through at the specified absorption efficiency.

bandgap of the PV cell E_g, which for Si is 1.12 eV. Excess energy of photons will be converted to heat.

The power efficiency is the ratio of the power output yielded by the converted photons to the incident solar power (in this case with an AM1.5g spectrum $S_{\mathrm{AM1.5}}(\lambda)$, expressed in photon flux). This leads to

$$\eta_{\mathrm{Power}} = \frac{\int_{\lambda=0}^{\infty} EQE(\lambda) \times E_g \times \Phi_{\mathrm{em}}(\lambda)\mathrm{d}\lambda}{A_{\mathrm{LSC}} \int_{\lambda=0}^{\infty} S_{\mathrm{AM1.5g}}(\lambda)\left(\frac{hc}{\lambda}\right)\mathrm{d}\lambda}, \tag{2.6}$$

with $EQE(\lambda)$ the wavelength-dependent external quantum efficiency and E_g the bandgap of the used PV cell, respectively. $\Phi_{\mathrm{em}}(\lambda)$ is the edge-emission spectrum, in terms of photons per second. A_{LSC} is the area of the LSC. $\frac{hc}{\lambda}$ is the energy-conversion factor ($1240/\lambda$ eV) from photon counts to energy.

Without self-absorption, the flux of converted photons Φ_{em} can be easily retrieved from the optical efficiency, combined with the emission spectrum of the LSC $S_{\mathrm{PL}}(\lambda)$:

$$\Phi_{\mathrm{em}}(\lambda) = \underbrace{\eta_{\mathrm{opt}} A_{\mathrm{LSC}} \int_{\lambda=0}^{\infty} S_{\mathrm{AM1.5g}}(\lambda)\mathrm{d}\lambda}_{\text{Rate of photon conversion}} \underbrace{\frac{S_{\mathrm{PL}}(\lambda)}{\int_{\lambda=0}^{\infty} S_{\mathrm{PL}}(\lambda)\mathrm{d}\lambda}}_{\text{Normalized emission}} \tag{2.7}$$

Figure 2.3b and c show the results of this calculation for our UV- and visible-light absorbing LSCs, respectively at different quantum yields. From Figure 2.3b, we

can see that a UV-absorbing LSC with unity quantum yield only becomes really effective at 100 % UV absorption (yielding $\eta_{\text{abs}} = 4.7\%$), and even then only when incorporated in large $> 4\,\text{m}^2$ windows. LSCs absorbing visible light perform more favorably, as shown in Figure 2.3c. Contrary to UV-absorbing LSCs, the visible-light-absorbing LSCs dim the incident visible light (as seen in the color bars below Figure 2.3b and c). Yet, a small amount of dimming already yields appreciable power efficiencies. To exceed $\Gamma = 1$, for a $1 \times 1 \times 0.05\,\text{m}^3$ LSC with a perimeter of Si solar cells at $\eta_{\text{QY}} = 1$, an η_{abs} of 12 % is needed, which amounts to only a minor amount of dimming, as can be seen in Figure 2.3c. Increasing the window size quickly yields $\Gamma > 1$ for LSCs absorbing the entire visible spectrum.

2.3 State-of-the-art LSC Materials

2.3.1 Measures for the Visual Performance of LSC Materials

As is evident from the previous sections, an ideal LSC is the result of a careful balancing exercise. To bolster efficiency, as much light as possible should be absorbed. Nevertheless, this absorption should have no overlap with the emission, as self-absorption is mostly detrimental to performance. For windows, high absorbance in the visible spectrum should be avoided because of their application as light sources: an opaque plate does not make for a good window. Next to the desired low absorption in the visible spectrum, the absorption spectrum should be featureless, so that the perceived color of objects illuminated through the window is still close to what it would be, were the object illuminated with white light.

A measure for the perceived color is the color rendering index R_a, introduced by the International Commission on Illumination [18]. R_a compares the spectrum measured from a light source (in our case, an LSC transmitting sunlight) with a standard illuminant operating at the same correlated color temperature (CCT). It does so by comparing the perceived color fourteen standard samples (listed in Table 2.1) acquire when illuminated by the tested light source (the LSC's transmission) to that of the standard illuminant (AM1.5g). The eventual difference gets assigned a value, with 100 being a perfect match with the reference, and mismatches being lower, and sometimes even negative values. The average

of the first eight of these values is the color rendering index. The European Standard (EN 12646:2011) requires a CCT between 3000 K and 5300 K (warm and intermediate white light) and a minimal R_a of 80 for work spaces like offices.

Table 2.1: List of test color samples.

Name	Approximate Munsell notation	Appearance under daylight	Swatch
TC S01	7,5 R 6/4	Light greyish red	
TC S02	5 Y 6/4	Dark greyish yellow	
TC S03	5 GY 6/8	Strong yellow green	
TC S04	2,5 G 6/6	Moderate yellowish green	
TC S05	10 BG 6/4	Light bluish green	
TC S06	5 PB 6/8	Light blue	
TC S07	2,5 P 6/8	Light violet	
TC S08	10 P 6/8	Light reddish purple	
TC S09	4,5 R 4/13	Strong red	
TC S10	5 Y 8/10	Strong yellow	
TC S11	4,5 G 5/8	Strong green	
TC S12	3 PB 3/11	Strong blue	
TC S13	5 YR 8/4	Light yellowish pink	
TC S14	5 GY 4/4	Moderate olive green (leaf)	

The perceived color of an LSC can be described by another CIE standard: the tristimulus values X, Y, Z. These values correlate the spectrum of the illuminant of interest to the spectral sensitivity of cone cells in human eyes. These values and can straightforwardly be found by integrating the transmitted spectrum $T(\lambda) \times S(\lambda)$, multiplied by the cone responsivity $\bar{x}(\lambda)$, $\bar{y}(\lambda)$, or $\bar{z}(\lambda)$ over the visible spectrum λ_{vis}:

$$X = K \int_{\lambda_{\text{vis}}} T(\lambda) S(\lambda) \bar{x}(\lambda) \, \mathrm{d}\lambda, \tag{2.8}$$

for X, with K a scaling factor between 0 and 100. For Y and Z similar formulas apply.

The tristimulus values can be normalized to chromaticity color coordinates x, y and z, e.g.:

$$x = \frac{X}{X + Y + Z}. \tag{2.9}$$

Here, x and y represent the chromaticity, and Y represents the luminance. These color coordinates make it possible to compare colors and can be plotted in a

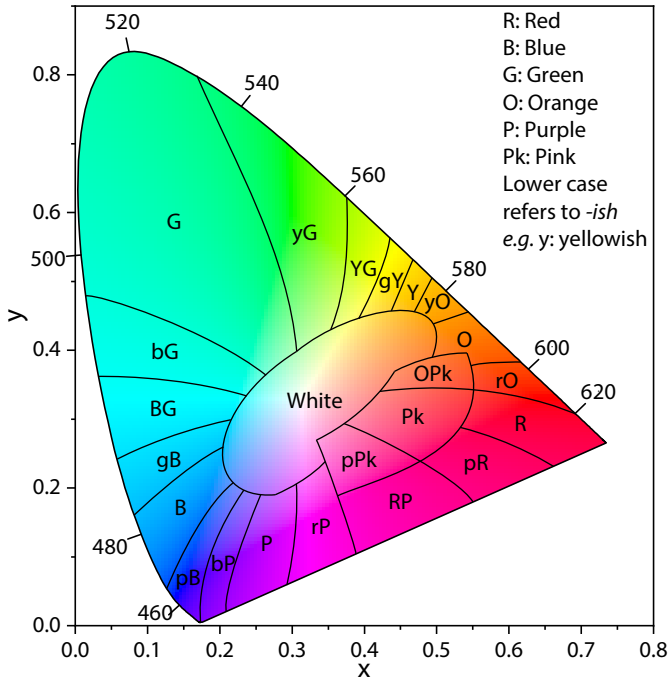


Figure 2.4: Example of the CIE 1931 color space chromaticity diagram with approximate regions and descriptions for colors added. The curve enclosing the colored regions indicates monochromatic light with wavelengths as displayed along the curve. Adapted from [19].

standardized CIE 1931 color space chromaticity diagram, an illustration of which is shown in Figure 2.4.

2.3.2 Evaluating the Performance of State-of-the-Art LSCs

To compare developments in LSCs, we have compiled a list of recently published luminescent materials and 'classical' LSC materials, such as BASF Lumogen F Red 305, and compared them based on a simulated $100 \times 100 \times 0.5\,\mathrm{cm}^3$ plate. This simulated plate is illuminated with AM1.5g light incident normal to the face of the plate. The performance of the plate is calculated with the Monte Carlo approach, as will be described in Chapter 3, using 10^6 photons. An assessment is made on the performance of the plate when transmitting 80 % of the incident

light, defined as

$$\frac{\int_{\lambda_{\text{vis}}} S_{\text{AM1.5}}(\lambda)\exp(-\alpha(\lambda)d)\ \mathrm{d}\lambda}{\int_{\lambda_{\text{vis}}} S_{\text{AM1.5}}(\lambda)\ \mathrm{d}\lambda} = 0.8\,. \tag{2.10}$$

A $100 \times 100 \times 0.5\,\text{cm}^3$ plate, without lamination on glass or tandem construction is presented, to provide a fair comparison between all LSC materials. $100 \times 100 \times 0.5\,\text{cm}^3$ is a realistic size for a window in the built environment. The performance of an LSC is highly dependent on the chosen PV cell, therefore no power efficiencies are calculated. To make a fairer comparison, we will calculate at the optical efficiencies of each LSC material. For each family of materials: dyes, rare-earth ions, and (doped) quantum dots, an overview of the photoluminescent quantum yield, CCT, and R_a at 80 % transmission can be found in their respective sections. An overview of absorption- and photoluminescent emission spectra, combined with the perceived color at 80 % transmission can be seen in Figures 2.5 to 2.9, also located in those sections. All materials are assumed to be evenly dispersed in PMMA plates ($n = 1.49$), with no absorption from the matrix material. The calculated efficiencies in the following section are therefore an upper limit for a realistic LSC plate. Setting these constraints allows for comparison of all active compounds, not limited by fabrication methods.

2.3.3 Dye-Based Luminescent Solar Concentrators

Table 2.2: Reported quantum yields and simulation results for 80 % visible light transmission of dye-based LSCs. Both the average R_a and the worst-performing R_i are reported. 'index' specifies the name of the worst-performing color test sample (see Table 2.1).

Name	η_{QY} (%)	CCT (K)	R_a	Minimal R_i	index i	η_{opt} (%)	Ref.
DPA	83	5451	99	98	TS C10	0.2	[20]
DTB	90	3698	83	43	TS C09	2.5	[20]
PP	80	6965	96	90	TS C09	2.6	[21]
Red305	100	5077	66	-26	TS C09	3.5	[21]
CY	14	5551	96	76	TS C09	0.0	[22]
HITCI	28	5965	96	75	TS C09	0.0	[22]

The dyes presented here are amongst the more 'classical' LSC materials, and therefore also the most mature ones. The overview of luminescent dyes presented

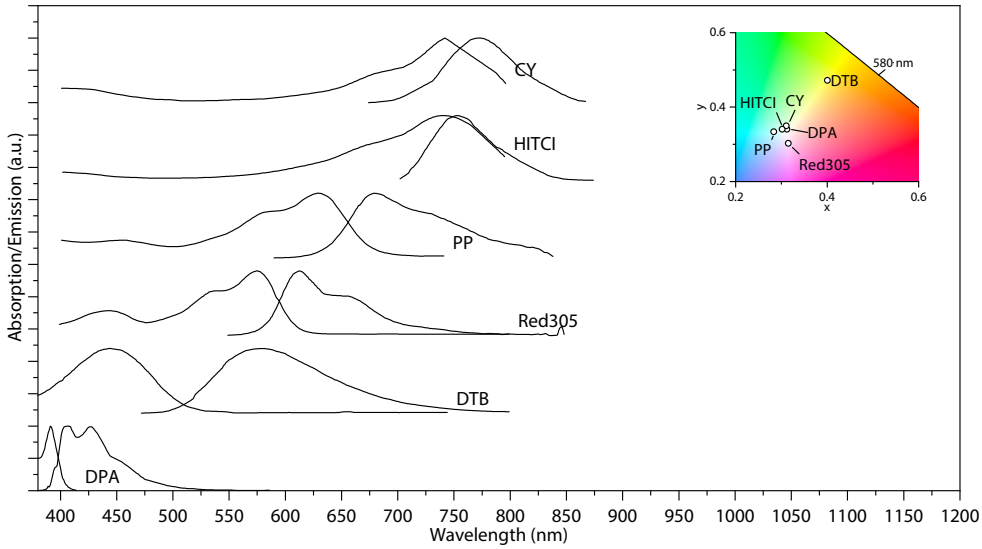


Figure 2.5: Absorption and emission spectra of dye materials used for LSCs. In the inset, the color coordinates in a zoomed-in CIE1931 diagram of the dyes at 80 % visible light transmission are shown.

in Figure 2.5 is far from exhaustive. Many other dyes not listed here exists, such as the Lumogen series from BASF, or the Fluorophores from Thermo Fisher [23]. Therefore, we have chosen to only present 'proven' dyes, used in large-scale experiments (BASF Lumogen F Red 305 [Red305], diphenylanthracene [DPA], di-benzo-thiadiazole [DTB] [20]), or recently published dyes with high experimental significance (perylene-perinone [PP] [21], and two cyanide derivatives: CY, HITCI [22]).

As can be seen in Table 2.2, the quantum yields of these classical dyes are excellent for luminescent solar concentrators, with Red305 repeatedly reported with achieving 100 % quantum yield. These dyes do, however, have their drawbacks. At 80 % visible transmission, some of these dyes have a faithful color reproduction, but are inefficient; with the UV- and blue-absorbing DPA only achieving 0.2 % optical efficiency. As seen in Figure 2.5, the coloration of DPA is low, with a high color rendering index (>90, see Table 2.2), centered around the 'white light' locus in the CIE 1931 chromaticity diagram (see Figure 2.4). Other dyes have an excellent optical efficiency, with DTB at 2.5 % and Red305 at 2.1 %, but suffer from heavy yellow and red coloration, respectively. The high efficiency dyes are therefore used in architectural applications where people are

only present for a short while. For instance, Red305 has been used as a luminescent solar concentrator noise barrier next to a highway [24], and a mixture of DPA and DTB has been utilized as a roof that charges electric bikes [20, 25].

A newer class of dye materials (CY and HITCI) aims to overcome the heavy coloration by shifting the absorption from the visible spectrum to the infrared. Unfortunately, these materials also face some challenges, as their small Stokes shift leads to much reabsorption, that the low quantum yields cannot compensate for.

2.3.4 Rare-Earth-Based Luminescent Solar Concentrators

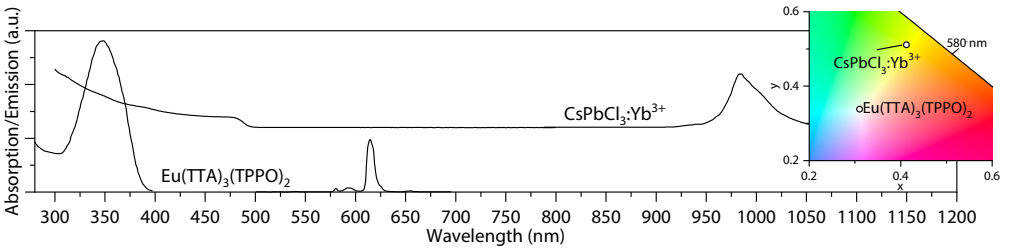


Figure 2.6: Absorption and emission spectra of rare-earth-based LSCs. In the inset, the color coordinates in a zoomed-in CIE1931 diagram of the rare-earths at 80 % visible light transmission are shown.

Table 2.3: Reported quantum yields and simulation results 80 % transmission of visible light LSC based of rare-earth ions. Both the average R_a and the worst-performing R_i are reported. 'index' specifies the name of the worst-performing color test sample (see Table 2.1).

Name	η_{QY} (%)	CCT (K)	R_a	Minimal R_i	index i	η_{opt} (%)	Ref.
$Eu(TTA)_3(TPPO)_2$	73	5492	99	97	TC S12	0.7	[26]
$CsPbCl_3:Yb^{3+}$	30[a]	3710	72	42	TC S09	1.5	[27]

[a] 200 % at extremely low photon incidence.

As seen in Figure 2.6, the europium-doped $Eu(TTA)_3(TPPO)_2$ is a clear example of the benefits and drawbacks of using UV-absorbing rare-earth organometallic complexes in LSCs. Due to the large shift in energy[4] between the absorption

[4]Not to be confused with Stokes shift, which only applies to a transition within the same electronic state.

by the $(TTA)_3(TPPO)_2^{3-}$ dye ligand, followed by a well-defined f-f emission at 614 nm, no self-absorption is observed. The almost exclusive UV-absorption leads to an excellent color rendering index of minimally 97 (see Table 2.3). Combined with the high quantum yield, nearly all absorbed photons will be emitted, contributing to the total device efficiency. Unfortunately, only a small fraction of all solar photons are available in the UV part of the solar spectrum, placing a serious cap on the efficiency. At 20 % visible light absorption, only 1.3 % of incident photons are absorbed. Combined with a trapping efficiency of 74 %, this yields a maximally achievable η_{opt} of 0.7 %.

A notable exception to the materials reported in this chapter are the Yb^{3+}-doped $CsPbCl_3$ perovskite nanocrystals [27]. This material belongs to a new class of LSC materials that try to increase the quantum yield for an LSC beyond 100 % by employing quantum cutting. Quantum cutting is a phenomenon in which one high energy photon (ideally) gets converted to two low energy photons by exploiting energy transfer within a material. This approach allows for an LSC that only absorbs UV photons, and is therefore transparent in visible light. The absorbed sunlight can then be emitted as infrared photons that do not suffer from reabsorption. Currently, quantum cutting only seems to work at low photon fluencies for Yb^{3+}-doped $CsPbCl_3$ perovskite nanocrystals, with quantum yields diminishing when exposed to high powers. This effect leads to a quantum yield of 30 % when exposed to sunlight [28].

2.3.5 Quantum-Dot- And Doped Quantum-Dot-Based Luminescent Solar Concentrators

The sheer size of the figures and tables presented in this section already indicates the popularity of quantum dots for LSC research. The tunable emission and absorption which, to a first degree, only depend on the size and chosen material of the dot, make QDs a versatile research direction. At the same time, QDs are cheap to fabricate and easily dispersed in organic waveguide materials, either in polycarbonate plates or in laminated layers. The ease of dispersion makes scaling up to LSC prototypes possible, while the material itself is still in the lab stage. A recent development for quantum dot LSCs attempts to free the dots of toxic materials, such as cadmium or lead. This is done by either choosing a different crystal, such as $CuInS_2$ or AlS, or by using properties of nanocrystalline carbon

or silicon.

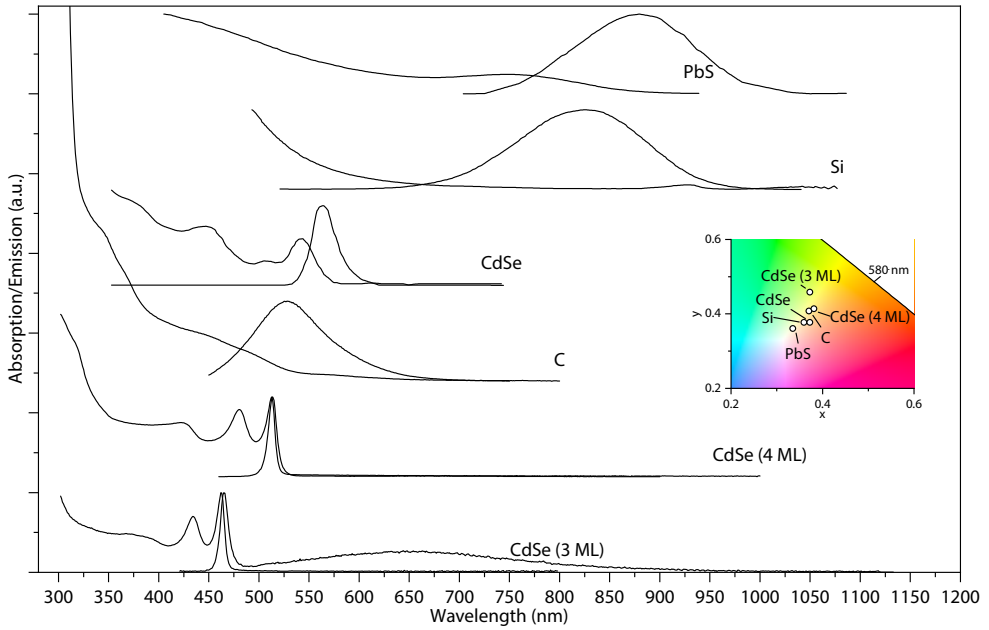


Figure 2.7: Absorption and emission spectra of LSCs based on core quantum dots. In the inset, the color coordinates in a zoomed-in CIE1931 diagram of the QDs at 80 % visible light transmission are shown.

As can be seen in Figure 2.7, QDs made up of only a core suffer from very small Stokes shifts. Growing the QD to a larger diameter leads to a smaller bandgap dictated by the quantum confinement effect, and therefore to a larger absorption. This effect can be seen by studying the difference in absorption between 3 and 4 monolayers of CdSe as a nanoplatelet, versus its "full" quantum dot form. Combined with the low quantum yield of these QDs, the optical efficiency of direct bandgap QDs does not exceed a few tenths of a percent. An exception to what is observed for core QDs are QDs composed solely from Si. Figure 2.7 shows that these Si QDs have almost no overlap between their emission and absorption. This effect can be attributed to the luminescence coming from the indirect bandgap of the Si QDs. This luminescence from the indirect bandgap dominates over the quantum confinement effect [34]. This smaller self-absorption in Si leads to an optical efficiency of 1.3 %, while still having a fair color rendering index, carrying mild yellow coloring (see Figure 2.7).

Table 2.4: Overview of simulation results for core quantum dots as well as reported quantum yields. Both the average R_a and the worst-performing R_i are reported. 'index' specifies the name of the worst-performing color test sample (see Table 2.1).

Name	η_{QY} (%)	CCT (K)	R_a	Minimal R_i	index i	η_{opt} (%)	Ref.
PbS	30	4638	99	96	TC S12	0.8	[29]
Si	46	3991	97	87	TC S09	1.3	[30]
CdSe	50[a]	3615	91	77	TC S12	0.3	[31]
C	30	3911	93	75	TC S09	0.1	[32]
CdSe (4 ML)[b]	5.8	4123	81	59	TC S09	0.1	[33]
CdSe (3 ML)[c]	24.3	3730	85	53	TC S09	0.1	[33]

[a] Quantum yield taken from Ref. [29]
[b] Nanoplatelets, 4 monolayers (ML) in thickness.
[c] Nanoplatelets, 3 ML in thickness.

Table 2.5: Overview of simulation results for core/shell quantum dots as well as reported quantum yields. Both the average R_a and the worst-performing R_i are reported. 'index' specifies the name of the worst-performing color test sample (see Table 2.1).

Name	η_{QY} (%)	CCT (K)	R_a	Minimal R_i	index i	η_{opt} (%)	Ref.
PbS/CdS (0.5-0.7 nm)	40	5170	95	81	TC S09	1.9	[35]
PbS/CdS (0.1-0.2 nm)	50	5419	97	86	TC S09	1.6	[35]
CISeS/ZnS	40	4803	98	94	TC S12	1.3	[36]
AlS/ZnS	60.3	4362	99	94	TC S12	2.7	[37]
$CuInS_2/ZnS$[a]	91(66)	4868	98	95	TC S12	4.0(2.8)	[38]
$CuInSe_2/ZnS$	78	4499	99	96	TC S12	2.8	[39]
$CuInS_2/CdS$	86	4704	98	92	TC S09	3.6	[40]
CdSe/CdS (14 ML)	45	3673	86	51	TC S09	1	[41]
CdSe/CdS (19 ML)	40	3698	81	47	TC S09	1.6	[37]

[a] reports both values for solution and when dispersed in a waveguide.

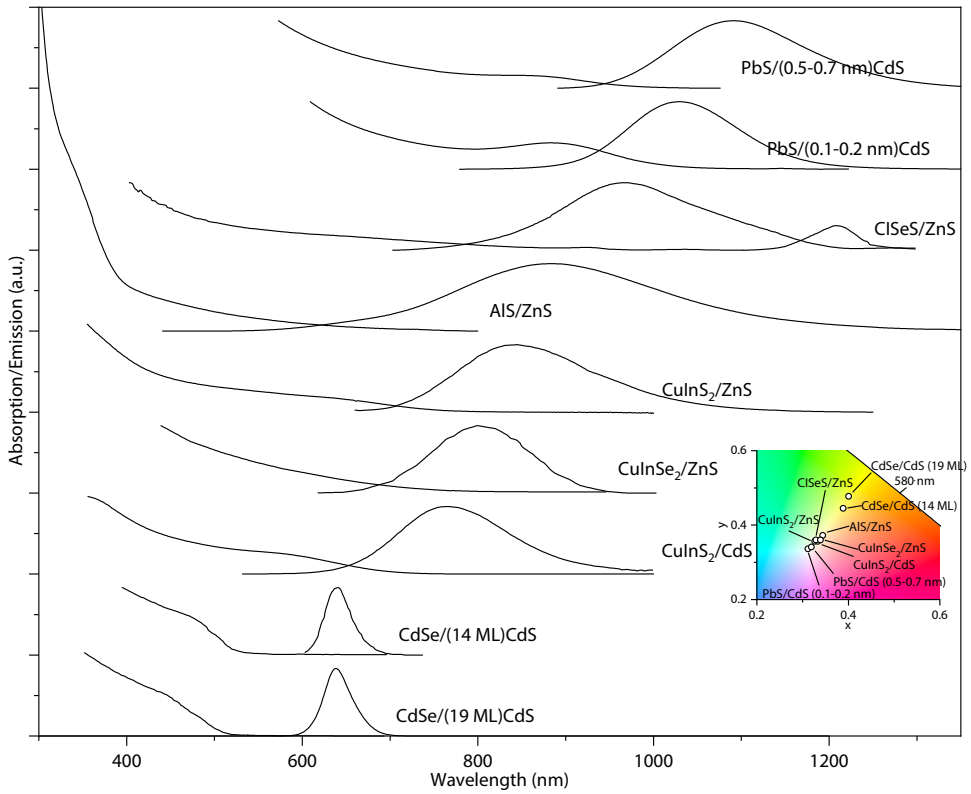


Figure 2.8: Absorption and emission spectra LSCs based on core/shell quantum dots. In the inset, the color coordinates in a zoomed-in CIE1931 diagram of the QDs at 80 % visible light transmission are shown.

In the core/shell QDs presented here, the shell acts as sensitizer, and the core as activator. The much broadened absorption provided by the shell leads to significantly improved color rendering over their core-only varieties. Furthermore, these QDs are typically reported with reasonable quantum yields of over 50 %. This combination leads to the core/shell quantum dots being amongst the most efficient LSC materials.

Notable systems are the $CuInSe_2$/ZnS, $CuInS_2$/ZnS and AlS/ZnS LSCs. For $CuInSe_2$/ZnS, a 6.4 % optical efficiency was shown in a $15.2 \times 15.2\,cm^2$ device. These $CuInSe_2$/ZnS QDs can yield a 2.4 % optical efficiency at 80 % transmission, without inducing artificial color blindness. The $CuInS_2$/ZnS quantum dots, for which an optical efficiency of 8.1 % was demonstrated for a $10 \times 10\,cm^2$ LSC [38], lead in our simulations to a 2.8 % efficiency at 80 % transmission, while still

Table 2.6: Overview of simulation results for doped core and doped core/shell quantum dots. Both the average R_a and the worst-performing R_i are reported. 'index' specifies the name of the worst-performing color test sample (see Table 2.1).

Name	η_{QY} (%)	CCT (K)	R_a	Minimal R_i	index i	η_{opt} (%)	Ref.
CdZnS/ZnS:Mn^{2+}	75	3864	85	67	TC S09	1.5	[39]
ZnSe/ZnS:Mn^{2+}	53	3685	81	45	TC S09	2.5	[42]
CdSe:Cu^{+}	40	4485	99	94	TC S09	1.7	[43]
CdSe (3 ML):Cu^{+}	80	4001	84	63	TC S09	1.2	[33]
CdSe (4 ML):Cu^{+}	97	3810	86	58	TC S09	2.4	[33]

boasting an excellent R_a, as seen in Table 2.5. Similarly, in AlS/ZnS QDs, high efficiencies of 2.7 % could be reached, while retaining excellent color rendering. What makes these last two systems notable is that they retain a high efficiency, without having to resort to toxic lead or cadmium.

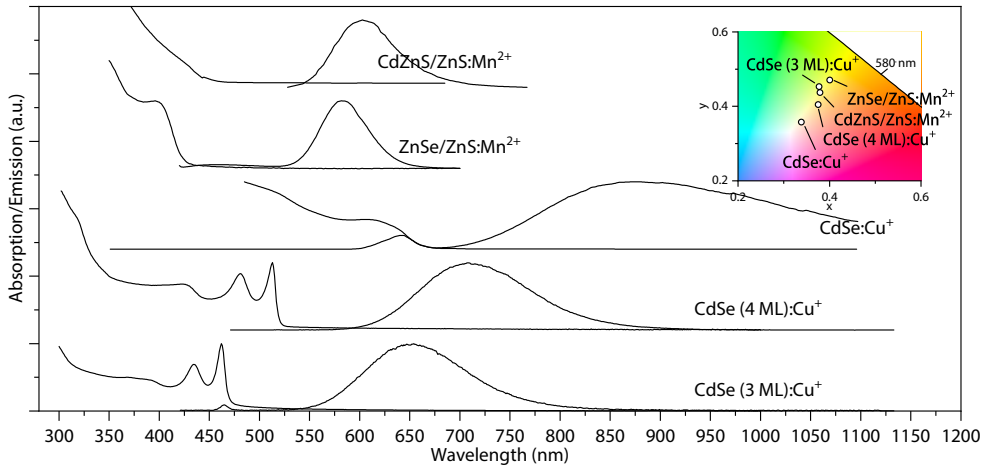


Figure 2.9: Absorption and emission spectra LSCs based on doped core and doped core/shell QDs. In the inset, the color coordinates in a zoomed-in CIE1931 diagram of the QDs at 80 % visible light transmission are shown.

The luminescence of the core QDs can be improved by doping the dots with transition metals, such as copper. For CdSe, doping with copper leads to the core of the QD acting as an activator, transferring the absorbed energy to the Cu dopant. The Cu dopant will then emit the absorbed energy with a higher quantum yield than the sole core would. At the same time, having Cu emit

shifts the emission out of the self-absorption region. The effect of this for CdSe nanoplatelets can be observed in Table 2.6. Doping with copper bumps the efficiency significantly, from 0.1 % to 2.4 %. Unfortunately, the CdSe still dictates the absorption, which does lead to a low R_a and yellow coloring.

Similar to the core-only QDs, core/shell QDs can be doped with transition metals to boost their efficiency, and remove overlap between absorption and emission. While the doped materials in literature do not show very broad absorption, limiting just over 400 nm for both Mn^{2+}-doped CdZnS/ZnS and ZnSe/ZnS, the lack of self-absorption still puts them near the top performers, demonstrating good scalability for practical applications. However, the limited absorption does yield color rendering indices that are only just sufficient for application in an office environment, when considering LSCs with 80 % visible light transmission.

2.4 Tm^{2+}-Doped Halide Luminescent Solar Concentrators

A recently emerged class of possible LSC materials is the family of alkali halide salts, doped with the rare-earth element thulium, in its 2+ valence state [13, 44]. As can be seen in Figure 2.10, it sets itself apart from most other contemporary LSC materials by having a very broad absorption spectrum, covering the entire visible spectrum. In the case of CaI_2, Tm^{2+} even absorbs 63 % of the entire solar spectrum. What furthermore makes thulium-doped halides unique amongst other LSC materials is the characteristic emission of Tm. As explained in Section 1.2.3, divalent thulium will emit most strongly at a single line centered around 1140 nm, regardless of what host it is doped in. For usage as an LSC, this infrared luminescence can be absorbed by using $CuInSe_2$ PV cells [13].

The broad absorption is due to the thirteen electrons in the partially-filled f-shell of Tm^{2+}. All these electrons lead to a system with many possible transitions to the unoccupied 5d-shell. These transitions have such low energies while being great in number that they are able to cover the entire visible spectrum. As an added advantage, because of the proximity of the lowest 5d-level to the highest 4f-level (in terms of energy), an excited Tm^{2+} cation can efficiently non-radiatively relax to the highest 4f-level. From the highest 4f-level, Tm^{2+} will then emit the characteristic 1140 nm light resultant from a $4f^{13}[^2F_{5/2}] \rightarrow 4f^{13}[^2F_{7/2}]$ transition.

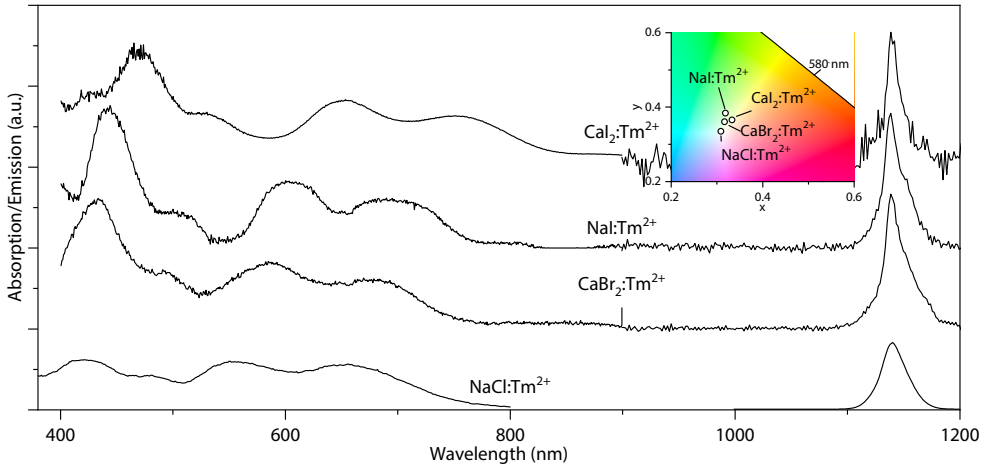


Figure 2.10: Absorption and emission of several Tm^{2+}-doped halides. In the inset, the color coordinates in a zoomed-in CIE1931 diagram of the Tm^{2+}-doped halides at 80 % visible light transmission are shown.

Table 2.7: Properties of Tm^{2+}-halide-based LSCs, at 80 % transmission of visible light. For these materials, the same assumptions are made as for the simulations presented in Section 2.3. Both the average R_a and the worst-performing R_i are reported. 'index' specifies the name of the worst-performing color test sample (see Table 2.1).

Name	CCT (K)	R_a	Minimal R_i	index i	η_{opt} (%)	Ref.
CaI_2:Tm^{2+}	4755	95	67	TC S09	4.5	[45]
NaI:Tm^{2+}	5274	91	76	TC S09	4.5	[45]
$CaBr_2$:Tm^{2+}	5276	98	94	TC S09	4.5	[45]
NaCl:Tm^{2+}	5601	95	88	TC S10	4.4	[13]

This all leads to a material with a difference between emission and absorption that is sufficiently large for Tm^{2+}-doped halides to have negligible self-absorption, as seen in Figure 2.10.

The divalent state for Tm^{2+} is not often encountered, due to the groundstate level of Tm often lying close to, or in, the conduction band. For a rare-earth ion to be stable in its 2+ state, the energetic difference between the Fermi-level and the lowest 4f-level ($E_{Ff} = E_{4f} - E_{Fermi}$) should ideally be smaller than 0 [46]. Due to the high-lying 4f-level of divalent Tm compared to other rare-earth elements, this condition is not often reached. The halides are an exception, because of

their low-lying valence band, combined with a large bandgap. This combination leads to the Fermi-level being sufficiently near the lowest 4f-level for the $E_{\mathrm{Ff}} \lesssim 0$ condition to be fulfilled.

Next to their broad absorption, Tm^{2+}-doped halides are also known for their remarkably high absorption coefficient. Research by Grimm et al. [47] shows a decadic absorption coefficient of $\sim 60\,\mathrm{at.\%^{-1}\,cm^{-1}}$ for Tm^{2+}-doped $CsCaCl_3$. Those materials were synthesized as single crystals using the Bridgman technique. While those measurements are done on bulk crystals, still something can be said about how their properties would translate to an LSC device. For most rare-earth materials, concentration quenching starts at around 1 % of doping. This means that, to absorb 20 % of the incoming light, a thin-film of 16 µm thickness would be required. To put those numbers into perspective: the concentration of Lumogen F Red 305 in PMMA can be increased to an absorption coefficient of $30\,\mathrm{cm^{-1}}$ before concentration quenching starts occurring[5]. This means that for a Red 305 LSC, 600 µm of material is required for 20 % absorption. In the case of Tm-doped halides, this opens the door for producing LSCs with physical vapor deposition [44, 45], as is commonly used in the glass industry for the application of, e.g., low-e coatings or anti-reflection layers. All materials presented in this section have already been successfully deposited as thin-films [44, 45].

A serious constraint on the successful development of a Tm-based LSC is the hygroscopic nature of the halides. Apart from NaCl, all halides presented in this section react with and dissolve in air. A halide LSC is possible, but an enclosing for the luminescent coating in a protective atmosphere also has to be developed. An important consideration for these environments is that, contrary to how regular window glass is sealed, the sealing should be transparent to 1140 nm light. Otherwise, the sealing will interfere with the workings of the LSC.

An estimation of the potential of Tm-based LSCs can be easily made, as these doped halides do not display any self-absorption. Table 2.7 presents an overview of simulated properties of halides doped with Tm^{2+}, using the same simulation conditions as in the previous sections. All halides still present good color rendering indices, with $CaBr_2$:Tm^{2+} performing best. $CaBr_2$:Tm^{2+} shows almost no

[5] Desmet et al. [21] report a $12\,\mathrm{cm^{-1}}$ decadic absorption coefficient for Red305 in PMMA at a concentration of 115 ppm. With PMMA having a molecular weight $M_w = 120000$, this leads to an intermolecular separation of 11.4 nm. Quenching starts at ~ 8 nm separation [48], leading to an absorption coefficient of $30\,\mathrm{cm^{-1}}$.

coloration, boasting a color rendering index higher than 94, with its color close to the white locus, seen in the inset of Figure 2.10. These simulations assume 100 % quantum yield, leading to optical efficiencies of $\sim 4.5\%$ for all halides presented. Because of the lack of self-absorption, a lower quantum yield can easily be taken into account with $\eta_{\text{opt}} = \eta_{\text{opt,QY=1}} \times \eta_{\text{QY}}$. Even at a low quantum yield, the lack of self-absorption would mean the Tm-based LSCs could outperform contemporary LSC materials. Based on work with Eu^{2+}, it is not expected that rare-earth-doped halides have a low quantum yield. Eu^{2+} has photoluminescent quantum yields at 100 % when doped in NaCl and NaBr [49]. It is therefore expected that Tm^{2+}-doped halides will behave similarly and will thus make an efficient LSC.

2.5 Conclusion

From the preceding sections it can be concluded that since the conception of the luminescent solar concentrator by Weber and Lambe in the 1970s, already much has been accomplished. These days, LSCs are mainly composed of one of three classes of luminophores: dyes, QDs, and rare-earth-doped hosts.

The traditional dyes are still performing well as LSC materials. For LSCs sized $100 \times 100 \times 0.5\,\text{cm}^3$ with 80 % transmission of sunlight, defined as AM1.5g, where waveguiding losses are neglected, BASF Lumogen F Red305 still performs admirably. In terms of optical efficiency, it still outperforms any other material that has been built as a small-scale demonstrator LSC at $\eta_{\text{opt}} = 3.5\,\%$. The main drawback with Red305 is its poor average R_a of only 66. This is not acceptable for European office spaces where an R_a of minimally 80 is required. Newer dyes have a much better average R_a, but an improvement in R_a is typically traded off with a decrease in η_{opt}.

For quantum dots, we can observe that QDs based on non-toxic $CuInS_2$/ZnS core/shell quantum dots can already reach an optical efficiency of more than 2.8 %, with an average color rendering index of 98. Such a material could find application in an office building as an electricity-generating window.

In the case of LSCs based on doping materials with rare-earths, reasonable efficiencies can be observed. The upconverting $CsPbCl_3$:Yb^{3+} is a promising material, but only shows upconversion at very low photon incidence. At higher incidence, more typical for materials exposed to sunlight, the η_{QY} drops from

200 % to 30 %, yielding $\eta_{opt} = 1.5$ at a low average $R_a = 72$. Other promising materials for LSCs based on rare-earths are Tm^{2+}-doped halides. If these materials can attain a high η_{QY}, their absorption of the entire visible spectrum could make them reach $\eta_{opt} = 4.5$, at high average color rendering indices of more than 91.

As the LSC concept is making its way out of the lab and into actual windows, new challenges start to emerge. Scaling up the windows to sizes such that higher-than-unity concentration factors can be reached will lead not only to broadband and uniform absorption being required, but will also lead to a window that is free from waveguide-losses due to scattering of light. Accomplishing these feats will still require significant efforts by the LSC community. However, as can be deduced from the previous sections, recent advances have brought us closer to a broadband absorbing, self-absorption free, non-scattering luminescent solar concentrator.

References

[1] F. M. Vossen, M. P. Aarts, and M. G. Debije, "Visual performance of red luminescent solar concentrating windows in an office environment," Energy and Buildings **113**, 123–132 (2016).

[2] C. L. Mulder, P. D. Reusswig, A. P. Beyler, H. Kim, C. Rotschild, and M. A. Baldo, "Dye alignment in luminescent solar concentrators: II Horizontal alignment for energy harvesting in linear polarizers," Optics Express **18**, A91 (2010).

[3] J. A. Sol, G. H. Timmermans, A. J. van Breugel, A. P. Schenning, and M. G. Debije, "Multistate Luminescent Solar Concentrator "Smart" Windows," Advanced Energy Materials **8**, 1–8 (2018).

[4] Z. Krumer, W. G. J. H. M. Van Sark, R. E. I. Schropp, C. De, and M. Donegá, "Compensation of self-absorption losses in luminescent solar concentrators by increasing luminophore concentration," Solar Energy Materials and Solar Cells **167**, 133–139 (2017).

[5] M. J. Kastelijn, C. W. Bastiaansen, and M. G. Debije, "Influence of waveguide material on light emission in luminescent solar concentrators," Optical Materials **31**, 1720–1722 (2009).

[6]M. Zettl, O. Mayer, E. Klampaftis, and B. S. Richards, "Investigation of Host Polymers for Luminescent Solar Concentrators," Energy Technology **5**, 1037–1044 (2017).

[7]D. K. G. de Boer, D. J. Broer, M. G. Debije, W. Keur, A. Meijerink, C. R. Ronda, and P. P. C. Verbunt, "Progress in phosphors and filters for luminescent solar concentrators.," Optics Express **20**, A395–405 (2012).

[8]F. Meinardi, F. Bruni, and S. Brovelli, "Luminescent solar concentrators for building-integrated photovoltaics," Nature Reviews Materials **2**, 17072 (2017).

[9]M. Rafiee, S. Chandra, H. Ahmed, and S. J. McCormack, "An overview of various configurations of Luminescent Solar Concentrators for photovoltaic applications," Optical Materials **91**, 212–227 (2019).

[10]L. H. Slooff, E. E. Bende, A. R. Burgers, T. Budel, M. Pravettoni, R. P. Kenny, E. D. Dunlop, and A. Büchtemann, "A luminescent solar concentrator with 7.1% power conversion efficiency," physica status solidi (RRL) - Rapid Research Letters **2**, 257–259 (2008).

[11]M. J. Currie, J. K. Mapel, T. D. Heidel, S. Goffri, and M. A. Baldo, "High-Efficiency Organic Solar Concentrators for Photovoltaics," Science **321**, 226–228 (2008).

[12]J. C. Goldschmidt, M. Peters, A. Bösch, H. Helmers, F. Dimroth, S. W. Glunz, and G. Willeke, "Increasing the efficiency of fluorescent concentrator systems," Solar Energy Materials and Solar Cells **93**, 176–182 (2009).

[13]O. M. ten Kate, K. W. Krämer, and E. van der Kolk, "Efficient luminescent solar concentrators based on self-absorption free, Tm^{2+} doped halides," Solar Energy Materials and Solar Cells **140**, 115–120 (2015).

[14]I. Papakonstantinou and C. Tummeltshammer, "Fundamental limits of concentration in luminescent solar concentrators revised: the effect of reabsorption and nonunity quantum yield," Optica **2**, 841 (2015).

[15]H. Li, K. Wu, J. Lim, H.-J. Song, and V. I. Klimov, "Doctor-blade deposition of quantum dots onto standard window glass for low-loss large-area luminescent solar concentrators," Nature Energy **1**, 16157 (2016).

[16]K. Yoshikawa, H. Kawasaki, W. Yoshida, T. Irie, K. Konishi, K. Nakano, T. Uto, D. Adachi, M. Kanematsu, H. Uzu, and K. Yamamoto, "Silicon heterojunction solar cell with interdigitated back contacts for a photoconversion efficiency over 26%," Nature Energy **2**, 17032 (2017).

[17]M. A. Green, E. D. Dunlop, D. H. Levi, J. Hohl-Ebinger, M. Yoshita, and A. W. Ho-Baillie, "Solar cell efficiency tables (version 54)," Progress in Photovoltaics: Research and Applications **27**, 565–575 (2019).

[18]International Commission on Illumination, *Method of Measuring and Specifying Colour Rendering Properties of Light Sources*, edited by C. internationale de l'éclairage (CIE Central Bureau, 1995).

[19]R. Nave, *The C.I.E. Chromaticity Diagram*, 2019.

[20]N. Aste, L. Tagliabue, C. Del Pero, D. Testa, and R. Fusco, "Performance analysis of a large-area luminescent solar concentrator module," Renewable Energy **76**, 330–337 (2015).

[21]L. Desmet, A. J. M. Ras, D. K. G. de Boer, and M. G. Debije, "Monocrystalline silicon photovoltaic luminescent solar concentrator with 4.2% power conversion efficiency," Optics Letters **37**, 3087–3089 (2012).

[22]Y. Zhao, G. Meek, B. Levine, and R. Lunt, "Near Infrared Harvesting Transparent Luminescent Solar Concentrators," Advanced Optical materials **2**, 606–611 (2014).

[23]*The Molecular Probes handbook. A guide to fluorescent probes and labeling technologies*, 11th ed. (Life Technologies, 2010).

[24]M. Kanellis, M. M. de Jong, L. Slooff, and M. G. Debije, "The solar noise barrier project: 1. Effect of incident light orientation on the performance of a large-scale luminescent solar concentrator noise barrier," Renewable Energy **103**, 647–652 (2017).

[25]N. Conenna, *Luminescent Solar Concentrator LSC*, 2017.

[26]T. Wang, J. Zhang, W. Ma, Y. Luo, L. Wang, Z. Hu, W. Wu, X. Wang, G. Zou, and Q. Zhang, "Luminescent solar concentrator employing rare earth complex with zero self-absorption loss," Solar Energy **85**, 2571–2579 (2011).

[27]T. A. Cohen, T. J. Milstein, D. M. Kroupa, J. D. MacKenzie, C. K. Luscombe, and D. R. Gamelin, "Quantum-cutting Yb 3+ -doped perovskite nanocrystals for monolithic bilayer luminescent solar concentrators," Journal of Materials Chemistry A **7**, 9279–9288 (2019).

[28]D. M. Kroupa, J. Y. Roh, T. J. Milstein, S. E. Creutz, and D. R. Gamelin, "Quantum-Cutting Ytterbium-Doped $CsPb(Cl_{1-x}Br_x)_3$ Perovskite Thin Films with Photoluminescence Quantum Yields over 190%," ACS Energy Letters **3**, 2390–2395 (2018).

[29]G. V. Shcherbatyuk, R. H. Inman, C. Wang, R. Winston, and S. Ghosh, "Viability of using near infrared PbS quantum dots as active materials in luminescent solar concentrators," Applied Physics Letters **96**, 13–16 (2010).

[30]F. Meinardi, S. Ehrenberg, L. Dhamo, F. Carulli, M. Mauri, F. Bruni, R. Simonutti, U. Kortshagen, and S. Brovelli, "Highly efficient luminescent solar concentrators based on earth-abundant indirect-bandgap silicon quantum dots," Nature Photonics **11**, 177–185 (2017).

[31]Y. Chen, J. Vela, H. Htoon, J. L. Casson, D. J. Werder, D. a. Bussian, V. I. Klimov, and J. a. Hollingsworth, ""Giant" Multishell CdSe Nanocrystal Quantum Dots with Suppressed Blinking," Journal of the American Chemical Society **130**, 5026–5027 (2008).

[32]Y. Zhou, D. Benetti, X. Tong, L. Jin, Z. M. Wang, D. Ma, H. Zhao, and F. Rosei, "Colloidal carbon dots based highly stable luminescent solar concentrators," Nano Energy **44**, 378–387 (2018).

[33]M. Sharma, K. Gungor, A. Yeltik, M. Olutas, B. Guzelturk, Y. Kelestemur, T. Erdem, S. Delikanli, J. R. McBride, and H. V. Demir, "Near-Unity Emitting Copper-Doped Colloidal Semiconductor Quantum Wells for Luminescent Solar Concentrators," Advanced Materials **29**, 1–10 (2017).

[34]D. C. Hannah, J. Yang, P. Podsiadlo, M. K. Chan, A. Demortière, D. J. Gosztola, V. B. Prakapenka, G. C. Schatz, U. Kortshagen, and R. D. Schaller, "On the origin of photoluminescence in silicon nanocrystals: Pressure-dependent structural and optical studies," Nano Letters **12**, 4200–4205 (2012).

[35]Y. Zhou, D. Benetti, Z. Fan, H. Zhao, D. Ma, A. O. Govorov, A. Vomiero, and F. Rosei, "Near Infrared, Highly Efficient Luminescent Solar Concentrators," Advanced Energy Materials **6**, 1–8 (2016).

[36]F. Meinardi, H. McDaniel, F. Carulli, A. Colombo, K. A. Velizhanin, N. S. Makarov, R. Simonutti, V. I. Klimov, and S. Brovelli, "Highly efficient large-area colourless luminescent solar concentrators using heavy-metal-free colloidal quantum dots," Nature Nanotechnology **10**, 878–885 (2015).

[37]W. Chen, J. Li, P. Liu, H. Liu, J. Xia, S. Li, D. Wang, D. Wu, W. Lu, X. W. Sun, and K. Wang, "Heavy Metal Free Nanocrystals with Near Infrared Emission Applying in Luminescent Solar Concentrator," Solar RRL **1**, 1700041 (2017).

[38]M. R. Bergren, N. S. Makarov, K. Ramasamy, A. Jackson, R. Guglielmetti, and H. McDaniel, "High-Performance $CuInS_2$ Quantum Dot Laminated Glass Luminescent Solar Concentrators for Windows," ACS Energy Letters **3**, 520–525 (2018).

[39]K. Wu, H. Li, and V. I. Klimov, "Tandem luminescent solar concentrators based on engineered quantum dots," Nature Photonics **12**, 105–110 (2018).

[40]K. E. Knowles, T. B. Kilburn, D. G. Alzate, S. McDowall, and D. R. Gamelin, "Bright $CuInS_2$/CdS nanocrystal phosphors for high-gain full-spectrum luminescent solar concentrators," Chemical Communications **51**, 9129–9132 (2015).

[41]F. Meinardi, A. Colombo, K. A. Velizhanin, R. Simonutti, M. Lorenzon, L. Beverina, R. Viswanatha, V. I. Klimov, and S. Brovelli, "Large-area luminescent solar concentrators based on 'Stokes-shift-engineered' nanocrystals in a mass-polymerized PMMA matrix," Nature Photonics **8**, 392–399 (2014).

[42]C. S. Erickson, L. R. Bradshaw, S. McDowall, J. D. Gilbertson, D. R. Gamelin, and D. L. Patrick, "Zero-Reabsorption Doped-Nanocrystal Luminescent Solar Concentrators," ACS Nano **8**, 3461–3467 (2014).

[43]L. R. Bradshaw, K. E. Knowles, S. McDowall, and D. R. Gamelin, "Nanocrystals for luminescent solar concentrators," Nano Letters **15**, 1315–1323 (2015).

[44]M. de Jong, W. Kesteloo, and E. van der Kolk, "Deposition of luminescent NaCl:Tm^{2+} thin films with a Tm concentration gradient using RF magnetron sputtering," Optical Materials **46**, 149–153 (2015).

[45]E. P. J. Merkx and E. van der Kolk, "Optimizing Tm^{2+}-doped Dihalide Thin Film Luminescent Solar Concentrators," in OSA Advanced Photonics Congress (AP) 2019 (IPR, Networks, NOMA, SPPCom, PVLED) (2019), PT1C.3.

[46]P. Dorenbos, "Valence stability of lanthanide ions in inorganic compounds," Chemistry of Materials **17**, 6452–6456 (2005).

[47]J. Grimm, E. Beurer, and H. U. Güdel, "Crystal Absorption Spectra in the Region of 4f→4f and 4f→5d Excitations in Tm^{2+} -Doped $CsCaCl_3$,$CsCaBr_3$, and $CsCaI_3$," Inorganic Chemistry **45**, 10905–10908 (2006).

[48]A. P. Green and A. R. Buckley, "Solid state concentration quenching of organic fluorophores in PMMA," Physical Chemistry Chemical Physics **17**, 1435–1440 (2015).

[49]J. Rubio, "Doubly-valent rare-earth ions in halide crystals," Journal of Physics and Chemistry of Solids **52**, 101–174 (1991).

— 3 —

Rapid Optimization of Large-Scale Luminescent Solar Concentrators: Evaluation For Adoption in the Built Environment

The phenomenon of self-absorption is by far the largest influential factor in the efficiency of luminescent solar concentrators (LSCs), but also the most challenging one to capture computationally. In this chapter a model that uses a multiple-generation light transport (MGLT) approach to quantify light transport through single-layer luminescent solar concentrators of arbitrary shape and size is presented. MGLT offers a significant speed increase over Monte Carlo (raytracing) when optimizing the luminophore concentration in large LSCs and more insight into light transport processes. Our results show that optimizing luminophore concentration in a lab-scale device does not yield an optimal optical efficiency after scaling up to realistically sized windows. Each differently sized LSC therefore has to be optimized individually to obtain maximal efficiency. We show that for strongly self-absorbing LSCs with a high quantum yield, parasitic self-absorption can turn into a positive effect at very high absorption coefficients. This is due to a combination of increased light trapping and stronger absorption of the incoming sunlight. We conclude that, except for scattering losses, MGLT can compute all aspects in light transport through an LSC accurately and can be used as a design tool for building-integrated photovoltaic elements. This design tool is therefore used to calculate many building-integrated LSC power conversion efficiencies.

This chapter has been published as: E.P.J. Merkx, O.M. ten Kate, and E. van der Kolk, "Rapid optimization of large-scale luminescent solar concentrators: evaluation for adoption in the built environment," Optics Express **25**, A547–A563 (2017)
All data supporting the figures in this chapter can be found at: `http://doi.org/uuid:374108c0-e5fe-4993-81bf-d203db86a625`

3.1 Introduction

Building-integrated photovoltaics (BIPVs) are a promising solution for the wide adoption of electricity generation through solar energy. With the trend towards large glass facades in public- and commercial buildings a (semi-) transparent BIPV could expect incorporation in the built environment [1]. A luminescent solar concentrator (LSC) is such a transparent potential BIPV. LSCs were intensely studied during the 1970s [2, 3] and are regaining more interest with the advent of new types of quantum dots (QDs), luminescent dyes and rare-earth materials. The window-like qualities of these new materials, such as letting the shape of the visible spectrum remain unaltered, make them suitable as BIPV. A typical LSC is either a polymer plate (mostly PMMA) doped with luminophores, or a glass sheet carrying a luminescent coating [4–6]. Figure 3.1 illustrates the luminescent solar concentrating process. Luminescent centers contained in these materials absorb part of the incoming diffuse and direct sunlight, followed by reemission at longer wavelengths. The emitted luminescence is waveguided through the LSC plate to its perimeter, where conventional photovoltaic (PV) cells convert this waveguided light into electricity. As a result, the strip-shaped PV cells will receive sunlight from a larger area than they would when directly exposed to the sun, which enhances their electricity generation. If the luminescent coating is semi-transparent, an electricity generating window ideal for BIPV applications can be achieved.

In many LSCs the range of absorbed and emitted wavelengths overlap. Reabsorbed light is often not reemitted with unity efficiency, and, even when reemitted, typically has a 25 % chance of being lost through the escape-cone. This parasitic self-absorption therefore yields increasing losses with bigger LSCs. Hence, an accurate and fast treatment of the effect of self-absorption on LSC efficiency is needed to both calculate LSC efficiency and to optimize this efficiency for large LSCs intended for BIPV use.

Light transport within an LSC was described using a series of absorption and reemission events by Batchelder *et al.* [3, 7], who referred to it as multiple-generation self-absorption. The analytical equations presented were solved for the simplified case of a semi-infinite rod. Most modern approaches to quantification of self-absorption are carried out with thermodynamic calculations [8–10], analytical models based on the Beer-Lambert law [11, 12], or using Monte Carlo

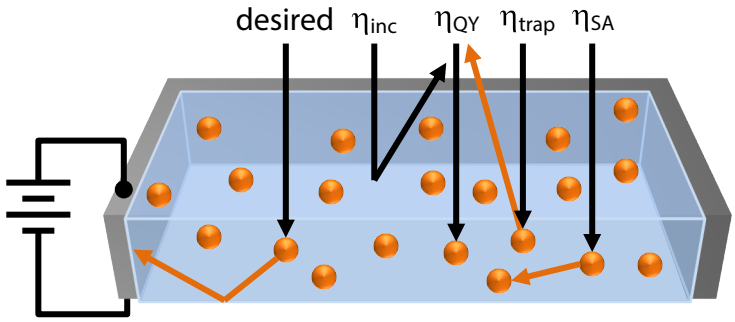


Figure 3.1: Schematic cross-section of the working of a single-layer LSC. Orange spheres represent the luminescent centers within a transparent medium. PV cells (gray) surround the perimeter of the concentrator plate. 'desired' shows the desired concentrating process without any losses. All other arrows show possible loss mechanisms within an LSC and their associated efficiency: non-unity incoupling due to reflection losses (η_{inc}), non-unity quantum yield due to non-radiative decay (η_{QY}), non-unity trapping due to escape-cone losses (η_{trap}) and losses due to self-absorption (η_{SA}). Losses due to scattering within the LSC are not considered in this work and therefore not depicted.

(MC) simulations [13–20], also referred to as raytracing. While MC simulations are relatively easy to implement, they rely on random numbers to calculate physical effects. As a result, a high demand is put on the collection of ever larger statistics as the size of the simulated system increases. In materials featuring a large amount of self-absorption and a high quantum yield η_{QY}, tracing a single photon in a system will take longer with increasing optical density. In this work we show that these two factors result in a long calculation time when optimizing a realistically-sized LSC. Furthermore, we present a method that fully describes light transport within an LSC. This method can quickly and accurately optimize large-size LSCs through the variation of luminophore concentration.

This chapter consists of three parts. In the first part we present a model that calculates all light transport processes within an LSC, based on multiple-generation light transport (MGLT). We will check the correctness and internal consistency of the model by comparing calculations with an MC model using the same input data. Here the calculation speed when optimizing large, high η_{QY} LSCs using MGLT as opposed to MC will be made evident. Results are presented for well-known luminescent polymers, like Lumogen Red305 as well as state-of-the-art polymer and QD-based LSCs, where all required data was published. In the second part we put the model to use by optimizing the luminophore

concentration for the presented materials, both for lab-scale (100 cm^2) and BIPV-scale (1 m^2) LSCs. In this optimization the potentially beneficial effects of self-absorption when η_{QY} of an LSC is near unity will be shown. Finally, the potential as BIPV window is evaluated for all presented LSCs, after optimizing their optical efficiency.

3.2 Multiple-Generation Light Transport

To characterize LSC performance an often used metric is the optical efficiency η [21]. η gives the ratio of photons collected at the side to incident solar photons. In the case of a waveguide without self-absorption, scattering or coupling losses at the perimeter

$$\eta_{ideal} = \eta_{inc}\eta_{LHE}\eta_{QY}\eta_{trap} \,. \tag{3.1}$$

Here η_{inc} is the incoupling efficiency: the amount of light entering the LSC, η_{LHE} the fraction of sunlight absorbed over the thickness of the LSC, η_{QY} the photoluminescent quantum yield of the luminescent centers and η_{trap} the fraction of light which remains trapped within the LSC after reemission.

Light incident on an LSC first has to enter the waveguide; here losses are quantified by the angular-dependent reflection, described by the Fresnel equations. For simplicity and comparability with earlier computations and experiments, the remainder of this work considers uniform unpolarized light entering perpendicular to the LSC's surface. In this case, the incoupling efficiency is given by

$$\eta_{inc} = 1 - \left|\frac{n_1 - n_2}{n_1 + n_2}\right|^2 \,, \tag{3.2}$$

with n_i the wavelength-independent refractive indices for the two media the light passes through, yielding for example $\eta_{inc} \approx 96\,\%$ for light transmitting from air to PMMA.

To contribute to photon transport to the edges, light entering the LSC has to be absorbed over the thickness t of the LSC. The light harvesting efficiency η_{LHE} gives the fraction of solar light which will be absorbed by the LSC after entering:

$$\eta_{LHE} = \frac{\int^{\lambda} S(\lambda)(1 - \exp(-\alpha(\lambda)t))\,\mathrm{d}\lambda}{\int^{\lambda} S(\lambda)\,\mathrm{d}\lambda} \,. \tag{3.3}$$

Here $S(\lambda)$ is the spectrum of the incident light expressed in amount of photons per wavelength and $\alpha(\lambda)$ the absorption coefficient per distance. The integration is done over the wavelength-domain λ of interest, in this work 280 nm to 4000 nm.

The absorbed fraction N_{absorbed} from an initial count of solar photons N will therefore be $N_{\text{absorbed}} = \eta_{\text{inc}}\eta_{\text{LHE}}N$. N_{absorbed} can now be converted by the luminescent centers. Following the derivation by Ten Kate *et al.* [22], conversion happens with the normalized emission spectrum of the LSC Φ_{em} as a rate of power

$$\frac{\Phi_{\text{em}}(\lambda)}{\lambda} = \frac{1}{\lambda}\frac{\epsilon(\lambda)}{\int^{\lambda}\epsilon(\lambda)\,\mathrm{d}\lambda}\,. \tag{3.4}$$

The conversion occurs with an efficiency provided by the quantum yield η_{QY}, assumed to be independent of luminophore concentration. Isotropic reemission follows, resulting in a reemission spectrum

$$\sigma_0(\lambda) = \eta_{\text{QY}}N_{\text{absorbed}}\frac{\Phi_{\text{em}}(\lambda)}{\lambda}\,. \tag{3.5}$$

For an isotropic point emitter, the radiant power $I(s)$, a distance $s = \sqrt{x^2+y^2}$ away from the emitter, is given by the Beer-Lambert law:

$$I(s) = I_0\exp(-\alpha s)\,, \tag{3.6}$$

where I_0 is the intensity of the emitter.

The amount of light absorbed in a circular segment $(s, s+\mathrm{d}s)$ equals the derivative of the Beer-Lambert law with respect to s. The corresponding absorption density factor $a(s,\lambda)$ per unit area, a distance s away from the emission center, is therefore

$$a(s,\lambda) = \frac{\alpha(\lambda)\exp(-\alpha(\lambda)s)}{2\pi s}\,. \tag{3.7}$$

$a(s,\lambda)$ is a density, independent of the initial intensity, hence I_0 is omitted.

To simplify the description of light transport through an LSC using this circular emission, two aspects need to be taken into account. First, the path length of light traveling to the perimeter has to be independent of depth. Figure 3.2 shows that, to reach a distance s horizontally, light has to traverse a distance $\frac{s}{\sin\theta}$ in an LSC plate, independent of emission depth. Second, the path the light takes needs to be independent of the polar emission angle θ. Redefining $\alpha(\lambda)$ to account

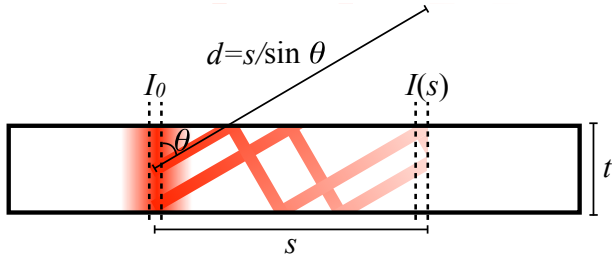


Figure 3.2: The two rays drawn are both emitted at an angle θ from different depths within the LSC. Both rays have to travel the same distance $s/\sin(\theta)$ to reach a column at a distance s, viewed from the top of the LSC. The radiant power $I(s)$ of the light from both rays is therefore equal at s, independent of the depth the light was emitted from.

for all possible emission angles, limited by the escape-cone, yields the effective absorption coefficient

$$\alpha'(\lambda) = \frac{\alpha(\lambda)}{\pi - 2\theta_c} \int_{\theta_c}^{\pi-\theta_c} \frac{1}{\sin(\theta)} \, \mathrm{d}\theta \,, \tag{3.8}$$

where θ_c is the LSC's critical angle.

The effective absorption coefficient allows us to work with depth- and emission-angle independent columns rather than having to take all separate luminescent centers (points) into account. We can therefore work in a 2D rather than in a 3D plane.

To obtain the reabsorption within a column $\gamma_i(x, y, \lambda)$, light emitted from all other columns within the LSC plane needs to be accounted for. A 2D convolution describes this problem. Convolving the absorption density factor and emission distribution provides

$$\gamma_i(x, y, \lambda) = (\eta_{\text{trap}} + \eta_{\text{CA}}(\lambda))\sigma_i(x, y, \lambda) ** a(x, y, \lambda) \,. \tag{3.9}$$

Here η_{trap} is the trapping efficiency and η_{CA} the cone absorption efficiency.

η_{trap} is defined as the ratio of light that will be subject to total internal reflection within the LSC plane after reemission. For an LSC in air

$$\eta_{\text{trap}} = \sqrt{1 - \frac{1}{n_2^2}} \,. \tag{3.10}$$

For PMMA with $n_2 \approx 1.5$ this means that the probability of a photon entering the escape-cone is around 25 %.

η_{CA} provides a measure to account for light that is emitted within the escape-cone but will be reabsorbed before escaping through the LSC's surface [22].

$$\eta_{\mathrm{CA}}(\lambda) = \frac{1}{t}\int_0^t \int_0^{\theta_c} \left(1 - e^{-\alpha(\lambda)z/\cos\theta}\right) \sin\theta \,\mathrm{d}\theta \,\mathrm{d}z \,. \tag{3.11}$$

Reabsorbed light can be emitted again to a next generation $i+1$. Similar to Equation (3.5), we sum over all absorbed photons and emit with the normalized emission spectrum as a rate of energy. Taking the quantum yield into account, this yields

$$\sigma_{i+1} = \eta_{\mathrm{QY}} \frac{\Phi_{\mathrm{em}}(\lambda)}{\lambda} \int^{\lambda} \lambda \gamma_i(x, y, \lambda) \,\mathrm{d}\lambda \,. \tag{3.12}$$

The process of reemission and reabsorption continues for many generations i until all photons have either escaped through the escape-cone, have been quenched, or have been collected at the LSC sides. In order to retrieve the amount of collected photons $C_i(\lambda)$ at the sides, we can simply take the difference between the emitted and the absorbed intensity of a generation over the entire LSC surface A_{LSC}. When we correct for escape-cone losses this yields

$$C_i(\lambda) = \eta_{\mathrm{trap}} \lambda \iint_{A_{\mathrm{LSC}}} \left(\sigma_i - \frac{1}{\eta_{\mathrm{trap}} + \eta_{\mathrm{CA}}} \gamma_i\right) \mathrm{d}x \,\mathrm{d}y \,. \tag{3.13}$$

The total number of collected photons C_Σ can be acquired through summation over all generations and integration over the wavelengths of interest.

With C_Σ the optical efficiency η from the MGLT model is calculated using

$$\eta = \eta_{\mathrm{inc}} \eta_{\mathrm{LHE}} \eta_{\mathrm{QY}} \eta_{\mathrm{trap}} \eta_{\mathrm{SA}} = \eta_{\mathrm{inc}} \eta_{\mathrm{LHE}} \frac{C_\Sigma}{N_{\mathrm{absorbed}}} \,. \tag{3.14}$$

To summarize, using only the experimentally measured absorption and emission spectra, index of refraction and quantum yield of an LSC material, the complete light transport through an LSC can be calculated by using multiple generations of reemission and reabsorption of light. It is important to note that the required absorption coefficient $\alpha(\lambda)$ is measured under the lowest possible luminophore concentration. $\alpha(\lambda)$ measured under high concentrations might cause self-absorption within the material to yield a different spectrum than the real absorption spectrum of the luminophore. Losses due to scattering are not

included in the model as presented, but can to a first order be estimated using an additional absorption term, in a similar fashion as presented in the work by Earp *et al.* [11]. This additional absorption term will not contribute to reemission in later generations. Since no assumption on the geometry of the LSC has been made, the MGLT model is usable for any shape and size of planar LSC window.

3.3 Monte Carlo Simulation

In order to verify the outcomes of the presented MGLT model, MC simulations were carried out. The MC simulations use the same absorption and emission spectra, wavelength-independent refractive indices, and concentration-independent quantum yields as input. A flowchart of the simulation is shown in Figure 3.3. To initialize the simulation, a photon P is generated incident on the surface of the LSC. P has a wavelength λ, pseudo-randomly chosen using the AM1.5 direct spectrum as distribution. The photon's initial position is determined by

$$\vec{x} = \begin{pmatrix} x \\ y \\ z \end{pmatrix} = \begin{pmatrix} \xi_x l \\ \xi_y w \\ t \end{pmatrix}, \tag{3.15}$$

where l, w and t are the LSC's length, width and thickness respectively. ξ_i is defined as a uniformly distributed random number. Each ξ_i mentioned in this work is a different $\xi_i \in [0, 1]$.

The path length d the photon will travel is found by rewriting the probability of absorption

$$p = 1 - \exp(-\alpha(\lambda)d) \tag{3.16}$$

to

$$d = -\frac{1}{\alpha(\lambda)} \log(1 - \xi_d)\,. \tag{3.17}$$

The photon's new position $\vec{x}'$ after traveling d, with azimuthal angle ϕ, can be found using

$$\vec{x}' = \vec{x} + \begin{pmatrix} d\frac{\sin\phi}{\sin\theta} \\ d\frac{\cos\phi}{\sin\theta} \\ \Delta z \end{pmatrix}, \tag{3.18}$$

where Δz is dependent on the number of reflections

$$R = \left\lfloor \frac{|d\cos\theta + z|}{t} \right\rfloor. \tag{3.19}$$

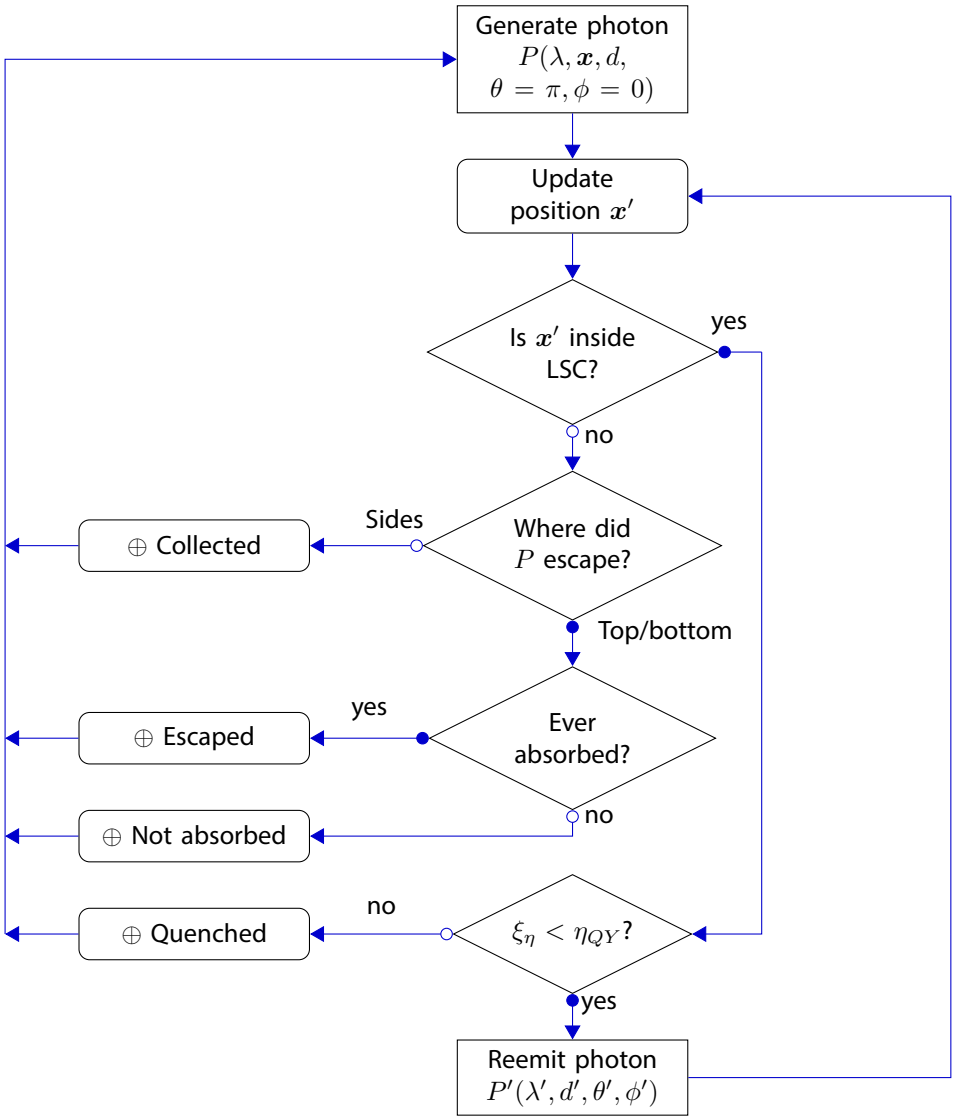


Figure 3.3: Schematic representation of the MC simulation.

If the photon is emitted outside of the escape-cone ($\theta_c < \theta < \pi - \theta_c$) and $(\theta - \frac{\pi}{2}) \times \mathrm{Ev}(R) > 0$, then

$$\Delta z = (|d\cos\theta + z| \bmod t) - z\,, \tag{3.20}$$

with $\mathrm{Ev}(R)$ returning 1 if R is even and -1 otherwise.

Else, if emission is outside of the escape-cone, but $(\theta - \frac{\pi}{2}) \times \mathrm{Ev}(R) < 0$, then

$$\Delta z = t - (|d\cos\theta + z| \bmod t) - z\,. \tag{3.21}$$

And otherwise, if emission happens within the escape-cone,

$$\Delta z = d\cos\theta\,. \tag{3.22}$$

$\phi = 0$ and $\theta = \pi$ for the initial photon, providing the same η_{inc} as in the MGLT model. If the photon is absorbed within the LSC, a random number is generated which determines if emission occurs, based on η_{QY}. Upon reemission a new wavelength λ' will be assigned to the photon by inverse transform sampling the LSC's emission spectrum. The photon will also acquire new emission angles

$$\phi' = 2\pi\xi_\phi\,, \tag{3.23}$$

$$\theta' = \arccos(2\xi_\theta - 1)\,. \tag{3.24}$$

When the photon exits the LSC through the sides, it is assumed to be collected by the PV cells. Otherwise, the photon has escaped through the escape-cone or has never been absorbed at all. Each simulation runs with $N_{\mathrm{input}} = 10^7$ photons to obtain a proper statistic. The optical efficiency is extracted as

$$\eta = \eta_{\mathrm{inc}} \frac{N_{\mathrm{collected}}}{N}\,. \tag{3.25}$$

3.4 Model Verification

In order to test the MGLT model, a selection of recent LSC materials was made for which all required data were available as published information. Although research on state-of-the-art materials has already started to shift its attention to Stokes' shift engineering the absorption and emission spectra, dyes featuring significant spectral overlap have also been selected. These materials with spectral overlap can aid in verifying the model's capabilities for quantifying self-absorption. See Data File 1 for the required spectroscopic properties and optical

efficiencies of all materials, calculated with both MC and MGLT. All calculations are done on a desktop computer with an Intel i5-6500 CPU clocked at 3.2 GHz.

When excluding materials with less than 1 % optical efficiency, excellent agreement between the two models is observed. Based on the simulation results from published data (Data File 1), the relative difference $\left(\frac{\eta^{\mathrm{MC}}-\eta^{\mathrm{MGLT}}}{\eta^{\mathrm{MC}}}\right)$ between MGLT and MC for 100 cm^2 plates is $2.1 \pm 6.3\,\%$, and for 1 m^2 plates is $4.4 \pm 7.7\,\%$. Materials with $\eta < 1\,\%$ have been excluded, as only a very minor difference in absolute calculated efficiency already causes a great increase in the difference in relative efficiency.

To illustrate the in-depth agreement with MC and functionality of the MGLT model, a $10 \times 10 \times 0.5\ \mathrm{cm}^3$ Lumogen Orange (LumoO) [23] LSC plate can be taken as example, since it features a strong self-absorption [see Figure 3.4a] and a high quantum yield ($\eta_{\mathrm{QY}} = 0.95$).

The self-absorption efficiency η_{SA} does not provide information about whether the photon was lost due to escaping or quenching. Therefore we have chosen to separate η_{SA} into an effective fraction of trapped photons $\eta_{\text{trap eff}}$ and an effective luminescent quantum yield $\eta_{\mathrm{QY\,eff}}$. Here

$$\eta_{\text{trap eff}} = 1 - \frac{N_{\text{escaped}}}{N_{\text{absorbed}} - N_{\text{quenched}}} \tag{3.26}$$

and

$$\eta_{\mathrm{QY\,eff}} = 1 - \frac{N_{\text{quenched}}}{N_{\text{absorbed}} - N_{\text{escaped}}}\,. \tag{3.27}$$

Note that these two effective efficiencies together do not provide the total device efficiency, but only show how great the amount of photons lost due to only escaping or quenching is. Table 3.1 provides the calculated (effective) efficiencies for each considered aspect of light transport and illustrates that, for each step of the light transportation process, MC and MGLT produce almost identical results.

The exact shape of the spectrum of the collected photons is highly susceptible to small changes in the treatment of physical input parameters, based on a model's assumptions. Therefore, this spectrum can serve as a rigorous test of physical correctness of the MGLT model. Figure 3.4a shows the spectrum transmitted through the perimeter of a LumoO-based LSC for both MC and MGLT. The transmitted spectra for MGLT and MC are almost identical, with MGLT displaying no random noise in the spectrum. The noise seen with MC is a direct consequence of the model's random nature, which would only decrease with a

Table 3.1: Calculated efficiencies for a $10 \times 10 \times 0.5\,\mathrm{cm}^3$ LumoO LSC using absorption coefficients as reported by Krumer *et al.* [23].

	MC	MGLT
η_{LHE} (%)	6.88	6.88
$\eta_{\mathrm{QY\,eff}}$ (%)	86.4	86.6
$\eta_{\mathrm{trap\,eff}}$ (%)	62.4	62.5
η (%)	3.76	3.76

large increase in simulated photons. It should be noted that the spectrum is also the same before normalization, which is a direct consequence of both models yielding the same optical efficiency. A significant redshift is seen even for a window of $100\,\mathrm{cm}^2$. The redshift can be explained by the overlap between absorption and emission, resulting in light emitted within the overlapping spectral area almost never reaching the window's edge.

These simulations can also be used to optimize LSC performance by changing the amount of absorption, which in practice would mean changing the luminophore concentration. Figure 3.4b shows that the majority of light transport takes place in the first generation (0 on the horizontal axis) of light reemission for the MGLT model. In this first generation a higher contribution η_i to the total η than in any of the succeeding generations is provided. Calculating just one generation is therefore sufficient for optimization, given $\eta_{\mathrm{QY}} < 1$ (see Section 3.8). The performance increase MGLT offers over MC is evident from Figure 3.4c. Optimizing a large LSC with MC requires a significant amount of photons to receive enough collected photons for a satisfactory simulation result. When η_{QY} and α rise, a single photon can remain trapped in the LSC for many reabsorption and reemission events, resulting in a long MC simulation time. MGLT, on the other hand, is generation-based, with a constant time required for each generation, resulting in a more constant and predictable time required to calculate optimal α. In MGLT, performance mainly scales with the amount of generations used, but also with how broad the overlap between the absorption and emission spectra is, as the most integration needs to be done across this overlap. Calculating the final efficiency of an optimized LSC is done quickest using a hybrid approach. First the LSC is optimized using one generation of MGLT. The optimal α is then used in an MC simulation to calculate the final efficiency as, for calculation of the full

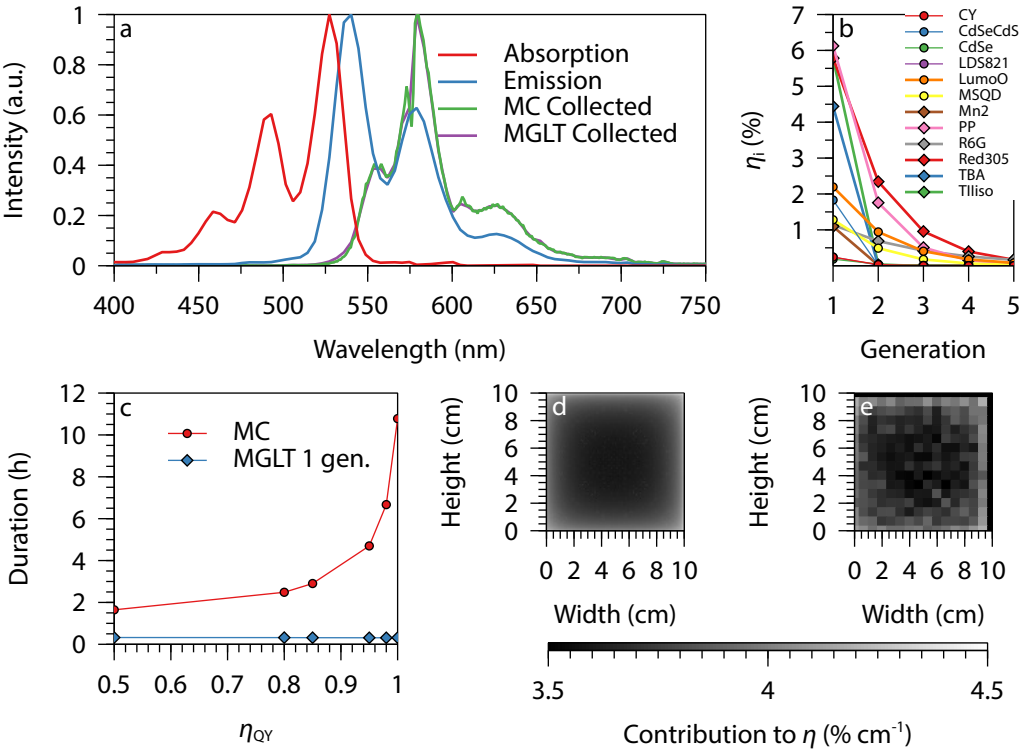


Figure 3.4: a: Comparison between MC and MGLT spectra for the simulated LumoO geometry received at the edges of the LSC. Absorption and emission spectra [23] are shown as well, signifying the large amount of redshift. **b:** Optical efficiency per generation for the MGLT model. All materials simulated have absorption coefficients as reported in their respective papers (see Published Data File 1 [24]). Materials with significant spectral overlap have many more generations contributing to the total η due multiple absorption and remission events. **c:** Calculation time needed in order to optimize the absorption coefficient for a $10 \times 10 \times 0.5\,\mathrm{cm}^3$ Red305 LSC with different quantum yields. Each datapoint has α ranging from $1 \times 10^{-1}\,\mathrm{cm}^{-1}$ to $1 \times 10^{8}\,\mathrm{cm}^{-1}$. **d:** Contribution to the optical efficiency per unit area of the LSC geometry, calculated by MGLT and **e:** by MC.

efficiency, MC is usually quicker than MGLT with many (> 5) generations.

Figure 3.4d (MGLT) and Figure 3.4e (MC) show that the simulations can help acquiring a more detailed view on what part of the LSC contributes most to edge transport. In Figures 3.4d and 3.4e each unit area receives the same amount of photons; the brightness of that area indicates how many of those photons will eventually reach the perimeter. While the bulk of the LSC provides the most photons, also most light is lost here. These losses can be explained by the distance between the place photons are absorbed and that of their collection. The self-absorption of LumoO causes photons absorbed in the center to become reabsorbed on their way to the perimeter. LumoO's high quantum yield causes most photons to still be reemitted while underway, but each extra absorption event adds to the chance of losing that photon through the escape-cone. Therefore, per unit area, the edge of the LSC contributes slightly more to the amount of collected photons than the bulk. The effect of an LSC's geometry can be studied in detail using MGLT, since the model is formulated around the LSC geometry [see Equation (3.9)]. Even after one generation of simulation (not shown) the effect of an LSC's geometry on light transport is clear. With MC a very large amount of photons is necessary to eliminate random noise. In Figure 3.4e 10^7 photons were binned over a 15×15 grid to reduce noise, resulting in a lesser resolution than observed with MGLT. Around 5×10^{11} photons would need to be simulated with MC to obtain a resolution comparable to MGLT. The geometry appears not to have a high impact on LSC efficiency. It could, however, still be possible to build an aesthetically pleasing LSC with sufficiently high efficiency by optimizing the geometry and opting for a fully transparent center.

Using the models as a design tool can help with understanding how a change in parameters will influence performance [25]. Here the strengths of both models can be used to complement each other. MGLT is formulated using physical laws, without a dependence on the collection of sufficient statistics. Changing one parameter will therefore after a limited amount (usually one) of generations show what influence such a change has on device performance. Once an optimum is found MC can be used to calculate the total device performance.

3.5 LSC Optimization Results

Maximizing the optical efficiency of an LSC would result in a maximally efficient BIPV element. Simulations can help designing such an optimal LSC by calculating the absorption coefficient $\alpha^\star$ with maximal optical efficiency $\eta^\star$ for the desired geometry or size.

Table 3.2 provides us with the results for such optimizations for both a $10 \times 10 \times 0.5\,\mathrm{cm}^3$ and a $100 \times 100 \times 0.5\,\mathrm{cm}^3$ LSC. The value of $\alpha^\star$ is calculated through MGLT, while the optical efficiency $\eta^\star$ with $\alpha = \alpha^\star$ comes from MC. What can be noted from Table 3.2 is that an optimized lab-scale LSC does not immediately yield an optimized $1\,\mathrm{m}^2$ LSC.

Table 3.2: Maximal possible efficiencies for two different LSC sizes for selected materials. $\alpha^\star_{\mathrm{max}}$ is the maximal absorption coefficient of the reported spectrum. When $\alpha^\star_{\mathrm{max}}$ is denoted as $\uparrow$, the highest possible luminophore concentration should be taken (in these calculations limited at $10^5\,\mathrm{cm}^{-1}$), for η_{LHE} has become the dominant factor in determining η for that material.

Material	$\alpha^\star_{\mathrm{max}10\times10}$ $\left(\mathrm{cm}^{-1}\right)$	$\eta^\star_{10\times10}$ (%)	$\alpha^\star_{\mathrm{max}100\times100}$ $\left(\mathrm{cm}^{-1}\right)$	$\eta^\star_{100\times100}$ (%)
CdSe [23]	2.9	0.4	1.0	0.1
CdSeCdS [26]	$\uparrow$	11.8	$\uparrow$	11.8
CY [27]	7.0	0.2	492.4	0.2
GQD [28]	7.4	2.5	3.3	1
LDS821 [15]	11.3	1.2	7.4	1
LumoO [23]	34.6	4.8	$\uparrow$	4.7
Mn2 [29]	$\uparrow$	3.4	$\uparrow$	3.4
MSQD [30]	25.7	2.0	1343.4	1.7
PP [4]	38.9	11	$\uparrow$	10.6
R6G [23]	17.0	3.0	7.4	0.7
Red305 [4]	$\uparrow$	13.5	$\uparrow$	13.5
TBA [31]	58.8	3.9	203.1	3.9
TIIiso [23]	2424.5	7.6	$\uparrow$	7.6

Figure 3.5 shows GQD as a notable example. The optical efficiency (circles) comes from two competing processes. A higher α means, on the one hand, an increased η_{LHE} (dashed); on the other, a decreased η_{SA} (diamonds), resulting in a geometry-specific optimum α_{max}. For GQD, a lab-scale device has a maximum of $\alpha^\star(\lambda = 474\,\mathrm{nm}) = 7.44\,\mathrm{cm}^{-1}$ with $\eta^\star_{10\times10} = 2.5\,\%$. If that maximum were

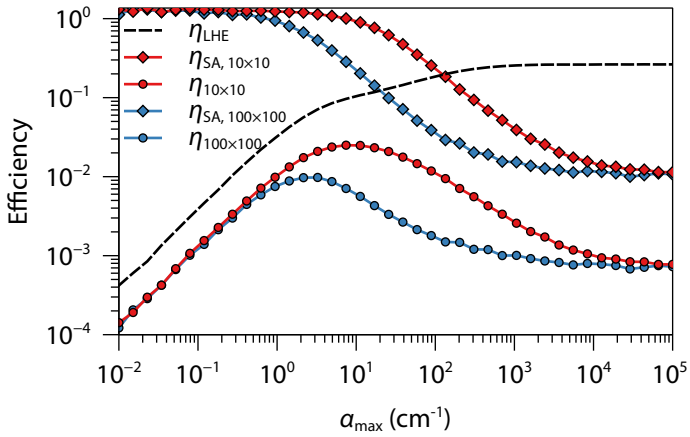


Figure 3.5: Optimization track for GQD ($\eta_{QY} = 0.45$) using two different LSC sizes. The displayed efficiency is the total optical efficiency, calculated through MC. Dotted lines indicate the maxima for the two simulated geometries.

to be used for the $100 \times 100 \times 0.5\,\mathrm{cm}^3$ window, a lower efficiency of $\eta_{100\times100} = 0.71\,\%$ would be obtained than when using $\alpha^\star(\lambda = 474\,\mathrm{nm}) = 3.26\,\mathrm{cm}^{-1}$ yielding $\eta^\star_{100\times100} = 0.98\,\%$. In line with [11, 12], we can conclude that dye concentration optimization needs to be done for the actual geometry of the LSC, as opposed to a lab-scale device. The combination of MGLT with MC allows us to do such optimization quickly. While Table 3.2 also shows drastic increases in $\alpha^\star_{max}$ for CY, MSQD and TBA, when comparing $10 \times 10\,\mathrm{cm}^2$ to $100 \times 100\,\mathrm{cm}^2$, the efficiencies for these materials are low throughout the entire range of absorption coefficients. Their efficiencies saturate quickly, since their efficiency is dominated by η_{LHE}. These materials show only a minute increase in η at the reported maximum.

In self-absorbing materials, the trapping efficiency as defined by Equation (3.10) is mostly an upper bound for the amount of photons that do not escape from the LSC's top or bottom surface. Figure 3.6a shows the impact of an increasing absorption coefficient α_{max} on the effective trapping efficiency $\eta_{trap\,eff}$ [Equation (3.26)] for a $100\,\mathrm{cm}^2$ Red305 with different quantum yields. From Figure 3.6a we can see that $\eta_{trap\,eff}$ can be separated into two regions: low and high optical density.

In the region with low optical density, the expected behavior for a self-absorbing material occurs. Photons are reabsorbed multiple times, and with each reemission there is a $\sim 25\,\%$ chance of entering the escape-cone and escaping through

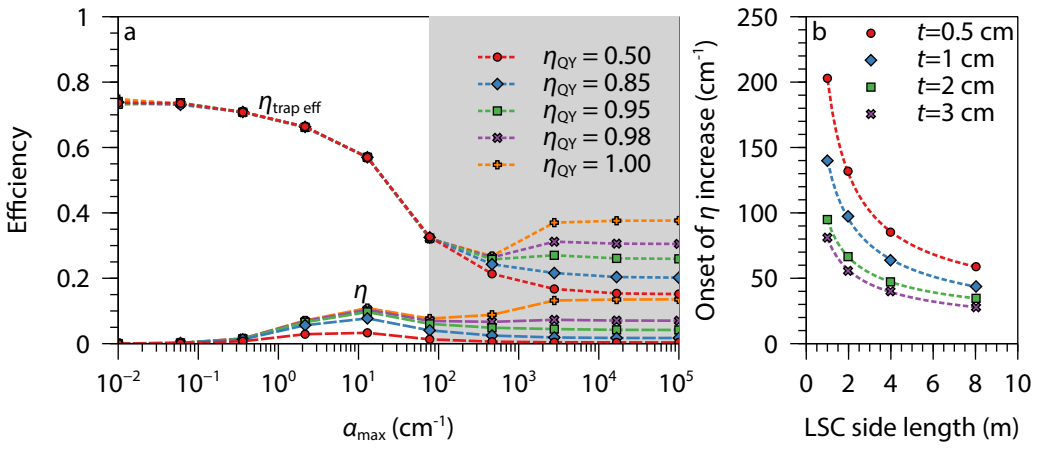


Figure 3.6: a: Optical efficiency η (dashed) and effective trapping efficiency $\eta_{\text{trap eff}}$ (dotted) in Red305 for increasing quantum yields. The white area indicates the region with low optical density, and the shaded area indicates high optical density. **b:** Onset of the increase in η for $\eta_{QY} = 1$ Red305 LSCs of varying sizes and thicknesses. This onset is defined as the point where η starts rising again. Lines are drawn as a guide to the eye.

the LSC's surface. A higher α means many reabsorption events, and therefore a higher possibility that a photon will end up escaping. In this region absorption within the escape-cone is outweighed by absorption during total internal reflection. Figure 3.5 shows that, when considering very low α, the still present escape-cone absorption gives a photon a chance to become absorbed before escaping. This still present trapping yields positive self-absorption, with $\eta_{SA} > 1$. Transport in the region of low optical density is hence governed by reabsorption and remission events during total internal refraction, resulting in a decreasing $\eta_{\text{trap eff}}$ as α_{max} rises.

In the region with high α_{max}, however, we see that $\eta_{\text{trap eff}}$ starts splitting up, depending on η_{QY}. In this region the redshifting of photons starts greatly influencing light transport. A photon will experience many reabsorption events over a short traveled distance. As η_{QY} rises, the probability for the photon to redshift outside of the LSC's absorption spectrum before quenching increases as well. When the photon redshifts outside of the LSCs absorption spectrum it cannot be absorbed again. Transport of the photon is then fully governed by total internal reflection. This leads to the effective trapping efficiency rising to near the theoretical η_{trap} for a large LSC, because when viewed from the perimeter, the absorption and emission spectrum of the LSC do not overlap anymore. Combined

with a high η_{QY}, this effect is accentuated, as almost every reabsorbed photon will be reemitted. For a high absorption maximum α_{max}, a local maximum of $\eta_{trap\,eff}$ coincides with a high amount of absorbed solar light, yielding a second, higher maximum in optical efficiency for strongly self-absorbing materials, with $\eta_{QY} \approx 1$, like Red305.

In most small-scale experimental setups the second maximum displayed in Figure 3.6a will not be visible. With high absorption coefficients ($\alpha_{max} > 60\,cm^{-1}$) luminescence quenching namely occurs [32]. Figure 3.6b shows that as the size or thickness of the LSC increases, the onset of the second maximum can become visible before luminescence quenching occurs. In large BIPV-scale LSCs of around $4 \times 4\,m^2$ this effect therefore could become perceivable at realistic concentrations of $\alpha_{max} < 60\,cm^{-1}$.

3.6 Expected BIPV Efficiencies

With the hybrid approach of MGLT for optimization and MC for a full efficiency calculation, it is possible to look at how the selected materials would perform as (colored) BIPV windows. Using the data from Table 3.2 would yield a theoretical maximum efficiency, but also visually opaque windows with potential luminescence quenching. Therefore as design critera we use (*i*) a $100 \times 100 \times 0.5\,cm^3$ window, (*ii*) maximally 25 % visible light (390 nm to 700 nm) absorption [33], (*iii*) $\alpha_{max} \leq 60\,cm^{-1}$ to avoid luminescence quenching.

An important figure of merit is the LSC's power efficiency η_{power}. The power efficiency is the ratio of power produced by the PV cells enclosing the LSC to the incoming sunlight [18]:

$$\eta_{power} = \frac{I_{sc} V_{oc} FF}{P_{in}} . \tag{3.28}$$

Here, I_{sc} is the short-circuit current and V_{oc} the open-circuit voltage of the entire BIPV device, i.e. the LSC combined with the solar cell; FF is the fill-factor of the attached solar cell, and P_{in} the total amount of solar power incident on the surface of the LSC. Assuming that these variables scale according to the solar cell's external quantum efficiency (EQE) only, the EQE curves of each PV material can be used to translate solar efficiency into LSC efficiency. Hence, the emission spectrum observed at the perimeter of the LSC is multiplied with a solar cell's EQE curve and integrated to determine I_{sc}.

The power efficiency does not yet tell if the LSC yields a higher efficiency than exposing the PV cells directly to sunlight. A parameter that captures this is the concentration factor [18]

$$\Gamma = G\frac{\eta_{\text{power}}}{\eta_{\text{PV}}}\,, \tag{3.29}$$

where the geometric gain $G = \frac{A_{\text{LSC}}}{A_{\text{PV}}}$, and η_{PV} is the efficiency of the solar cell when exposed to the AM1.5 spectrum.

To match the output spectrum of an LSC with a solar cell, data on the current record GaAs [34] ($\eta_{\text{PV}} = 27.6\,\%$), CIGS [35] ($\eta_{\text{PV}} = 21.0\,\%$), CdTe [36] ($\eta_{\text{PV}} = 21.0\,\%$), CZSSe [37] ($\eta_{\text{PV}} = 7.6\,\%$), CZTS [37] ($\eta_{\text{PV}} = 9.8\,\%$), Perovskite [37] ($\eta_{\text{PV}} = 22.1\,\%$), Dye [38] ($\eta_{\text{PV}} = 11.9\,\%$), Organic [37] ($\eta_{\text{PV}} = 11.2\,\%$), and Si [39] ($\eta_{\text{PV}} = 25.6\,\%$) cells were used to select the cell which would give the best performance.

First, two generations of MGLT are used to get an indication of what α_{max} an LSC would be most efficient with when combined with each of the solar cells. From this range the α_{max} that yields the highest estimated η_{power} adhering to the design-constraints is selected. Finally accurate values for η_{power} and Γ are calculated with MC. The results for the five best performing $100 \times 100 \times 0.5\,\text{cm}^3$ LSCs are shown in Table 3.3. A theoretical maximum, if there was no concentration quenching, for all LSCs from Table 3.2 can be found in Data File 2 [24]. In the theoretical case, the second maximum of Red305 yields $\eta_{\text{power}}^{\text{GaAs}} = 8.6\,\%$ as maximal power efficiency.

From Table 3.3 we see that most presented LSCs would already function as efficient PV solar concentrators, evident from $\Gamma \gg 1$. These could be of use in e.g. noise barriers [40], where no clear visible light throughput at the rear of the LSC is required. Also as BIPV windows, in places where no solar cells would otherwise be placed, the LSCs can still perform their function as a BIPV concentrator. Even when a serious constraint of $\eta_{\text{LHE}}^{\text{vis}} = 25\,\%$ is placed on the LSCs, $\Gamma > 1$.

One remark that can be made is that the older LSC materials, Perylene perinone (PP) and Red 305, are still among the most efficient. With the constraint of $\eta_{\text{LHE}}^{\text{vis}} = 25\,\%$ the efficiency of PP does however drop significantly. This is due to the overlap between the visible solar spectrum and the absorption of PP being larger than in the other presented LSCs. $\eta_{\text{LHE}}^{\text{vis}} = 25\,\%$ is therefore a more severe constraint on PP than on any of the other presented materials.

One can also notice the significant redshift observed in the output spectrum

Table 3.3: Power conversion efficiencies and concentration factors for $100 \times 100 \times 0.5\,\mathrm{cm}^3$ LSC materials with PV cells covering the entire perimeter with $\alpha_{\max} = 60\,\mathrm{cm}^{-1}$ (except for Red305, where $\alpha_{\max} = 5.5\,\mathrm{cm}^{-1}$ and LumoO with $\alpha_{\max} = 7.9\,\mathrm{cm}^{-1}$) and where only 25 % of the visible spectrum is absorbed ($\eta^{\mathrm{vis}}_{\mathrm{LHE}} = 25\,\%$). Here $\lambda^{\mathrm{out}}_{\max}$ is the LSC's output spectrum observed at the perimeter and $\eta^{\mathrm{GaAs}}_{\mathrm{power}}$ the highest power efficiency using a GaAs solar cell. $\eta^{\mathrm{alt}}_{\mathrm{power}}$ is the best alternative (non-GaAs) cell's power efficiency, with concentration factor Γ^{alt}.

		PV solar concentrator $\alpha_{\max} \leq 60\,\mathrm{cm}^{-1}$			BIPV window $\eta^{\mathrm{vis}}_{\mathrm{LHE}} = 25\,\%$				
Material	$\lambda^{\mathrm{out}}_{\max}$ (nm)	$\eta^{\mathrm{GaAs}}_{\mathrm{power}}$ (%)	$\eta^{\mathrm{alt}}_{\mathrm{power}}$ (%)	Γ^{alt}	$\alpha_{\max}$ $\left(\mathrm{cm}^{-1}\right)$	$\eta^{\mathrm{GaAs}}_{\mathrm{power}}$ (%)	$\eta^{\mathrm{alt}}_{\mathrm{power}}$ (%)	Γ^{alt}	Best alt. cell
CdSeCdS	640	4.1	3.3	8.4	12.9	3.0	2.4	6.1	Perovskite
LumoO	579	*1.4*	*1.1*	*2.8*	7.9	1.4	1.1	2.8	Perovskite
PP	(743) 720	5.9	4.3	10.2	1.4	1.8	1.3	3.0	CdTe
Red305	642	*3.6*	*2.7*	*7.0*	2.0	2.3	1.8	4.6	Perovskite
TIIiso	840	3.3	2.9	5.6	2.2	1.2	1.0	2.0	Si

of PP when increasing the concentration by more than 40× (noted between parentheses in Table 3.3). This redshifting can be explained by the large overlap between the absorption and emission spectra of PP.

Optimizing dye concentration with respect to the highest possible η is not always the best approach. For all materials there is a non-constant discrepancy between η and η_{power}. When regarding practical applications it's better to optimize α_{max} with respect to the PV cells available, for maximal power efficiency or concentration factor. We can see that optical efficiency of each material only gives an indication of how well an LSC will perform when connected to a PV element compared to others, i.e. materials with a higher η will also perform better when connected to a solar cell. An example of this is TIIiso. TIIiso has $\eta = 6.7\,\%$ for $\alpha_{\text{max}} = 60\,\text{cm}^{-1}$, while its $\eta_{\text{power}}^{\text{GaAs}} = 3.3\,\%$. This can be explained by the mismatch of the LSC's output spectrum and any PV cell's quantum efficiency curve. Most LSCs will have their peak perimeter-output still within the higher ranges of a PV cell's EQE curve, but due to redshifting from self-absorption, much of the spectrum will fall in the lower EQE region. Another consequence of this redshifted spectrum observed at the perimeter of an LSC, is that the optimal solar cell choice varies widely. This variation puts an emphasis on the need to either design a solar cell for a specific LSC, or, if the LSC were to be designed for use with a specific solar cell, to optimize the redshift of LSC output spectra by altering the LSC's geometry or maximal absorption coefficient.

Variations in materials producing similar η_{power}, but carrying a different concentration factor can be explained by the solar conversion efficiency of the cell. An example of this variation is seen with LumoO and TIIiso. Even with almost the same conversion efficiency for $\eta_{\text{LHE}}^{\text{vis}} = 25\,\%$, the higher η_{PV} of the Si cell results in a lower concentration factor for LumoO. A similar table could be constructed showing which solar cell would offer the maximum concentration factor. Solar cells with much lower η_{PV} would dominate such a table, as the difference between η_{PV} and η_{power} becomes lower for these cells. Optimization for maximum concentration factor or a compromise situation, yielding quickest return of investment, could be done in a similar fashion.

3.7 Conclusions

We have shown that, using a multiple-generation light transport model based on Beer-Lambert's law, light transport without scattering through an LSC of arbitrary geometry can be precisely and fully characterized, with only a relative difference of $4.4 \pm 7.7\,\%$ between MGLT and MC for $1\,m^2$ LSCs. Using the MGLT approach, calculating only the first generation of light transport is sufficient to optimize the luminophore concentration of an LSC. The total efficiency of this optimized LSC can then be calculated using MC. Most insight in most materials can however be gained if both models are used in conjunction with each other. The MGLT model can show in great detail what areas of the LSC will contribute to edge transport, whereas MC can more quickly provide an accurate assessment of what efficiencies one could expect. It has been shown that the optimal luminophore concentration is dependent on the size of an LSC. Therefore, an optimized lab-scale LSC's concentration is not transferable to LSCs of different sizes. The power conversion efficiency of $1\,m^2$ LSCs does not exceed a theoretical 9 % and a practical 6 % for the luminescent materials addressed in this work. These materials can still function very well as BIPV elements, owing to the high concentration factors. As BIPV element, the LSC functions both as a PV solar concentrator and as a semi-transparent power-generating window, which would be complementary to non-transparent solar cells on the building envelope. Finally, we have shown and quantified that for an LSC with a large overlap between its absorption- and emission spectrum, but a high quantum efficiency, self-absorption can be beneficial to its optical efficiency. Photons trapped inside such LSCs will remain trapped until they are redshifted outside of the LSC's absorption spectrum when the LSC has a sufficiently high absorption maximum. The results obtained in this chapter can help in designing efficient, aesthetically pleasing LSCs for use in the built environment.

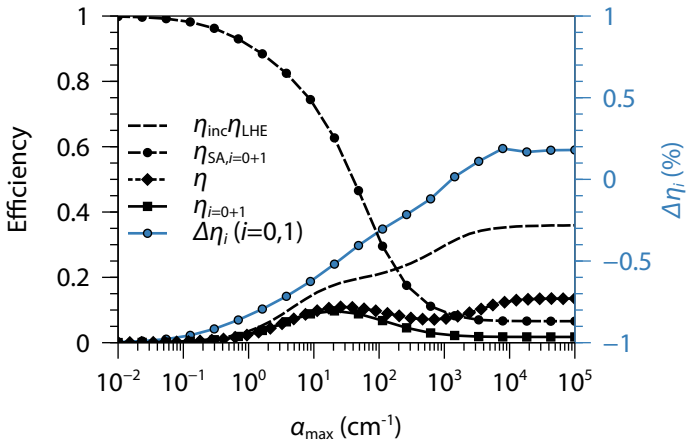


Figure 3.7: Optimization track of a $10 \times 10 \times 0.5\,\mathrm{cm}^3$ Red305 LSC with $\eta_{QY} = 1$. A second maximum is seen in the optical efficiency. Here the second MGLT generation contributes more to the edge-transmission than the first generation.

3.8 Appendix: Positive Self-Absorption in MGLT

Optimizing while taking positive self-absorption into account doesn't require calculating the total efficiency of the material. The local maxima occurring due to positive self-absorption can also be observed using the MGLT model with 2 generations. Figure 3.7 shows that, when $\eta_{QY} = 1$ in Red305, the difference in collected fraction $\Delta\eta_i$ between two generations decreases as the absorption maximum increases. This indicates that the increasing amount of light absorbed between the first to the second generation does not quench or escape, but rather keeps contributing to collection on the perimeter. For sufficiently high α the second generation starts contributing more to total transport than the first, at the same point that the material's optical efficiency η starts rising again, giving an indication of a potential efficiency increase due to positive self-absorption.

References

[1] F. Frontini, P. Bonomo, A. Chatzipanagi, G. Verberne, M. van den Donker, K. Sinapis, W. Folkerts, M. van den Donker, K. Sinapis, and W. Folkerts, *BIPV Product Overview For Solar Facades and Roofs*, tech. rep. (2015), pp. 1–12.

[2] W. H. Weber and J. Lambe, "Luminescent greenhouse collector for solar radiation.," Applied Optics **15**, 2299–2300 (1976).

[3]J. S. Batchelder, A. H. Zewai, and T. Cole, "Luminescent solar concentrators 1: Theory of operation and techniques for performance evaluation," Applied Optics **18**, 3090–3110 (1979).

[4]L. Desmet, A. J. M. Ras, D. K. G. de Boer, and M. G. Debije, "Monocrystalline silicon photovoltaic luminescent solar concentrator with 4.2% power conversion efficiency," Optics Letters **37**, 3087–3089 (2012).

[5]J. C. Goldschmidt, M. Peters, A. Bösch, H. Helmers, F. Dimroth, S. W. Glunz, and G. Willeke, "Increasing the efficiency of fluorescent concentrator systems," Solar Energy Materials and Solar Cells **93**, 176–182 (2009).

[6]M. de Jong, W. Kesteloo, and E. van der Kolk, "Deposition of luminescent NaCl:Tm^{2+} thin films with a Tm concentration gradient using RF magnetron sputtering," Optical Materials **46**, 149–153 (2015).

[7]J. S. Batchelder, A. H. Zewail, and T. Cole, "Luminescent solar concentrators 2: Experimental and theoretical analysis of their possible efficiencies," Applied Optics **20**, 3733 (1981).

[8]A. J. Chatten, K. W. J. Barnham, B. F. Buxton, N. J. Ekins-Daukes, and M. A. Malik, "A new approach to modelling quantum dot concentrators," Solar Energy Materials and Solar Cells **75**, 363–371 (2003).

[9]L. Fang, T. S. Parel, L. Danos, and T. Markvart, "Photon reabsorption in fluorescent solar collectors," Journal of Applied Physics **111**, 076104 (2012).

[10]I. Papakonstantinou and C. Tummeltshammer, "Fundamental limits of concentration in luminescent solar concentrators revised: the effect of reabsorption and nonunity quantum yield," Optica **2**, 841 (2015).

[11]A. Earp, G. Smith, P. Swift, and J. Franklin, "Maximising the light output of a Luminescent Solar Concentrator," Solar Energy **76**, 655–667 (2004).

[12]A. A. Earp, G. B. Smith, J. Franklin, and P. Swift, "Optimisation of a three-colour luminescent solar concentrator daylighting system," Solar Energy Materials and Solar Cells **84**, 411–426 (2004).

[13]J. Sansregret, J. M. Drake, W. R. L. Thomas, and M. L. Lesiecki, "Light transport in planar luminescent solar concentrators: the role of DCM self-absorption," Applied Optics **22**, 573–577 (1983).

[14]M. Carrascosa, S. Unamuno, and F. Agullo-Lopez, "Monte Carlo simulation of the performance of PMMA luminescent solar collectors.," Applied optics **22**, 3236 (1983).

[15]V. Sholin, J. D. Olson, and S. A. Carter, "Semiconducting polymers and quantum dots in luminescent solar concentrators for solar energy harvesting," Journal of Applied Physics **101**, 123114 (2007).

[16]L. R. Wilson, B. C. Rowan, N. Robertson, O. Moudam, A. C. Jones, and B. S. Richards, "Characterization and reduction of reabsorption losses in luminescent solar concentrators.," Applied optics **49**, 1651–1661 (2010).

[17]D. Şahin, B. Ilan, and D. F. Kelley, "Monte-Carlo simulations of light propagation in luminescent solar concentrators based on semiconductor nanoparticles," Journal of Applied Physics **110**, 033108 (2011).

[18]S. R. Wilton, M. R. Fetterman, J. J. Low, G. You, Z. Jiang, and J. Xu, "Monte Carlo study of PbSe quantum dots as the fluorescent material in luminescent solar concentrators," Optics Express **22**, A35 (2014).

[19]A. Kerrouche, D. A. Hardy, D. Ross, and B. S. Richards, "Luminescent solar concentrators: From experimental validation of 3D ray-tracing simulations to coloured stained-glass windows for BIPV," Solar Energy Materials and Solar Cells **122**, 99–106 (2014).

[20]V. I. Klimov, T. A. Baker, J. Lim, K. A. Velizhanin, and H. McDaniel, "Quality Factor of Luminescent Solar Concentrators and Practical Concentration Limits Attainable with Semiconductor Quantum Dots," ACS Photonics, acsphotonics.6b00307 (2016).

[21]M. G. Debije and P. P. C. Verbunt, "Thirty Years of Luminescent Solar Concentrator Research: Solar Energy for the Built Environment," Advanced Energy Materials **2**, 12–35 (2012).

[22]O. M. ten Kate, K. M. Hooning, and E. van der Kolk, "Quantifying self-absorption losses in luminescent solar concentrators," Applied Optics **53**, 5238 (2014).

[23]Z. Krumer, S. J. Pera, R. J. van Dijk-Moes, Y. Zhao, A. F. de Brouwer, E. Groeneveld, W. G. van Sark, R. E. Schropp, and C. de Mello Donegá, "Tackling self-absorption in luminescent solar concentrators with type-II colloidal quantum dots," Solar Energy Materials and Solar Cells **111**, 57–65 (2013).

[24]E. P. J. Merkx, O. M. ten Kate, and E. van der Kolk, "Rapid optimization of large-scale luminescent solar concentrators: evaluation for adoption in the built environment," Optics Express **25**, A547–A563 (2017).

[25]D. Alonso-Álvarez, D. Ross, E. Klampaftis, K. R. McIntosh, S. Jia, P. Storiz, T. Stolz, and B. S. Richards, "Luminescent down-shifting experiment and modelling with multiple photovoltaic technologies," Progress in Photovoltaics: Research and Applications **23**, 479–497 (2015).

[26]I. Coropceanu and M. G. Bawendi, "Core/Shell Quantum Dot Based Luminescent Solar Concentrators with Reduced Reabsorption and Enhanced Efficiency," Nano Letters **14**, 4097–4101 (2014).

[27]Y. Zhao, G. Meek, B. Levine, and R. Lunt, "Near Infrared Harvesting Transparent Luminescent Solar Concentrators," Advanced Optical materials **2**, 606–611 (2014).

[28]F. Meinardi, A. Colombo, K. A. Velizhanin, R. Simonutti, M. Lorenzon, L. Beverina, R. Viswanatha, V. I. Klimov, and S. Brovelli, "Large-area luminescent solar concentrators based on 'Stokes-shift-engineered' nanocrystals in a mass-polymerized PMMA matrix," Nature Photonics **8**, 392–399 (2014).

[29]C. S. Erickson, L. R. Bradshaw, S. McDowall, J. D. Gilbertson, D. R. Gamelin, and D. L. Patrick, "Zero-Reabsorption Doped-Nanocrystal Luminescent Solar Concentrators," ACS Nano **8**, 3461–3467 (2014).

[30]J. Bomm, A. Büchtemann, A. J. Chatten, R. Bose, D. J. Farrell, N. L. Chan, Y. Xiao, L. H. Slooff, T. Meyer, A. Meyer, W. G. van Sark, and R. Koole, "Fabrication and full characterization of state-of-the-art quantum dot luminescent solar concentrators," Solar Energy Materials and Solar Cells **95**, 2087–2094 (2011).

[31]Y. Zhao and R. R. Lunt, "Transparent Luminescent Solar Concentrators for Large-Area Solar Windows Enabled by Massive Stokes-Shift Nanocluster Phosphors," Advanced Energy Materials **3**, 1143–1148 (2013).

[32]A. P. Green and A. R. Buckley, "Solid state concentration quenching of organic fluorophores in PMMA," Physical Chemistry Chemical Physics **17**, 1435–1440 (2015).

[33]F. M. Vossen, M. P. Aarts, and M. G. Debije, "Visual performance of red luminescent solar concentrating windows in an office environment," Energy and Buildings **113**, 123–132 (2016).

[34]M. A. Green, K. Emery, Y. Hishikawa, W. Warta, and E. D. Dunlop, "Solar cell efficiency tables (version 40)," Progress in Photovoltaics: Research and Applications **20**, 606–614 (2012).

[35]M. A. Green, K. Emery, Y. Hishikawa, W. Warta, and E. D. Dunlop, "Solar cell efficiency tables (version 46)," Progress in Photovoltaics: Research and Applications **23**, 805–812 (2015).

[36]M. A. Green, K. Emery, Y. Hishikawa, W. Warta, and E. D. Dunlop, "Solar cell efficiency tables (Version 45)," Progress in Photovoltaics: Research and Applications **23**, 1–9 (2015).

[37]M. A. Green, K. Emery, Y. Hishikawa, W. Warta, and E. D. Dunlop, "Solar cell efficiency tables (version 48)," Progress in Photovoltaics: Research and Applications **24**, 905–913 (2016).

[38]M. A. Green, K. Emery, Y. Hishikawa, W. Warta, and E. D. Dunlop, "Solar cell efficiency tables (version 41)," Progress in Photovoltaics: Research and Applications **21**, 1–11 (2013).

[39]M. A. Green, K. Emery, Y. Hishikawa, W. Warta, and E. D. Dunlop, "Solar cell efficiency tables (version 44)," Progress in Photovoltaics: Research and Applications **22**, 701–710 (2014).

[40]M. Kanellis, M. M. de Jong, L. Slooff, and M. G. Debije, "The solar noise barrier project: 1. Effect of incident light orientation on the performance of a large-scale luminescent solar concentrator noise barrier," Renewable Energy **103**, 647–652 (2017).

— 4 —

A Method for the Detailed Characterization of Co-Sputtered Inorganic Luminescent Material Libraries

Understanding the behavior of combinatorially developed luminescent materials requires detailed characterization methods that have been lacking thus far. We developed a device for directly surveying the luminescent properties of thin-film libraries created through combinatorial gradient sputter deposition. Step-scan recorded excitation-, emission- and luminescence decay spectra of a thin-film library were resolved and combined with EDX measurements on the same film, relating composition to luminescent properties. This technique was applied to a single-substrate gradient thin-film library of $NaBr_{0.73}I_{0.27}$ to $NaBr_{0.09}I_{0.91}$, doped with 6.5 % to 16.5 % Eu^{2+}. This gradient film closely followed Vegard's law, with emission fluently shifting from 428 nm to 439 nm. In comparison, pure NaBr:Eu^{2+} showed emission at 428 nm and NaI:Eu^{2+} at 441 nm. Luminescence decay measurements demonstrated a great degree of concentration quenching in the gradient film. From these measurements we could conclude that an optimized phosphor would most efficiently luminesce when close to NaI:Eu^{2+}. This gradient film confirmed that the method presented in this work allows to both study and optimize luminescent behavior in a broad range of host- and dopant systems.

This chapter has been published as: E.P.J. Merkx and E. van der Kolk, "Method for the Detailed Characterization of Cosputtered Inorganic Luminescent Material Libraries," ACS Combinatorial Science **20**, 595–601 (2018)
All data supporting the figures in this chapter can be found at: http://doi.org/uuid:840f234a-c79c-4a5b-a63b-ea3707d74e2a

4.1 Introduction

Combinatorial synthesis finds broad application in many fields, but in the case of phosphor synthesis only a limited number of reports exist. This lack of past works can be explained by that combinatorial methods, when applied to conventional searches like the search for white light LEDs, usually converge to known phosphors [1]. In addition, the analysis methods used for combinatorially synthesized libraries of luminescent materials are often limited to (color-filtered) charge-coupled device (CCD) photography of a library under UV illumination [2–10], substrate-scanning with color filters to isolate emission peaks [11, 12], or cathode luminescence with no information on low energy excitations [13]. These coarse characterizations still have to be followed by powder synthesis to fully analyze the luminescent properties of a material of interest.

In this chapter, we present a novel method that enables the detailed characterization of a luminescent composition library, based on combinatorial gradient deposition of thin-films using DC/RF magnetron sputtering. This gradient is realized by taking advantage of the low mobility of sputtered adatoms when depositing without substrate heating [13]. The presented method is capable of resolving position-dependent structural and compositional information, as well as photoluminescent excitation-, emission- and decay spectra. This combination allows us to link the position-dependent structural and compositional information to the recorded luminescence properties, thereby retrieving direct composition-property relations.

Determination of the structure and composition is done with step-scan X-ray diffraction (XRD) for crystallinity and phase determination. Energy-dispersive X-ray spectroscopy (EDX) is used to resolve the local composition of the gradient thin-film. Photoluminescence measurements are done using a combination of laser excitation and an xy-stepping stage, with luminescence captured by either a CCD spectrometer, or a photomultiplier tube (PMT) coupled to a digitizer.

In binary halides, substitution of anions can lead to a fluent shifting of emission wavelength between the two mixed compounds, in line with Vegard's law. For instance, $KCl_{1-x}Br_x$ crystals doped with Eu^{2+} have shown this fluent shifting of emission [14]. Therefore, to illustrate the capabilities of the method, we have chosen a continuously varying mixed-phase library of NaBr:Eu^{2+} and NaI:Eu^{2+} as an example. While the individual phosphors have previously been

researched [14], the behavior of the mixed-phase phosphor has not yet been studied. The endpoints of this library are therefore well-known, while the mixed-phase in between provides new data on the behavior of mixed binary halides. The combination of luminescent, compositional and structural information is employed to see if these two phosphors will also display behavior following Vegard's law. Furthermore, the possibility of optimizing luminescent behavior in terms of quantum efficiency is explored with this library.

4.2 Results and Discussion

4.2.1 Library Creation and Method for Characterization

To provide an illustration of the combinatorial synthesis and characterization route, NaBr, NaI and Eu were magnetron co-sputtered at a 90° angle from each other on a $5 \times 5\,cm^2$ UV fused silica substrate. Figures 4.1a and 4.1b respectively show the layout of the sputtering chamber prior to deposition and during deposition. UV fused silica was chosen since it does not show luminescence, contrary to other glass types [15]. As with Tm [16], Eu sputtered together with binary alkali halides readily forms its divalent state, without the need for any additional oxidizing gases or heat treatments. The library was therefore deposited at room temperature using an inert Ar atmosphere, without further treatment. In addition, being SiO_2 of high purity, it will not have overlap with the EDX lines for Na, Br, I and Eu. Because of the hygroscopic nature of NaBr and NaI, the as-deposited film was transported from the sputtering chamber to a nitrogen-filled glovebox using an airtight container under vacuum. In the glovebox, the sample (Figure 4.1c) was transferred to a N_2-filled, airtight sample holder with a UV fused silica or polyimide foil window for optical or XRD measurements, respectively.

Figures 4.1d to 4.1f show the elemental concentrations based on EDX measurements at 40 locations and an interpolation between these points.

Direct EDX measurements of the Eu concentration carry a high uncertainty. Contrary to Eu, the ratio of Na to Br and I can be repeatedly measured with good certainty across the film. The composition of the film should be charge-neutral. The Eu concentration can therefore be derived from the measured ratio of Na to Br and I by setting the ratio of Eu^{2+} and Na^+ to Br^- and I^- equal to unity.

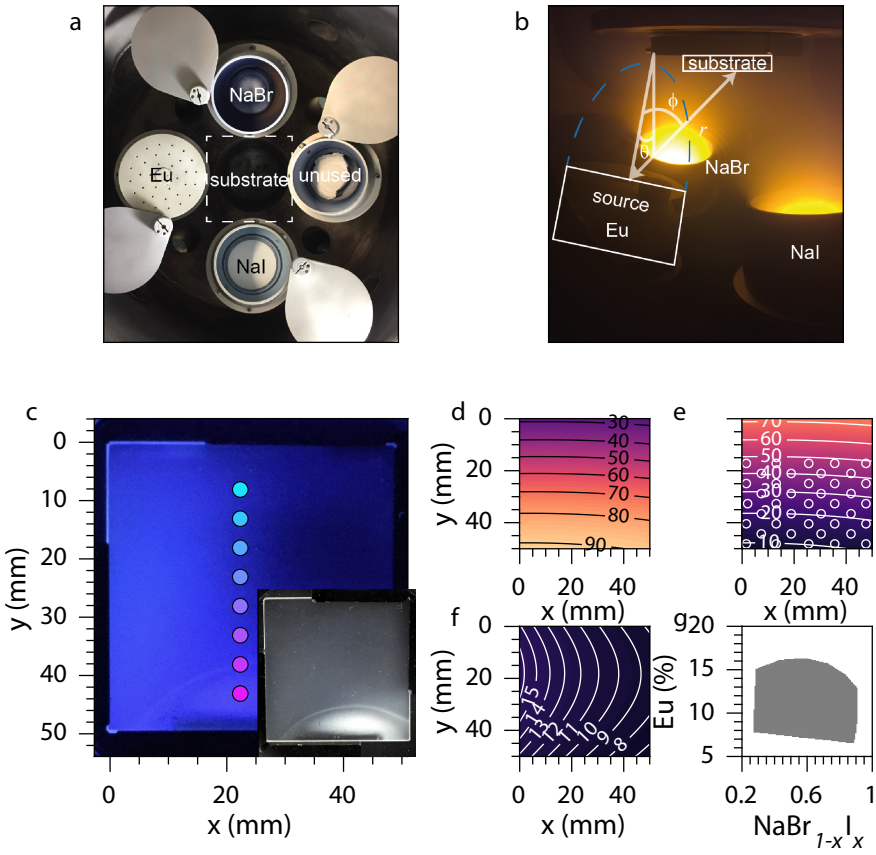


Figure 4.1: Compositional library of a gradient of NaBr to NaI doped with varying concentrations of Eu. **a:** Photograph of the layout of the sputtering sources used to fabricate the gradient library. The source with Eu has a mask applied to reduce the sputtering yield, as sputtering at a lower power leads to an unstable plasma. This and all subsequent images have been oriented with NaI always depicted at the bottom, NaBr at the top and Eu to the left. **b:** Photograph of the sputtering chamber during deposition. Overlaid is a schematic of the parameters used in Equation (4.1). The dashed lines are an illustration of the elongated spherical distribution of material sputtered from the Eu source. **c:** Photograph of the sample under UV excitation, and (inset) white light illumination. Colored dots show where XRD measurements were taken. **d, e, f:** EDX data across the substrate displaying atomic concentrations of I, Br and doping concentration of Eu respectively. The white circles in **e:** mark the locations where EDX measurements were taken. **g:** Area showing the span of NaBr−NaI−Eu compositions covered by the substrate.

The interpolation is obtained by fitting with the surface-source evaporation equation. The surface-source evaporation equation for a single source is based on the mass deposited on the substrate per unit area $\mathrm{d}M_s/\mathrm{d}A_s$, given by [13, 17]

$$\frac{\mathrm{d}M_S(x,y)}{\mathrm{d}A_S} = M_T \frac{(n+1)\cos^n\phi(x,y)\cos\theta}{2\pi r^2(x,y)} . \tag{4.1}$$

Here M_T is the total mass exiting the sputtering source, n determines the sharpness of the elongated sphere of material being sputtered from the source, ϕ is the angle between the source normal and a line extending from the center of the source to a position on the substrate, θ is the angle between the source normal and the substrate normal, and r is the distance between the source and any position on the substrate's surface. These parameters are illustrated in Figure 4.1b. Fitting the concentration c_j of a material $j \in i$ when using N target materials i can be accomplished with

$$c_j(x,y) = \frac{\left(\frac{\mathrm{d}M_s}{\mathrm{d}A_s}\right)_j}{\sum_i \left(\frac{\mathrm{d}M_s}{\mathrm{d}A_s}\right)_i} , \tag{4.2}$$

where the fitting parameters are the respective n_i and $M_{T,i}$ of the sputtering sources.

The resultant c_j for j =I, Br and Eu are respectively shown in Figures 4.1d to 4.1f.

The sputtering yield of NaI is larger than that of NaBr. The iodide concentration therefore follows the distribution yielded by the gun with NaI, which leads to the semi-circles seen in Figure 4.1d. Figure 4.1g brings all EDX results together and shows that this single substrate comprises a variation of 6.5 % to 16.5 % Eu, and a variation of $NaBr_{0.73}I_{0.27}$ to $NaBr_{0.09}I_{0.91}$. Across the substrate, this means an average slope of $0.05\,\%\,\mathrm{mm}^{-1}$ from NaBr to NaI and an average slope in Eu-doping percentage of $0.15\,\%\,\mathrm{mm}^{-1}$ (all concentrations mentioned are in atomic percent).

A custom computer-controlled dual xy-translation stage that is synchronized with an optical parametric oscillator (OPO) laser and a data-acquisition system, referred to as the XY-scanner, was developed for mapping the luminescent properties across the thin-film surface. A schematic of the entire characterization system is shown in Figure 4.2. Light ranging from 193 nm to 2600 nm with 0.3 nm linewidth generated by a 100 Hz (3 ns to 5 ns FWHM pulses) OPO laser is

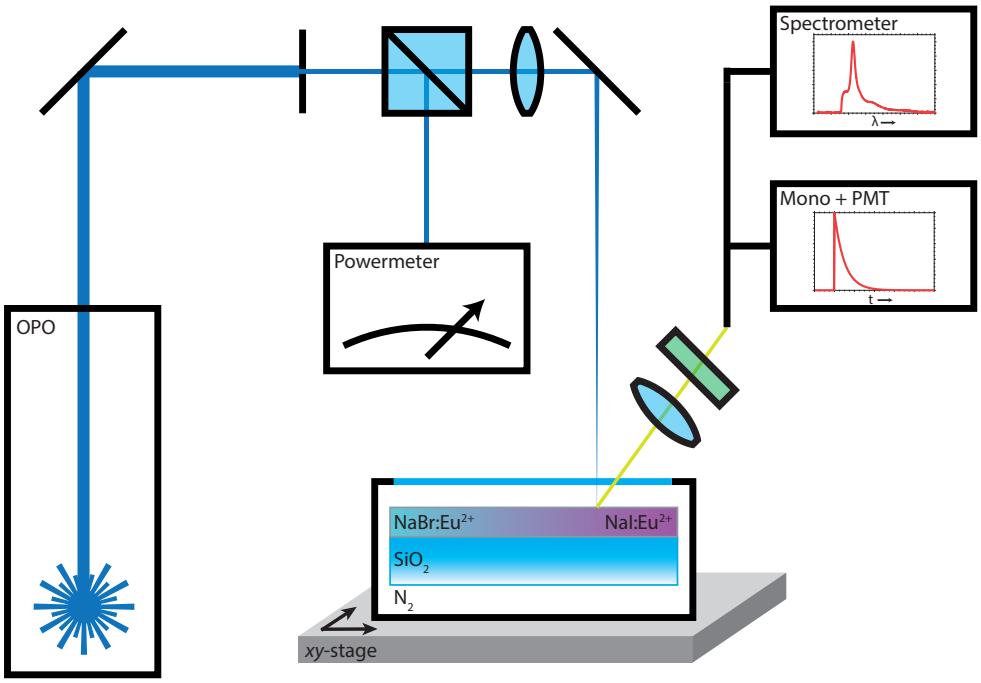


Figure 4.2: Schematic of the XY-scanner setup consisting of an OPO laser, a powermeter, an *xy*-translation stage containing the substrate and a fiber-optic CCD spectrometer or a monochromator with PMT. A laser spot diameter of about 70 µm is used to not damage the sample with the highest available laser power of 1.8 W.

guided towards the stage to serve as an excitation source. The laser light is passed through a diaphragm to compensate for fluctuations in the position of the laser spot on the thin-film when stepping across wavelengths. A UV fused silica plate placed at a 45° angle reflects 4 % of this incident light towards a powermeter that is used to correct for wavelength- and time dependent laser power fluctuations. Following excitation, luminescence passes through a longpass filter to remove reflected laser light and is focused into an optical fiber that guides the light to a detector. This detector can either be a CCD spectrometer for emission- and excitation measurements, or a monochromator coupled to a PMT (Mono+PMT) connected to a digitizer for decay measurements. Excitation- and emission measurements produced with the XY-scanner show excellent agreement with what is measured with conventional methods, as shown in the appendix of this chapter: Figure 4.8.

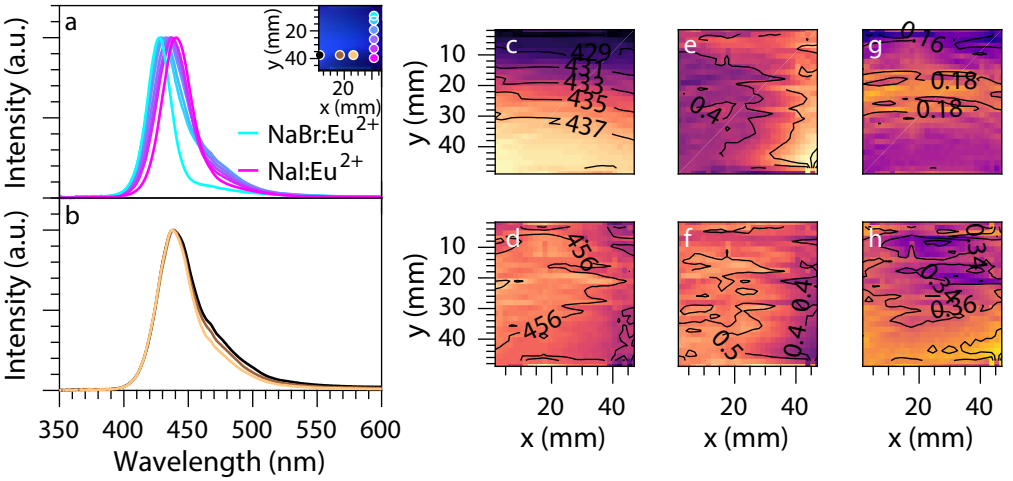


Figure 4.3: Relation between position and luminescence properties on the thin-film. **a:** Normalized emission spectra (λ_{ex} = 350 nm, taken at the locations marked by the blue-to-pink points shown in the inset) across the NaBr−NaI gradient with comparable Eu concentration. Pure NaBr:Eu^{2+} and NaI:Eu^{2+} are also shown. **b:** Normalized emission spectra across the Eu^{2+} gradient with identical Br/I ratio [λ_{ex} = 350 nm, taken at the locations marked by copper-colored points running right-to-left shown in the inset of panel a]. Respective **c, d:** central wavelengths (in nm), **e, f:** normalized areas (w.r.t. the total area of the emission) and **g, h:** bandwidths (FWHM, in eV) of the two deconvoluted Gaussians (adjusted-$R^2 > 0.9993$).

4.2.2 Luminescent Alkali-Halide Library

Figures 4.3a and 4.3b show the emission ($4f^6 5d\left[t_{2g}\right] \rightarrow 4f^7$) of the NaI−NaBr:$Eu^{2+}$ thin-film library under laser excitation at 350 nm. Scanning over the film with the laser yields emission spectra per position on the film. This data can be summarized in an RGB color plot, shown in the inset of Figure 4.3a, which closely resembles the photograph shown in Figure 4.1c. This color-coded image is obtained by converting the measured emission spectra to CIE-coordinates and translating those to RGB values.

Figure 4.3a shows that the emissions have a fluent transition from 428 nm at the NaBr-rich side, to 438 nm at the NaI-rich side of the film. A closer look at the emission reveals that it is actually comprised of two bands and a broad (FWHM> 0.8 eV) side-band of low intensity, possibly comprised of multiple smaller bands. In the further discussion, this broad (> 0.8 eV) low energy emission is not shown due to its low intensity, and since it is most likely comprised of many higher order defects. Figure 4.3b illustrates this presence of multiple bands. We can see a

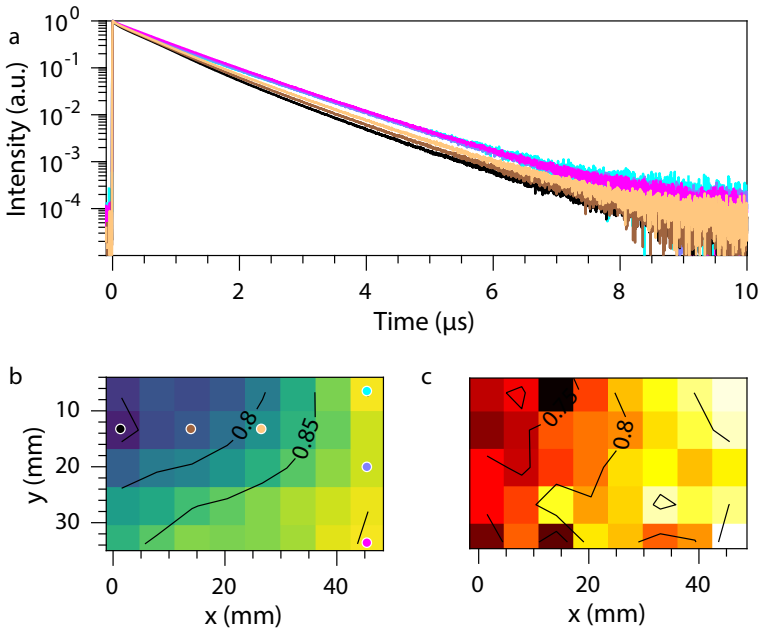


Figure 4.4: Decay characteristics of the NaI−NaBr:Eu^{2+} measured at 430 ± 15 nm. **a:** Individual decay spectra, the blue-to-pink series run from NaI to NaBr rich, with a low Eu concentration, the copper-colored lines run from high to low Eu concentration, with approximately equal NaBr and NaI content. The exact locations where the spectra were taken are shown in **b,** where also a full overview of the mean decay times (in µs) is provided. **c:** Estimated quantum yields, based on a tail-fitting as explained in the main text (adjusted-$R^2 > 0.98$).

second band at higher wavelengths developing when moving towards increased Eu concentration, while the other band stays centered at the same position. This qualitative analysis can be made more quantitative by deconvoluting the emission into two separate Gaussians. The central wavelengths of these Gaussians are displayed in Figures 4.3c and 4.3d, with relative areas in Figures 4.3e and 4.3f and bandwidths in Figures 4.3g and 4.3h. The emission of the narrow (0.16 eV to 0.18 eV) and intense band at 428 nm to 438 nm (Figures 4.3c, 4.3e and 4.3g) closely resembles the semi-circles caused by the higher sputtering yield of NaI over NaBr, as seen in Figure 4.1d. The broader (0.34 eV to 0.38 eV) emission's central wavelength (Figures 4.3d, 4.3f and 4.3h) follows the increasing Eu concentration, moving towards lower energy and increasing in prominence with higher Eu concentration.

The luminescence quantum yield η_{QY} is an important measure for the performance of a phosphor, as it indicates the presence of luminescence quenching, for instance due to an overly high dopant concentration. The observed intensity (Figures 4.3e and 4.3f) is not a direct measure of η_{QY}, because the intensity also depends on the absorption, which in turn depends on the thickness of the film. A measure for η_{QY} independent of the luminescence intensity is the decay time.

Figure 4.4a shows individual luminescent decay spectra across the substrate. These spectra were measured with a slitwidth such that all light from 415 nm to 445 nm is collected. The exact locations of these measurements are displayed in Figure 4.4b. Because of the non-exponential nature of the measured decays, a mean decay time [18]

$$\tau_{mean} = \frac{\int_0^\infty tI(t)\,\mathrm{d}t}{\int_0^\infty I(t)\,\mathrm{d}t} \tag{4.3}$$

is determined. Here, $I(t)$ is the emission intensity at time t after a laser pulse. τ_{mean} makes comparison between decay spectra possible, even if the exact behavior of the decay is unknown. Figure 4.4b shows a mapping of τ_{mean}.

The quantum yield of each composition can be estimated using a fitting of the tail of the decay spectrum. Fitting a single exponential to the tail of the decay spectra yields the decay time for an isolated ion τ_{tail} [18]. Alkali-halides with a low Europium doping are known to have near unity quantum yield at room temperature [19]. It is therefore possible to relate the mean decay time to an estimated quantum yield as

$$\eta_{QY} = \frac{\tau_{mean}}{\tau_{tail}}\,.$$

This estimated quantum yield is shown in Figure 4.4c. Comparison between Figures 4.4b and 4.4c shows that the mean decay time does not directly correlate with quantum efficiency. The determined values should therefore not be compared per position, but per composition, as will be discussed in the following.

Using the XY-scanning technique, important luminescence properties of the film at room temperature are determined, while EDX measurements provide the composition of the same film. Since these measurements have the position of the film in common, these measurements can be combined to directly relate the deconvoluted emission, decay times and estimated quantum yields to the composition. These composition-property relationships, which leave out irrelevant position information, are shown in Figure 4.5.

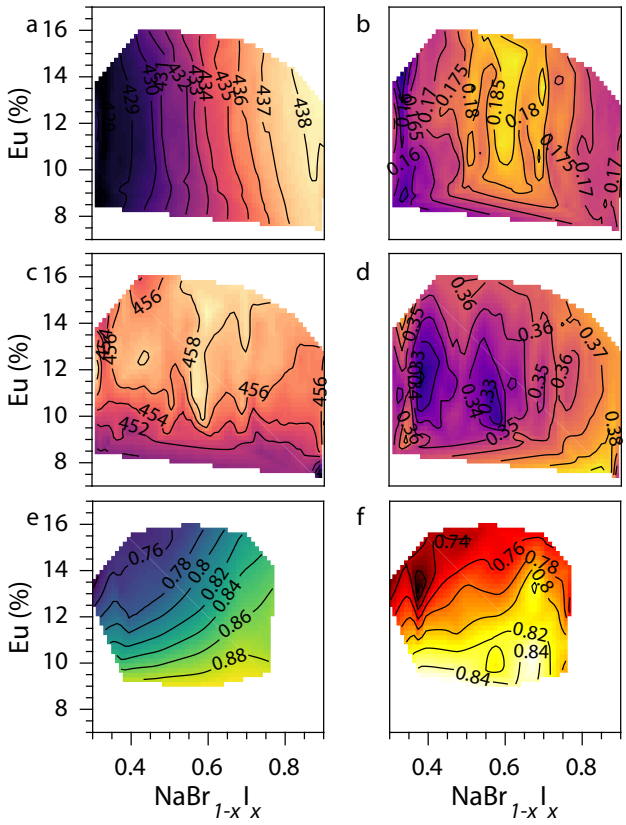


Figure 4.5: Relation between material composition and luminescence properties. **a:** The emission wavelengths (in nm) and **b:** bandwidths (in eV) as presented in Figures 4.3c and 4.3g directly related to the composition as presented in Figures 4.1d to 4.1f. **c:** The emission wavelengths (in nm) and **d:** bandwidths (in eV) as presented in Figures 4.3d and 4.3h related to the composition. **e:** The decay time (in µs) and **f:** estimated η_{QY} from Figures 4.4b and 4.4c related to the composition data from Figures 4.1d to 4.1f.

Figure 4.5a shows that the high-energy band shifts in concert with the Br to I ratio, from 428 nm at $NaBr_{0.73}I_{0.27}$ to 438 nm at $NaBr_{0.09}I_{0.91}$. From Figure 4.3a we know that thin-films of pure NaBr:Eu^{2+} and NaI:Eu^{2+} show a dominant emission at 428 nm and 441 nm, respectively. These emissions are attributed to substitutional defects, where Eu^{2+} replaces Na^{+} combined with a charge-compensating defect outside of the first coordinating sphere [14]. Between NaBr and NaI, the only changes in this first coordinating sphere are the type of the anions (becoming more electronegative from Br to I) and the distance of the anions (having a larger ionic radius from Br to I). From a well-mixed phase that follows Vegard's

law we would therefore expect the emission to change fluently from NaBr at 428 nm to NaI at 441 nm, irrespectively of Eu concentration.

Another consequence of this mixed phase is that Europium becomes statistically coordinated with the surrounding anions. Because of this variation in the direct surroundings of Eu, the emission peak broadens. This broadening is shown in Figure 4.5b. The emission of the substitutional defect in pure NaBr:Eu^{2+} has a bandwidth of 0.13 eV, where in NaI:Eu^{2+} it has a bandwidth of 0.16 eV. This difference leads to the maximal bandwidth in Figure 4.5b not being displayed at $NaBr_{0.5}I_{0.5}$, but shifted slightly closer to NaI, at $NaBr_{0.43}I_{0.57}$.

The emission band at lower energy (Figure 4.5c) might be attributed to a more complex defect. Previous research attributed a defect emitting at 453 nm in NaBr:Eu^{2+} to a $EuBr_2$-type precipitate, and emission at 461 nm in NaI:Eu^{2+} to a EuI_2-type precipitate [14]. The emission shown in Figure 4.5c, supported by the larger bandwidth shown in Figure 4.5d, might therefore also be attributed to a $EuBr_2$- or EuI_2-type precipitate, or a mixture thereof. The band's emission center shifts to lower energies with increasing Eu concentration. This redshifting might be a consequence of reabsorption of higher energy emission, which becomes more profound with more absorbing centers present.

Figure 4.5e shows that for the substitutional defect a decrease in Eu concentration leads to an increase in decay time. Because of the strong correlation with Eu concentration, we can conclude that a high degree of concentration quenching is present in our sample. For comparison, the highest τ_{mean} of 0.89 µs is observed for $NaBr_{0.36}I_{0.64}$:9%Eu, where pure NaBr:Eu^{2+} with a low Eu-doping would show $\tau_{tail} = 1.05 \pm 0.1$ µs and NaI:Eu^{2+} would show $\tau_{tail} = 1.05 \pm 0.03$ µs, as can be found in Section 4.6. Lowering the concentration of Eu would increase the decay time, and thus the luminescence quantum yield. This relation is confirmed by Figure 4.5f. In Figure 4.5f we can also see that the estimated quantum yield for compounds closer to NaI:Eu^{2+} rises more quickly with Eu^{2+} concentration than for those closer to NaBr:Eu^{2+}. We can therefore expect that NaI:Eu^{2+}-type compounds will yield a brighter phosphor, when fully optimized for photoluminescent yield.

From Figure 4.6 we see that the fluent shifting behavior is not limited to the emission bands, but also occurs in the excitation bands ($4f^7\left[^8S_{7/2}\right] \rightarrow 4f^6 5d^1$). The crystal field splitting ϵ_{cfs} decreases when moving from NaBr to NaI. This

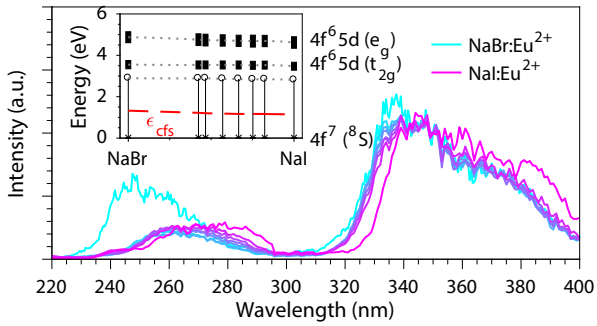


Figure 4.6: Normalized (at $\lambda_{ex} = 350\,nm$) excitation spectra of the substitutional defect, taken at $\lambda_{em} = 420\,nm$ to minimize influence of other defects. Spectra were recorded at the same positions as shown in Figure 4.3a. Excitation spectra of pure NaBr:Eu^{2+} and NaI:Eu^{2+} are shown in purple and light blue. The inset schematically shows the energy of the 5d energy levels. Arrows show the observed emission maximum. The centers of the e_g and t_{2g} levels are taken as the center of gravity (first moment) and their bandwidths as the second moment of their respective excitation bands [14]. Dotted lines are drawn through the centers of the e_g and t_{2g} levels and the emission energies as a guide to the eye. The crystal field splitting is shown as a red dashed curve.

decrease is a result of the larger distance between Eu^{2+} and the surrounding halogen ions due to the larger ionic radius of I ions compared to Br ions [20]. However, the emission for NaI:Eu^{2+} is still at lower energy than for NaBr:Eu^{2+}. Hence, we can conclude that the shifting of the emission band from the substitutional defect is mainly dominated by a drop in the centroid energy, because the d-orbitals of the Eu^{2+} ion can expand further when surrounded with I^- than when surrounded with Br^-.

As final confirmation of the existence of a well-mixed phase, XRD measurements should show diffraction peaks fluently shifting from NaBr, with lattice parameter $a = 2.987\,Å$, to NaI, with $a = 3.235\,Å$. This fluent shift can be seen in Figure 4.7.

Figure 4.7 also shows a broadening of the diffraction peaks when moving from $NaBr_{0.14}I_{0.86}$ to $NaBr_{0.52}I_{0.48}$. This broadening has a similar origin as the broadening observed Figure 4.5b. As with the broadening of the emission, the broadening of the diffraction peaks is a consequence of the lattice spacing becoming more variable when more equal amounts of I and Br are included.

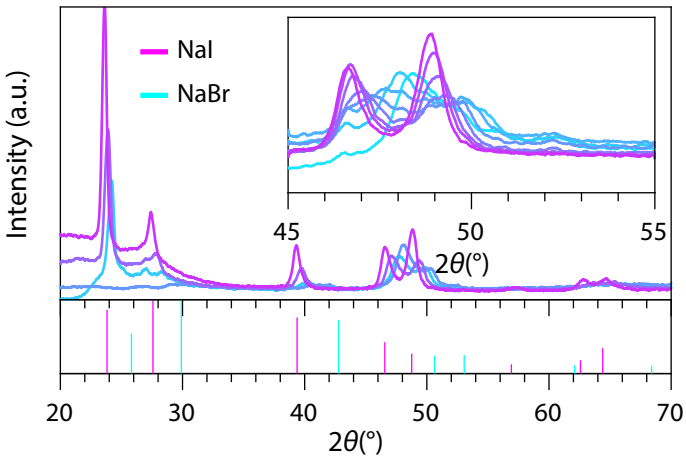


Figure 4.7: Diffractograms taken across the substrate following the colors as shown in Figure 4.1c, which correspond to $NaBr_{0.52}I_{0.48}$ (blue) to $NaBr_{0.14}I_{0.86}$ (purple). The purple pattern underneath is reference pattern #1820477 for NaI and the blue lines are #1400153 for NaBr. The inset shows a close-up from $45-55\,°2\theta$ of the shifting of the diffraction peaks from NaI to NaBr. Relative peak intensities of the reference and measured diffractograms differ, since our measurements were done with constant-area X-ray illumination, where the reference is done with constant intensity.

4.3 Conclusion

We have shown that it is possible to create a luminescent thin-film composition- and concentration material library. In a single gradient film the Eu concentration changes from 6.5 % to 16.5 % and the host composition from $NaBr_{0.73}I_{0.27}$ to $NaBr_{0.09}I_{0.91}$. Using the XY-scanning characterization method it is now possible to directly relate composition to photoluminescent emission-, excitation- and decay properties. The method can generally be applied to a wide variety of material libraries with composition-, concentration- and thickness gradients, not limited to a single doping or host precursor target.

The luminescence of NaI:Eu^{2+} and NaBr:Eu^{2+} has previously been explored, but the behavior of these phosphors in a mixed state was still unknown. Therefore, a NaI−NaBr−Eu^{2+} gradient thin-film served as an example for this method. The excitation and emission observed for the endpoints of the gradient, NaI:Eu^{2+} and NaBr:Eu^{2+}, agree with what has previously been observed [14]. In the mixed compound, we have seen that the NaBr−NaI gradient closely follows Vegard's law, which is expressed as a fluent shift in luminescence from 428 nm when

NaBr-rich, to 438 nm when NaI-rich. This following of Vegard's law is further confirmed by XRD measurements, which show a fluent shifting of the diffraction peaks. These shifts agree with what is expected when moving between the two pure-phase compounds, as also observed in $KCl_{1-x}Br_x:Eu^{2+}$ crystals, where x was varied from 0 to 1 [14].

From decay measurements we can conclude that the deposited film exhibited concentration quenching, but that, when optimized for photoluminescent yield, compounds closer to $NaI:Eu^{2+}$ will yield a brighter luminescent material than compounds close to $NaBr:Eu^{2+}$.

In conclusion, the XY-scanning method presented in this work makes it possible to systematically analyze a broad range of host compositions and dopant concentrations to study the behavior of luminescent materials, using only a single deposition. The results from the thin-film phosphors are highly comparable to those observed with traditional powder-based techniques. Hence, the method may provide a toolbox capable of accelerating the discovery and optimization of phosphors for a wide range of applications such as lighting, display and scintillation, but also for solar-conversion, afterglow, and many other types of photo-activated materials.

4.4 Experimental Procedures

The $NaBr{-}NaI:Eu^{2+}$ gradient thin-film was fabricated in an AJA Orion 5 magnetron sputtering system with a base pressure of 1×10^{-9} bar. A 5 cm diameter Eu metal target (99.99 %, Demaco) and 5 cm diameter NaBr and NaI pressed-powder targets (both 99.99 %, Alfa Aesar, pressed at 36 MPa for 5 min) were simultaneously sputtered at a 90° angle from each other at room temperature in a 4×10^{-2} mbar Ar atmosphere (6N purity, 32 sccm flow rate) onto a $5 \times 5\,cm^2$ UV fused silica substrate (PGO). Prior to deposition, the substrate was cleaned for 15 min in an ultrasonic bath with a solution of soapy water, after which it was rinsed with acetone, ethanol and DI-water, and left to dry in an oven at 200 °C for more than 1 h. The substrate and substrate carrier were loaded into the sputtering chamber while both were >100 °C to prevent moisture contamination. The NaBr (RF), NaI (RF) and Eu (DC) sputter powers were fixed at 25 W ($0.04\,nm\,s^{-1}$), 31 W ($0.08\,nm\,s^{-1}$) and 10 W ($<1 \times 10^{-3}\,nm\,s^{-1}$) respectively. The Eu target's chimney was masked using a stainless steel mask, with a pattern of

concentric holes 1.2 mm in diameter, blocking 99 % of the surface of the chimney (shown in Figure 4.1a). This finally led to a film with an estimated thickness of 0.86 µm in the center, 0.9 µm at the side of the film closest to NaI and 0.8 µm at the side of the film closest to NaBr. Deposition happened at room temperature, without any further heat treatment. Using the same process, two reference films with only (1) NaBr:Eu^{2+} or (2) NaI:Eu^{2+} were fabricated. (1) had sputter settings fixed at 40 W for NaBr (RF, 0.08 nm s^{-1}), 10 W for Eu (DC, $<1 \times 10^{-3}$ nm s^{-1}). (2) used NaI at 35 W (RF, 0.13 nm s^{-1}) and Eu at 10 W (DC, $<1 \times 10^{-3}$ nm s^{-1}). All films were sputtered for 2 h. Deposition rate determination was carried out using a quartz crystal microbalance.

SEM/EDX analysis was carried out using a JEOL JSM-IT100 operated at 20 kV, with probing current at 70 % for 2 min per measurement, leading to a total duration of 80 min. Elemental compositions were quantified at 3000× magnification, corresponding to an area of 31×23 µm^2. Low vacuum mode (35 Pa pressure) was used to facilitate quantitative elemental analysis without a conductive coating.

The sample stage of the XY-scanner was made out of two stacked Thorlabs DDSM100 linear translation stages. An Ekspla NT230 OPO Laser was used as excitation source. Two polarizers and a 500 µm diaphragm were placed in the laser beam to reduce intensity of the laser light and to avoid fluctuations of the beam position. The intensity was reduced to prevent saturation of the luminescent centers in the sample. 4 % of the incident laser light was split off the main beam by a UV fused silica plate. This split-off light was directed towards a Thorlabs S120VC sensor connected to a Thorlabs PM100D calibrated powermeter for online correction of the laser power. The main laser beam was focused onto the film using a $f = 100.3$ mm Thorlabs LA4380 lens. Emission passed through a 355 nm longpass filter (Semrock, BLP01-355R-25), followed by a $f = 100.3$ mm Thorlabs LA4380 lens. This lens focused the emission into an Ocean Optics QP600-2-SR-BX fiber. Emission was integrated during 100 ms and averaged 5 times using an Ocean Optics QE65000 CCD Spectrometer (100 µm slit, 300 grooves/mm grating, leading to an uncertainty in emission wavelength of ±1.69 nm) and corrected for the quantum efficiency and non-linearity of the detector. Prior to any emission measurement, the background was measured using identical settings and subtracted from the final measurement, leading to a measurement duration of 1 s. 32×32 ($\Delta x = 1.56$ mm, $\Delta y = 1.56$ mm) emission measurements were conducted across the entire substrate, leading to a total measurement duration of 17 min.

For decay studies, the emission passed through an Acton Spect-Pro2300 monochromator coupled to a Hamamatsu R7600U-03 PMT, with the PMT linked to a CAEN DT5730 Digitizer. The digitizer was constantly recording, but started storing information upon reception of a trigger signal from the laser. When a trigger was received by the digitizer, the output of the PMT was stored ranging from $\sim 0.6\,\mu s$ before the start of a laser pulse and to $\sim 54.6\,\mu s$ after a laser pulse, with a resolution of $\Delta t = 2\,ns$. Decays were recorded using 1000 laser pulses, resulting in an error for the calculated mean decay time below 1 % (typically below $\pm 7\,ns$). With the 100 Hz OPO laser, this yields 10 s per measurement. Here, measurements were conducted across the substrate with an 8×8 grid, yielding a total duration of 11 min. All devices pertaining to the XY-scanner were controlled using in-house developed Python software.

XRD measurements were performed using a PANalytical X'pert Pro MPD diffractometer with a Cu Kα anode ($\lambda = 0.1540598\,nm$) operating at 45 kV and 40 mA in a Bragg-Brentano geometry measured from 2θ =20° to 70°, $\Delta 2\theta$ = 0.0083731° in 1 h. The area illuminated by the X-ray beam was around $1 \times 5\,mm^2$ in size. The film was placed in a hygroscopic sample holder. The measurement locations on the film were set using a manually operated homemade *xy*-micromanipulator stage.

4.5 Appendix: Comparison XY-Scanner and Conventional Photoluminescence Setup

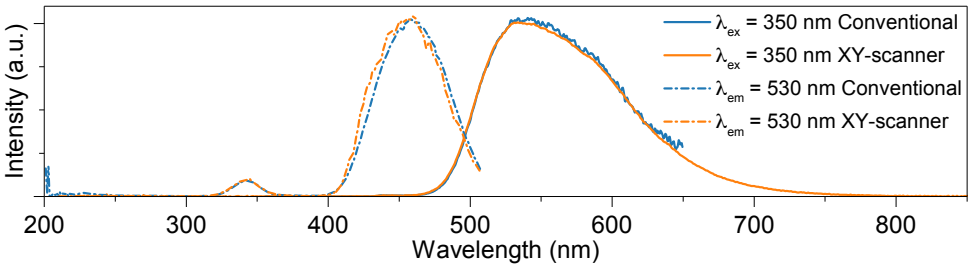


Figure 4.8: Comparison of excitation- and emission spectra of $Y_2Al_5O_{12}$:0.01 Ce^{3+}powder between a conventional [21] photoluminescence setup and the XY-scanner. The conventional setup consists of a 450 W Xe lamp coupled into an excitation monochromator (Horiba, Gemini 180) leading to the sample chamber. Light emitted from the sample passes through an emission monochromator (Acton, Spect-Pro2300), employing a 300 grooves/mm grating. Finally, the emitted light reaches a PMT (Hamamatsu, R7600U-03, operated at −800 V), the output of which is recorded. The XY-scanner operates as described in the main text. The emissions recorded by both setups are corrected with a calibrated Halogen light source (TOP Sensor Systems, HL2000-CAL). The excitation spectrum of the XY-scanner is corrected as described in the main text. For the conventional setup, a calibrated Si detector (Opto Diode, UVG100) is used to correct the excitation spectrum. With the conventional setup, emission is studied using slits that provide a 3 nm FWHM resolution, integrated for 0.3 s, with 350 ± 5 nm excitation. Excitation is studied for emission 530 ± 5 nm, integrated for 0.3 s, with an excitation resolution of 3 nm FWHM. For the XY-scanner, emission integrated over 50 ms is averaged 10×; resolutions are as described in the main text. Both excitation experiments filter out the lamp signal with a 495 nm longpass filter (Newport, Stabilife). Both emission experiments filter out the lamp signal with a 430 nm longpass filter (Semrock, Brightline).

4.6 Appendix: Additional Characterization of NaI:Eu^{2+} and NaBr:Eu^{2+}

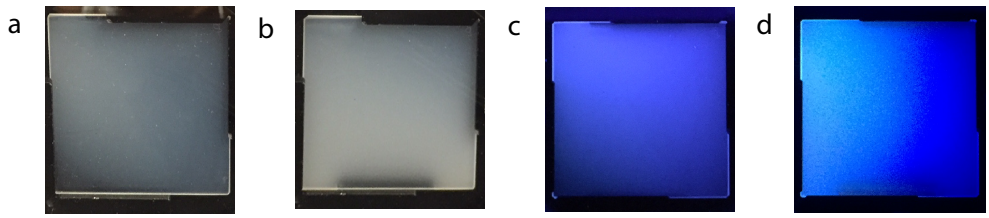


Figure 4.9: Photographs of the pure **a:** NaBr:Eu^{2+}, **b:** NaI:Eu^{2+} samples under white light illumination and **c:** NaBr:Eu^{2+}, **d:** NaI:Eu^{2+} samples under UV illumination. Deposition took place with the sputtering sources in the same orientation as in the main text. The NaBr source (when used) was closest to the top of the films, NaI (when used) to the bottom and Eu to the left.

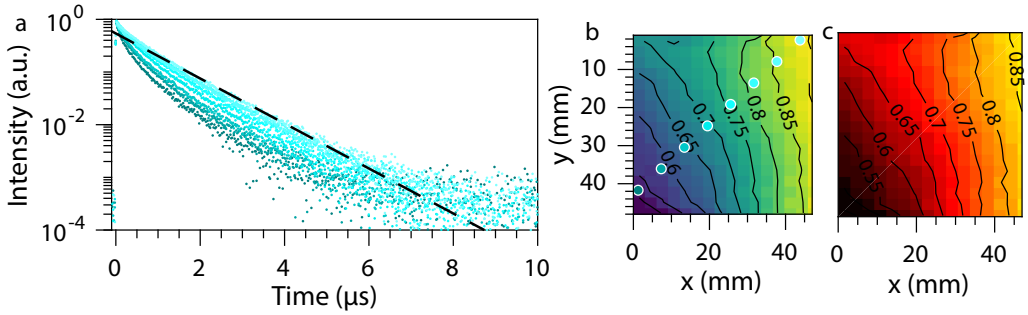


Figure 4.10: Decay characteristics ($\lambda_{ex} = 350\,nm$, $\lambda_{em} = 430 \pm 15\,nm$, averaged over 500 laser pulses) of a gradient of NaBr with varying concentrations of Eu. **a:** Overview of individual decay spectra across the gradient. The dashed black line shows the result of the tailfitting, with $\tau_{tail} = 1.05 \pm 0.1\,\mu s$ as described in the main text. τ_{tail} matches well with $\tau = 1.03\,\mu s$ found by Muñoz et al. [19] The exact locations where the spectra were taken are shown in **b,** where also a full overview of the mean decay times (in µs) is provided. **c:** Estimated quantum yields, based on a tail-fitting as explained in the main text (adjusted-$R^2 > 0.98$).

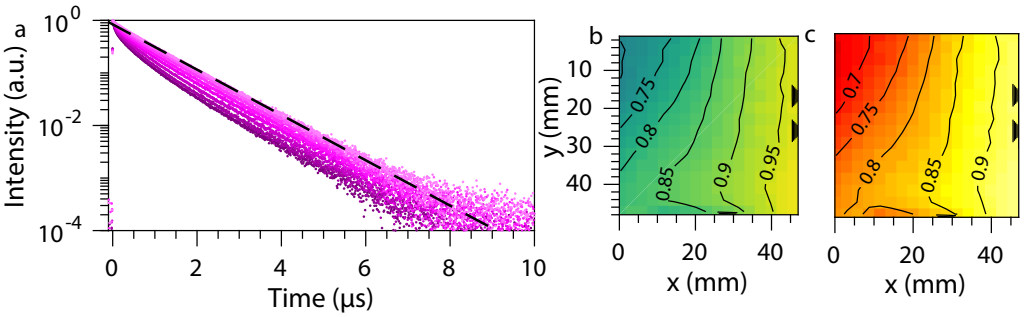


Figure 4.11: Decay characteristics ($\lambda_{ex} = 350\,nm$, $\lambda_{em} = 430 \pm 15\,nm$, averaged over 500 laser pulses) of a gradient of NaI with varying concentrations of Eu. **a:** Overview of individual decay spectra across the gradient. The dashed black line shows the result of the tailfitting, with $\tau_{tail} = 1.05 \pm 0.03\,\mu s$ as described in the main text. The exact locations where the spectra were taken are shown in **b,** where also a full overview of the mean decay times (in µs) is provided. **c:** Estimated quantum yields, based on a tail-fitting as explained in the main text (adjusted-$R^2 > 0.99$).

References

[1]W. B. Park, S. P. Singh, C. Yoon, and K.-S. Sohn, "Eu^{2+} luminescence from 5 different crystallographic sites in a novel red phosphor, $Ca_{15}Si_{20}O_{10}N_{30}:Eu^{2+}$," Journal of Materials Chemistry **22**, 14068 (2012).

[2]W. H. Weinberg, E. Danielson, J. H. Golden, E. W. McFarland, C. M. Reaves, and X. D. Wu, "A combinatorial approach to the discovery and optimization of luminescent materials," Nature **389**, 944–948 (1997).

[3]E. Danielson, M. Devenney, D. M. Giaquinta, J. H. Golden, R. C. Haushalter, E. W. McFarland, D. M. Poojary, C. M. Reaves, W. H. Weinberg, X. D. Wu, C. M. R. Damodara M. Poojary, W. H. Weinberg, and X. D. Wu, "A Rare-Earth Phosphor Containing One-Dimensional Chains Identified Through Combinatorial Methods," Science **279**, 837–839 (1998).

[4]X.-D. Sun, C. Gao, J. Wang, and X.-D. Xiang, "Identification and optimization of advanced phosphors using combinatorial libraries," Applied Physics Letters **70**, 3353–3355 (1997).

[5]Q. Wei, J. Wan, G. Liu, Z. Zhou, H. Yang, J. Wang, and Q. Liu, "Combinatorial Optimization of La, Ce-co-Doped Pyrosilicate Phosphors as Potential Scintillator Materials," ACS Combinatorial Science **17**, 217–223 (2015).

[6]R. Takahashi, H. Kubota, M. Murakami, Y. Yamamoto, Y. Matsumoto, and H. Koinuma, "Design of Combinatorial Shadow Masks for Complete Ternary-Phase Diagramming of Solid State Materials," Journal of Combinatorial Chemistry **6**, 50–53 (2004).

[7]B. Lee, S. Lee, H. G. Jeong, and K.-S. Sohn, "Solid-State Combinatorial Screening of $(Sr,Ca,Ba,Mg)_2Si_5N_8:Eu^{2+}$ Phosphors," ACS Combinatorial Science **13**, 154–158 (2011).

[8]L. Chen, Y. Fu, G. Zhang, J. Bao, and C. Gao, "Optimization of Pr^{3+}, Tb^{3+}, and Sm^{3+} Co-Doped $(Y_{0.65}Gd_{0.35})BO_3:Eu^{3+}_{0.05}$ VUV Phosphors through Combinatorial Approach," Journal of Combinatorial Chemistry **10**, 401–404 (2008).

[9]T.-S. Chan, Y.-M. Liu, and R.-S. Liu, "Combinatorial Search for Green and Blue Phosphors of High Thermal Stabilities under UV Excitation Based on the $K(Sr_{1-x-y})PO_4:Tb_x^{3+}Eu_y^{2+}$ System," Journal of Combinatorial Chemistry **10**, 847–850 (2008).

[10]S. Frost, S. Guérin, B. E. Hayden, J.-P. Soulié, and C. Vian, "High-Throughput Synthesis and Characterization of Eu Doped $Ba_xSr_{2-x}SiO_4$ Thin Film Phosphors," ACS Combinatorial Science, acscombsci.8b00045 (2018).

[11]J. L. Wu, E. Danielson, S. P. DenBaars, M. Devenney, E. W. McFarland, V. I. Srdanov, and H. Weinberg, "Combinatorial synthesis and screening of Cerium-doped garnet phosphors for application in white GaN-based LEDs," in Solid state lighting and displays, Vol. 4445, edited by I. T. Ferguson, Y.-S. Park, N. Narendran, and S. P. DenBaars (International Society for Optics and Photonics, 2001), pp. 70–81.

[12]K. Yano, S. Takeshita, Y. Iso, and T. Isobe, "Combinatorial optimization of the atomic compositions for green-emitting $YBO_3:Ce^{3+},Tb^{3+}$ and red-emitting $YBO_3:Ce^{3+},Tb^{3+},Eu^{3+}$ phosphors using a microplate reader," RSC Advances **7**, 17586–17592 (2017).

[13]J. D. Fowlkes, J. M. Fitz-Gerald, and P. D. Rack, "Ultraviolet emitting $(Y_{1-x}Gd_x)_2O_{3-\delta}$ thin films deposited by radio frequency magnetron sputtering: combinatorial modeling, synthesis, and rapid characterization," Thin Solid Films **510**, 68–76 (2006).

[14]J. Rubio, "Doubly-valent rare-earth ions in halide crystals," Journal of Physics and Chemistry of Solids **52**, 101–174 (1991).

[15]G. Siegel, "Ultraviolet spectra of silicate glasses: A review of some experimental evidence," Journal of Non-Crystalline Solids **13**, 372–398 (1974).

[16]M. de Jong, W. Kesteloo, and E. van der Kolk, "Deposition of luminescent NaCl:Tm^{2+} thin films with a Tm concentration gradient using RF magnetron sputtering," Optical Materials **46**, 149–153 (2015).

[17]M. Ohring, *Materials Science of Thin Films* (2001), pp. 95–201.

[18]E. Nakazawa, "Fundamentals of luminescence," in *Phosphor Handbook*, edited by W. M. Yen, S. Shionoya, and H. Yamamoto, 2nd ed. (CRC Press, 2006) Chap. 2.8, pp. 99–110.

[19]G. H. Muñoz, C. L. de la Cruz, A. F. Muñoz, and J. O. Rubio, "High-temperature luminescence properties of Eu^{2+}-activated alkali halide phosphor materials," Journal of Materials Science Letters **7**, 1310–1312 (1988).

[20]P. Dorenbos, "Relation between Eu^{2+} and Ce^{3+} f → d-transition energies in inorganic compounds," Journal of Physics Condensed Matter **15**, 4797–4807 (2003).

[21]A. J. Bos, R. M. van Duijvenvoorde, E. van der Kolk, W. Drozdowski, and P. Dorenbos, "Thermoluminescence excitation spectroscopy: A versatile technique to study persistent luminescence phosphors," Journal of Luminescence **131**, 1465–1471 (2011).

— 5 —

Functionalizing Window Coatings with Luminescence Centers by Combinatorial Sputtering of Scatter-Free Amorphous SiAlON:Eu^{2+} Thin-Film Composition Libraries

In the glass industry, SiAlON-type materials are widely used as coatings for glass. Doping these SiAlONs with rare-earths adds luminescent functionality, which could be applied in photovoltaics. By using a combinatorial reactive sputtering approach, an amorphous thin-film composition library with a Si:Al ratio from 0.062 : 1 to 3.375 : 1 and a Eu doping from 4.8 at.% to 26 at.% is created. This library uniquely combines high absorption, strong emission and absence of light scattering. By combining position-dependent EDX measurements with transmission and emission spectra, the index of refraction, absorption strength, emission wavelength and decay times of the library can directly be related to the composition. The library has an index of refraction of 1.63 ± 0.03, typical for a film with low nitrogen content. The library also shows a large absorption coefficient of $1294 \pm 8\,\mathrm{cm}^{-1}\,\mathrm{at.\%}^{-1}$. Emission spectra show that the library has a strong redshift from 500 nm to 550 nm with increasing Al concentration. An increase in Eu concentration also causes a shift of the emission to red. Decay spectra show that a high degree of Si greatly improves the luminescence intensity. These functionalized SiAlON coatings can be of great interest for transparent and scatter-free luminescent solar concentrators applied as windows.

This chapter has been published as: E.P.J. Merkx, S. van Overbeek, and E. van der Kolk, "Functionalizing window coatings with luminescence centers by combinatorial sputtering of scatter-free amorphous SiAlON:Eu^{2+} thin film composition libraries," Journal of Luminescence **208**, 51–56 (2019)

All data supporting the figures in this chapter can be found at: `https://data.mendeley.com/datasets/x9ypt9353r`

5.1 Introduction

Thin-film coatings based on the elements Al, Si, O and N (SiAlON) are applied routinely by the glass industry on a large scale, e.g. for scratch-protection and anti-reflection purposes, because of the coatings' mechanical strength, chemical inertness and thermal resistance [1–3]. The application range of SiAlON coatings may be expanded by functionalizing them with luminescence centers that can absorb and convert parts of the solar spectrum for electricity generation, utilizing the principle of a luminescent solar concentrator (LSC) [4–6]. The polycrystalline nature of most luminescent films, however, presents a problem. A polycrystalline material causes light scattering, which lowers applicability for LSCs intended to replace conventional windows. For such a window coating to find broad application, the absence of scattering (haze) in the visible spectrum is a strict requirement. Therefore, scatter-free amorphous luminescent films are desired.

Rare-earth luminescence centers as dopants in SiAlON-based polycrystalline phosphors (also known as SiAlON ceramics) have attracted a great deal of attention for application in white light emitting diodes. In particular, SiAlONs doped with Eu^{2+}, whose emission properties strongly depend on the size and symmetry of the coordinating ions, are actively researched [7–11]. The SiAlON host provides a wide tuning range of luminescence across the visible spectrum when varying the ratio of Si to Al or the concentration of Eu^{2+} [8]. As a result, a wide range of compositions of polycrystalline SiAlON phosphors exist, where the composition corresponds to emissions ranging from blue to red. Although the wide range of possible SiAlON compositions is beneficial for tuning, exploring all these compositions is time-consuming and challenging.

In this chapter, we present magnetron co-sputtering of Si, Al and Eu in a reactive O_2+N_2+Ar plasma as a technique to explore the luminescence properties of amorphous thin-films within a large composition range, requiring only a single deposition. We will show how these SiAlON:Eu^{2+} composition libraries are sputtered and how position-dependent composition is determined through energy dispersive X-ray (EDX) spectroscopy. Following this, position-dependent emission wavelength and intensity, absorption strength, index of refraction and decay time are determined. Combined with the EDX data, we show how these position-dependent data are converted to ternary diagrams which directly relate

composition to the properties of the thin-film library. These diagrams allow for a wealth of data to be displayed in a single figure, showing the dependence of a property on three parameters within a single graph. Ternary diagrams are however not often encountered in the field of luminescence. In SiAlON:Eu, these diagrams can show the influence of exchanging cations for each other e.g. Si over Eu, while keeping Al fixed. To read the data in these diagrams, the direction of the axis ticks should be followed. In the Section 5.9 a more extensive guide can be found.

We will further show that the library spans a composition range that is amorphous, with a haze below 1.1 %, and that the different compositions exhibit emission colors ranging from blue-green to yellow-orange.

5.2 Experimental

Library creation The Eu-doped SiAlON thin-film library was deposited on a square $50 \times 50\,mm^2$ single crystal MgF_2 substrate within an AJA ATC Orion 5 magnetron sputtering system with a base pressure of 1×10^{-9} bar, at room temperature. Prior to the deposition, the substrate had been cleaned for 15 min in an ultrasonic cleaner with soap solution and had been subsequently rinsed with acetone, ethanol and DI water. The deposition was carried out with 5.08 cm diameter metal Al (99.9995 %, Lesker), Si (99.999 %, Lesker) and Eu (99.99 %, Demaco) targets that were reactively co-sputtered with 75 W DC power, 60 W RF power and 25 W RF power respectively for 11.25 h. The deposition rate of Eu was reduced with a stainless steel mask, with a pattern of concentric holes 5.45 mm in diameter, blocking 60 % of the surface of the Eu target. The process gas flow consisted of 18 sccm 6 N purity Ar, 0.5 sccm 5 N purity O_2 and 13.5 sccm 5 N purity N_2 into the sputtering chamber at a working pressure of 4×10^{-3} mbar. O_2 and N_2 were introduced next to the substrate, while Ar was introduced at the Al source. To realize a gradient thin-film, the substrate was sputtered without rotation. Hence, the deposition from each source followed a gradient distribution of the sputtered material on the substrate.

Following the sputter deposition, the library was annealed repeatedly in a Solaris 150 rapid thermal processing (RTP) system to activate the luminescence, while avoiding crystallization. The library underwent one RTP cycle of 60 min at 600 °C, one cycle of 45 min at 650 °C and four cycles of 30 min at 700 °C. The

annealing procedure was optimized such that the highest possible PL intensity could be reached before crystallization occurred. The annealing temperatures were reached with a ramp rate of 5 °C s^{-1} and the RTP system was flushed with 9 SLM N_2 containing 7 % H_2 (5 N purity) during the entire annealing procedure.

Composition analysis SEM/EDX analysis was carried out using a JEOL IT-100 operated at 15 keV, with PC 70. Low vacuum mode (35 Pa pressure) was used to facilitate quantitative elemental analysis without a conductive coating. Elemental compositions were quantified at 1000× magnification. XRD measurements were performed using a PANalytical X'pert Pro MPD diffractometer with a Cu Kα anode (λ = 0.1540598 nm) operating at 45 kV and 40 mA. The area illuminated by the X-ray beam was around 1×5 mm^2 in size.

XY-Scanning technique A PerkinElmer Lambda 950 UV/VIS spectrophotometer with diffuse reflectance accessory was used to measure haze. The sample was illuminated with a tungsten halogen lamp in the 300 nm to 1300 nm spectral range using a step size of 1 nm. Because of the low degree of haze, transmission measurements were carried out by measuring the direct transmittance. The transmission was measured by placing the film between two 600 µm diameter multimode optical fibers, terminated on either side of the film with an achromatic fiber collimator (74-ACR, Ocean Optics). The top fiber was coupled to a focused deuterium lamp (Acton Research, Model 775) and functioned as an unpolarized light source of 4 mm in diameter. After passing through the sample, the transmitted light was collected by the bottom fiber which led to an Ocean Optics USB4000 CCD Spectrometer. The film was clamped to an optical post placed on top of two stacked Thorlabs DDSM100 linear translation stages. These stages facilitate movement of the film between the fibers. Transmission spectra were recorded at 24×24 positions across the library, at 200 nm to 850 nm with an integration time of 5 ms and averaged 100×.

The sample stage of the XY-scanner was made of the same stages as the transmission set-up. An Ekspla NT230 OPO Laser was used as excitation source, operated at an excitation wavelength of 280 nm. Emission was recorded across 32×32 locations on the substrate, using an Ocean Optics QE65000 CCD Spectrometer with a 325 nm longpass filter to remove reflected laser light. The emission was corrected for the quantum efficiency and non-linearity of the detector. Emission

was integrated for 500 ms and averaged 10×. For decay studies, the emission, filtered with a 355 nm longpass filter, passed through an Acton Spect-Pro2300 monochromator, using 2 mm slit width set to let 520 nm (20 nm fwhm resolving power) light through with a 300 grooves/mm grating. The monochromator led to a Hamamatsu R7600U-03 PMT operating at −600 V, with the PMT linked to a CAEN DT5730 Digitizer. Decay traces were collected over 1000 laser pulses. Further details on the operating conditions and procedures of the XY-Scanner can be found in Chapter 4.

5.3 Results and Discussion

5.3.1 Fabrication of the Library

The SiAlON:Eu composition library is fabricated using three elemental sputtering sources (Figure 5.1a) in a reactive O_2 + N_2 + Ar atmosphere at room temperature. Following deposition, the luminescence of the library is improved by repeated heating in a rapid thermal processor. This treatment leads to a scatter-free thin-film, with luminescence clearly visible by the naked eye when excited with UV light (Figure 5.1b).

With a the XY-scanner setup from Chapter 4 a rasterized image of the luminescence is made. Figure 5.1c shows such an image, obtained by measuring 32×32 individual points of emission across the area of interest (dashed outline in Figure 5.1b) after local excitation with a tunable OPO laser at 280 nm. To obtain this image, the emission spectra are converted to CIE 1931 xyY coordinates, which in turn are mapped to their respective RGB value. The RGB-based colors shown in Figure 5.1c closely resemble the photograph of Figure 5.1b. A clearer view of the color emitted by the library is obtained by normalizing all measured emission spectra, which leads to leaving out luminance information captured by the Y CIE coordinate. These normalized color data are shown in Figure 5.1d and will be used throughout this chapter to indicate where on the library measurements were taken.

EDX is carried out on 40 positions across the library (shown in Figure 5.1g) to determine the local chemical composition. These measurements are interpolated using the surface-source equation [19], also seen in Chapter 4, to retrieve the continuous composition spread across the library. Si varies from 5 at.% to 62 at.%

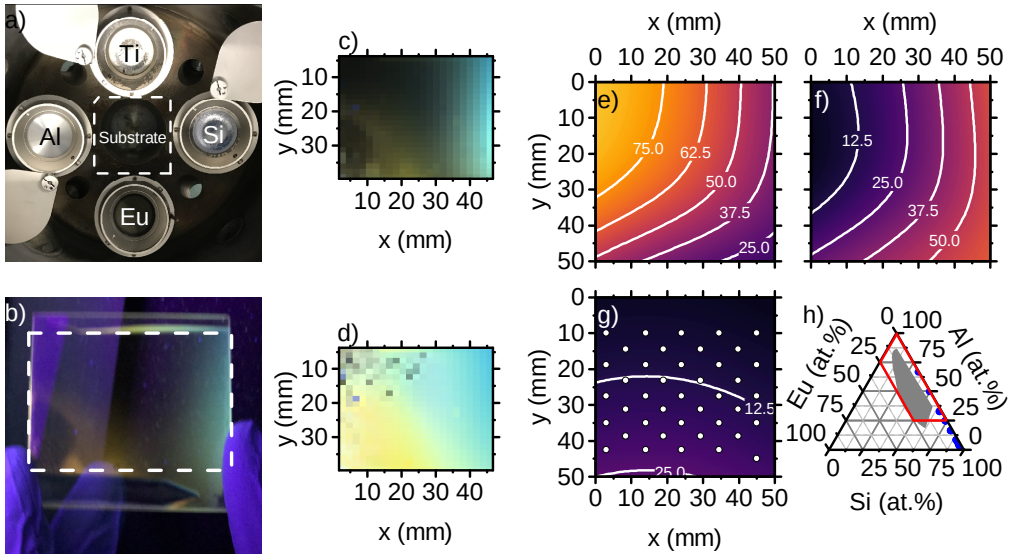


Figure 5.1: Compositional library of SiAlON doped with Eu. **a:** Photograph inside of the sputtering system. The Ti source is not used. **b:** Photograph of the library under UV illumination, after annealing. The triangular cutouts in the film are a result of how the substrate was attached in the sputtering system. The dashed outline indicates the region under investigation. **c:** RGB color mapping of emission emanating from the library after 280 nm laser excitation. **d:** RGB mapping of the emission from panel c with normalized emission spectra. Respective distribution of **e:** aluminum, **f:** silicon, **g:** europium across the MgF_2 substrate. Presented data is fit ($R^2 > 0.94$) based on EDX measurements at 40 positions (white dots shown in panel g). The presented percentages are relative to the sum of all cations. **h:** Ternary overview, here the direction of the axis ticks should be followed to read the data. The gray area is the total composition space present in the library. The red outline shows the cropping which is applied in all following ternary diagrams. Blue dots are compositions previously presented in literature [7–9, 12–18].

(Figure 5.1e), Al from 18 at.% to 87 at.% (Figure 5.1f) and Eu from 4.8 at.% to 26 at.% (Figure 5.1g). The curved shapes of EDX mappings are a consequence of the spherical sputtering distribution of the individual sources. At the top ($y < 20$ mm) the shape is mainly dictated by the high sputtering yield of Al. At the bottom ($y > 20$ mm) the combination of the high yields of Eu and Al makes the white iso-concentration lines mainly follow the shape imposed by those two sources. Figure 5.1h shows a ternary overview of the total compositional space this library spans. As can be seen in Figure 5.1h, Eu-doped SiAlONs with such high Al concentration are not often encountered in literature. SiAlONs richer in Si are more commonly synthesized [7, 9, 13, 15–18, 20]. Exceptions are the works

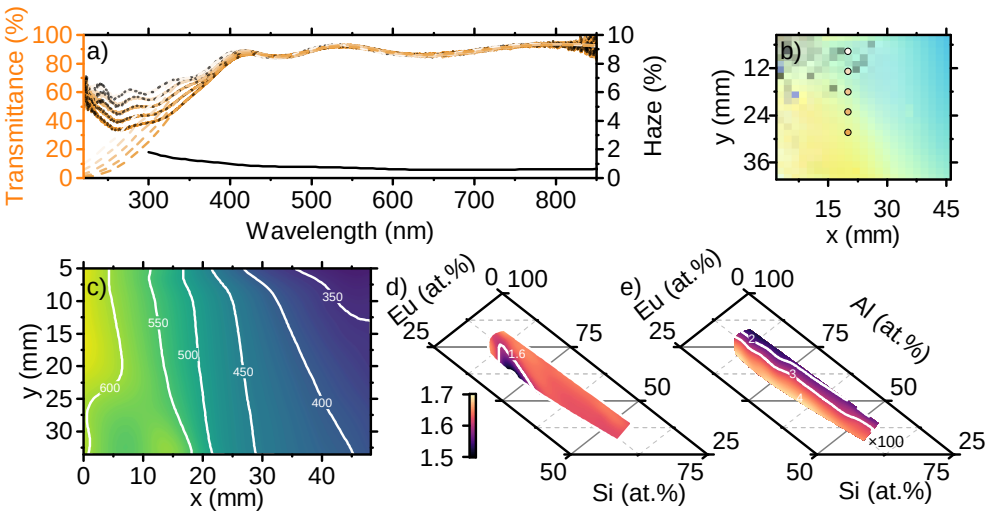


Figure 5.2: a: Transmittance at locations shown in panel b. Colored dashed lines are fits to the transmission data ($R^2 = 0.992 \pm 0.005$ for $\lambda > 310\,\text{nm}$), black dotted lines are the fit corrected for Eu-absorption. **c:** Thickness (in nm) across the film. Respective ternary plots of **d:** the index of refraction (at 589 nm) and **e:** the extinction coefficient (at 267 nm, multiplied by a factor 100).

by Xie et al. [8], Ho Ryu et al. [14] and Zhu et al. [12], where Al:Si ratios as high as 2 : 1 are reported. The library under investigation in this work spans a composition space complimentary to what has been found in the literature cited above. The onset of loss of external quantum efficiency (EQE) is commonly reported at Eu concentrations between 3 at.% and 10 at.% in powdered phosphors [21–24]. This EQE loss is caused by concentration quenching outweighing absorption. In these powdered phosphors, the incident light is scattered, which causes more absorption than in thin-film systems [5]. Therefore, the EQE starts decreasing at higher dopant concentrations in luminescent thin-films. Based on this and (unpublished) preliminary observations, our library is deposited with Eu concentrations between 4.8 at.% and 26 at.%. This can be seen as a compromise between absorption and concentration quenching. X-ray diffraction measurements (Figure S1) confirm the amorphous nature of the library.

5.3.2 Index of Refraction and Absorption

Figure 5.2a shows the direct transmittance and the amount of haze from the thin-film library. The library shows no absorption in the visible range, but strong

4f → 5d absorption by Eu^{2+} in the UV. The library exhibits a low degree of haze (the ratio of diffuse to the total transmission) in the visible range, which remains below 1.1 %. For comparison, uncoated UV fused silica has a maximal haze of 0.7 %.

The transmission is measured at 24×24 locations across the substrate. The dashed lines in Figure 5.2a are a fit to the interference fringes and provide the thickness, extinction coefficient and index of refraction n. The fitting procedure and the extended Sellmeier model behind it [25] are explained in detail in Section 5.7. It follows that the thickness of the film varies from 322 nm to 639 nm (Figure 5.2c) as a result of the higher sputter yield of the Al source in comparison to the yields from the Si and Eu sources.

The fitted values for the index of refraction can be combined with the compositional data from Figures 5.1e to 5.1g, leading to the ternary diagram as seen in Figure 5.2d. These ternary diagrams directly relate the composition with other properties, by leaving out position information. Figure 5.2d shows that the refractive index remains quite constant at $n = 1.63 \pm 0.03$. A minimum of $n = 1.46$ is found at 20 at.% Si, 64 at.% Al and 16 at.% Eu. The index of refraction can assist in clarifying the oxide or nitride nature of the library, which cannot reliably be determined by EDX. Based on the refractive indices of AlN (2.16 [26]), Si_3N_4 (2.04 [27]), Al_2O_3 (1.76[28, pp. 4–143]) and SiO_2 (1.46[28, pp. 10–249]), we can conclude that the library lies closer to an oxide-type than to a nitride-type material. Within a material, the anions are mainly responsible for the value of n. Since n is constant for most of the library, we can conclude that the O:N ratio within our SiAlONs are the same throughout the library, with only the cations varying. The emergence of the minimum of $n = 1.46$ can however not be explained, as it greatly deviates from the gradual change of n observed in the rest of the library.

The shape of the UV absorption cannot be described with a monotonically decreasing function as employed by the extended Sellmeier model. However, the model describes the transmission in the range of low absorption very well. It is therefore possible to extrapolate this data to the UV and extract the absorption caused by Eu, expressed as the extinction coefficient, as seen in Figure 5.2e. Figure 5.2e shows that the extinction coefficient displays a direct correlation with the doping percentage of Eu, supporting our reasoning that the absorption is caused by Eu. Across the library, this amounts to a (Napierian) attenuation coefficient of $1294 \pm 8\ \mathrm{cm^{-1}\,at.\%^{-1}}$ at the absorption maximum of 267 nm.

5.3.3 Luminescent Properties

Figure 5.1d shows that the dominant emission color varies across the SiAlON:Eu library from yellow to blue. The emission observed is a broad band (Figure 5.3a) attributable to 5d → 4f transitions in Eu^{2+}. The wavelength at which the emission is most intense varies from 550 nm at 59.7 at.% Si, 29.9 at.% Al and 10.4 at.% Eu to 500 nm at 82.0 at.% Si, 16.4 at.% Al and 1.6 at.% Eu. This variation corresponds to yellow emission when the library is rich in Al with a shift to blue when the Si concentration is increased. A redshift in emission when the Al:Si ratio increases is often reported in literature for Eu-doped SiAlONs [7, 8, 14, 16].

Figures 5.3a to 5.3c show that the emission can be deconvoluted into three separate Gaussians. Figure 5.3a shows all three Gaussians: an intense band, centered at 550 nm, and two bands of lower intensity on both sides of this central band. These three bands change in position and intensity, dependent on the composition of the library. The band at higher wavelengths starts to become discernible when starting at the right (Si-rich side) of the library and moving to a decreasing Si concentration (Figure 5.3b), with measurement positions shown in the inset of Figure 5.3a. The band at lower wavelengths becomes clearly visible at higher Eu and Al concentrations (bottom left of the library, as seen in the inset).

The three bands are fit to the spectra of all emission measurements. The fitting protocol is similar to that for the transmission measurements, explained in Section 5.8. A limitation is placed on how much the width (fwhm) of each band is allowed to vary across the library. This limitation asserts that the bands have the same physical origin in the host lattice, as opposed to producing the numerically best fit. This yields a variation of 0.73 ± 0.06 eV fwhm for the band at low wavelengths, 0.64 ± 0.07 eV fwhm for the center band, and 0.67 ± 0.05 eV fwhm for the band at high wavelengths. The center attributed to a band is allowed to vary by at most 0.05 eV per step in position ($\Delta x = 1.72$ mm, $\Delta y = 1.89$ mm). This limitation asserts that the gradual shifting of composition is reflected in the fitting of the emission. No limitations are placed on the maximal or minimal intensity of the bands.

The amorphous nature complicates a discussion of the origin of the luminescent properties derived from the material's crystal structure. However, the widths of the different emissions show limited variation while still producing a good fit. We can therefore conclude that the observed emissions originate from

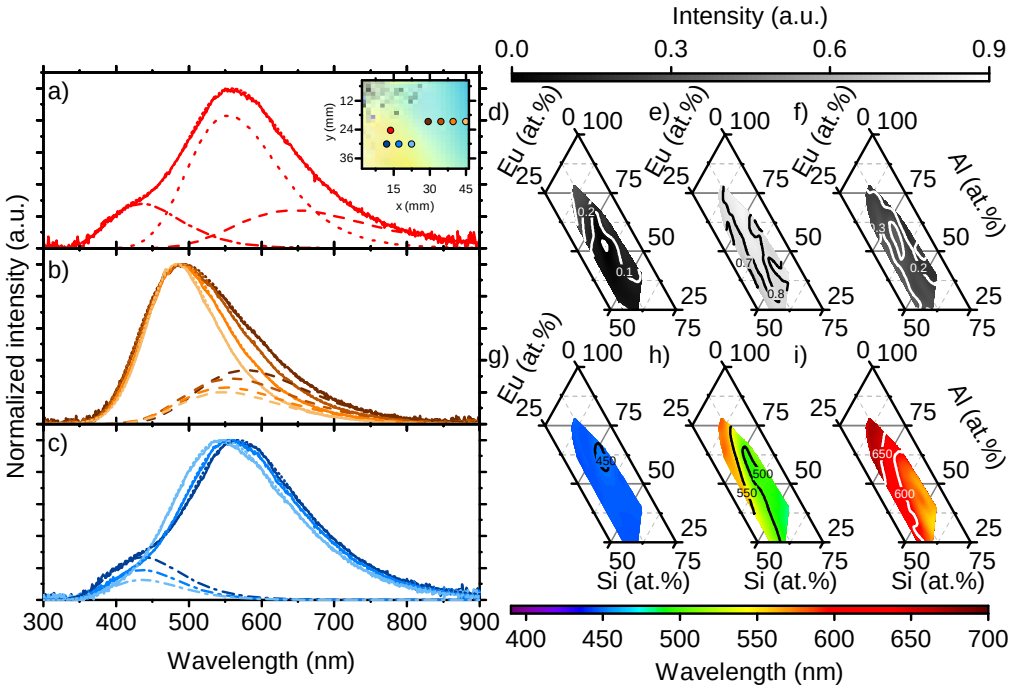


Figure 5.3: Relation between composition and luminescent emission ($\lambda_{ex} = 280\,nm$) properties of the library. **a:** Emission spectrum observed at the red point in the inset, showing the three different Gaussians that build up the observed emission. The measured emission is a solid line, fits are dotted. **b:** Normalized emission spectra (yellow-to-brown points shown in the inset of panel a) showing the development of the band at high wavelengths (dashed), while the center and low wavelength bands remain constant. **c:** Normalized emission spectra where the presence of the band at low wavelengths (dash-dotted) becomes visible (light-to-dark blue points in the inset of panel a). Ternary diagrams of the deconvoluted intensities of the normalized spectra for **d:** the low-wavelength band, **e:** the center band, **f:** the high wavelength band. Centers (in nm) of these bands are respectively shown in **g:**, **h:**, **i:** (adjusted-$R^2 > 0.99$).

three defects for which the first coordination sphere does not change throughout the library. This corresponds with the constant index of refraction throughout the library, further establishing that the O:N ratio in the library is constant to a great degree.

Like the data resultant from the fitting of the transmissions, the properties of the Gaussians can also be directly related to the composition. Figures 5.3d to 5.3f show ternary diagrams for the emission intensities and Figures 5.3g to 5.3i for the center wavelengths of the three deconvoluted Gaussians.

Comparing the ternary intensity diagrams shows that the central band (at $\sim 500-550\,\mathrm{nm}$) is most intense throughout the entire library. This central band is therefore mainly responsible for the observed emission color. The band at low wavelengths (Figures 5.3d and 5.3g) becomes relatively more intense at higher Al concentrations, while the intensities of the other two bands show no clear correlation with the composition.

From the ternary emission diagrams (Figures 5.3g to 5.3i), the influence of substituting the cations in SiAlON:Eu for each other becomes immediately visible. For the two emissions at higher wavelengths (Figures 5.3h and 5.3i), a shift of the emission to the red can be observed when (*i*) substituting Si for Al at a fixed Eu concentration, and (*ii*) increasing the Eu concentration, where Eu substitutes either Si or Al.

In the case of (*i*), a change in the second coordination sphere surrounding the emitting Eu can explain the increasing emission wavelengths. In this second coordination sphere, the distribution of Al and Si cations can be assumed to vary statistically, based on the measured composition. Since Al has a lower electronegativity than Si, it tends to bind the electrons of the neighboring anion less strongly. Consequently, the anions in the first coordination sphere of Eu^{2+} become more polarizable (i.e. have a higher spectroscopic polarizability [29].) This increase in polarizability leads to a decrease in centroid energy [29] (difference between the 4f groundstate and average 5d-level) when the Al concentration increases, and thus to a higher emission wavelength. This same effect of redshifting emission when replacing Si with Al in the second coordination sphere has been observed in Tb^{3+}-doped $Y_2Ca_2Si_2O_9$ and $Y_4Al_2O_9$ [30].

The redshift related to an increased Eu concentration (*ii*) can be caused by reabsorption of the high-energy shoulder of the emission. This reabsorption effect becomes more profound with more absorbing centers present and will

therefore yield a phosphor emitting at low energy and thus high wavelength [31].

Contrary to the other two emissions, the band at lower wavelength (Figure 5.3g) remains at a relatively constant wavelength, moving from 444 nm to 452 nm. A blue-violet emission in Al-rich SiAlONs has been previously reported in literature by Zhu et al. [12] and Yang et al. [15] It appears that this defect is located at a site where the emission is unaffected by changes in overall host composition. The relative intensity of this emission does however start increasing when the concentration of Al is increased (Figure 5.3d), as is also observed by Zhu et al. [12] This blue-violet emission has been attributed to a defect site with higher oxygen content in its first coordination sphere than defects showing emission at higher wavelengths [12]. This higher oxygen content should go paired with a lower index of refraction. Figure 5.2d confirms that this is indeed the case, as a lower n is observed at higher Al concentrations, where this defect becomes visible.

5.3.4 Luminescent Quantum Efficiency

The photoluminescent (PL) intensity (Figure 5.1c) varies strongly as a function of position and hence composition. Since the thickness and amount of dopant vary throughout the film, the PL is not a direct measure for the efficiency with which the dopants convert the absorbed light [i.e. the luminescent quantum efficiency (LQE)]. A measure for the LQE independent of all these parameters is the decay time, which only depends on properties of the composition itself.

Section 5.3.4 shows that the photoluminescent decay of the library after excitation at 280 nm is strongly non-exponential. Therefore, the decay time cannot be fitted with a single exponent, which would yield the decay time. To still have a comparative measure, a mean decay time [32]

$$\tau_{\text{mean}} = \frac{\int_0^\infty tI(t)\,\mathrm{d}t}{\int_0^\infty I(t)\,\mathrm{d}t} \tag{5.1}$$

is calculated. Here, $I(t)$ is the emission intensity at time t after excitation.

Section 5.3.4 shows the mean decay times summarized in a ternary diagram. The quantum efficiency can be estimated by comparing τ_{mean} to an ideal decay time of an isolated emitting center. Assuming that this ideal decay time does not vary greatly across the different compositions, τ_{mean} can be taken as a relative

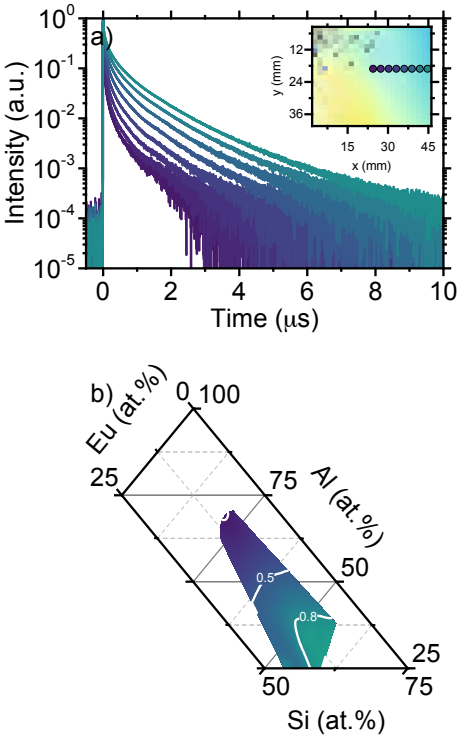


Figure 5.4: Decay times across the substrate (λ_{ex} = 280 nm, λ_{em} = 510 nm to 530 nm). **a:** Moving from the locations rich in Si to rich in Al at equal Eu (see inset). **b:** Ternary plot of mean decay times (in µs).

estimate of the LQE. Section 5.3.4 shows that an increase in Si concentration over Al leads to an increase in τ_{mean}. Combined with the higher PL intensity seen in Figure 5.1c, we can therefore conclude that when increasing the Si concentration, also the quantum efficiency increases. This increasing quantum efficiency with higher Si concentrations agrees with what is observed in literature, where for crystalline Eu-doped β-SiAlON the highest quantum efficiencies were found for a Si:Al ratio greater than 5 : 1, with decreasing quantum efficiency as this ratio decreases [8].

The decrease in decay time for decreasing Si content over Al might be related to two different effects. As the Si:Al ratio decreases, the distance between all atoms increases and the overall structure becomes less rigid [8, 11]. This can yield a smaller radial overlap between the 4f and 5d orbitals of Eu^{2+}, which has a decreased decay time as a consequence [33]. Another possibility is that the decrease in decay time comes from a decrease in thermal stability as the Si:Al ratio decreases. As the 5d energy level lowers towards the 4f level, the parabolas describing the two in a configurational coordinate diagram will intersect at lower

energy. Physically, this means a higher likelihood of a radiationless transition at room temperature, which goes paired with a lower decay time.

5.4 Conclusion

We have shown that it is possible to create an amorphous luminescent thin-film material library with a specific Al:Si:Eu composition range in a SiAlON host, with a haze below 1.1 % in the visible spectrum and strong PL emission. The library shows clear composition-dependent emission varying from 500 nm to 550 nm after UV excitation. An increase in Al concentration over Si goes together with an increase in emission wavelength. This behavior can be best explained by that the composition of the second coordination sphere of the dominant Eu defect shifts the emission to the red. Simultaneously with shifting the emission to the red, the quantum efficiency drops. We can therefore conclude that a higher degree of Si in our SiAlON:Eu^{2+} thin-film improves the quantum efficiency of the Eu^{2+} emission.

The low haze combined with the amorphous nature of the library opens up possibilities for functionalizing sputter deposited luminescent SiAlONs as a luminescent solar concentrator. The Eu doping shown in this chapter only absorbs the UV portion of sunlight, which could make for a visibly transparent luminescent solar concentrator with low power output. However, using the same methods of library creation with sputter coating and subsequent analysis, other rare-earths, like Sm^{2+} and Tm^{2+}, can be doped into similar amorphous SiAlON hosts. These rare-earths could expand the absorption range to span the visible range and therefore greatly increase the total achievable solar-to-electric conversion efficiency.

5.5 Acknowledgements

The authors would like to acknowledge Rudi Santbergen for assisting with the haze measurements. The results in this chapter are from equal contributions by Evert Merkx and Sadiq van Overbeek.

5.6 Appendix: X-Ray Diffraction Data

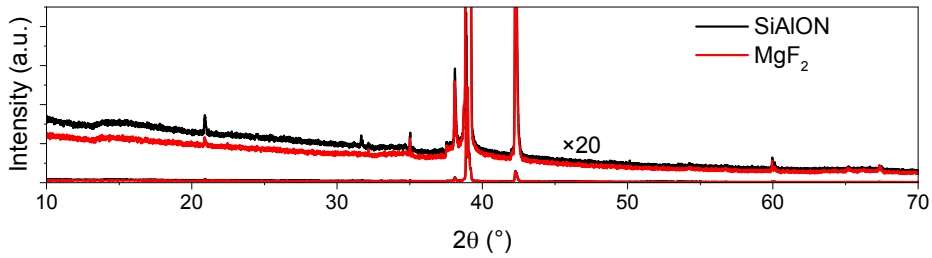


Figure 5.5: Diffractogram of the luminescent SiAlON thin-film and of the MgF_2 substrate. No diffraction peaks signifying crystallinity other than the MgF_2 substrate can be discerned on the SiAlON sample, whereas the amorphous component does show an increase in intensity. The small peak at 32° seen in SiAlON can still be attributed to the MgF_2 substrate, due to the slightly different angle under which the SiAlON was measured.

5.7 Appendix: Fitting Transmission Spectra

Transmission measurements provide a wealth of information on a thin-film. Based on the interference fringes observed in a transmission spectrum, the (local) thickness d, index of refraction n and extinction coefficient k can be calculated [34, 35]. For a luminescent thin-film the index of refraction is important as it can both give information on the composition of the film, as well as show how much light can be coupled into the film. The thickness, combined with the amount of absorption, yields the absorptivity of the film. The transmission T of light incident normal to the surface of an absorbing thin-film deposited on a thick non-absorbing substrate can be described as [34]

$$T = \frac{Ax}{B - Cx + Dx^2}, \tag{5.2}$$

with

$$
\begin{aligned}
A &= 16 n_s (n^2 + k^2), \\
B &= \Big[(n+1)^2 + k^2\Big]\Big[(n+1)(n+n_s^2) + k^2\Big], \\
C &= \Big[(n^2 - 1 + k^2)(n^2 - n_s^2 + k^2) - 2k^2(n_s^2 + 1)\Big] 2\cos\phi \\
&\quad - k\Big[2(n^2 - n_s^2 + k^2) + (n_s^2 + 1)(n^2 - 1 + k^2)\Big] 2\sin\phi, \\
D &= \Big[(n-1)^2 + k^2\Big]\Big[(n-1)(n-n_s^2) + k^2\Big], \\
\phi &= \frac{4\pi n d}{\lambda}, \\
x &= \exp(-\alpha d), \\
\alpha &= \frac{4\pi k}{\lambda}.
\end{aligned}
\tag{5.3}
$$

Even though a fully written out form of eq. (5.3) looks quite daunting, it only depends on 5 variables: the refractive index $n \equiv n(\lambda)$, extinction coefficient $k \equiv k(\lambda)$, thickness d of the thin-film, and the refractive index n of the substrate, which is usually known and taken to be independent of the wavelengths λ in the region of interest. For MgF_2, $n_s = 1.36$.

In turn, many descriptions for n and k exist. A variety of these descriptions has been reviewed by Poelman and Smet [35]. Based on this review and the work by Alvarez et al. [25], the single term semi-empirical Sellmeier description, where

$$n^2 = a + \frac{b\lambda^2}{\lambda^2 - c^2}$$

has been chosen as description for the refractive index. Here a, b and c are fitting parameters.

To extract k, the work by Alvarez et al. [25] is followed. In the description an absorption bandgap zone [36], combined with a Cauchy-like Taylor expansion of the dispersion relation is included as:

$$k = 1240 \cdot a_k \lambda \left(\frac{1}{\lambda} - \frac{1}{\lambda_0}\right)^2 \theta(\lambda_0 - \lambda) + b_k + \frac{c_k}{\lambda} + \frac{d_k}{\lambda^2}.$$

Here a_k, b_k, c_k, d_k are fitting parameters, λ_0 represents the onset of a strong absorber, and $\theta(\cdot)$ is the Heaviside step function.

Luminescent thin-films exhibit absorption spectra not observed in other dielectric or metal thin-films. These absorption spectra are a result of the transitions between the different intra-bandgap orbitals of the luminescent dopant.

While the absorption spectrum for a luminescent dopant can in principle still be captured using e.g. the Cauchy dispersion relation, or by including many oscillators in a Drude-Lorentz type description, a very high order expansion of such relations would be required to fully describe the absorption behavior.

When considering luminescent thin-films, the transmission should therefore be fit to the spectral regions featuring a low degree of absorption. If the region with low absorption can be well-described, the data can be extrapolated to the regions with higher absorption. This extrapolation can then be used to retrieve the absorption of the rare-earth dopant. The ratio between the measurement and the fit yields this absorption, which can be included into the description of k. One should be careful and assert that the absorption does represent expected absorption by a rare-earth dopant.

Transmission spectra are recorded using an xy-scanning setup as described in the main text. Light from a deuterium lamp is coupled into a 600 µm optical fiber and turned into a parallel beam with a diameter of ~ 5 mm. This beam is placed at normal incidence on the thin-film. Behind the film a collecting lens and fiber are present. These collection optics lead to an Ocean Optics USB4000 spectrometer with a slitwidth of 25 µm. The resulting transmission spectra are recorded at 200 nm to 850 nm with an integration time of 5 ms and averaged 100×. The film is moved through the parallel beam, which finally leads to a 32×32 grid of transmission spectra.

From this data a single transmission spectrum is chosen that looks descriptive of the general behavior of the entire thin-film. This spectrum is manually fitted using OPTIFIT [25], with the substrate refractive index fixed to the known MgF_2 value of 1.36. The results of this manual fit are used as 'seed-fit' for the remainder of the procedure, shown graphically in Figure 5.6. Since this work involves a compositional gradient, we can expect n, k and d to vary only gradually. Hence, the resultant fitting parameters of our seed-fit are used as starting point for the measurements immediately surrounding it. The resultant fitting parameters of those fittings is then used as initial condition for their surroundings and so on, until all available data has been addressed.

Using the seed-fit, a fitting of the entire film with lowest adjusted $R^2 > 0.96$ can be made. To improve the fitting quality, the top 10 % points are chosen as input parameters to fit their surroundings of lower quality. As with the initial fitting, the surroundings are fitted again with the resultant values from their

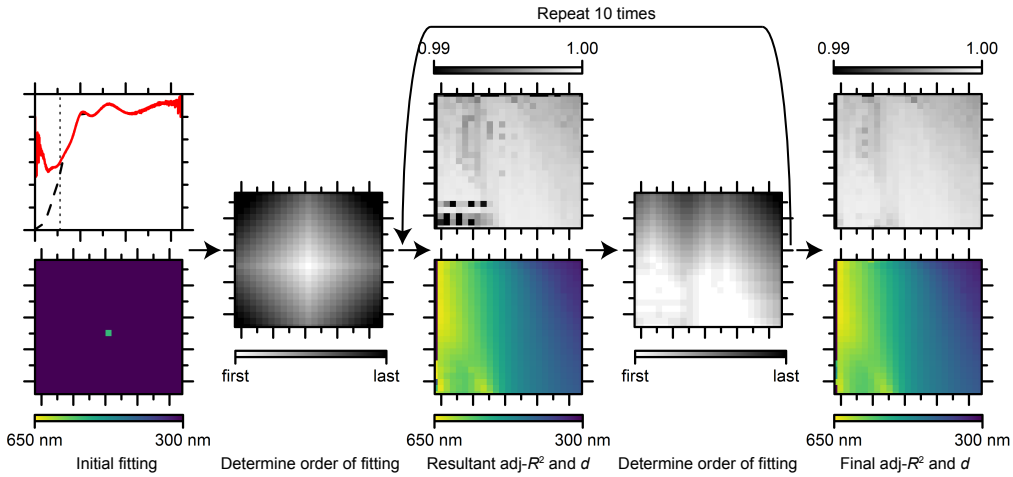


Figure 5.6: Workflow of fitting a transmission spectrum. At the "Initial fitting" step, an initial fit is made with OPTIFIT (top), leading to (among others) the thickness shown below. Based on this initial fitting, all surrounding points are fit, starting at white and going to black. For each next point, the previous fit is used as initial condition. This fitting leads to an adjusted R^2 and thickness d shown respectively on the top and bottom panels of "Resultant adj-R^2 and d". The top 10 % best adjusted R^2 values are selected and from those a new order of fitting is made. This process is repeated 10 times, which eventually leads to the adjusted R^2 and thicknesses respectively shown on the top and bottom of the final image.

previously addressed nearest neighbors as starting parameters and so on. If the adjusted R^2 of the new fitting is greater than the old one, the better fit is chosen. This process of selection and neighbor-fitting is repeated 10 times, since only minimal changes in fitting quality occur in subsequent fits. After these repetitions, the final fitting is determined.

5.8 Appendix: Fitting Emission Spectra

The same procedure as applied to the transmission spectra is used to fit the emission spectra. For the luminescence three Gaussians are fit instead of eq. (5.2). As additional constraint, the Gaussians are only allowed to vary 0.02 eV, 0.05 eV and 0.01 eV in FWHM and 0.025 eV, 0.05 eV and 0.0015 eV in center between points, for the bands centered at low, central and high wavelengths respectively.

5.9 Appendix: Ternary Diagrams of Optical Data

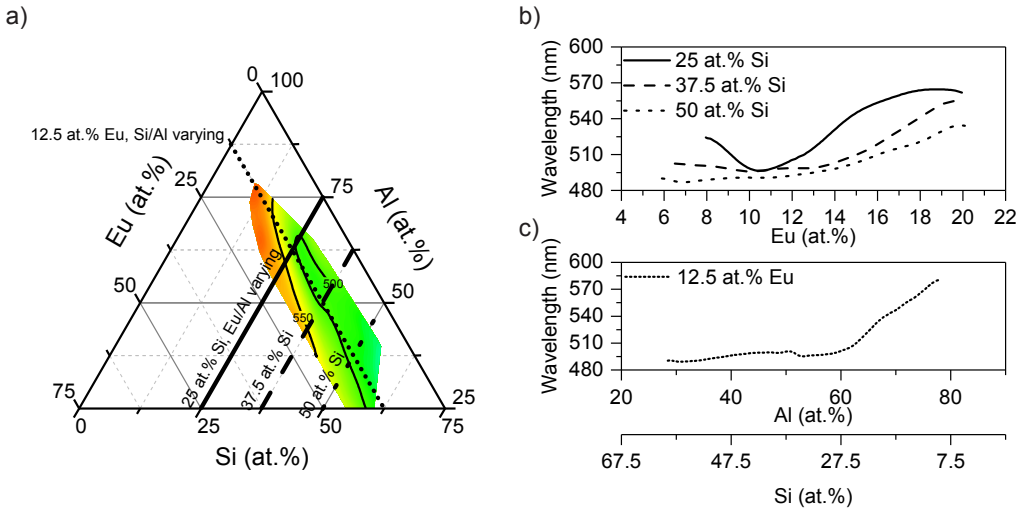


Figure 5.7: Expanded version of Figure 5.3h. **a:** Ternary diagram of the dominant emission of the luminescence libary under investigation in the main text, spanning 75 at.% for every element involved. In the ternary diagram, green indicates short wavelengths, and red indicates longer wavelengths. Exact numbers are given in the contour lines. Indicated are four lines, which explore the effects of keeping one element fixed, with the other two varying. These lines are essentially extensions of the axis ticks of the element that is kept fixed. The straight, dashed, and dotted lines parallel to the Eu-axis have a fixed Si concentration. Following these lines, the influence of substituting Al for Eu can be seen. **b:** The underlying data from the straight, dashed, and dotted lines from panel a. **c:** The underlying data from the short dotted line parallel to the Al axis in panel a. This line shows what effect substituting Si for Al has on the luminescence. As can be seen from these graphs, ternary diagrams are an effective way to present data on four variables [elemental composition (3) and luminescence (1)] in a single graph.

References

[1]R.-J. Xie and H. T. Hintzen, "Optical Properties of (Oxy)Nitride Materials: A Review," Journal of the American Ceramic Society **96**, edited by D. Johnson, 665–687 (2013).

[2]G. Bernhardt, J. Krassikoff, B. Sturtevant, and R. Lad, "Properties of amorphous SiAlON thin films grown by RF magnetron co-sputtering," Surface and Coatings Technology **258**, 1191–1195 (2014).

[3]T. Ekstrom and M. Nygren, "SiAlON Ceramics," Journal of the American Ceramic Society **75**, 259–276 (1992).

[4]W. H. Weber and J. Lambe, "Luminescent greenhouse collector for solar radiation.," Applied Optics **15**, 2299–2300 (1976).

[5]D. K. G. de Boer, D. J. Broer, M. G. Debije, W. Keur, A. Meijerink, C. R. Ronda, and P. P. C. Verbunt, "Progress in phosphors and filters for luminescent solar concentrators.," Optics Express **20**, A395–405 (2012).

[6]M. Debije, "Renewable energy: Better luminescent solar panels in prospect," Nature **519**, 298–299 (2015).

[7]C. Cozzan, G. Laurita, M. W. Gaultois, M. Cohen, A. A. Mikhailovsky, M. Balasubramanian, and R. Seshadri, "Understanding the links between composition, polyhedral distortion, and luminescence properties in green-emitting β-$Si_{6-z}Al_zO_zN_{8-z}$:Eu^{2+} phosphors," Journal of Materials Chemistry C **5**, 10039–10046 (2017).

[8]R.-J. Xie, N. Hirosaki, H.-L. Li, Y. Q. Li, and M. Mitomo, "Synthesis and Photoluminescence Properties of β-sialon:Eu^{2+} ($Si_{6-z}Al_zO_zN_{8-z}$:Eu^{2+})," Journal of The Electrochemical Society **154**, J314 (2007).

[9]N. Hirosaki, R.-J. Xie, K. Kimoto, T. Sekiguchi, Y. Yamamoto, T. Suehiro, and M. Mitomo, "Characterization and properties of green-emitting β-SiAlON:Eu^{2+} powder phosphors for white light-emitting diodes," Applied Physics Letters **86**, 211905 (2005).

[10]R.-J. Xie and N. Hirosaki, "Silicon-based oxynitride and nitride phosphors for white LEDs–A review," Science and Technology of Advanced Materials **8**, 588–600 (2007).

[11]X. Zhang, M.-H. Fang, Y.-T. Tsai, A. Lazarowska, S. Mahlik, T. Lesniewski, M. Grinberg, W. K. Pang, F. Pan, C. Liang, W. Zhou, J. Wang, J.-F. Lee, B.-M. Cheng, T.-L. Hung, Y.-Y. Chen, and R.-S. Liu, "Controlling of Structural Ordering and Rigidity of β-SiAlON : Eu through Chemical Cosubstitution to Approach Narrow-Band-Emission for Light-Emitting Diodes Application," Chemistry of Materials **29**, 6781–6792 (2017).

[12]X. W. Zhu, Y. Masubuchi, T. Motohashi, and S. Kikkawa, "The z value dependence of photoluminescence in Eu^{2+}-doped β-SiAlON ($Si_{6-z}Al_zO_zN_{8-z}$) with $1 \leq z \leq 4$," Journal of Alloys and Compounds **489**, 157–161 (2010).

[13]C.-Y. Chung, J. H. Ryu, D. S. Yoo, S.-H. Lee, and Y.-C. Chung, "First-principles calculation and luminescence property of Eu_x:$Si_5Al_{1-x}O_{1+x}N_{7-x}$ green phosphor," Computational Materials Science **49**, S359–S363 (2010).

[14]J. Ho Ryu, Y.-G. Park, H. Sik Won, S. Hyun Kim, H. Suzuki, and C. Yoon, "Luminescence properties of Eu^{2+}-doped β-$Si_{6-z}Al_zO_zN_{8-z}$ microcrystals fabricated by gas pressured reaction," Journal of Crystal Growth **311**, 878–882 (2009).

[15]H. Yang, Q. Liu, Q. Wei, Z. Zhou, J. Wan, G. Liu, and R.-J. Xie, "Eu-Doped β-SiAlON Phosphors: Template-Assistant Low Temperature Synthesis, Dual Band Emission, and High-Thermal Stability," Journal of the American Ceramic Society **97**, edited by D. Johnson, 3164–3169 (2014).

[16]Y. Li, N. Hirosaki, R. Xie, T. Takeda, and M. Mitomo, "Crystal and electronic structures, luminescence properties of Eu^{2+}-doped $Si_{6-z}Al_zO_zN_{8-z}$ and $M_ySi_{6-z}Al_{z-y}O_{z+y}N_{8-z-y}$ (m=2li, mg, ca, sr, ba)," Journal of Solid State Chemistry **181**, 3200–3210 (2008).

[17]T. Wang, Z. Xia, Q. Xiang, S. Qin, and Q. Liu, "Relationship of 5d-level energies of Ce^{3+} with the structure and composition of nitride hosts," Journal of Luminescence **166**, 106–110 (2015).

[18]J. H. Chung and J. H. Ryu, "Photoluminescence and led application of b−SiAlON:Eu^{2+} green phosphor," Ceramics International **38**, 4601–4606 (2012).

[19]J. D. Fowlkes, J. M. Fitz-Gerald, and P. D. Rack, "Ultraviolet emitting $(Y_{1-x}Gd_x)_2O_{3-\delta}$ thin films deposited by radio frequency magnetron sputtering: combinatorial modeling, synthesis, and rapid characterization," Thin Solid Films **510**, 68–76 (2006).

[20]S. Yamada, H. Emoto, M. Ibukiyama, and N. Hirosaki, "Properties of SiAlON powder phosphors for white LEDs," Journal of the European Ceramic Society **32**, 1355–1358 (2012).

[21]S. W. Kim, T. Hasegawa, T. Ishigaki, K. Uematsu, K. Toda, and M. Sato, "Efficient Red Emission of Blue-Light Excitable New Structure Type $NaMgPO_4$:Eu^{2+} Phosphor," ECS Solid State Letters **2**, R49–R51 (2013).

[22]C. Zhang, J. Yang, C. Lin, C. Li, and J. Lin, "Reduction of Eu^{3+} to Eu^{2+} in $MAl_2Si_2O_8$ (M=Ca, Sr, Ba) in air condition," Journal of Solid State Chemistry **182**, 1673–1678 (2009).

[23]X. Qiao and H. J. Seo, "A Novel Blue-Emitting Phosphor of Eu^{2+}-Activated Magnesium Haloborate $Mg_3B_7O_{13}Cl$," Journal of the American Ceramic Society **98**, edited by R.-J. Xie, 594–600 (2015).

[24]T.-W. Kuo, C.-H. Huang, and T.-M. Chen, "Novel yellowish-orange $Sr_8Al_{12}O_{24}S_2$:Eu^{2+} phosphor for application in blue light-emitting diode based white LED," Optics Express **18**, A231 (2010).

[25]R. Alvarez, A. Garcia-Valenzuela, C. Lopez-Santos, F. J. Ferrer, V. Rico, E. Guillen, M. Alcon-Camas, R. Escobar-Galindo, A. R. Gonzalez-Elipe, and A. Palmero, "High-Rate Deposition of Stoichiometric Compounds by Reactive Magnetron Sputtering at Oblique Angles," Plasma Processes and Polymers **13**, 960–964 (2016).

[26]S. Adachi, *Optical Constants of Crystalline and Amorphous Semiconductors: Numerical Data and Graphical Information* (Springer US, Boston, MA, 1999), p. 714.

[27]K. Luke, Y. Okawachi, M. R. E. Lamont, A. L. Gaeta, and M. Lipson, "Broadband mid-infrared frequency comb generation in a Si_3N_4 microresonator," Optics Letters **40**, 4823 (2015).

[28]D. R. Lide, *CRC Handbook of Chemistry and Physics* (2007), p. 2640.

[29]P. Dorenbos, "5d-level energies of Ce^{3+} and the crystalline environment. I. Fluoride compounds," Physical Review B **62**, 640–649 (2000).

[30]G. Blasse and A. Bril, "Investigations of Tb^{3+}-activated phosphors," Philips Research Reports **22**, 481–502 (1967).

[31]C.-Y. Wang, T. Takeda, O. M. ten Kate, R.-J. Xie, K. Takahashi, and N. Hirosaki, "Suck it," Journal of Materials Chemistry C **4**, 10358–10366 (2016).

[32]E. Nakazawa, "Fundamentals of luminescence," in *Phosphor Handbook*, edited by W. M. Yen, S. Shionoya, and H. Yamamoto, 2nd ed. (CRC Press, 2006) Chap. 2.8, pp. 99–110.

[33]S. Poort, A. Meyerink, and G. Blasse, "Lifetime measurements in Eu^{2+}-doped host lattices," Journal of Physics and Chemistry of Solids **58**, 1451–1456 (1997).

[34]R. Swanepoel, "Determination of the thickness and optical constants of amorphous silicon," Journal of Physics E: Scientific Instruments **16**, 1214–1222 (1983).

[35]D. Poelman and P. F. Smet, "Methods for the determination of the optical constants of thin films from single transmission measurements: a critical review," Journal of Physics D: Applied Physics **36**, 1850–1857 (2003).

[36]N. Ghobadi, "Band gap determination using absorption spectrum fitting procedure," International Nano Letters **3**, 2 (2013).

— 6 —

Modeling and Optimization of UV Absorbing Photovoltaic Windows Using a Thin-Film AlN:Eu^{3+} Luminescence Library

Paramount to an efficient luminescent solar concentrator are non-overlapping absorption and emission spectra, to avoid self-absorption. This non-overlap can be achieved by absorbing incoming UV light and emitting in the red to infrared. In this chapter, we present a technique for optimizing LSCs without self-absorption, using Eu^{3+}-doped AlN as a model system. The parameters affecting light absorption, emission and transport are extracted from a combinatorially sputtered gradient material library. This library results from a single deposition, with a gradient in thickness and Eu concentration. AlN:Eu^{3+} absorbs strongly until 450 nm, with a peak solar absorption of 499 cm^{-1} at.%$^{-1}$ at 350 nm due to a charge transfer band. The strongest emission is at 622 nm, thereby exhibiting no self-absorption. The presented optimization model strikes a balance between concentration quenching and absorptivity of Eu dopants by using the parameters extracted from the material library. For thicker films, concentration quenching can be avoided by using a lower dopant concentration, while still outperforming thinner films due to fast increasing absorption. The results demonstrate that, while AlN:Eu^{3+} itself should only be viewed as a model system, thin-films doped with rare-earths can yield industry-compatible, high efficiency LSCs because of their high absorption coefficients and lack of self-absorption.

This chapter has been published as: E.P.J. Merkx, T.G. Lensvelt, and E. van der Kolk, "Modelling and optimization of UV absorbing photovoltaic windows using a thin film AlN:Eu^{3+} luminescence library," Solar Energy Materials & Solar Cells **200**, 110032 (2019)
All data supporting the figures in this chapter can be found at: `https://data.mendeley.com/datasets/x3dr6v9v5j`

6.1 Introduction

Building-integrated photovoltaics (BIPVs) can turn the passive building envelope into a source of electricity. For example, when utilizing the principle of a luminescent solar concentrator (LSC), luminescent thin-films on window glass can transform these windows into electricity generating surfaces. Figure 6.1a shows the working principle of a thin-film LSC. Sunlight incident on the window is captured by luminescent centers in the coating on the window, which convert the captured light to a different wavelength. The converted light is emitted isotropically. Light emitted at an angle larger than the critical angle of the LSC is then waveguided through the LSC towards the windowpane by total internal reflection. In the windowpane PV cells are placed, which face the edges of the LSC. These cells convert the waveguided light into electricity. The light absorbed by the LSC is effectively concentrated on the PV cells. The area covered by the PV cells is therefore very small compared to the large LSC surface. In addition, the cells only need to be optimized for the LSC emission, a much narrower range of wavelengths than the solar spectrum. Therefore, the PV cells can have unity external quantum efficiency (EQE) at the LSC emission wavelengths. LSCs could replace ordinary windows as transparent energy generating BIPV at no high additional investment and no wiring blocking the view.

The concept of LSCs has existed since the 1970s [1], but wide adaptation was mainly impeded by these LSCs displaying bright coloration, making them unsuitable for use as windows in the building envelope. A recent development in LSCs is to use materials that absorb in the ultraviolet (UV) and have a large shift between absorption and emission wavelengths [2–4]. This combination leads to high transmission in the visible spectrum, and emission in the red to near-infrared (NIR), yielding the appearance of an ordinary window without coloring. Another advantage of this non-overlapping absorption and emission is that no parasitic absorption of the luminescence center itself (self-absorption) occurs. The absence of self-absorption means that when a photon is emitted under total internal reflection (in a perfect waveguide), it will reach the perimeter of the LSC, regardless of the LSC's size. The absence of self-absorption is therefore of great importance to the overall efficiency of the LSC.

Optimization of the composition of the luminescent coating is often a laborious process. The light-conversion efficiency of the LSC material has to be

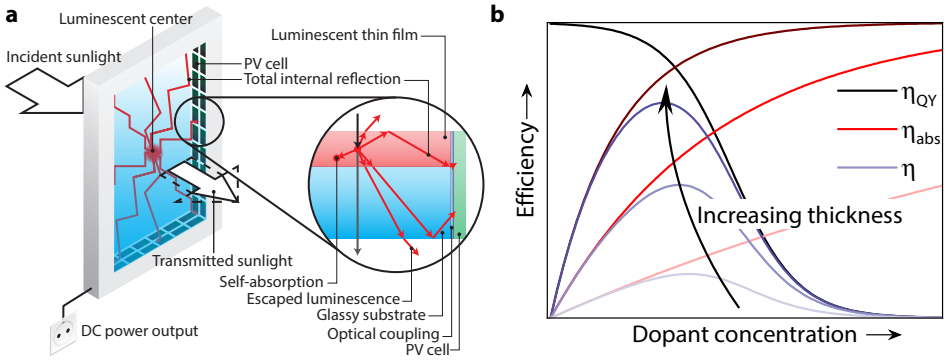


Figure 6.1: a: Schematic of the workings of a thin-film luminescent solar concentrator. **b:** Sketch of the influence of changing thickness or dopant concentration on the individual and overall LSC efficiencies.

measured for many individual samples with differing compositions. To overcome this laborious optimization, another approach is to fabricate thin-film libraries of LSC materials using combinatorial gradient magnetron sputtering, as seen in Chapter 4. With combinatorial gradient magnetron sputtering, a single substrate from a single deposition provides many compositions (a composition library) that can all be characterized automatically. Additionally, magnetron sputtering is already commonly used for window coatings [5]. The optimal composition found by this gradient method can therefore be implemented in glass coating on an industrial scale with relative ease.

In this chapter, we want to optimize the optical efficiency of an LSC without self-absorption based on experimental data from a composition library. As a model system for materials absorbing in the UV and having emission in the red to NIR, a good choice for a thin-film LSC coating is Eu^{3+}-doped AlN. AlN:Eu^{3+} can be excited by light below 400 nm, shows strong emission at 600 nm to 625 nm at room temperature [6–8], can be coated on glass through sputter deposition [9], and is chemically inert [10].

The optical efficiency of an LSC can be described with (see Chapter 3)

$$\eta_{\text{opt}} = (1 - R)\eta_{\text{abs}}\eta_{\text{QY}}\eta_{\text{trap}}\eta_{\text{WG}}\eta_{\text{SA}} \,. \tag{6.1}$$

Here, each factor describes one step in the light conversion-concentration process. $1 - R$ describes the amount of light transmitted into the film. η_{abs} is the fraction of transmitted light absorbed by the luminescent particles. η_{QY} is the internal photoluminescent quantum efficiency of Eu^{3+}, i.e. the ratio of photons

emitted to photons absorbed by Eu^{3+}. η_{trap} is the fraction of emitted photons that remain trapped within the LSC through total internal reflection. η_{WG} describes the efficiency of the waveguiding of light to the perimeter of the LSC. η_{WG} can be affected by scattering losses and absorption by the waveguide. η_{SA} is a factor to take self-absorption into account.

Assuming an optical density of 0.8 and an index of refraction of $n = 2$, a UV-absorbing LSC without self-absorption could have an optical efficiency of 2.3 % to 5.8 % when $\eta_{QY} = 1$. This value is highly dependent on where the absorption maximum of the LSC lies. When this maximum lies to the visible spectrum, the amount of photons in the solar spectrum increases tremendously. In practice, these optical efficiencies are not attained with UV-absorbing LSCs due to low η_{QY} of typically $\sim 10\,\%$ for quantum dots, to $\sim 80\,\%$ for dye molecules.

The product $\eta_{abs} \times \eta_{QY}$, shown in Figure 6.1b, is crucial to the overall performance of an LSC. When the concentration of luminescent centers is low, η_{QY} tends to be high, but at the same time, η_{abs} is low due to the low amount of absorbing centers. Conversely, at higher concentrations, η_{abs} is high due to many absorbing centers, but η_{QY} drops as a consequence of concentration quenching [11]. Apart from the dopant concentration within the film, the film thickness (at equal dopant concentration) will increase η_{abs} (to a first order, when disregarding interference effects). The optimum for $\eta_{abs} \times \eta_{QY}$ is therefore also specific to the thickness of the luminescent layer. As industrial throughput decreases (and cost increases) with increasing film thickness, it is of great importance to establish methods that can find the optimal dopant concentration for the desired thickness.

In this chapter, we present a general approach that only requires the deposition of a single thin-film to optimize $\eta_{abs} \times \eta_{QY}$. We do this optimization in three steps. Firstly, we deposit a film with a thickness- and a Eu concentration gradient, employing off-axis combinatorial sputtering of Al and Eu sources in a reactive O_2+N_2+Ar atmosphere. Here O_2 is added as dopant, which reduces the need for heat treatments to improve the intensity of the luminescence. Secondly, we determine the composition-dependent thickness, index of refraction, absorption, and quantum efficiency through a combination of energy-dispersive X-ray spectroscopy (EDX) and automated mapping of the transmission and laser-excited luminescence properties of the thin-film. Thirdly, using the parameters extracted

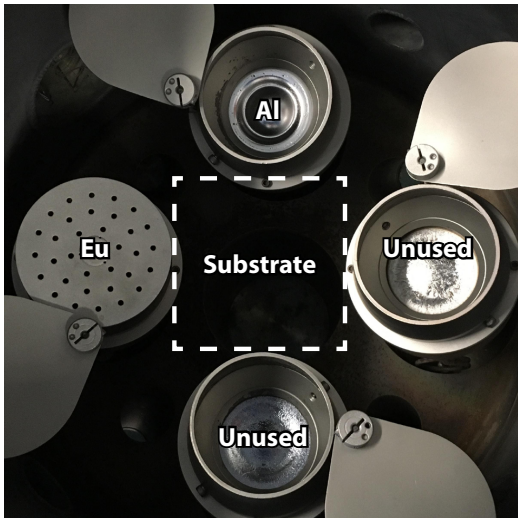


Figure 6.2: Top-down photograph of the inside of the sputtering chamber, with the sources used for fabrication; the right and bottom sources are not used for fabrication.

from the gradient thin-film, we maximize the optical efficiency of AlN:Eu^{3+} thin-film LSCs as a function of both thickness and Eu concentration, through optics simulations employing the transfer-matrix method.

6.2 Experimental

Library creation The AlN : Eu thin-film library was deposited on a square $44 \times 44\,\mathrm{mm}^2$ UV fused silica substrate (PGO) within an AJA ATC Orion 5 magnetron sputtering system (Figure 6.2) with a base pressure of 1×10^{-9} bar. Prior to the deposition, the substrate had been cleaned by rinsing three times with DI water and ethanol, followed by a 15 min bath in an ultrasonic cleaner with DI water. The deposition was carried out with 5.08 cm diameter metal Al (99.9995 %, Lesker) and Eu (99.99 %, Demaco) targets, which were reactively co-sputtered with respectively 150 W and 32 W RF power for 12.5 h. The deposition rate of Eu was reduced by a stainless steel mask with a pattern of concentric holes, blocking 88 % of the surface of the Eu target. The process gas flow consisted of 18 sccm 6N purity Ar, 0.25 sccm 5N purity O_2 and 13.75 sccm 5N purity N_2 into the sputtering chamber at a working pressure of 4×10^{-3} mbar. Oxygen was included in small amounts to the sputtering gas, and therefore to AlN, as alternative to thermal treatments at high temperatures [12]. O_2 and N_2 were introduced next to the substrate, while Ar was introduced at the Al source. Just before deposition, the substrate was heated to 400 °C. During the deposition, the sample was not

actively heated. The cooling of the sample during deposition can be seen in Figure 6.8 in the appendix: Section 6.6. To realize a thin-film with both a gradient in Eu and in film thickness, the substrate was sputtered without rotation.

Following the deposition, the luminescence of the library was improved by subsequently heating to 300 °C and 500 °C, both for 20 min, in a Solaris 150 rapid thermal processing (RTP) system. The RTP system was flushed with 9 standard liters per minute (SLM) N_2 (5N purity) during the entire annealing procedure. Figure 6.9 in the appendix: Section 6.6 shows that this annealing treatment yields a 12-fold improvement in luminescence.

An undoped AlN reference sample was made with identical treatment, but with the Eu source switched off.

Composition analysis A JEOL IT-100, operated at 15 keV with probing current at 70 %, was used for SEM/EDX analysis. Quantitative elemental analysis without a conductive coating was achieved by employing the device in low vacuum mode (35 Pa pressure). Elemental compositions were quantified at 3000× magnification ($31 \times 23\,\mu m^2$ measurement area). XRD measurements were performed using a PANalytical X'pert Pro MPD diffractometer in Bragg-Brentano geometry, with a Cu Kα anode ($\lambda = 0.1540598\,nm$) operating at 45 kV and 40 mA. The area illuminated by the X-ray beam was around $1 \times 5\,mm^2$ in size.

Optical characterization The total transmission was measured by placing the samples between a collimated (2.7 mm diameter) xenon light source and the entrance port of a 5.08 cm diameter integrating sphere (IS200-4, Thorlabs), with an Ocean Optics QEPro spectrometer (200 µm slit width) connected to the off-axis detector port. The samples were moved through the collimated beam with a sample holder placed on top of two stacked Thorlabs DDSM100 linear translation stages. Transmission spectra were recorded across the samples at 16×16 positions with a step size of 2.6 mm. Each position is recorded with an integration time of 250 ms and averaged 32×. Dark spectra were recorded by blocking the entrance of the integrating sphere with highly absorbing and reflecting Al tape. Lamp spectra were recorded by directly exposing the integrating sphere to the collimated light. The presented transmission spectra were corrected using these two reference measurements, measured with identical settings.

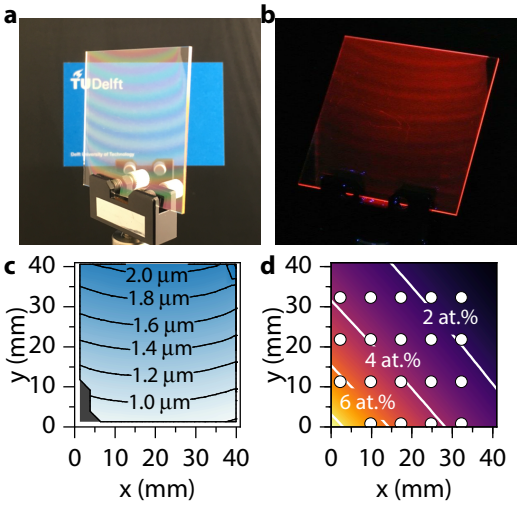


Figure 6.3: Concentration library of AlN doped with Eu. Photographs of the library under **a:** white light with a colored background, **b:** UV illumination (250 nm) on a dark background, after annealing. The white dashed line indicates the presence of a luminescence optimum. **c:** Thickness across the film. **d:** Distribution of the Eu concentration across the substrate (RMSE < 0.2 at.%), based on 24 local EDX measurements, marked by the white dots.

Photoluminescent excitation, emission, and decay measurements were carried out with a home-built xy-scanner setup, as described in Chapter 4. An Ekspla NT230 OPO Laser was used as excitation source, operated at excitation wavelengths ranging from 210 nm to 420 nm in steps of 0.25 nm. Combined emission/excitation spectra were integrated for 300 ms and averaged 4× per excitation wavelength. These spectra were recorded with an Ocean Optics QE65000 spectrometer with a 100 µm entrance slit. A 430 nm longpass filter (Semrock) was used to remove reflected laser light. The emission was corrected for the quantum efficiency and non-linearity of the detector. For decay studies, the emission, filtered with a 355 nm longpass filter, was passed directly to a Hamamatsu R7600U-03 PMT operating at −600 V linked to a CAEN DT5730 Digitizer with 64 ns per channel. The sample was excited at 350 nm, with the laser pulsing at 50 Hz. Decay traces were collected over 200 laser pulses at 20 × 20 locations across the film, with 2 mm between steps.

6.3 Results and Discussion

Figure 6.3a and Figure 6.3b show the final product: a thin-film, transparent in the visible spectrum, but with red emission when excited by UV light. The interference fringes are a consequence of the thickness gradient of the film, which ranges from 0.8 µm to 2.1 µm, as reported in Figure 6.3c. The thickness is retrieved from fitting 16 × 16 local transmission measurements (see Figure 6.11) to

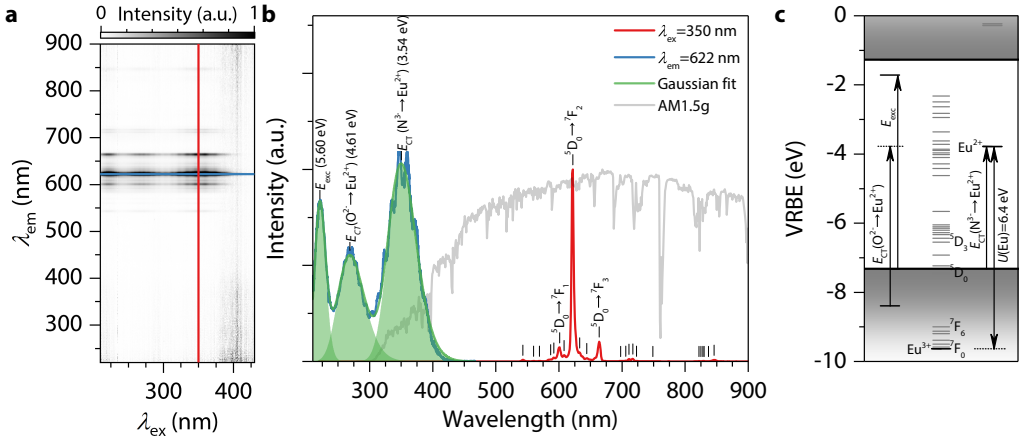


Figure 6.4: Luminescent properties of the AlN:Eu^{3+} library. **a:** Simultaneous emission and excitation mapping of the photoluminescence of the AlN:Eu^{3+} thin-film. Around 400 nm the noise increases due to low laser power. **b:** Excerpt taken at the blue and red lines from panel a. The gray curve shows the photon counts of the solar spectrum. Green surfaces are Gaussian fits to the three bands. **c:** Vacuum referred binding energy diagram for the AlN:Eu^{3+} thin-film. Dashes for the separate 4f levels of Eu^{3+} are merely indicative and not at absolute energy scale.

an extended Sellmeier model, as presented in Chapter 5. A low Eu concentration is already indicated by the thickness measurement. If the Eu concentration was high, the shape of the thickness gradient would more follow the cosine distribution caused by the Eu source. In this case, the thickness directly follows the cosine sputtering distribution dictated by the Al source.

EDX measurements provide the local chemical composition of the gradient thin-film at 24 positions, shown by the white dots in Figure 6.3d. These measurements can be accurately fit (RMSE < 0.2 at.%) and interpolated with the surface-source evaporation equation [13] (see Chapter 4). Figure 6.3d shows the result of this fitting, with the Eu concentration varying from 0.6 at.% to 8.6 at.%. X-ray diffraction measurements (Figure 6.10) show that the AlN film has a hexagonal wurtzite structure, with a preferential growth direction.

Figure 6.4a provides the excitation-emission map taken at an arbitrary location [(x,y)=(30 mm, 40 mm)] on the film. Figure 6.4a shows that AlN:Eu^{3+} produces red emission when excited from 210 nm to 420 nm. The multiple emission lines are all resultant from 4f-4f emission of Eu^{3+}. The relative intensities

of the emission lines are the same for all excitation wavelengths, and all emission lines have the same excitation spectrum, which is a strong indication that Eu^{3+} occupies a single site within the AlN lattice. A closer look at the strongest emission at 622 nm (indicated by the blue line in Figure 6.4a), displayed in Figure 6.4b, shows that the excitation can be clearly resolved in 3 Gaussian bands. The 0.53 eV wide (FWHM) band, centered at 3.54 eV ($\sim$ 350 nm) can be attributed to the charge transfer (CT) band from the valence band of AlN to Eu^{3+} [14, 15]. The CT band is the energy required to displace an electron from a neighboring nitride (valence) anion onto Eu^{3+}, therefore providing the energy difference between the valence band and the Eu^{2+} ground state [16], shown by the arrow marked $E_{\mathrm{CT}}\left(\mathrm{N}^{3-} \rightarrow \mathrm{Eu}^{2+}\right)$ in Figure 6.4c. The 0.52 eV wide band at $E_{\mathrm{exc}} = 5.60\,\mathrm{eV}$ ($\sim$ 221 nm) can be attributed to the creation of an exciton. The optical bandgap for the thin-film AlN : Eu is 6.05 eV wide, 8 % above the exciton energy [17], in agreement with Guo and Yoshida [18].

With these properties, a vacuum referred binding energy (VRBE) diagram can be constructed [19]. Such a diagram is helpful in elucidating how the energy levels of defects compare to the same defects in other hosts. Based on what is reported for other nitride-type materials [20], the energy difference $U(\mathrm{Eu})$ between Eu^{3+} and Eu^{2+} is taken at 6.4 eV. Using the relation [21]

$$E_{\mathrm{VRBE}}(\mathrm{Eu}^{2+}) = -24.92 + \frac{18.05 - U(\mathrm{Eu})}{0.777 - 0.0353U(\mathrm{Eu})}$$

the energy level of the 4f ground state of Eu^{2+} in relation to the vacuum can be placed. This placement leads to the VRBE diagram shown in Figure 6.4c.

The 0.84 eV wide Gaussian at 4.61 eV (269 nm) is also placed in Figure 6.4c. The $O^{2-} \longrightarrow Eu^{2+}$ CT band is usually positioned around 4.7 eV in aluminates [16]. Therefore, since the thin-film is produced in an environment containing O_2, the band at 4.61 eV can most likely be attributed to the $O^{2-} \longrightarrow Eu^{2+}$ CT band.

When comparing Figure 6.3b with Figure 6.3c and Figure 6.3d, we see that the AlN:Eu^{3+} library presents local maxima in emission intensity (indicated by the white dashed line) at different thicknesses and Eu concentrations. When following the white dashed line shown in Figure 6.3b, we can observe that the thicker the film, the lower the optimum Eu concentration. These optima imply that for each thickness within the film there is a balance between quantum yield and absorption strength, as shown schematically in Figure 6.1b. To evaluate

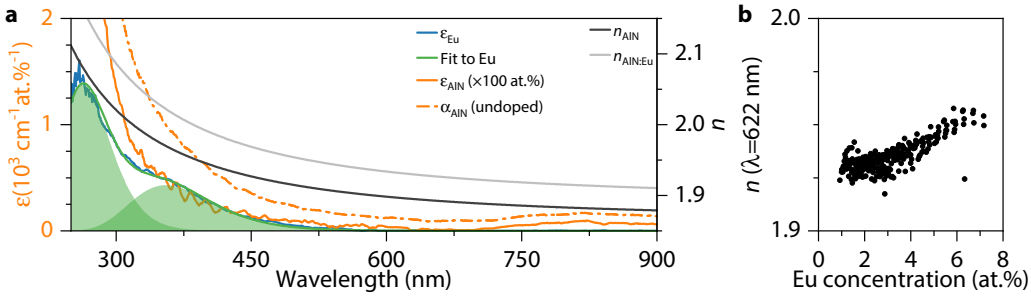


Figure 6.5: a: Average index of refraction n, molar absorption coefficients ε for all wavelengths for both undoped AlN (average adj. $R^2 = 0.94$) as well as Eu-doped AlN (average adj. $R^2 = 0.92$). α_{AlN} is the absorbance ($\varepsilon \times 100$ at.%) of AlN without a Eu doping. Green surfaces are Gaussian fits to $\varepsilon_{\mathrm{Eu}}$, with the same centers as reported in Figure 6.4b. These fits show the CT bands in the absorption of Eu. **b:** Index of refraction at 622 nm as a function of Eu concentration

if these optima translate to an optimum for LSC functionality, the absorption of light and quantum yield are resolved as a function of film thickness and Eu concentration in the next section.

To retrieve the concentration-dependent index of refraction n and molar absorption coefficient ε, the measured transmittance is fit to the thin-film transmittance equation [22] for every measured wavelength. From this equation, ε can be derived from the extinction coefficient k with

$$\varepsilon_{\mathrm{Eu}} = \frac{4\pi k_{\mathrm{Eu}}}{\lambda c_{\mathrm{Eu}}},$$

where k is assumed to scale with the Eu concentration c_{Eu} (in at.%) as

$$k = k_{\mathrm{Eu}} c_{\mathrm{Eu}} + k_{\mathrm{AlN}} (100 \text{ at.\%} - c_{\mathrm{Eu}}) \ .$$

This type of fitting yields n and ε, as presented in Figure 6.5a for both undoped and Eu-doped AlN. In the appendix (Section 6.8, Figures 6.11 and 6.12) a more in-depth explanation is given on how the fittings are done.

For undoped AlN, an index of refraction of $n = 1.90$ is found at $\lambda = 622$ nm. An increase in Eu concentration goes paired with an increase in refractive index, from $n = 1.92$ at 0.9 at.% to $n = 1.96$ at 6.7 at.% (Figure 6.5b). The molar absorption coefficient of Eu^{3+} in AlN (Figure 6.5a) shows the same bands as observed in the excitation spectrum (Figure 6.4b). The $N^{3-} \longrightarrow Eu^{2+}$ CT band at 350 nm has a molar absorption coefficient of 499 cm^{-1} at.%$^{-1}$. In absorption, the bands have

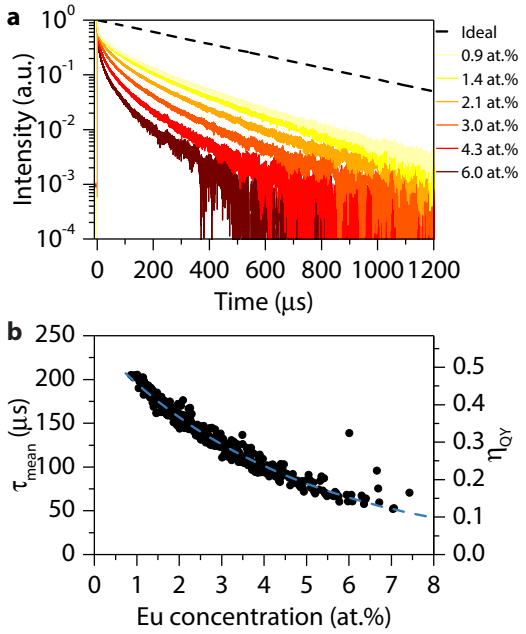


Figure 6.6: Decay times across the substrate (λ_{ex} = 350 nm). **a:** Individual decay traces for different Eu concentrations. **b:** Mean decay times for all Eu concentrations on the thin-film, with on the right y-axis the associated estimated η_{QY}. The dashed blue line shows the trend of τ_{mean}.

a different relative intensity than in excitation. This difference in intensity can come from different relaxation pathways for the different CT transitions. A different relaxation pathway goes associated with a different quantum yield, which alters the intensity of the band in excitation, where only radiative relaxation can be measured.

Figure 6.5a reveals that doping Eu in AlN slightly alters the absorption of AlN itself. AlN is mostly reported to have no absorption for wavelengths larger than 400 nm [23], while in our films the absorption extends to longer wavelengths. It might therefore be that our film contains defects that may be removed when e.g. growing the film at elevated temperatures or annealing in a N_2+H_2 atmosphere. Given the emissions as reported in Figure 6.4a, Eu exhibits no self-absorption and the emission is not absorbed by the AlN host either.

The quantum yield η_{QY} can be estimated from the decay spectra, shown in Figure 6.6a. In the first hundred nanoseconds a very quick decay can be observed. After this initial quick drop, the decay for any concentration in the library shows

strong non-exponential behavior. As seen in Figure 6.6a for selected concentrations, and in Figure 6.6b for the entire library, the decay time decreases at higher Eu concentrations. Given the faster decays at higher concentrations, this effect can be explained by concentration quenching.

The data presented in Figure 6.6b is collected at 20×20 locations across the film, which gives multiple data points for a specific concentration. These data come from areas with markedly different thicknesses. No relation between decay time and thickness is found, confirming that the decay time solely depends on the dopant concentration. The good correspondence between measured decay time and the interpolated Eu concentration (Figure 6.3d) also confirms the correctness of the EDX measurements and the usage of the source-surface evaporation equation.

To obtain η_{QY} per concentration, the decay can be compared to decays reported at much lower concentrations, where concentration quenching can be excluded. Jadwisienczak et al. [24] report a decay of $\tau = 428\,\mu\mathrm{s}$ for an AlN:Eu^{3+} thin-film doped with 5 ppm Eu. This low-concentration Eu film does not show thermal quenching of the intensity of cathodoluminescence. This implies that in the film of Jadwisienczak et al. both concentration-quenching and thermal-related quenching behavior can be excluded. Therefore, when assuming the decay of 428 µs corresponds to $\eta_{\mathrm{QY}} = 1$, η_{QY} in our thin-film can be estimated as

$$\eta_{\mathrm{QY}} = \frac{\tau_{\mathrm{mean}}}{\tau} \,,$$

with $\tau_{\mathrm{mean}} = \frac{\int_{t=0}^{\infty} tI(t)\,\mathrm{d}t}{\int_{t=0}^{\infty} I(t)\,\mathrm{d}t}$ the average decay time. This average decay time is largely uninfluenced by the fast decay in the first hundred nanoseconds, as the surface underneath the curve is negligible compared to the surface from the remaining hundreds of microseconds. Figure 6.6b shows both τ_{mean} and the estimated η_{QY}. Even for a Eu doping as low as 1 at.%, AlN:Eu^{3+} does not exceed a quantum efficiency of 50 percent. From Figure 6.6b, η_{QY} can be extrapolated to its value at 0 at.% Eu. Extrapolating the dashed curve would lead to $\eta_{\mathrm{QY}}(0\ \text{at.\%}) \neq 1$. In materials with a CT band at low energy, the CT state can overlap with the Eu^{3+} ground state [25]. This overlap with the Eu^{3+} ground state opens a temperature-independent non-radiative pathway for relaxation of the excited Eu to the ground state. In practice this means that even at 0 K, the quantum yield does not equal unity. The energy of the $N^{3-} \longrightarrow Eu^{2+}$ CT band in AlN:Eu^{3+} is relatively low

[comparable to $LaAlO_3$:Eu^{3+} (315 nm)]. It is therefore possible that, independent of temperature or Eu concentration, $\eta_{QY} \neq 1$ for AlN:Eu^{3+}. However, even for non-unity η_{QY} when $\tau_{mean} = \tau$, the method presented in this chapter is still valid. The results found here will then have to be multiplied by this non-unity quantum yield to obtain the correct efficiencies.

An optimum in optical efficiency for an AlN:Eu^{3+} LSC can now be retrieved, because the parameters required by eq. (6.1) have been determined as a function of Eu concentration and film thickness, as will be detailed in the following.

As this study concerns a thin-film, the amount of absorbed incident light cannot be calculated using geometrical optics. The transfer-matrix method [26] that takes multiple reflections at the interfaces of the thin-film into account is used to calculate how much sunlight (AM1.5g) is absorbed. The absorbance and index of refraction reported by Figure 6.5a are used to calculate the number of reflected, transmitted and absorbed solar photons. The amount of emission is calculated by multiplying the number of photons absorbed by Eu^{3+} by the estimated η_{QY} from Figure 6.6b. Eu^{3+} is assumed to be distributed randomly in the AlN host. Therefore, we can safely assume light emitted by Eu^{3+} to be transported incoherently through the thin-film and the substrate [27]. Thanks to this incoherent transport, geometrical optics can be used to calculate the light transport after emission. The amount of trapped light can be calculated by multiplying the number of emitted photons by $\eta_{trap}(\lambda = 622\ \text{nm}) = 85.5\%$. This takes both transport through the film and through the glass substrate into account. A perfect (scatter-free) waveguide is assumed: $\eta_{WG} = 1$. Since no reabsorption of Eu^{3+} is present, $\eta_{SA} = 1$ and the efficiency optimization is irrespective of the overall LSC geometry (see Chapter 3).

Figure 6.7a shows the result of this optimization. The percentages shown in Figure 6.7a are the optical efficiencies of the LSC for AM1.5g solar photons until 450 nm. These photons constitute 7.7 % of the total amount of photons in the solar spectrum. To retrieve the optical efficiency when considering the entire solar spectrum, the percentages reported in Figure 6.7a should be multiplied with a factor 0.077. Figure 6.7a reflects what was already observed in Figure 6.3b: a higher concentration of Eu^{3+}, at equal film thickness, does not have to imply a higher optical efficiency. The white curve, drawn perpendicular to the contour lines, indicates the optimum concentration per thickness. This curve follows the behavior schematically sketched in Figure 6.1b: at higher thickness, a lower Eu

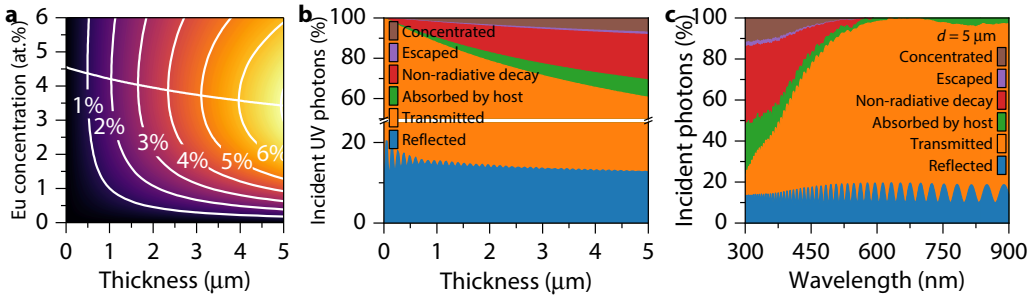


Figure 6.7: Simulated optimization of an AlN:Eu^{3+} thin-film LSC for maximal optical efficiency. **a:** Calculated optical efficiency for photons until 450 nm, as a function of both thickness and Eu concentration. The white line through the contour lines indicates the maximal optical efficiency per thickness. **b:** Eventual fate of all solar photons until 450 nm incident on the LSC, for the optimal concentrations as a function of thickness (white line in panel a). The photons that are concentrated are the photons responsible for the eventual power-output of the LSC. The oscillation between reflected and transmitted photons is a consequence of thin-film interference. **c:** Fate of incident AM1.5g solar photons for an optimized 5 µm thick film.

concentration is required to achieve optimal optical efficiency.

Figure 6.7b details the distribution of the incident AM1.5g UV photons (integrated until 450 nm) for the optimized Eu concentrations at every thickness. At film thicknesses below 2 µm, the effect of thin-film interference is evident in the transmission and reflection, with transmission being the most prevalent fate for an incident photon. With increasing film thicknesses, the reflection starts converging to what would be expected from geometrical optics, while the transmission drops drastically as a result of increased absorption. At the same time, the fraction of absorbed photons yielding luminescence increases for thicker films. This increase is a consequence of the lower Eu concentration an optimized LSC with a thicker film requires, hence resulting in less concentration quenching. However, even with this lowered quenching, only 7 % of incoming UV photons will be converted and concentrated at the LSC's edges for a 5 µm thick film.

Figure 6.7c provides a breakdown of the eventual fate of all incident solar photons for an optimized 5 µm thick LSC. The interference effect caused by a thin-film can still be clearly observed from the oscillations between transmission and reflection. The effect of the $N^{3-} \longrightarrow Eu^{2+}$ CT absorption (Figure 6.5a) can also be observed, with most absorption and conversion resulting from this band. The high absorption from this CT band (1697 cm^{-1} at 350 nm) does not counteract

the high non-radiative loss due to the low quantum yield of 27 % at 3.4 at.% Eu doping.

In an idealized case, where the dashed curve displayed in Figure 6.6b is scaled such that $\eta_{QY} = 1$ at 0 at.% Eu, illustrated in the appendix (Section 6.9, Figure 6.13), 3.4 at.% Eu doping has $\eta_{QY} = 47\%$. In this idealized case, 13 % of the incident UV photons will be concentrated at the LSC's edges for a 5 µm thick film. The goal of this study is however to present a method where experimental data from a luminescence library is used to model, understand, and optimize a thin-film LSC, not to produce an LSC of high efficiency. Even so, to put the efficiency of this simulated AlN:Eu^{3+} thin-film LSC into perspective, a comparison can be drawn to other emerging UV-absorbing LSCs without self-absorption. A recent example of such a UV-absorbing LSC are perovskite nanocrystals doped with Mn^{2+} dissolved in a polymer matrix, laminated on glass. The absorptance of these laminated nanocrystals lies between 1 to 2 cm^{-1} [4]. These perovskites have non-overlapping absorption (until 400 nm) and emissions (maximal at 600 nm), comparable to AlN:Eu^{3+}. Given the low absorptance, these perovskites require much thicker ($\sim$ 1 mm thick) films to achieve absorption equivalent to a 1 µm thick AlN:Eu^{3+} film. Even with such thick films, the nanocrystals' low quantum yields culminates into an LSC of low efficiency. Compared to these nanocrystals, rare-earth-doped thin-films show their potential as LSC due to their high absorptivity. Rare-earth-doped thin-films are compatible with industrial fabrication processes, and, with materials that exhibit a lower degree of concentration quenching, can yield an LSC with a high optical efficiency.

6.4 Conclusion

We have shown that using the deposition of a single thin-film, it is possible to calculate the thickness-dependent optimum dopant concentration of a thin-film LSC, yielding a maximized optical efficiency. As a model system, we have fabricated an AlN:Eu^{3+} library co-doped with O^{2-}. The library shows red 4f-4f emission after UV excitation and features a large thickness- and Eu^{3+} concentration gradient. Optimization shows that a 5 µm thick film performs best with 3.4 at.% Eu doping. This combination would yield an optimal optical efficiency for incoming UV light of 7 %. The fabrication and optimization method presented in this chapter can assist in quickly finding the maximally achievable performance for

a self-absorption free thin-film LSC.

6.5 Acknowledgements

The authors would like to thank P. Dorenbos and H.T. Hintzen for valuable discussions and A. Golova for proofreading the manuscript.

6.6 Appendix: Thermal Treatments

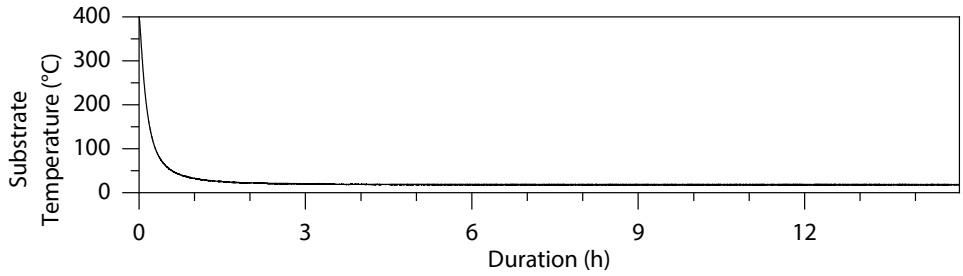


Figure 6.8: Substrate temperature during deposition.

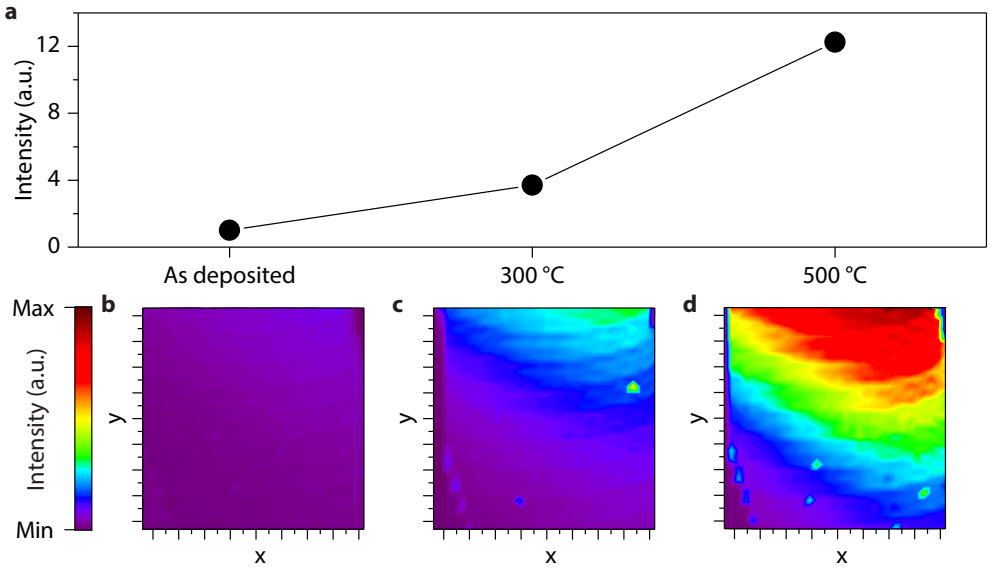


Figure 6.9: Influence of subsequent annealing for 20 min in a 9 SLM N_2 atmosphere on the luminescence intensity. **a:** Average integrated luminescence intensity after excitation at 350 nm, compared to the sample as deposited. Intensity mapping of the luminescence intensity across the sample **b:** as deposited, **c:** after treatment at 300 °C, **d:** after treatment at 500 °C. Given the LSC application, optimization was terminated at 500 °C, as higher temperatures would be incompatible with float glass.

6.7 Appendix: X-Ray Diffraction

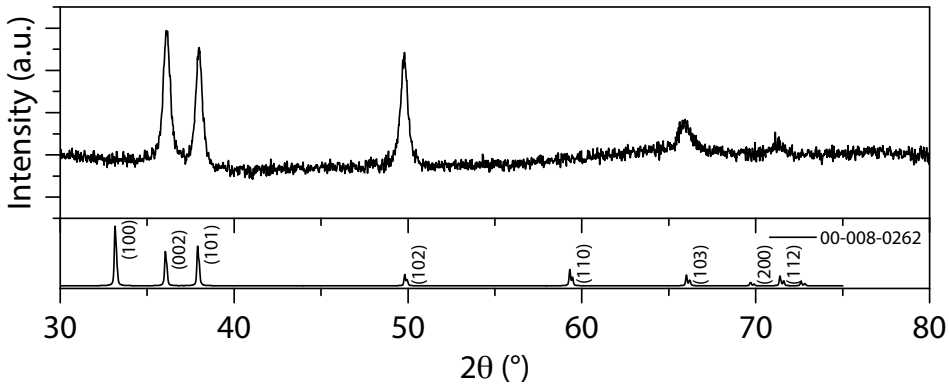


Figure 6.10: X-Ray diffractogram for the AlN:Eu^{3+} thin-film, with below the AlN reference card 00-008-0262. In parentheses the Miller indices of the planes. The absence of the (100) at $2\theta = 33.16°$ and (110) at $2\theta = 59.30°$ peaks suggests a preferential growth direction for the thin-film.

6.8 Appendix: Determination of the Complex Index of Refraction

Figure 6.11a shows the measured transmittance for a selected set of points across the film. All these points have different thicknesses d and Eu concentrations c_{Eu}, as displayed in Figure 6.11b and Figure 6.11c respectively. Since the thickness and concentration are known, all transmission values at a specific wavelength can be plotted as a function of thickness and Eu concentration on a 2D grid. This plot can be seen in Figure 6.12a for the transmission of all measured transmissions on the film at $\lambda = 350\,\mathrm{nm}$. The selected points from Figure 6.11 are also indicated here as stars, while all other transmissions are indicated with dots. The colors of these stars and dots correspond to their transmission percentage at $\lambda = 350\,\mathrm{nm}$.

As expected, both an increase in thickness and an increase in Eu concentration lead to a lowered transmittance. This relation is in first order in accordance with the Beer-Lambert law. However, since we consider a thin-film, interference effects have a large influence on the amount of transmittance, as is for instance evident from Figure 6.11a, where the waves and crests in transmission move as a function of (among others) the thickness of the film.

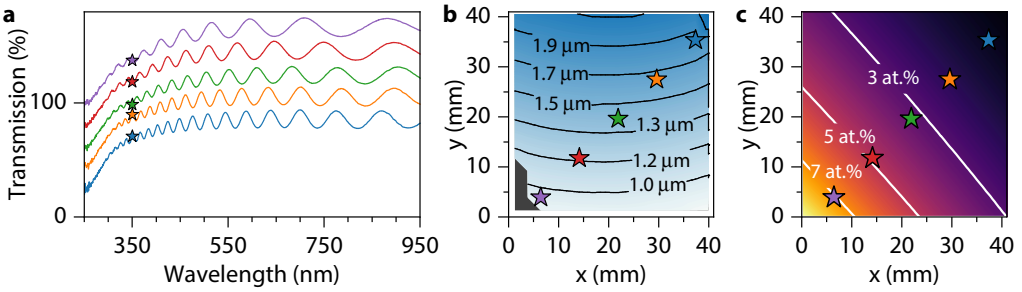


Figure 6.11: a: Transmission spectra at selected points across the sample. The scale is given for the lowest curve. All other curves are offset by 20 % relative to the curve below them. **b:** Locations on the sample for spectra in panel a as a function of sample thickness. The colors of the stars correspond to the curves in panel a. **c:** Locations on the sample for spectra in panel a as a function of Eu concentration. The colors of the stars correspond to the curves in panel a.

To determine the concentration-dependent index of refraction n and extinction coefficient k, the measured transmittance is fit to the thin-film transmittance equation [22]. As indicated in the main text, k is assumed to scale with the Eu concentration c_{Eu} (in at.%) as

$$k = k_{\mathrm{Eu}} c_{\mathrm{Eu}} + k_{\mathrm{AlN}} (100\ \text{at.\%} - c_{\mathrm{Eu}}) \ .$$

The filled area shown in Figure 6.12b shows the result of such a fitting to the thin-film transmittance equation. In this case, n, k_{Eu}, and k_{AlN} at $\lambda = 350\,\mathrm{nm}$ are yielded. This same fitting can be done for all measured wavelengths, providing the indices of refraction and extinction coefficients shown in Figure 5a of the main text.

6.9 Appendix: Idealized Luminescence Optimization

As can be seen in Figure 6.9, the luminescence intensity improves tremendously after thermal annealing. It is therefore possible that higher thermal treatments or different annealing environments reduce non-radiative relaxation pathways for the luminescence, thereby markedly improving the quantum yield. A simulation is done in the same vein as in the main text. Here we assume that the quantum yield follows the same trend as in Figure 5b, but shifted upwards such that $\eta_{\mathrm{QY}} = 1$ at 0 at.% Eu concentration (Figure 6.13a). With this assumption we do not deny the effect of concentration quenching, but see what would happen if the PL

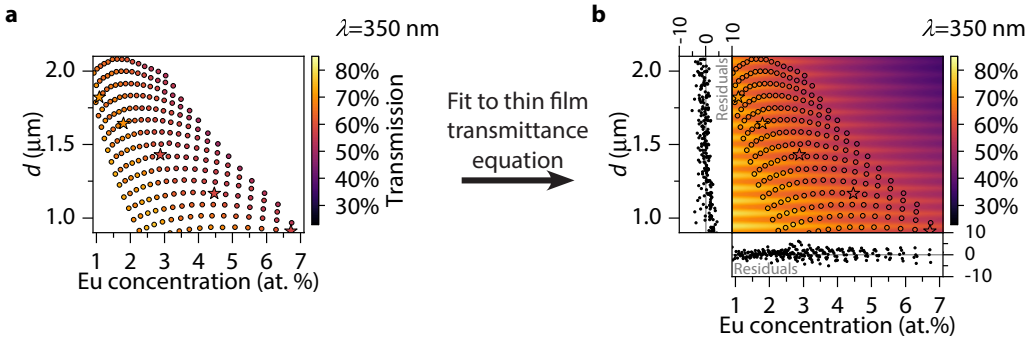


Figure 6.12: a: Measured transmittance (points) at $\lambda = 350\,\text{nm}$. The colors indicate the amount of transmittance. Stars correspond to the selected measurements displayed in Figure 6.11. **b:** Surface fit (filled area) for transmittance T at $\lambda = 350\,\text{nm}$ underneath the measured data from in panel a. The residuals after fitting ($T_{\text{measured}} - T_{\text{model}}$) for thickness and concentration are shown in the left and bottom inset, respectively.

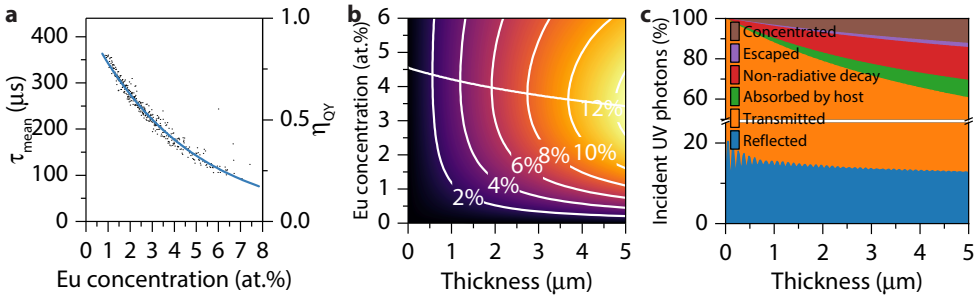


Figure 6.13: Optimization track for an idealized LSC. **a:** Quantum yield scaled such that $\eta_{\text{QY}} = 1$ at 0 at.% Eu. **b:** Calculated optical efficiency for photons until 450 nm, as a function of both thickness and Eu concentration. The white line through the contour lines indicates the maximal optical efficiency per thickness. **c:** Distribution of incident solar photons until 450 nm for the optimal concentrations as a function of thickness (white line in panel b).

intensity would improve by another factor 2. Figure 6.13b and Figure 6.13c show that this leads to the same optimal Eu concentration per thickness as reported in the main text, but in this instance a 13 % of the incident UV photons (integrated to 450 nm) will, after conversion, reach the LSC perimeter as a consequence of the higher quantum yield.

References

[1]W. H. Weber and J. Lambe, "Luminescent greenhouse collector for solar radiation.," Applied Optics **15**, 2299–2300 (1976).

[2]C. S. Erickson, L. R. Bradshaw, S. McDowall, J. D. Gilbertson, D. R. Gamelin, and D. L. Patrick, "Zero-Reabsorption Doped-Nanocrystal Luminescent Solar Concentrators," ACS Nano **8**, 3461–3467 (2014).

[3]Y. Zhao and R. R. Lunt, "Transparent Luminescent Solar Concentrators for Large-Area Solar Windows Enabled by Massive Stokes-Shift Nanocluster Phosphors," Advanced Energy Materials **3**, 1143–1148 (2013).

[4]F. Meinardi, Q. A. Akkerman, F. Bruni, S. Park, M. Mauri, Z. Dang, L. Manna, and S. Brovelli, "Doped Halide Perovskite Nanocrystals for Reabsorption-Free Luminescent Solar Concentrators," ACS Energy Letters **2**, 2368–2377 (2017).

[5]G. Bräuer, B. Szyszka, M. Vergöhl, and R. Bandorf, "Magnetron sputtering – Milestones of 30 years," Vacuum **84**, 1354–1359 (2010).

[6]M. Peres, A. Cruz, M. Soares, A. Neves, T. Monteiro, K. Lorenz, and E. Alves, "Optical and structural studies in Eu-implanted AlN films," Superlattices and Microstructures **40**, 537–544 (2006).

[7]J. B. Gruber, U. Vetter, T. Taniguchi, G. W. Burdick, H. Hofsäss, S. Chandra, and D. K. Sardar, "Spectroscopic analysis of Eu^{3+} in single-crystal hexagonal phase AlN," Journal of Applied Physics **110**, 023104 (2011).

[8]K. Wang, K. P. O'Donnell, B. Hourahine, R. W. Martin, I. M. Watson, K. Lorenz, and E. Alves, "Luminescence of Eu ions in $Al_xGa_{1-x}N$ across the entire alloy composition range," Physical Review B **80**, 125206 (2009).

[9]M. Maqbool, W. M., and M. E., "Cathodoluminescence from Amorphous and Nanocrystalline Nitride Thin Films Doped with Rare Earth and Transition Metals," in *Cathodoluminescence* (InTech, Mar. 2012).

[10]M. Maqbool, "Luminescence and Thermal Annealing of Sputtered Deposited Thulium- and Samarium-doped Amorphous AlN Films," Surface Review and Letters **12**, 767–771 (2005).

[11]D. L. Dexter and J. H. Schulman, "Theory of Concentration Quenching in Inorganic Phosphors," The Journal of Chemical Physics **22**, 1063–1070 (1954).

[12]M. L. Caldwell, P. G. Van Patten, M. E. Kordesch, and H. H. Richardson, "Visible Luminescent Activation of Amorphous AlN:Eu Thin-Film Phosphors with Oxygen," MRS Internet Journal of Nitride Semiconductor Research **6**, e13 (2001).

[13]J. D. Fowlkes, J. M. Fitz-Gerald, and P. D. Rack, "Ultraviolet emitting $(Y_{1-x}Gd_x)_2O_{3-\delta}$ thin films deposited by radio frequency magnetron sputtering: combinatorial modeling, synthesis, and rapid characterization," Thin Solid Films **510**, 68–76 (2006).

[14]P. Dorenbos and E. van der Kolk, "Location of lanthanide impurity energy levels in the III-V semiconductor $Al_xGa_{1x}N$ $(0 \leq x \leq 1)$," Optical Materials **30**, 1052–1057 (2008).

[15]T. Shibata, K. Asai, S. Sumiya, M. Mouri, M. Tanaka, O. Oda, H. Katsukawa, H. Miyake, and K. Hiramatsu, "High-quality AlN epitaxial films on (0001)-faced sapphire and 6H-SiC substrate," physica status solidi (c) **2026**, 2023–2026 (2003).

[16]P. Dorenbos, "Charge transfer bands in optical materials and related defect level location," Optical Materials **69**, 8–22 (2017).

[17]P. Dorenbos, "The Eu^{3+} charge transfer energy and the relation with the band gap of compounds," Journal of Luminescence **111**, 89–104 (2005).

[18]Q. Guo and A. Yoshida, "Temperature Dependence of Band Gap Change in InN and AlN," Japanese Journal of Applied Physics **33**, 2453–2456 (1994).

[19]P. Dorenbos and E. van der Kolk, "Lanthanide impurity level location in GaN, AlN, and ZnO," in Gallium nitride materials and devices ii, edited by H. Morkoc and C. W. Litton (Feb. 2007), p. 647313.

[20]P. Dorenbos, "Relation between Eu^{2+} and Ce^{3+} f $\rightarrow$ d-transition energies in inorganic compounds," Journal of Physics Condensed Matter **15**, 4797–4807 (2003).

[21]P. Dorenbos, "Determining binding energies of valence-band electrons in insulators and semiconductors via lanthanide spectroscopy," Physical Review B **87**, 035118 (2013).

[22]R. Swanepoel, "Determination of the thickness and optical constants of amorphous silicon," Journal of Physics E: Scientific Instruments **16**, 1214–1222 (1983).

[23]S. Adachi, *Optical Constants of Crystalline and Amorphous Semiconductors: Numerical Data and Graphical Information* (Springer US, Boston, MA, 1999), p. 714.

[24]W. M. Jadwisienczak, H. J. Lozykowski, I. Berishev, A. Bensaoula, and I. G. Brown, "Visible emission from AlN doped with Eu and Tb ions," Journal of Applied Physics **89**, 4384–4390 (2001).

[25]G. Blasse, A. Bril, and J. A. de Poorter, "Radiationless Transitions in the Eu^{3+} Center in $LaAlO_3$," The Journal of Chemical Physics **53**, 4450–4453 (1970).

[26]S. J. Byrnes, "Multilayer optical calculations," (2016).

[27]J. Gutmann, M. Peters, B. Bläsi, M. Hermle, A. Gombert, H. Zappe, and J. C. Goldschmidt, "Electromagnetic simulations of a photonic luminescent solar concentrator," Optics Express **20**, A157 (2012).

— 7 —

The Potential of Transparent Sputtered NaI:Tm^{2+}, $CaBr_2$:Tm^{2+}, and CaI_2:Tm^{2+} Thin-Films as Luminescent Solar Concentrators

In this chapter, the parameters governing the performance of a luminescent solar concentrator (LSC) are determined for sputtered thin-films of NaI:Tm^{2+}, $CaBr_2$:Tm^{2+}, and CaI_2:Tm^{2+}. These parameters are determined by using six gradient thin film material libraries, combinatorially sputtered from metallic and pressed-powder targets. These films show strong $4f^{13} \rightarrow 4f^{12}d^1$ absorption of maximally 752 cm^{-1} at.%$^{-1}$ for NaI:Tm^{2+}, 31 cm^{-1} at.%$^{-1}$ for $CaBr_2$:Tm^{2+}, and 473 cm^{-1} at.%$^{-1}$ for CaI_2:Tm^{2+} This absorption covers the entire visible spectrum and does not overlap with the infrared 4f-4f emission at 1140 nm. Decay measurements are used to estimate the quantum yields of the thin-films. These quantum yields can be as high as 44 % for NaI:Tm^{2+}, when doped with 0.3 at.% Tm. Even at doping percentages as low as 0.3 at.%, the films appear to show luminescence quenching. The concentration-dependent absorption and quantum yield are combined with the index of refraction, resolved from transmission measurements, to simulate the optical efficiency of a thin film Tm^{2+}-doped halide LSC. These simulations show that LSCs based on Tm^{2+} can display excellent color rendering indices of up to 99 %, and neutral color temperatures, between 4500 K and 6000 K. Under optimal conditions, thin-films constrained to a thickness of 10 µm and 80 % transmission of the visible spectrum, would be able to display optical efficiencies of 0.71 %. This optical efficiency compares favorably to the maximally achievable 3.5 % under these constraints. This efficiency is largely independent of the size of LSC itself.

7.1 Introduction

Halides doped with divalent thulium (Tm^{2+}) have been suggested as possible materials for a luminescent solar concentrator (LSC) [1, 2]. Some aspects of the performance of these materials have been investigated in powder form [3–10]. Until now, a full study on the applicability of these Tm^{2+}-doped halides as a luminescent solar concentrator has not yet been undertaken. To evaluate the performance of these materials, we present a combinatorial study on the LSC characteristics of some of these Tm^{2+}-doped halides. In this chapter, we will cover sputter-deposited thin-films of NaI, $CaBr_2$, and CaI_2 doped with a concentration gradient of Tm, applied directly on a glass waveguide.

LSCs are an electricity-generating replacement for window glass, commonly found in windows or facades. This type of energy-generating replacement for building materials is called building-integrated photovoltaics (BIPV). These LSCs generate electricity through a luminescent coating deposited on the window glass. This coating harvests a fraction of the incoming sunlight and converts this to luminescent light. This luminescence is isotropically emitted and therefore remains largely trapped between the coating and the window glass, due to total internal reflection. For a refractive index of $n = 1.7$, around 80 % of the emitted light remains trapped. The trapped light travels by total internal reflection to the edges of the window. At the edges, the light impinges on photovoltaic (PV) cells that face the perimeter of the window. The PV cells then convert the trapped light to electricity. Due to their electricity-generating capabilities, LSCs can become part of the building envelope to realize net-zero energy buildings, in line with goals of the European Union [11].

Much progress has already been made in the LSC community. With the advent of efficient non-toxic type-II quantum dots (QDs) that are cheap to fabricate at large scale [12], LSCs are on their way to becoming a part of the building envelope. A disadvantage of these QDs, however, is their non-uniform light absorption. These QDs typically have an absorption that shoots up towards lower wavelengths. At high QD concentrations, this non-uniform absorption of light can lead to a sepia-colored appearance of the room illuminated through the LSC.

An LSC made from glass with low absorption of near-infrared light, covered by a thin-film of Tm^{2+}-doped halides avoids this sepia coloring thanks to the

almost uniform absorption of the Tm^{2+} across the visible spectrum. Furthermore, because Tm^{2+} absorbs visible light and emits infrared light, it does not suffer from any losses due to parasitic self-absorption of its own emission. To efficiently convert this infrared emission to electricity, $CuInSe_2$ (CIS) PV cells can be used [2].

The optical efficiency of an LSC, defined as the ratio of photons incident on the LSC surface to the photons emitted at the edge, is given by [13]

$$\eta_{\text{opt}} = (1 - R)\eta_{\text{abs}}\eta_{\text{QY}}\eta_{\text{trap}}\eta_{\text{WG}}\eta_{\text{SA}}. \tag{7.1}$$

Here, $1 - R$ is the fraction of incident light coupled into the LSC, η_{abs} is the fraction of light absorbed by the luminescent particles, η_{QY} is the photoluminescent quantum yield: the ratio of the number of photons absorbed by the luminescent particle, to the number of photons emitted; η_{trap} is the trapping efficiency, which gives the fraction of light that will remain in the LSC after conversion, through total internal reflection; η_{WG} is the efficiency of the waveguide, i.e., the fraction of light that will be lost during transport to the edges of the waveguide due to scattering effects. η_{SA} is the self-absorption efficiency. This factor takes into account how the efficiency is altered by having overlapping absorption and emission.

All parameters from Eq. (7.1) can be derived from measurements on a model system. $(1 - R)\eta_{\text{abs}}\eta_{\text{trap}}$ is a function of the complex refractive index $\tilde{n}(\lambda) = n(\lambda) + ik(\lambda)$, with $n \equiv n(\lambda)$ the (real part of the) refractive index and $k \equiv k(\lambda)$ the extinction coefficient. k, in turn, is related to the molar absorption coefficient $\varepsilon(\lambda)$ through

$$\varepsilon(\lambda) = \frac{4\pi k(\lambda)}{\lambda c_{\text{Tm}}}. \tag{7.2}$$

Here, λ is the wavelength of light and c_{Tm} the concentration of the used dopant, Tm in our case.

η_{QY} is straightforward to determine when using diffuse phosphor powders. In the case of powders, one takes the ratio of integrated emission to integrated absorption of light from a known excitation source using integrating sphere measurements (see e.g., Ref.[14]). For luminescent thin-films, η_{QY} cannot be determined so directly, because of the influence of the waveguide. A way to overcome this difficulty is by measuring the mean photoluminescent decay time τ of the thin-film and taking the ratio to the decay time of a (powdered phosphor) reference of the same material with a known quantum yield $\eta_{\text{QY,ref}}$ and known

decay time τ_{ref} (see Section 7.6 for the full derivation):

$$\eta_{\text{QY}} = \frac{\tau}{\tau_{\text{ref}}} \eta_{\text{QY,ref}}. \tag{7.3}$$

Since η_{WG} is not a parameter that depends on our material, but rather on the chosen waveguide, we leave it out of consideration and assume it to be unity.

η_{SA} cannot be measured *per se*, but whether self-absorption occurs can be derived by checking if there is any overlap between the absorption and the luminescent emission of the material. Tm^{2+}-doped halides are already known to have no overlap between their absorption and emission at room temperature [1, 2, 10].

A high η_{opt} is desirable in an LSC. This high efficiency can, however, not come at a loss of the general window functionality of the LSC. If the LSC absorbs too much light or causes artificial color blindness for a sufficient η_{opt}, it will not make for a good building-integrated photovoltaic equivalent of a window [15]. To quantify how a material would serve as a window, the EN 12646:2011 standard can be taken as guideline. This guideline specifies that a European office requires a correlated color temperature (CCT) between 3000 K and 5300 K and a minimal color rendering index R_a of 80. A high CCT means that the room behind the LSC will look cooler, that is, have a bluer appearance. A low CCT means a warm appearance of the room, that is, a redder, sepia-like appearance. R_a can be calculated from the simulated transmission spectrum, expressed as a normalized spectral power distribution [16]. If the CIE 1931 xyY color coordinates are calculated from a simulated transmission spectrum (see Ref.[17, Ch. 4]), these coordinates can be translated to the CCT [16, 18].

In this chapter, we determine the optical efficiency η_{opt} of sputter-deposited thin-films of NaI, $CaBr_2$, and CaI_2, doped with a concentration gradient of Tm^{2+}. We do so by resolving the parameters constituting η_{opt}, as defined in Eq. (7.1). First, we determine the luminescent properties of our thin-films. Here the negligible self-absorption η_{SA} of Tm-doped halides is shown. Second, we determine the index of refraction $n(\lambda)$ from these luminescent films using transmission measurements to calculate reflection R and trapping efficiency η_{trap}. Third, we determine the relation between the quantum yield η_{QY} and Tm concentration c_{Tm} by comparing the thin-films to a reference powdered sample. Fourth, we determine the molar absorption coefficient $\varepsilon(\lambda)$, which will provide the absorption

efficiency η_{abs}, using transmission measurements of films with high Tm concentrations. Here $\varepsilon(\lambda)$ is checked against the previously measured excitation. Finally, the results of all these measurements are gathered to make predictions on how efficient a thin-film LSC based on the presented materials could be. These simulations are complimented with values for the color rendering index and correlated color temperature.

7.2 Methods

7.2.1 Library Synthesis

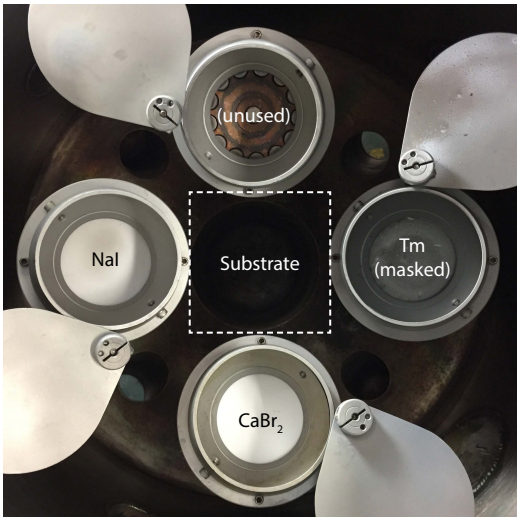


Figure 7.1: Example of the layout of the sputtering chamber. The metallic Tm target was used either with a mask on top, reducing the deposition rate for luminescent films, or without to produce highly absorbing films. For absorbing CaI_2:Tm^{2+} films, a pressed-powder CaI_2 target took the place of $CaBr_2$, and in the case of luminescent CaI_2:Tm^{2+}, the Tm target was swapped for a pressed-powder target made from a mix of 95 % CaI_2 + 5 % TmI_2.

The thulium-doped gradient thin-films (hereafter referred to as 'libraries') were combinatorially sputtered in an AJA Orion 8 magnetron sputtering system with a base pressure of 1×10^{-9} bar. A 5-cm-diameter Tm-metal target (4N, Demaco) together with a pressed-powder target (pressed at 36 MPa for 5 min), 5 cm in diameter, made from either NaI (4N, Alfa Aesar), $CaBr_2$ (2N5), Alfa Aesar), or CaI_2 (4N, Alfa Aesar), or a mix of 95 % CaI_2 + 5 % TmI_2 (3N, Sigma Aldrich)

were simultaneously RF sputtered at room temperature in a 4×10^{-2} mbar Ar atmosphere (6N, 32 standard cubic centimeters per minute flow rate) onto 5×5 cm^2 borosilicate substrates (PGO). An example of the layout of the sputtering chamber is shown in Figure 7.1. Prior to deposition, the substrates were cleaned for 15 min in an ultrasonic bath with a solution of soapy water, after which the substrates were rinsed with acetone and ethanol, followed by a 15 min ultrasonic bath of DI-water. The substrates were dried with a stream of N_2 and left to fully dry in an oven at 200 °C for more than 1 hour. The substrate and substrate carrier were heated to 100 °C in the sputtering chamber to prevent moisture contamination. No heating was applied during deposition.

The chimney of the Tm target was masked with a pattern of concentric holes, blocking part of the surface of the chimney and thereby reducing the amount of deposited Tm. The sputter parameters used for the synthesis of all libraries can be found in Table 7.1.

Table 7.1: Sputter parameters used in the synthesis of the various libraries. Two libraries are produced for each material type: One for the measurement of luminescent properties, typically with lower Tm powers applied, resulting in a film doped with 0.1–4.8 at.% Tm, indicated with (L). The other with higher Tm powers applied, yielding 4.7–54 at.% Tm doping, for determination of the absorption coefficient, indicated with (A).

Library	Power on Tm (W)	Reducing mask installed?	Power on host (W)	Duration (h)	Orientation host/Tm (see Figure 7.1)
$CaBr_2$:$Tm^{2+\,(L)}$	30	Yes	80	2	Bottom/Right
$CaBr_2$:$Tm^{2+\,(A)}$	30	No	80	1	Bottom/Right
CaI_2:$Tm^{2+\,(L)}$	50*	*	120	8	Bottom/Right
CaI_2:$Tm^{2+\,(A)}$	13	No	120	4	Bottom/Right
NaI:$Tm^{2+\,(L)}$	20	Yes	35	2	Left/Right
NaI:$Tm^{2+\,(A)}$	30	No	35	1	Left/Right

* a mixed-powder 95 % CaI_2 + 5 % TmI_2 target was used instead of the Tm metal target.

After deposition, the libraries were removed in a vacuum-tight enclosing and immediately transported to a nitrogen-filled glovebox for storage and further measurements. All powdered samples were fabricated and characterized as described in Ref. [10].

7.2.2 Luminescence

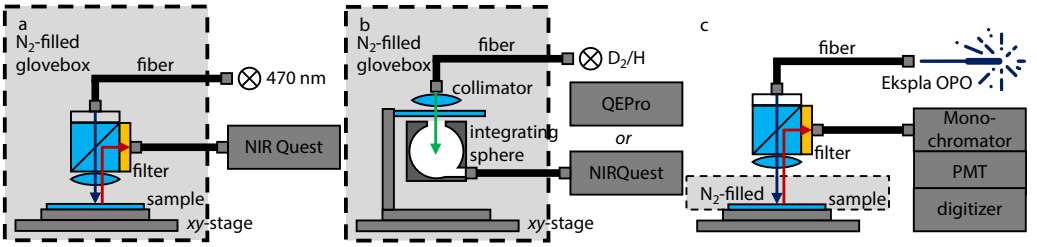


Figure 7.2: Setups used to measure local luminescent properties. **a:** Local emission setup in glovebox. **b:** Local transmission setup in glovebox. **c:** Local decay setup with custom N2-filled sample holder.

Figure 7.2a shows the setup used to record emission spectra. These spectra were recorded by exciting the library locally, using a focused 470 nm LED light source (M470L4, Thorlabs). Excitation light passed through a beam splitter, after which the light was focused on the thin-film. Luminescence was collimated using the same focusing lens. The collimated light was then reflected by the beamsplitter into a 1000 nm long-pass filter (Newport Stabilife 10CGA-1000), which was placed in front of an optical fiber connected to an Ocean Optics NIRQuest512. The *xy*-mapping of local emissions was achieved by placing the library on top of two stacked linear translation stages (LTS150/M, Thorlabs).

Emission spectra were recorded using 1×4 s integration time over 16×16 different positions, with a step size of 3.06 mm between each measurement. Prior to the measurement, the background signal was subtracted by conducting an identical measurement with the LED switched off. All emission measurements were done at room temperature (RT) in a dark nitrogen-filled glovebox.

Excitation spectra were collected at RT using a Horiba QuantaMaster QM-8075-11 spectrofluorometer with two single monochromators and an LN_2-cooled QM-NIR-IGA solid state NIR detector. Luminescence entering the NIR detector was filtered using a 1000 nm long-pass filter (Newport Stabilife 10CGA-1000). The thin-film libraries were placed in a custom sample holder for hygroscopic thin-films, with the film behind a large UV-fused silica window. The sample holder remained filled with N_2 after extraction from the glovebox.

Excitation measurements for all libraries were done in three steps: 1. Excitation from 250 nm to 600 nm with a 300 nm long pass excitation filter; 2. Excitation from 350 nm to 800 nm with a 405 nm long pass excitation filter; 3. The same

excitation spectra, but with a 800 nm long pass excitation filter to correct for stray light. Emission was recorded at 1137 nm (NaI:Tm^{2+}), or 1140 nm ($CaBr_2$:Tm^{2+}, CaI_2:Tm^{2+}).

7.2.3 Tm Concentration

The local concentration of Tm was determined using electron-dispersive X-ray spectroscopy (EDX) on a JEOL IT-100, operated at 15 keV with probing current at 70 %, under ultra-high vacuum conditions. Quantitative elemental analysis was accomplished by coating the libraries with a 30 nm thick Pd layer after all other analysis steps had been completed. Elemental compositions were quantified at 3000× magnification ($31 \times 23\,\mu m^2$ measurement area).

7.2.4 Transmission

Figure 7.2b shows the setup used to record transmission spectra. All transmission spectra were measured by placing the libraries between a 2.5 mm diameter collimated (using a Thorlabs RC02SMA-F01) deuterium-halogen (D_2/H) light beam (AvaLight-DH-S, Avantes) and the entrance port of a 5.08 cm diameter integrating sphere (IS200-4, Thorlabs). An Ocean Optics QE65Pro spectrometer (200 µm slit width) and an Ocean Optics NIRQuest512 spectrometer were connected to the off-axis detector port. The libraries were moved through the collimated beam while resting on an anodized Al sample holder, on top of two stacked linear translation stages (LTS150/M, Thorlabs).

Transmission spectra were recorded across the libraries at 10×10 positions with a step size of 4.2 mm and an integration time of 4×500 ms. Dark spectra were recorded by blocking the entrance of the integrating sphere with the edges of the sample holder. Lamp spectra were recorded by directly exposing the integrating sphere to the collimated light. The presented transmission spectra were corrected using these two reference measurements, performed with identical settings. All transmission measurements were carried out at RT in a dark nitrogen-filled glovebox.

7.2.5 Photoluminescent Decay

Decay traces were measured using the same type of setup as described for recording the local emission, shown in Figure 7.2c. In the case of decay traces, the library was excited at 430 nm using a pulsed Ekspla NT230 OPO laser, operating at 33 Hz (3–5 ns FWHM pulse width). These measurements were done at RT outside of the glovebox. To this aim, the libraries were placed in the same sample holder used for the excitation measurements. Luminescence passed through a 1000 nm long-pass filter (Newport Stabilife 10CGA-1000) into an optical fiber which was coupled into an Acton Spect-Pro2300 monochromator coupled to a Hamamatsu H1033A-75 NIR-PMT. The PMT was linked via a pulse-discriminator to a CAEN DT5724F Digitizer. This setup was used for time-correlated single photon counting.

Because of the large amount of data coming from the digitizer (40 ms of data, i.e., ~ 40 million channels of raw 12 bits data, which would mean that 1 sample can be processed per second over USB 2.0, whereas 33 samples are produced each second), the internal decimation option of the digitizer was used for online averaging. This decimation from online averaging over $7^2 = 49$ traces led to the 33 Hz laser being the limiting factor in data output. In total, each data point is an average of 2000 decay traces.

7.3 Results and Discussion

7.3.1 Local Luminescence

Figures 7.3a, 7.3d and 7.3g show the local Tm concentration for all emitting films. EDX measurements give the local chemical composition of the gradient thin-films at 36 positions. These measurements are accurately fit (RMSE < 0.31 at.%) and interpolated with the surface-source evaporation equation [19, 20]. From these fits, it follows that the Tm concentration varies from 0.29 at.% to 3.0 at.% in the NaI:Tm^{2+} film, from 0.13 at.% to 4.8 at.% in the $CaBr_2$:Tm^{2+} film, and 0.46 at.% to 4.6 at.% in the CaI_2:Tm^{2+} film.

The emission of the thin-films was measured as deposited, without any further treatment. All areas of the thin-films emit 4f-4f line emission at approximately 1140 nm after excitation at 470 nm, as seen in Figures 7.3b, 7.3e and 7.3h. Scanning over the entire thin-film concentration gradient shows that the emission

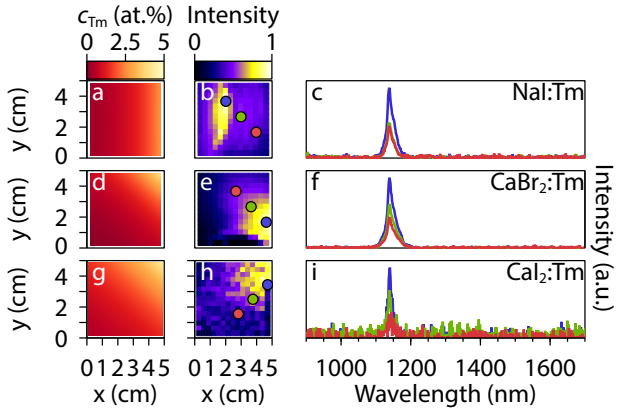


Figure 7.3: Local properties of the investigated films. **a, d, g:** Local Tm concentration c_{Tm}. **b, e, h:** Emission intensity at 1137 nm for NaI:Tm^{2+}, or 1140 nm, for $CaBr_2$:Tm^{2+} and CaI_2:Tm^{2+} after excitation at 470 nm mapped across the gradient film, normalized to the most intense emission. **c, f, i:** Emissions of the locations marked in the preceding panel. Panels a, b, c apply to the NaI:Tm^{2+} gradient thin-film; panels d, e, f apply to the $CaBr_2$:Tm^{2+} gradient thin-film; panels g, h, i apply to the CaI_2:Tm^{2+} gradient thin-film.

at 1140 nm occurs independent of concentration. While a difference in emission intensity is visible that could be correlated with the Tm concentration, this does not have to imply more efficient luminescence. The observed emission intensity is dependent on the film's local morphology (which is responsible for light scattering and thereby light collection efficiency), quantum yield, and amount of absorption. Therefore, it is necessary to individually measure the absorption strength and the quantum yield of a Tm center, as will be done in the later sections.

Figure 7.4 shows the excitation spectra (solid line) of the $^2F_{5/2}\rightarrow{}^2F_{7/2}$ Tm^{2+} emission (dashed) for (a) NaI:Tm^{2+}, (b) $CaBr_2$:Tm^{2+}, and (c) CaI_2:Tm^{2+}, with the AM 1.5g solar spectrum in the background. The excitation spectrum exhibits several $4f^{13} \rightarrow 4f^{12}5d^1$ broad-band transitions in the range of 200-800 nm. The mechanism for splitting of Tm^{2+} 4f-5d transitions and the shift of excitation wavelength in different halides is described in detail in Ref. [2]. What can be concluded from Figure 7.4 is that Tm^{2+} shows no overlap between 5d-4f excitation and f-f emission and is unlikely to show self-absorption of the emission at 1140 nm. It is still possible for self-absorption through the $^2F_{5/2}\rightarrow{}^2F_{7/2}$ transition itself to occur (f-f absorption). f-f absorption is, however, very weak, typically over 100 times weaker than the f-d absorption [2].

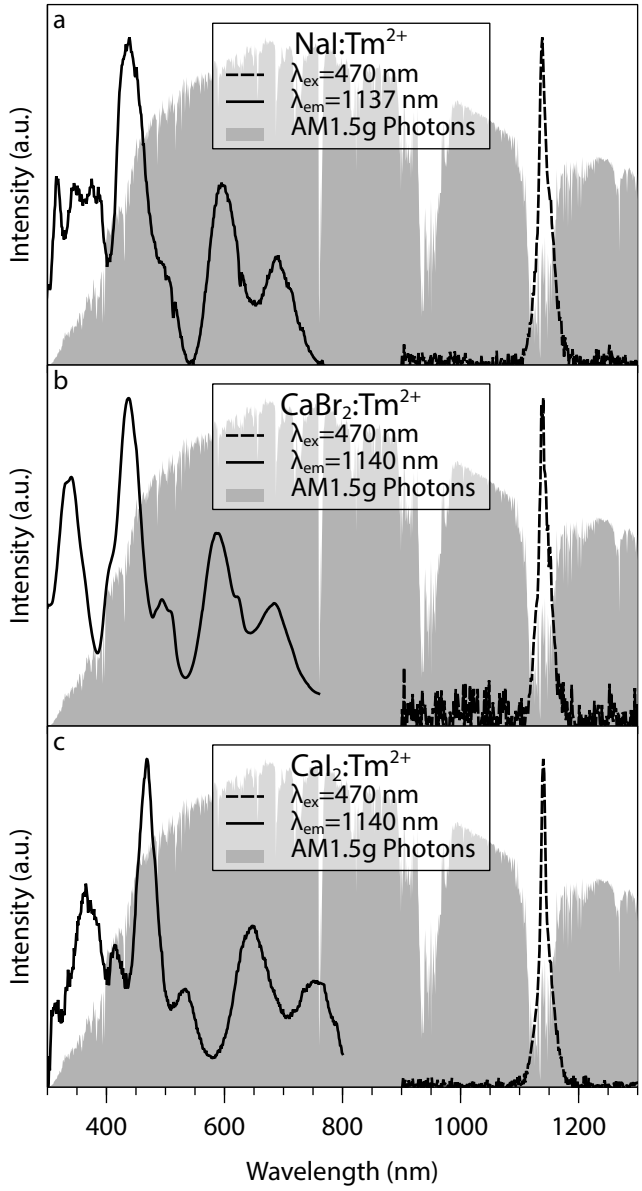


Figure 7.4: Excitation and emission spectra for **a:** NaI:Tm^{2+}, **b:** $CaBr_2$:Tm^{2+}, **c:** CaI_2:Tm^{2+} thin-films superimposed on the AM1.5g solar spectrum. All spectra clearly display the typical 4f-5d bands in excitation, which leads to the distinct $^2F_{5/2} \rightarrow {}^2F_{7/2}$ 4f-4f emission centered at approx. 1140 nm. For all materials, the 4f-5d excitation bands cover the entire visible spectrum.

7.3.2 Thickness and Index of Refraction

As written in the introduction, we are seeking to individually resolve the factors required to calculate the optical efficiency of an LSC (Eq. (7.1)). In Eq. (7.1), we first encounter the amount of reflection from the top surface R. R is a function of the complex index of refraction $\tilde{n}(\lambda) = n(\lambda) + ik(\lambda)$, as is trapping efficiency η_{trap}, later encountered in Eq. (7.1). Retrieving $\tilde{n}(\lambda)$ will thus give us both R and η_{trap}. We can locally extract $\tilde{n}(\lambda)$ from transmission spectra, by using the Extended-Sellmeier method [21, 22]. This method also gives the local thickness of the thin-film.

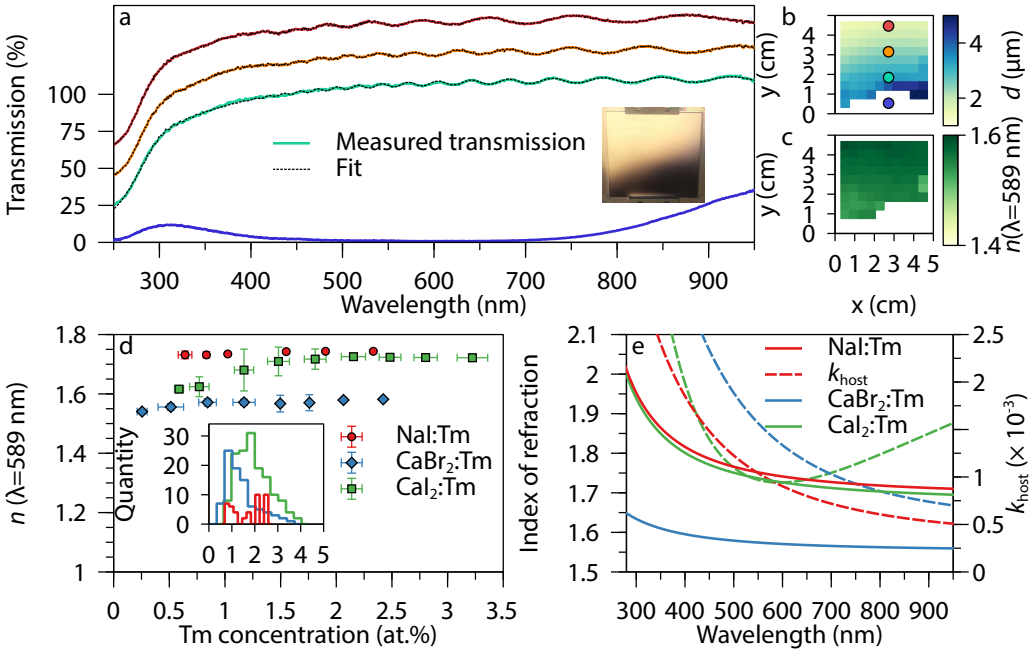


Figure 7.5: Properties extracted from fitting the local transmission of the thin-films with the Extended-Sellmeier method. **a:** Transmissions measured at the locations indicated in panel b and accompanying fits. All curves are offset from each other by 20 %. Close to the $CaBr_2$ gun, the transmission suddenly decreases (blue curve), as also visible in the inset. **b:** Thickness distribution for $CaBr_2$:Tm^{2+} in µm. The white area marks where adjusted-R^2<0.99 due to sudden high absorption of the thin-film. **c:** Local index of refraction n of the $CaBr_2$:Tm^{2+} thin-film. **d:** n for all Tm concentrations on the thin-films, grouped per concentration. The inset shows how the measured locations were distributed in these groups. Groups with less than 3 measured locations are not shown. **e:** Index of refraction (solid lines) and host extinction (dashed lines) at 1 % Tm concentration.

These fitted (adjusted-R^2>0.99) local transmission measurements, shown for

$CaBr_2$:Tm^{2+} in Figure 7.5a, agree very well with what we expected. All films show a gradient in thickness that is proportional to the distance from the sputter gun that carried the host. From Figure 7.5b, we see that the film thickness of $CaBr_2$:Tm^{2+} varies from 1.4 µm to 4.5 µm, while the refractive index (Figure 7.5c) stays relatively constant, between 1.55 and 1.58 at λ =589 nm. The refractive indices can be directly related to the concentration, using the concentration data from Figure 7.3d. Figure 7.5d shows that n rises slightly as the Tm concentration increases. The fitted n agrees well with values for other bromide-type materials, such as KBr and RbBr, with refractive indices of 1.560 and 1.553 at λ =589 nm, respectively [23]. As can be seen from Figure 7.5a, the many 5d-bands of Tm cannot be resolved from transmission data. Therefore, only the extinction coefficient of the host k_{Host} is resolved.

At very low Tm concentrations (low y in Figure 7.5b), the fit quality reduces due to a sudden decrease in transmission, caused by an intense absorption, as can be seen from the dark area on the photograph in the inset of Figure 7.5a. This absorption can be seen as the lowest, blue line in Figure 7.5a. We tentatively attribute this sudden absorption to a non-stoichiometric number of anions to cations, as is often observed when sputtering from ceramic sources in a non-reactive environment [24, p. 479], which leads to the formation of highly absorbing color centers. The locations that show this type of absorption are not included in our subsequent analysis.

For CaI_2 and NaI, the wavelength-dependent index of refraction is also shown in Figure 7.5e. The value of n at 589 nm, shown in Figure 7.5d, is around 1.75 for NaI:Tm^{2+} and around 1.73 for CaI2:Tm. These values agree well with the 1.774 reported for NaI in literature [23]. For all materials, k_{Host} is shown in Figure 7.5e. This host absorption is quite low and should therefore not be taken as a very precise fitting.

7.3.3 Photoluminescent Quantum Yield

The second parameter required to simulate LSC performance, is the concentration-dependent quantum yield $\eta_{\mathrm{QY}}(c_{\mathrm{Tm}})$. Tm^{2+}, when embedded in halides, can display many types of photoluminescent decay processes [10]. In this chapter, we are solely interested in emission from the $^2F_{5/2}\rightarrow{}^2F_{7/2}$ transition (emission at 1140 nm).

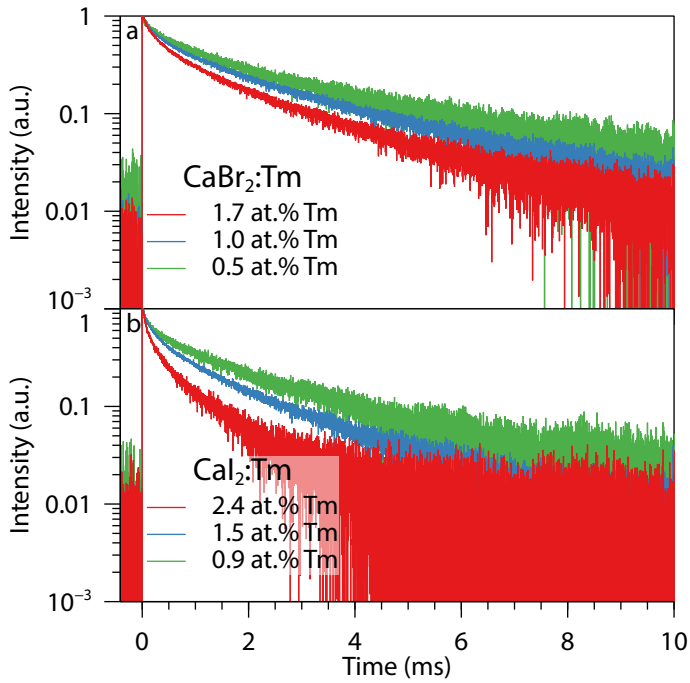


Figure 7.6: Decays of **a:** $CaBr_2$:Tm^{2+}, **b:** CaI_2:Tm^{2+}, after excitation at 430 nm at various Tm concentrations.

To determine $\eta_{QY}(c_{Tm})$, we have to know which energetic path Tm^{2+} takes to get from its excited state to the ground state. which can be done by monitoring the photoluminescent decay. In Figure 7.6, the photoluminescence decay curves are shown for the $^2F_{5/2}\rightarrow{}^2F_{7/2}$ transtition for (a) $CaBr_2$:Tm^{2+}, and (b) CaI_2:Tm^{2+}, respectively. These transitions have a decay time ranging across several milliseconds, typical for the parity-forbidden f-f transition. With higher Tm-doping, the transition becomes faster, which is most likely related to concentration quenching [25, Ch. 5].

Illumination with 430 nm light first leads to a $4f^{13} \rightarrow 4f^{12}d^1$ excitation, which can relax back to either the $^2F_{5/2}$ excited f-state, or the $^2F_{7/2}$ groundstate. Since no rise-time of the $^2F_{5/2}\rightarrow{}^2F_{7/2}$ emission is observed in $CaBr_2$:Tm^{2+} and CaI2:Tm, we do not expect there to be sufficient time for energy transfer from the excited 5d-state to neighboring ions. Thus, the non-radiative decay from the 5d-state is independent of Tm concentration. The quantum yield of our entire system is

therefore defined as:

$$\eta_{QY}(c_{Tm}) = \eta_{5d\rightarrow{}^2F_{5/2}}\eta_{QY,{}^2F_{5/2}\rightarrow{}^2F_{7/2}}(c_{Tm}),$$

with $\eta_{5d\rightarrow{}^2F_{5/2}}$ the concentration-independent quantum yield at which excited 5d-states decay back to the $^2F_{5/2}$ excited state.

If the system reaches the $^2F_{5/2}$ state, non-radiative return to the groundstate can either happen independently of Tm concentration through multiphonon relaxation, in accordance with the modified energy gap law [26], or through the aforementioned concentration quenching. The $^2F_{5/2}\rightarrow{}^2F_{7/2}$ transition is therefore described by a simple two-level system, with the non-radiative decay rate $\Gamma_{nr}(c_{Tm})$ and radiative decay rate Γ_{rad}. This gives for the quantum yield of the 4f-4f emission:

$$\eta_{QY,{}^2F_{5/2}\rightarrow{}^2F_{7/2}}(c_{Tm}) = \frac{\Gamma_{rad}}{\Gamma_{rad} + \Gamma_{nr}(c_{Tm})}.$$

In NaI:Tm^{2+}, the photoluminescent decay becomes more complicated. As seen in Figure 7.7a, when monitoring the intensity of the $^2F_{5/2}\rightarrow{}^2F_{7/2}$ emission over time, a rise-time can be observed. Contrary to what is observed for $CaBr_2$:Tm^{2+} and CaI_2:Tm^{2+}, the system appears to remain in the excited 5d-state sufficiently long for energy migration to happen. This rise-time can be attributed to a feeding from the higher lying 5d-states to the excited $^2F_{5/2}$ level. The rise-time $\tau_{rise}(c_{Tm})$ and the luminescent decay of the $^2F_{5/2}$level can be modeled as simple exponential decays, with A and B fitting constants:

$$I(t) = A\exp\left(-\frac{t}{\tau(c_{Tm})}\right) + B\exp\left(-\frac{t}{\tau_{rise}(c_{Tm})}\right). \tag{7.4}$$

As seen in Figure 7.7b, both the decay times and the rise-times decrease with an increase in Tm concentration. In this chapter, we will not go into the details of this complicated decay process. However, to still give an upper bound for $\eta_{QY}(c_{Tm})$, the fitted decay times for NaI can be treated in the same way as those for $CaBr_2$:Tm^{2+} and CaI_2:Tm^{2+}. We choose to neglect the rise-times and the impact of the system remaining longer in the excited 5d-state, and therefore assume there is no concentration quenching by energy migration in the 5d excited state.

The (assumed) concentration-independence of the non-radiative relaxation from the 5d-levels to the 4f-levels makes it possible to give an estimate of $\eta_{QY}(c_{Tm})$

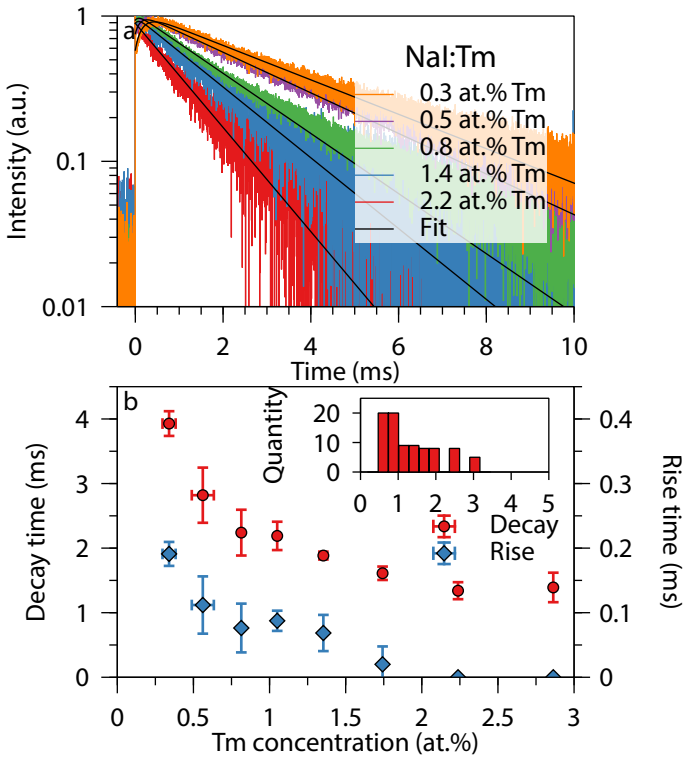


Figure 7.7: Photoluminescent decay of NaI:Tm^{2+} after excitation at 430 nm. **a:** Decay at several Tm concentrations. Black lines through the curves are fits according to Eq. (7.4). **b:** Distribution of the results of the fitting of the decay and rise-time (red dots and blue diamonds, respectively associated with the left and right vertical axes) for all Tm concentrations measured. The inset shows how the different measurements were grouped according to Tm concentration.

based on $\tau(c_{\mathrm{Tm}})$, combined with a reference measurement of $\eta_{\mathrm{QY,ref.}}$ and the mean decay time $\tau_{\mathrm{ref.}}$ from a powder made of the same material, in accordance with Eq. (7.3). These reference measurements have been made for NaI:Tm^{2+}, $CaBr_2$:Tm^{2+}, CaI_2:Tm^{2+} powders. $\tau_{\mathrm{ref.}}$ and, for $CaBr_2$:Tm^{2+} and CaI_2:Tm^{2+}, $\tau(c_{\mathrm{Tm}})$ are calculated as a mean decay time:

$$\tau = \frac{\int_0^\infty tI(t)\,\mathrm{d}t}{\int_0^\infty I(t)\,\mathrm{d}t}, \tag{7.5}$$

with $I(t)$ the luminescence intensity over time t.

For NaI:Tm^{2+}, $\tau(c_{\mathrm{Tm}})$ is the decay time presented in Figure 7.7b. $\tau_{\mathrm{ref.}}$ and $\eta_{\mathrm{QY,ref.}}$ for all powdered samples are displayed in Table 7.2.

Table 7.2: Measured mean decay times and quantum yields for powdered samples with Tm concentration $c_{Tm,ref}$. $\tau_{ref.}$ is the mean decay time of the reference powder measured at excitation wavelength $\lambda_{ex,decay}$. $\eta_{QY,ref.}$is the measured quantum yield at excitation wavelength $\lambda_{ex,QY}$.

Powdered Sample	$\lambda_{ex,decay}$ (nm)	$\tau_{ref.}$ (ms)	$\lambda_{ex,QY}$ (nm)	$\eta_{QY,ref.}$ (%)	c_{ref} (at.%)
NaI:Tm^{2+}	420	3.0	715	33.2	0.86
$CaBr_2$:Tm^{2+}	420	4.1	645	22.4	1.2
CaI_2:Tm^{2+}	475	3.7	760	28.1	0.8

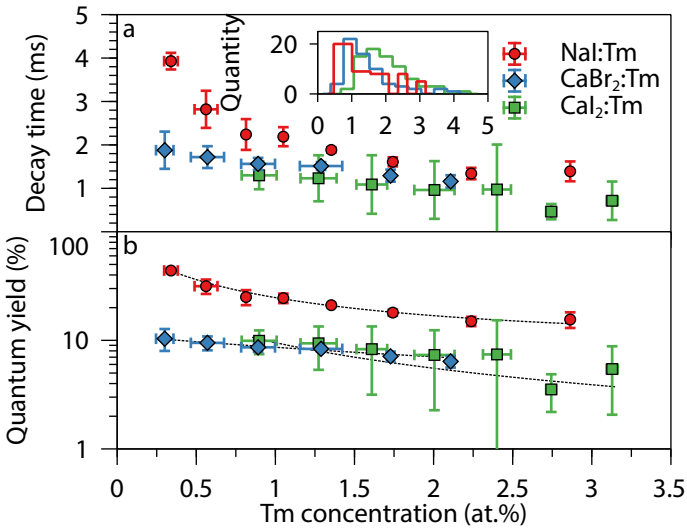


Figure 7.8: Luminescent lifetimes of all films studied. **a:** Mean decay time per concentration after excitation at 430 nm. The inset shows the distribution of Tm concentrations. Only concentrations with more than 2 measured points are shown in panels a and b. **b:** Estimated quantum yield, calculated using reference powder, following Eq. (7.3). Note that these quantum yields are an upper bound for the true quantum yield. This upper bound especially applies to NaI:Tm^{2+}, which displays rise-times from higher lying d-states. The dashed line is a best fit, following a logistic curve.

Using Eq. (7.5) and by overlaying the decay data with our previously measured data on the local c_{Tm} (Figures 7.3a, 7.3d and 7.3g), we can calculate $\tau(c_{Tm})$ for our $CaBr_2$:Tm^{2+} and CaI_2:Tm^{2+} films (see Figure 7.8a). As shown in Figure 7.8b, $\eta_{QY}(c_{Tm})$ is calculated from $\tau(c_{Tm})$ and the data from the reference powders (Table 2) using Eq. (7.3). $\eta_{QY}(c_{Tm})$ decreases from 10 % at 0.3 at.% Tm to 6.4 % at 2.1 at.% Tm in CaBr2:Tm, and from 10 % at 0.9 at.% Tm to 5.4 % at 3.1 at.% Tm in CaI2:Tm. For NaI:Tm^{2+}, $\eta_{QY}(c_{Tm})$ decreases from 44 % at 0.3 at.%

Tm, to 15 % at 2.9 at.% Tm. Because of the rise-time, the calculated quantum yields from Figure 7.8b are an upper bound for $\eta_{QY}(c_{Tm})$ of NaI:Tm^{2+}.

What should be remarked here is that for the thin-films, the decay times are consistently lower than for the powders at equal Tm concentration. At 0.8 at.%, the $^2F_{5/2} \rightarrow {}^2F_{7/2}$ transition of NaI:Tm^{2+} has a decay time of about 2.2 ms, compared to 3.0 ms in the powder. For the dihalides, at approximately equal dopant concentrations the decays are 1.5 ms and 1.3 ms, respectively for $CaBr_2$:Tm^{2+} and CaI_2:Tm^{2+} in films, and 4.1 ms and 3.7 ms, respectively in powders. This mismatch between the decay times at equal concentrations can be explained by the higher amount of defects and therefore quenching sites in the thin-films. Even though higher quantities of Tm^{2+} amend the vacancies caused by a shortage of cations, the films are not expected to be perfectly stoichiometric.

7.3.4 Absorption of Thulium

The third requirement to simulate LSC performance is the concentration-dependent absorption of our Tm-doped halides. The concentration of Tm in the luminescent libraries presented before is too low to measure absorption. Therefore, we deposited films with the same hosts, under the same synthesis conditions, but with a less dense mask on the Tm target to warrant a higher Tm deposition rate. Similar to the films with a lower Tm concentration, rasterized transmission measurements were carried out across these thin-films. The higher Tm deposition rate yields films displaying very pronounced Tm absorption. For instance, in $CaBr_2$:Tm^{2+}, seen in Figure 7.9a, we can observe that the normally gradual interference pattern (seen in Figure 7.5a for the $CaBr_2$:Tm^{2+} film with low absorption) has the characteristic Tm^{2+} 4f-5d transition spectrum (as seen in Figure 7.4b) superimposed. The sharp drop-off of the transmission below 320 nm is due to the substrate, made from borosilicate glass. The high absorption of Tm makes it impossible to use the Extended-Sellmeier method reliably for wavelengths below 600 nm. Therefore, the thickness and index of refraction of these films are determined by expanding the measured transmissions to the near-infrared. Fitting is now done in the wavelength domain from 600 nm to 1600 nm, where the libraries do not absorb. Figure 7.9a shows that this still leads to fits of high quality (average RMSE of 2.5 %). The dashed curve from the fitting can hardly be discerned from the dotted measured transition. These fits yield the local thickness

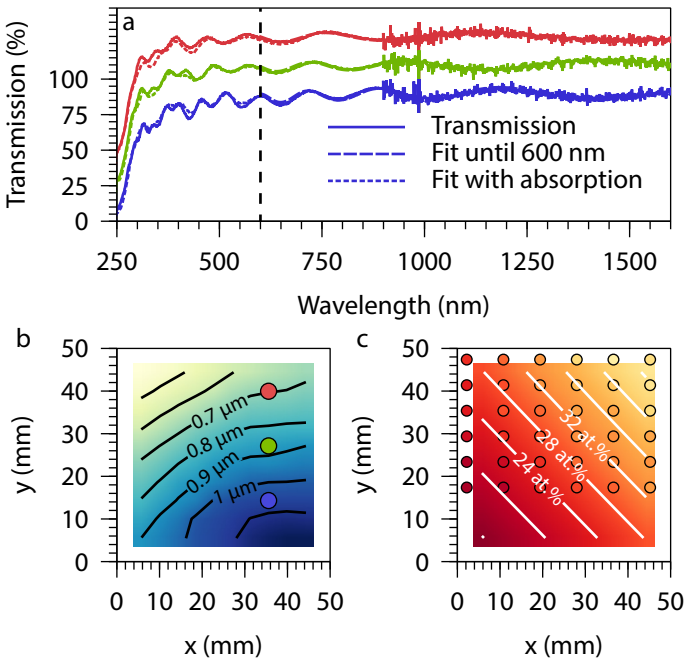


Figure 7.9: Properties of the absorbing $CaBr_2$:Tm^{2+} film. **a:** Local transmission spectra collected at locations marked in panel b. Solid lines show the measured transmission. Dashed lines show a fit to the absorption in wavelength-domain where the library does not strongly absorb, 600 nm until 1600 nm. Dotted lines show the fit that does include the absorption. For clarity, alc_{Tm}l curves are offset from each other by 20 %. **b:** Thickness of the library, as determined by fitting the transmission from 600 nm until 1600 nm. **c:** Tm concentration across the library determined by fitting the surface-source evaporation equation through local EDX measurements. Dots show the local EDX measurements. The color of those dots uses the same colormap as the contour plot of the fitted concentration. The color of the dot therefore shows the measured Tm concentration. The fit is cropped to coincide with the transmission measurement.

d, as seen for the absorbing $CaBr_2$:Tm^{2+} in Figure 7.9b.

Following the same EDX protocol as before, the local Tm concentration is determined (RMSE < 1.8 %). In these three films with a higher Tm concentration, the Tm concentration varies from 4.7 at.% to 7.4 at.% in the NaI:Tm^{2+} film, from 16 at.% to 44 at.% in the $CaBr_2$:Tm^{2+} film (see Figure 7.9c), and 45 at.% to 54 at.% in the CaI_2:Tm^{2+} film.

With d, n, k_{Host} and c_{Tm} now determined for the chosen hosts, we can utilize the minimization protocol described in the Section 7.7 and obtain the absorption coefficient $\varepsilon_{Tm}(\lambda)$. In Figure 7.10, the results of this minimization are displayed

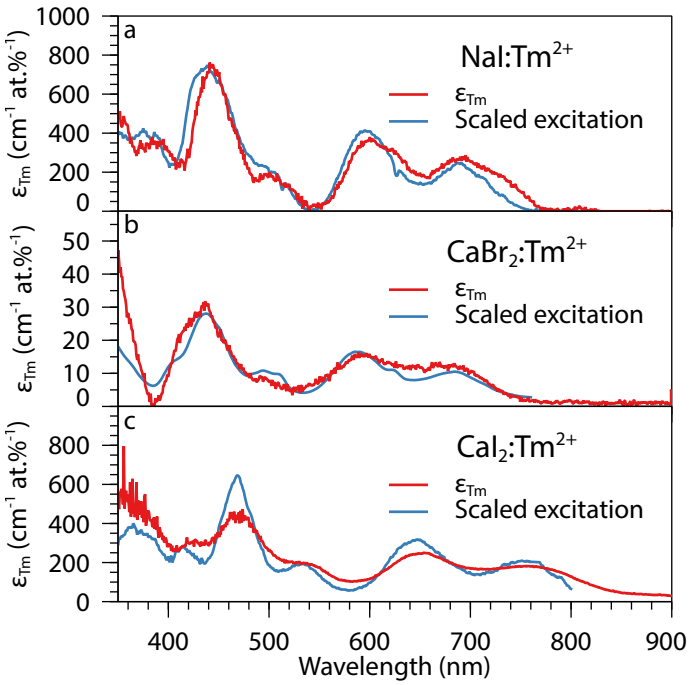


Figure 7.10: Fitted absorption strength (measured on libraries with a high Tm^{2+} concentration) of all halides under consideration compared to their respective excitation spectra (measured on libraries with a low Tm^{2+} concentration), as presented in Figure 7.4. **a:** Absorption for NaI:Tm^{2+}. **b:** Absorption for $CaBr_2$:Tm^{2+}. **c:** Absorption for CaI_2:Tm^{2+}.

for all hosts under consideration. As expected, ε_{Tm} closely follows the excitation spectrum. In a study on crystalline Tm-doped perovskites, high f-d absorption strengths of hundreds of cm^{-1} at.$\%^{-1}$ were found [7]. In our current study, we find similarly large values, but then measured through thin-film transmission using a wide range of concentrations. In the visible spectrum, from 400 nm to 750 nm, NaI:Tm^{2+} has a visible absorption maximum of 752 cm^{-1} at.$\%^{-1}$ at 444 nm, $CaBr_2$:Tm^{2+} 31 cm^{-1} at.$\%^{-1}$ at 437 nm, and CaI_2:Tm^{2+} 473 cm^{-1} at.$\%^{-1}$ at 472 nm. The cause of the lower absorption of $CaBr_2$:Tm^{2+} compared to the other halides is beyond the scope of this study.

7.3.5 Prognosis for a Luminescent Solar Concentrator

We now have all parameters required to simulate the optical efficiency of a thin-film LSC without self-absorption, for any desired Tm concentration and thickness. To simulate this LSC, we can follow a protocol similar to the one presented

in Ref. [22]. Using the transfer matrix method, implemented by using the free open-source `tmm` module [27], the reflection $R(\lambda, c_{\mathrm{Tm}}, d)$ and transmission $T(\lambda, c_{\mathrm{Tm}}, d)$ of an LSC comprising a film of thickness d coated on 5 mm thick BOROFLOAT®33 glass is calculated. BOROFLOAT is chosen as substrate, since it has negligible absorption at the emission wavelength of Tm. For the thin-film, the complex index of refraction

$$\tilde{n}(\lambda, c_{\mathrm{Tm}}) = n(\lambda, c_{\mathrm{Tm}}) + ik(\lambda) \times c_{\mathrm{Tm}}$$

is used, with $n(\lambda, c_{\mathrm{Tm}})$ as presented in Figures 7.5b and 7.5c, and $k(\lambda)$ as presented in Figure 7.10, calculated with Eq. (7.2). These numbers are converted to fractions of the AM1.5g solar spectrum $S_{\mathrm{AM1.5g}}(\lambda)$, with

$$T_{\mathrm{total}}(d, c_{\mathrm{Tm}}) = \frac{\int_0^\infty S_{\mathrm{AM1.5g}}(\lambda) T(\lambda, d, c_{\mathrm{Tm}})\, \mathrm{d}\lambda}{\int_0^\infty S_{\mathrm{AM1.5g}}(\lambda)\, \mathrm{d}\lambda}.$$

The total amount of reflection $R_{\mathrm{total}}(d, c_{\mathrm{Tm}})$ is calculated analogously.

Absorption is calculated as

$$A_{\mathrm{total}}(d, c_{\mathrm{Tm}}) = 1 - T_{\mathrm{total}}(d, c_{\mathrm{Tm}}) - R_{\mathrm{total}}(d, c_{\mathrm{Tm}}).$$

All absorbed light is converted with the fitted quantum yield $\eta_{\mathrm{QY}}(c_{\mathrm{Tm}})$ from Figure 7.8b. This converted light is then concentrated to the perimeter of the LSC. Since our films do not exhibit self-absorption, the amount of concentrated light can be calculated by multiplying the amount of converted light $I_{\mathrm{converted}}(d, c_{\mathrm{Tm}})$ with the trapping efficiency [28]

$$\eta_{\mathrm{trap}}(\lambda, c_{\mathrm{Tm}}) = \frac{\sqrt{n(\lambda, c_{\mathrm{Tm}})^2 - 1}}{n(\lambda, c_{\mathrm{Tm}})},$$

yielding the optical efficiency

$$\eta_{\mathrm{opt}}(d, c_{\mathrm{Tm}}) = A_{\mathrm{total}}(d, c_{\mathrm{Tm}}) \eta_{\mathrm{QY}}(d, c_{\mathrm{Tm}}) \eta_{\mathrm{trap}}(\lambda = 1140\,\mathrm{nm}, c_{\mathrm{Tm}}).$$

Since our films do not exhibit self-absorption, the calculated $\eta_{\mathrm{opt}}(d, c_{\mathrm{Tm}})$ is the same for every planar size of the LSC, assuming no further waveguide losses.

If the Tm concentration is sufficiently low that no concentration quenching is occurs, the only limitations on η_{opt} of the halide systems would be the total absorption of the thin-film, and the loss channels present in the single ion $\eta_{\text{QY}}(c_{\text{Tm}} \to 0)$. In the presented systems, at an absorption of 80 % of the visible spectrum, that would imply a maximal $\frac{\eta_{\text{opt}}}{\eta_{\text{QY}}(c_{\text{Tm}} \to 0)} = A_{\text{total}}\eta_{\text{trap}}$ of 3.5 % for NaI:Tm^{2+}, 3.9 % for $CaBr_2$:Tm^{2+}, and 4.2 % for CaI_2:Tm^{2+}. For films with a constraint on thickness however, a balance must be struck between the absorption and quantum yield.

For our simulation, we have chosen three situations: a thin-film LSC with

1. A thickness of at most 10 µm.

2. An additional constraint of at least 80 % transmission of the visible spectrum, expressed in photons

$$T_{\text{vis}}(d, c_{\text{Tm}}) = \frac{\int_{\lambda=380\text{ nm}}^{780\text{ nm}} S_{\text{AM1.5g}}(\lambda) T(\lambda, d, c_{\text{Tm}})\, \mathrm{d}\lambda}{\int_{\lambda=380\text{ nm}}^{780\text{ nm}} S_{\text{AM1.5g}}(\lambda)\, \mathrm{d}\lambda} = 0.8.$$

3. The same conditions as the previous simulations, but with the decays scaled such that all films perform equal to their powdered counterparts, i.e., instead of using Eq. (7.3), we state that

$$\eta_{\text{QY,film}}(c_{\text{Tm}}) = \frac{\tau_{\text{film}}(c_{\text{Tm}})}{\tau_{\text{film}}(c_{\text{Tm,ref}})} \eta_{\text{QY,powder}}(c_{\text{Tm,ref}})\,.$$

With regards to the situations, a constraint for a thickness of 10 µm is chosen to remain within what is achievable for the used sputter system. As films become thicker, the amount of stress in the film increases, therefore so does the chance of delamination. Therefore, a thin-film is preferred over a thicker film.

Table 3 shows these results for the final η_{opt}, CCT and R_a for the first situation, where the film thickness is limited to 10 µm. From Table 7.3, we can see that a 10 µm halide thin-film, as sputtered, can maximally achieve η_{opt} = 0.35% for a NaI:Tm^{2+} thin-film, with a doping of 1.6 at.% Tm, while retaining an excellent CCT and R_a. Here we do have to remark that NaI:Tm^{2+} has a $\eta_{\text{QY}}(c_{\text{Tm}})$ that is estimated to be on the high end, by neglecting the rise-time phenomena.

Table 7.3: Results of simulating thin-film LSCs coated on 1 mm thick BOROFLOAT®33 glass with a thickness constraint of 10 µm.

Material	d (µm)	c_{Tm} (at.%)	T (%)	η_{opt} (%)	CCT (K)	R_a
NaI:Tm^{2+}	10	1.6	80	0.35	5301	96
$CaBr_2$:Tm^{2+}	10	2.1	90	0.03	5820	99
CaI_2:Tm^{2+}	10	1.8	62	0.30	4586	90

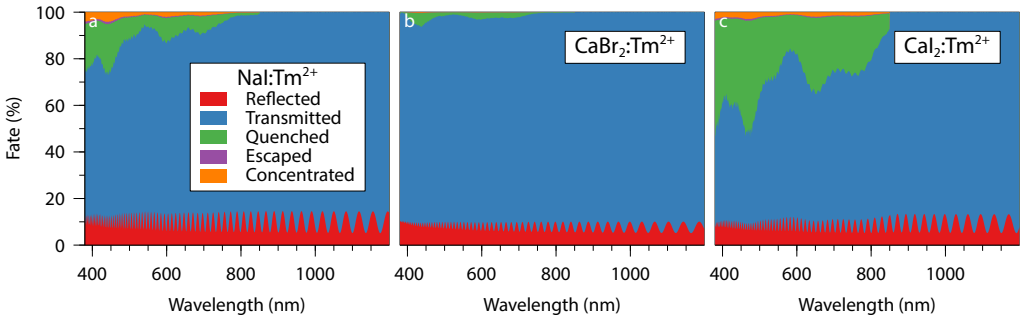


Figure 7.11: Fates of all incident photons for the best performing simulated halide thin-film LSCs with a coating thickness of 10 µm and no constraints on the total transmission. **a:** NaI:Tm^{2+}, **b:** $CaBr_2$:Tm^{2+}, **c:** CaI_2:Tm^{2+}.

In Figure 7.11, the fates of all photons incident on the simulated LSCs are shown. In the best performing NaI:Tm^{2+} (Figure 7.11a), most light is lost to reflection (9.9 % of all sunlight, including ultraviolet and infrared) and transmission (87.9 %). At this thickness, the absorption could be increased, but that would come at a loss of quantum yield, which would not be compensated by the increased absorption. Due to the non-unity quantum yield, 80.5 % of absorbed light (1.8 % of all light) is lost by quenching. After this conversion step, still 3.7 % of the absorbed light (0.08 % of all light) escapes. Eventually, 15.8 % of the absorbed light will be concentrated to the edges of the window. Increasing the quantum yield is therefore key for this material.

From Figure 7.11, the differences between the three simulated films and their performances become clear. While CaI_2:Tm^{2+} (Figure 7.11c) has the lowest $\eta_{QY}(c_{Tm})$ of all three sputtered halides, the high absorption makes it possible to achieve a η_{opt} that is higher than for $CaBr_2$:Tm^{2+} (Figure 7.11b), at the same thickness. This high absorption does come with a loss of R_a and CCT. Whereas the other thin-film LSCs retain CCTs of 5000–6000 K and almost perfect R_a, in

the case CaI_2:Tm^{2+}, the high absorption of the blue wavelengths leads to warmer coloring of 4586 K, and an R_a of 90.

Table 7.4: Simulation outcome with the additional constraint of 80 % transmission applied. The last two entries are provided for comparison. These entries show simulated high-performance LSCs consisting of a $100 \times 100 \times 0.5\,cm^3$ PMMA waveguide, with non-scattering luminescent particles dispersed within.

Material	d (µm)	c_{Tm} (at.%)	T (%)	η_{opt} (%)	CCT (K)	R_a
NaI:Tm^{2+}	10	1.6	80	0.35	5301	96
$CaBr_2$:Tm^{2+}	10	2.1	90	0.03	5820	99
CaI_2:Tm^{2+}	7	0.9	80	0.18	5342	96
Red305 [29, 30]	5.0×10^3	-	80	3.5	5077	66
$CuInS_2$/ZnS [30, 31]	5.0×10^3	-	80	2.8	4868	98

Table 7.4 shows what happens when further constraining the film to transmit 80 % of the visible spectrum. Such constraints on transmission better emulate what would be applicable as a BIPV window. The additional constraint causes CaI_2:Tm^{2+} to drop in efficiency. Due to its high absorption coefficient, a reduction in absorption is only possible when both the film thickness and Tm concentration drop significantly. Even though a lower Tm concentration implies less concentration quenching and therefore a higher quantum yield, this is not enough to offset the decrease in efficiency that CaI_2:Tm^{2+} would gain from having high absorption. The other halides already showed 80 % transmission as optimal for 10 µm, therefore the simulation results for those are identical to the ones presented in Table 7.3.

Table 7.4 provides a comparison of the LSCs studied in this chapter to $100 \times 100 \times 0.5\,cm^3$ PMMA plates with BASF Lumogen F Red 305 (Red305) or $CuInS_2$/ZnS colloidal quantum dots (QDs) dispersed within, held to the same constraint of 80 % transmission. Red305 features unity quantum yield [29], and the $CuInS_2$/ZnS QDs has a quantum yield of 66 % when dispersed in a waveguide [31]. Even though these LSCs show self-absorption, their high quantum yields let them reach much higher efficiencies than the optical efficiencies observed in the halides under study.

Table 7.5 shows the results of the same types of simulations, but then for the final situation. Here, the quantum yields of the films are scaled so that they

Table 7.5: Results of simulating 10 µm thick thin-film LSCs coated on BOROFLOAT®33 glass, 1 mm in thickness. The quantum yields of the Tm^{2+} are scaled so that at equal concentrations, films and powders perform the same.

Material	d (µm)	c_{Tm} (at.%)	T (%)	η_{opt} (%)	CCT (K)	R_a
NaI:Tm^{2+}	10	1.6	80	0.71	5301	96
$CaBr_2$:Tm^{2+}	10	2.1	90	0.07	5820	99
CaI_2:Tm^{2+}	10	1.8	62	0.39	4586	90
CaI_2:Tm^{2+}	7	0.9	80	0.24	5342	96

perform equal to their powdered counterparts at the same concentration, but retain the concentration quenching behavior measured in the thin-films. Due to the much increased quantum yield of NaI:Tm^{2+}, its optical efficiency as a 10 µm thick coating doubles, from 0.35 % to 0.71 %. This doubling in efficiency is also seen for $CaBr_2$:Tm^{2+}, but its low absorption causes it to still display the lowest η_{opt}. At these raised quantum yields, the halide thin-films can be seen as good competitors to the Red305 dye, as well as to the $CuInS_2$/ZnS QDs. Even though the efficiencies for the halide LSCs are not as high, their excellent color rendering indices and neutral CCT still make them suitable for integration in the built environment.

7.4 Conclusion

NaI, $CaBr_2$, and CaI_2 doped with Tm^{2+}, that have previously been suggested as materials for a thin-film LSC, have in this chapter been investigated on their potential as LSCs. These films prove viable as LSC materials, absorbing the entire visible spectrum and emitting at 1140 nm, without self-absorption. When sputtered from separate targets, with one target containing the host, and another containing the Tm dopant, substoichiometry of the deposited films can be observed, expressed as deep absorption. The large number of defects in the thin-films can explain the lower decay times, and therefore lower quantum yield of the films, when compared to powders made from the same materials. All films under investigation show quenching of luminescence, even at concentrations as low as 0.3 at.% Tm.

NaI:Tm^{2+} and CaI_2:Tm^{2+} show high absorptions of respectively 752 cm^{-1} at.%$^{-1}$, and 473 cm^{-1} at.%$^{-1}$. In the case of NaI:Tm^{2+}, this leads to the highest simulated LSC optical efficiency of 0.35 % (15.8 % concentration of all absorbed light), at 80 % visible light transmission, using the measured data from thin-films. In the absence of defects caused by sputtering, this efficiency can rise to 0.71 % (31.5 % concentration of all absorbed light), compared to a maximally achievable optical efficiency of 3.5 %. A challenge for future research is therefore to resolve the defects present in the films, and thus increase the quantum yield. This could be achieved with post-synthesis treatment of the film in a gas of the missing component. Another option would to fabricate the film through evaporation from a premixed target, instead of sputter deposition. This evaporation synthesis would be usable for the finalized LSC with optimal composition, since evaporating from a single target leads to a film that is homogenous in composition. Depositing the film using evaporation can also lead to much faster deposition, which would assist with viability for larger scale applications.

The excellent color rendering indices ($R_a > 90$), neutral CCT between 5000 and 6000 K, and lack of self-absorption make that Tm-doped halide LSCs can find use in the built environment as large scale LSCs, when covered with a suitable sealant.

7.5 Acknowledgements

The authors would like to acknowledge Vasilii M. Khanin for the fruitful discussions and the careful proofreading of the manuscript. This work was supported by the Netherlands Organization for Scientific Research (NWO/OCW) as part of the LumiCon project (15024).

7.6 Appendix: Relation Mean Decay Time and Photoluminescent Quantum Yield

Assuming that the process of luminescence can be modeled as a simple two-level system, a certain quantity of centers $N(t)$ will occupy the excited state at a time t after excitation of a material with a single type of identical luminescent centers. These centers can leave the excited state under emission of a photon at (time independent) rate Γ_{rad}, or non-radiatively, at rate Γ_{nonrad}. Therefore, the time evolution of the number of excited states is described with

$$\frac{\mathrm{d}N}{\mathrm{d}t} = -N(t)(\Gamma_{\text{rad}} + \Gamma_{\text{nonrad}}).$$

Solving this differential equation gives us

$$N(t) = N(0)e^{-(\Gamma_{\text{rad}}+\Gamma_{\text{nonrad}})t}, \tag{7.6}$$

with $N(0)$ the number of excited centers just after excitation.

The luminescence intensity $I(t)$ only depends on the generation of photons. Therefore

$$I(t) = -\frac{\mathrm{dN_{rad}}}{\mathrm{d}t} = N(t)\Gamma_{\text{rad}}.$$

Filling in the expression for $N(t)$ found in Eq. (7.6) yields

$$I(t) = N(0)\Gamma_{\text{rad}}e^{-(\Gamma_{\text{rad}}+\Gamma_{\text{nonrad}})t}.$$

This yields, if we integrate this over all time, yields

$$\int_0^\infty I(t)\mathrm{d}t = N(0)\frac{\Gamma_{\text{rad}}}{\Gamma_{\text{rad}} + \Gamma_{\text{nonrad}}} = N(0)\eta_{\text{QY}}.$$

In practical materials, a case can be made for identical isolated luminescent centers when the dopant concentration is sufficiently low. In such materials, it is safe to assume that each luminescent center has the same surroundings and therefore behaves identical to one another. This implies that the quantum yield and mean decay time are related to each other in such a material. The mean decay time τ_{mean} is defined as the first moment of the intensity:

$$\tau_{\text{mean}} = \frac{\int_0^\infty tI(t)\mathrm{d}t}{\int_0^\infty I(t)\mathrm{d}t}.$$

For single exponential decay of isolated luminescent centers

$$\tau_{\text{mean,isolated}} = \frac{1}{\Gamma_{\text{rad}} + \Gamma_{\text{nonrad}}}.$$

Therefore, if both the photoluminescent decay and the quantum yield have been independently measured, we can solve for Γ_{rad}:

$$\Gamma_{\text{rad}} = \frac{\eta_{\text{QY}}}{\tau_{\text{mean, isolated}}}. \tag{7.7}$$

In an imperfect crystal, it is possible for some of these centers to have slightly different surroundings. These surroundings can contain what is referred to as a 'killer site' [25]. If such a site is sufficiently close to the luminescent center, energy from the excited luminescent center can be transferred to the killer site, whereupon the luminescence has a high probability of quenching. In practice, this causes the probability for non-radiative decay to increase for this luminescent center, which is expressed as an increase of $\Gamma_{\text{nonrad},i}$ for this center i.[1]

Energy can not only be transferred between luminescent centers and killer sites, but also between luminescent centers themselves. If the local concentration of luminescent centers is sufficiently high, with one of these centers bordering a killer site, it is possible for the excited energy to be transferred amongst the centers. Eventually, this energy can end up at the center bordering the killer site, leading to quenching of the luminescence. Again, this quenching of the luminescence is expressed as an increase of $\Gamma_{\text{nonrad},i}$. This phenomenon is commonly referred to as 'concentration quenching' [25].

In a macroscopic material, several clusters of luminescent centers will be present. Each of these clusters can be characterized as having a specific non-radiative decay rate. Given a discrete distribution of clusters, where the concentration of these clusters is described with c_i, the observed intensity of light

$$I(t) = N(0)\Gamma_{\text{rad}} e^{-\Gamma_{\text{rad}} t} \sum_i c_i e^{-\Gamma_{\text{nonrad},i} t}.$$

In this case,

$$\tau_{\text{mean}} = \sum_i c_i \frac{1}{\Gamma_{\text{rad}} + \Gamma_{\text{nonrad},i}}. \tag{7.8}$$

[1] The core assumption here is that Γ_{rad} is the same for all luminescent centers of the same species. There are examples where this is not the case and the local density of states of a material is sufficiently different for all luminescent centers, such that all centers carry a different Γ_{rad} [32].

If the quantum yield of a system with isolated luminescent centers $\eta_{\mathrm{QY,isolated}}$ of the same species in the same host, as well as its $\tau_{\mathrm{mean,isolated}}$, is known, then η_{QY} of a system with clusters is easily calculated from Eq. (7.7) and Eq. (7.8):

$$\eta_{\mathrm{QY}} = \frac{\tau_{\mathrm{mean}}}{\tau_{\mathrm{mean,isolated}}} \eta_{\mathrm{QY,isolated}}. \tag{7.9}$$

Using this same logic, it is possible to get a relative estimate of the efficiency of a material, even if $\eta_{\mathrm{QY,isolated}}$ is not known. Using Eq. (7.9), we can relate the $\eta_{\mathrm{QY,ref.}}$ and $\tau_{\mathrm{mean,ref.}}$ of a known reference system, to those of an unknown system, as long as these are for the same material:

$$\eta_{\mathrm{QY}} = \frac{\tau_{\mathrm{mean}}}{\tau_{\mathrm{mean,ref.}}} \eta_{\mathrm{QY,ref.}}$$

If no reference is available, we can use the fact that Γ_{nonrad} for an isolated center is always equal or lower than that of a cluster of luminescent centers. At the end of a decay trace (given sufficient signal) only the decay of isolated centers will be measured. Fitting this tail of the decay with a single exponential will therefore yield $\tau_{\mathrm{mean,isolated}}$. The ratio of τ_{mean} and the fitted $\tau_{\mathrm{mean,isolated}}$ can then be taken to give a measure for how close to $\eta_{\mathrm{QY,isolated}}$ the material is.

7.7 Appendix: Determining the Molar Absorption Coefficient of Rare-Earth-Doped Thin-Films in Wide-Bandgap Insulators

If the local dopant concentration of a thin-film with a gradient in dopant concentration is known, and the film presents appreciable absorption in one wavelength range, but leaves another range unaffected, then it is possible to acquire the molar absorption coefficient $\varepsilon_{\mathrm{Tm}}(\lambda)$ of that dopant in the host in question.[2] If also the excitation of the host is known, it makes acquiring a good fit even easier. To determine $\varepsilon_{\mathrm{Tm}}(\lambda)$, we assume that the extinction coefficient k linearly depends on the dopant concentration c_{Tm}:

$$k(\lambda, c_{\mathrm{Tm}}) = k_{\mathrm{Tm}}(\lambda)\, c_{\mathrm{Tm}} + k_{\mathrm{Host}}(\lambda)(1 - c_{\mathrm{Tm}}), \tag{7.10}$$

[2] This is a general derivation, but because the main text uses Tm as a dopant, Tm is used as subscript for the dopant.

where

$$\varepsilon_{\mathrm{Tm}}(\lambda) = \frac{4\pi k_{\mathrm{Tm}}(\lambda)}{\lambda c_{\mathrm{Tm}}}. \tag{7.11}$$

is the molar absorption we eventually want to calculate.

From the thin-film transmission equation, as written by Swanepoel [33]:

$$T = \frac{Ax}{B - Cx + Dx^2}, \tag{7.12}$$

with

$$\begin{aligned}
A &= 16 n_s (n^2 + k^2), \\
B &= \left[(n+1)^2 + k^2\right]\left[(n+1)(n+n_s^2) + k^2\right], \\
C &= \left[(n^2 - 1 + k^2)(n^2 - n_s^2 + k^2) - 2k^2(n_s^2 + 1)\right] 2\cos\phi \\
&\quad - k\left[2(n^2 - n_s^2 + k^2) + (n_s^2 + 1)(n^2 - 1 + k^2)\right] 2\sin\phi, \\
D &= \left[(n-1)^2 + k^2\right]\left[(n-1)(n-n_s^2) + k^2\right], \\
\phi &= \frac{4\pi n d}{\lambda}, \\
x &= \exp(-\alpha d),
\end{aligned} \tag{7.13}$$

we see that the transmission of a thin-film coated on top of a non-absorbing substrate T is a function of the index of refraction of the film itself n and the substrate n_s, the extinction coefficient of the thin-film k and the thickness of the thin-film d.

When combining Eqs. (7.12) and (7.13) with Eqs. (7.10) and (7.11) we can see that $T \equiv T(n, c_{\mathrm{Tm}}, \varepsilon_{\mathrm{Tm}}, k_{\mathrm{Host}}, d, \lambda)$, where we assume n to be independent of the dopant concentration at high dopant concentrations ($c_{\mathrm{Tm}} > 10$ at.%). If we have a thin-film with a concentration gradient, this means that we have a wide ensemble of c_{Tm} and d to determine all other parameters that are dependent on on the wavelength.

For an absorbing thin-film, the visible range is unsuitable to determine d with a transmission measurement, since the absorption makes the interference fringes difficult to discern, as can be seen in Figure 7.9a of the main chapter for $CaBr_2$:Tm^{2+}. Therefore, we have measured from red to the near-infrared (600 nm to 1600 nm) where our film does not absorb. Here, we assume $\varepsilon_{\mathrm{Tm}} \approx 0$, making it possible to use the Extended-Sellmeier method [21, 22] to determine n (which varies with λ), and d (which varies with position). Figure 7.9a of the main chapter displays the results of these fits at a few locations on the thin-film. The derived

film thickness can be found in Figure 7.9b of the main chapter. Figure 7.12 displays the average n from these fits which will be used in our subsequent analysis.

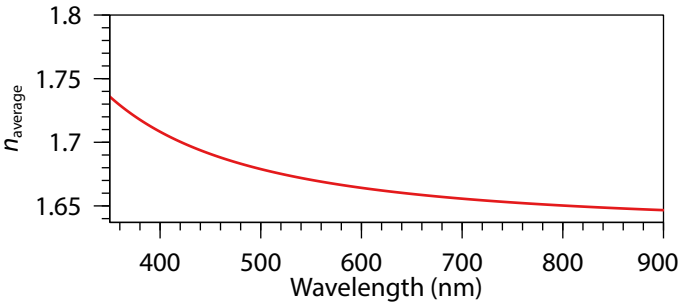


Figure 7.12: Average index of refraction $n_{average}$ for $CaBr_2$:Tm^{2+} with a high doping concentration of Tm^{2+}.

With the local d determined, the wavelength-dependent values for n and k_{Host} (see Figure 7.5e of the main chapter), and the local c_{Tm} from EDX (see Figure 7.9c of the main chapter), it is now possible use the full wavelength range of the local transmission measurements to determine the remaining $\varepsilon_{Tm}(\lambda)$. Determining $\varepsilon_{Tm}(\lambda)$ is achieved by solving for T as a minimization problem:

$$\min RMSE\left(T_{fit}(n, c_{Tm}, \varepsilon_{Tm}, k_{Host}, d, \lambda) - T_{measured}\right). \tag{7.14}$$

In our protocol for Eq. (7.14), λ and c_{Tm} are fixed, and n, k_{Host}, and d are allowed to vary from their initial values by 1 %. For $\varepsilon_{Tm}(\lambda)$, an initial value of $0\,cm^{-1}\,at.\%^{-1}$ is chosen, bound between $0\,cm^{-1}\,at.\%^{-1}$ and $1\times10^{8}\,cm^{-1}\,at.\%^{-1}$. With these parameters and these bounds, a first pass of fittings is done over all wavelengths λ. d should, of course, be constant for every wavelength. Therefore, in a second pass the constraints are tightened by setting the outcomes of the first pass as initial parameters, with d averaged from the results for all λ. In this second pass, bounds on n, k_{Host}, and d are placed such that they can only vary from their initial values by 0.001 %. $\varepsilon_{Tm}(\lambda)$ can still vary freely, but the results from the previous pass are chosen as the initial guess. For the minimization MATLAB is used with `fminsearchbnd` by John D'Errico [34]. The derived $\varepsilon_{Tm}(\lambda)$ fits well with the excitation spectrum, as can be seen in Figure 7.10b of the main chapter.

References

[1]M. de Jong, W. Kesteloo, and E. van der Kolk, "Deposition of luminescent NaCl:Tm^{2+} thin films with a Tm concentration gradient using rf magnetron sputtering," Optical Materials **46**, 149–153 (2015).

[2]O. M. ten Kate, K. W. Krämer, and E. van der Kolk, "Efficient luminescent solar concentrators based on self-absorption free, Tm^{2+} doped halides," Solar Energy Materials and Solar Cells **140**, 115–120 (2015).

[3]E. Beurer, J. Grimm, P. Gerner, and H. U. Güdel, "Absorption, light emission, and upconversion properties of Tm^{2+}-doped $CsCaI_3$ and $RbCaI_3$," Inorganic Chemistry **45**, 9901–9906 (2006).

[4]E. Beurer, J. Grimm, P. Gerner, and H. U. Güdel, "New type of near-infrared to visible photon upconversion in Tm^{2+}-doped $CsCaI_3$," Journal of the American Chemical Society **128**, 3110–3111 (2006).

[5]J. Grimm, E. Beurer, P. Gerner, and H. U. Güdel, "Upconversion between 4f-5d excited states in Tm^{2+}-doped $CsCaCl_3$, $CsCaBr_3$, and $CsCaI_3$," Chemistry - A European Journal **13**, 1152–1157 (2007).

[6]J. Grimm, E. Beurer, and H. U. Güdel, "Crystal Absorption Spectra in the Region of 4f→4f and 4f→5d Excitations in Tm^{2+} -Doped $CsCaCl_3$,$CsCaBr_3$, and $CsCaI_3$," Inorganic Chemistry **45**, 10905–10908 (2006).

[7]J. Grimm, O. S. Wenger, K. W. Krämer, and H. U. Güdel, "4f–4f and 4f–5d excited states and luminescence properties of Tm^{2+}-doped CaF_2, $CaCl_2$, $SrCl_2$ and $BaCl_2$," Journal of Luminescence **126**, 590–596 (2007).

[8]J. Grimm, E. Beurer, and H. U. Güdel, "Crystal Absorption Spectra in the Region of 4f-4f and 4f-5d Excitations in Tm^{2+}-Doped $CsCaCl_3$, $CsCaBr_3$, and $CsCaI_3$," Inorganic Chemistry **45**, 10905–10908 (2006).

[9]J. Grimm and H. U. Güdel, "Five different types of spontaneous emission simultaneously observed in Tm^{2+} doped $CsCaBr_3$," Chemical Physics Letters **404**, 40–43 (2005).

[10]M. P. Plokker and E. van der Kolk, "Temperature dependent relaxation dynamics of luminescent NaX:Tm^{2+} (X=Cl, Br, I)," Journal of Luminescence, 10.1016/j.jlumin.2019.116694 (2019).

[11]European Union, "Directive 2010/31/EU of the European Parliament and of the Council of 19 May 2010 on the energy performance of buildings (recast)," Official Journal of the European Union, 13–35 (2010).

[12]R. A. Ferreira, S. F. Correia, A. Monguzzi, X. Liu, and F. Meinardi, "Spectral converters for photovoltaics – what's ahead," Materials Today **33**, 105–121 (2020).

[13]E. P. J. Merkx, O. M. ten Kate, and E. van der Kolk, "Rapid optimization of large-scale luminescent solar concentrators: evaluation for adoption in the built environment," Optics Express **25**, A547–A563 (2017).

[14]J. C. de Mello, H. F. Wittmann, and R. H. Friend, "An improved experimental determination of external photoluminescence quantum efficiency," Advanced Materials **9**, 230–232 (1997).

[15]A. Rogora, G. Scudo, B. Ferrari, and D. Testa, "Luminescent, transparent and colored, pv systems in architecture: potential diffusion and integration in the built environment," in *30th international plea conference* (CEPT University, 2014).

[16]T. Mansencal, M. Mauderer, M. Parsons, N. Shaw, K. Wheatley, S. Cooper, J. D. Vandenberg, L. Canavan, K. Crowson, and O. Lev, "Colour," 10.5281/ZENODO.3627408 (2020).

[17]S. Westland and C. Ripamonti, *Computational colour science using matlab* (John Wiley & Sons, Ltd, Mar. 2004).

[18]G. Wyszecki and W. S. Stiles, *Cie method of calculating d-illuminants*, 2nd ed. (Wiley, 2000).

[19]J. D. Fowlkes, J. M. Fitz-Gerald, and P. D. Rack, "Ultraviolet emitting $(Y_{1-x}Gd_x)_2O_{3-\delta}$ thin films deposited by radio frequency magnetron sputtering: combinatorial modeling, synthesis, and rapid characterization," Thin Solid Films **510**, 68–76 (2006).

[20]E. P. J. Merkx and E. Van Der Kolk, "Method for the Detailed Characterization of Cosputtered Inorganic Luminescent Material Libraries," ACS Combinatorial Science **20**, 595–601 (2018).

[21]R. Alvarez, A. Garcia-Valenzuela, C. Lopez-Santos, F. J. Ferrer, V. Rico, E. Guillen, M. Alcon-Camas, R. Escobar-Galindo, A. R. Gonzalez-Elipe, and A. Palmero, "High-Rate Deposition of Stoichiometric Compounds by Reactive Magnetron Sputtering at Oblique Angles," Plasma Processes and Polymers **13**, 960–964 (2016).

[22]E. P. J. Merkx, T. G. Lensvelt, and E. van der Kolk, "Modelling and optimization of UV absorbing photovoltaic windows using a thin film AlN:Eu^{3+} luminescence library," Solar Energy Materials and Solar Cells **200**, 110032 (2019).

[23]W. M. Haynes, D. R. Lide, and T. J. Bruno, eds., *Crc handbook of chemistry and physics*, 97th ed. (CRC Press, 2016).

[24]D. L. Smith, *Thin-film deposition: principles and practice* (McGraw-Hill Inc., 1996).

[25]G. Blasse and B. C. Grabmaier, *Luminescent Materials*, Vol. 148, 3743 (1941), pp. 118–119.

[26]J. M. F. van Dijk and M. F. H. Schuurmans, "On the nonradiative and radiative decay rates and a modified exponential energy gap law for 4 f –4 f transitions in rare-earth ions," The Journal of Chemical Physics **78**, 5317–5323 (1983).

[27]S. J. Byrnes, "Multilayer optical calculations," (2016).

[28]J. W. E. Wiegman and E. van der Kolk, "Building integrated thin film luminescent solar concentrators: detailed efficiency characterization and light transport modelling," Solar Energy Materials and Solar Cells **103**, 41–47 (2012).

[29]L. Desmet, A. J. M. Ras, D. K. G. de Boer, and M. G. Debije, "Monocrystalline silicon photovoltaic luminescent solar concentrator with 4.2% power conversion efficiency," Optics Letters **37**, 3087–3089 (2012).

[30]E. P. J. Merkx and E. van der Kolk, "Luminescent solar concentrators," in *Indoor photovoltaics*, edited by M. Freunek, 1st ed. (Wiley-Scrivener, 2020) Chap. 6.

[31]M. R. Bergren, N. S. Makarov, K. Ramasamy, A. Jackson, R. Guglielmetti, and H. McDaniel, "High-Performance $CuInS_2$ Quantum Dot Laminated Glass Luminescent Solar Concentrators for Windows," ACS Energy Letters **3**, 520–525 (2018).

[32]A. F. van Driel, I. S. Nikolaev, P. Vergeer, P. Lodahl, D. Vanmaekelbergh, and W. L. Vos, "Statistical analysis of time-resolved emission from ensembles of semiconductor quantum dots: interpretation of exponential decay models," Physical Review B - Condensed Matter and Materials Physics **75**, 10.1103/PhysRevB.75.035329 (2006).

[33]R. Swanepoel, "Determination of the thickness and optical constants of amorphous silicon," Journal of Physics E: Scientific Instruments **16**, 1214–1222 (1983).

[34]J. D'Errico, "Fminsearchbnd, fminsearchcon (https://www.mathworks.com/matlabcentral/fileexchange/8277-fminsearchbnd-fminsearchcon)," (2012).

Summary and Conclusions

Results Presented in this Thesis

The makeup of the global electricity landscape is expected to move to renewable electricity at an accelerating rate. This increase in renewables can be attributed not only to an increase in regulations requiring renewable energy, but also to the ever higher efficiencies of the renewable electricity sources. Silicon photovoltaics (PV) are approaching the Shockley-Queisser limit, and research on multi-junction photovoltaics reports ever higher solar cell efficiencies every year. These electricity producers can be installed where a large part of their produced energy is consumed: in urban areas. However, conventional PV can only be installed on rooftops or on walls, leaving the areas occupied by window glass unused. To overcome this limitation of space, it is possible to integrate PV into the window glass, leading to so-called building integrated photovoltaics (BIPV). A novel application to convert incoming sunlight to electricity comes in the form of thin-films doped with luminescent centers coated on window glass. In such windows, called luminescent solar concentrators (LSCs), the luminescent coating converts sunlight incident on the face of the window to a longer wavelength and emits this light isotropically, causing 75 % to 80 % to remain trapped within the glass. Through total internal reflection, this trapped light is guided to the perimeter of the window, where photovoltaic cells are placed. This way, by concentration of the sunlight incident on the face of the window to the perimeter, electricity can be generated.

In the first part of this thesis, an overview of the state-of-the-art of LSC research is given with an emphasis on practical applicability. It presents this overview using a model system: LSC-windows sized $100 \times 100 \times 0.5\,\mathrm{cm}^3$ with

80 % transmission of sunlight, defined as AM1.5g. This part seeks to answer what optical efficiencies η_{opt} (the ratio of photons exiting the perimeter to photons incident on the LSC), average color rendering indices R_a, and correlated color temperatures can be reached in that model system. Using Monte Carlo (MC) ray-tracing simulations, these efficiencies and color rendering indices of many recently developed and 'conventional' LSCs are calculated in Chapter 2. From these results it can be concluded that the traditional BASF Red305 dye still outperforms most recent materials, with $\eta_{\text{opt}} = 3.5\,\%$. However, given its bright reddish purple color, its R_a is too low for practical usage.

When waveguiding losses are not a problem, a $100 \times 100 \times 0.5\,\text{cm}^3$ LSC based on non-toxic $CuInS_2$/ZnS core/shell quantum dots can already reach an optical efficiency of more than 2.8 %. At the same time, the quantum dots display excellent R_a, averaging at 98, well above the minimal requirement for European offices of 80.

LSCs based on doping materials with rare-earths also show reasonable efficiencies. $CsPbCl_3:Yb^{3+}$ shows $\eta_{\text{opt}} = 1.5\,\%$, but displays a low average color rendering index of 72. Tm^{2+}-doped halides are also a potential LSC material. Their absorption of the entire visible spectrum lets them reach $\eta_{\text{opt}} = 4.5\,\%$, at high average color rendering indices of more than 91, given that high quantum yields can be attained.

A disadvantage of calculating LSCs using MC is that MC is a statistical approach. As the LSC of interest grows larger in size or becomes more absorbing, the duration of the simulation increases drastically. Therefore, an alternative model to the standard MC approach called the 'multiple-generation light transport' (MGLT) model is presented in Chapter 3. This model efficiently calculates the light transport through an LSC consisting of a single plate. The MGLT model does so by considering absorption, emission and reabsorption in the LSC's escape cone of the entire LSC in a single step. Such a step is referred to as a 'generation'. At the end of a generation, the model evaluates: the fraction of the incident light still remaining within the LSC; the fraction that has escaped through the front and back of the LSC, including the location on the surface of that escape; and the fraction that has contributed to useful output at the LSC's perimeter. The model is evaluated for correctness and benchmarked against the aforementioned MC simulations. Results of these benchmarks show that there is

an almost perfect overlap between the results produced by MC and MGLT, proving the correctness of the MGLT model. Using the MGLT model, the efficiency of an LSC can be calculated in typically two to three generations of transport, irrespective of the LSC's amount of absorption or size. This leads to a constant simulation time, making the model ideal for finding the optimal LSC absorption and size for pre-determined constraints. These properties set the MGLT model apart from the statistical MC approach. Furthermore, optimization of the self-absorbing BASF Lumogen F Red305 dye with near-unity quantum yield shows for the first time that, given a high enough absorption, reabsorption of luminescence in the escape cone of the LSC can actually lead to an increase in optical efficiency. For all simulated quantum yields, a local optimum for the Napierian absorption maximum of a $100 \times 100 \times 0.5\,\mathrm{cm}^3$ Red305 LSC lies around $10\,\mathrm{cm}^{-1}$. However, Chapter 3 shows that when the quantum yield of the self-absorbing dye Red305 exceeds 98 %, a second optimum emerges for this LSC at absorptions of more than $1 \times 10^3\,\mathrm{cm}^{-1}$. This is caused by reabsorption of light that would normally escape the LSC through the escape cone, effectively increasing the trapping efficiency. This positive reabsorption effect shows that self-absorption is not necessarily detrimental to the overall performance of an LSC when the quantum yield approaches unity.

In the second part of this thesis, the focus shifts to high-throughput combinatorial synthesis and characterization of luminescent thin-films. High-throughput combinatorial synthesis and characterization is not often used in the field of luminescent materials, mainly due to the lack of detailed characterization methods. In LSC research, high-throughput synthesis of materials can be crucial for the discovery and optimization of ideal materials. Techniques that perform automated detailed analysis on the synthesis products are however not yet available. Therefore, combinatorial synthesis of luminescent materials through combinatorial reactive sputter deposition and automated analysis of the synthesis products is presented.

The technique to analyze these luminescent combinatorially deposited libraries unites local composition measurements through energy-dispersive X-ray spectroscopy, with local luminescence and transmission measurements, automatically mapped using an xy-translation stage. The luminescent properties: local excitation, emission, and decay of the luminescent library are mapped with a spot size $\sim 10\,\mu\mathrm{m}$ to $100\,\mu\mathrm{m}$ in diameter, first presented in Chapter 4. These

gradient libraries can feature gradients of 0.15 at.% mm^{-1}, meaning that a single spot effectively measures what can be considered a homogeneous composition. This same setup is expanded in Chapter 5 and Chapter 6 to also locally resolve the thin-film transmission and haze. These transmissions can be automatically fit to the thin-film transmittance equation, yielding the local index of refraction, extinction coefficient, and film thickness. As the EDX measurements and the local luminescence and transmission measurements are performed at the same spatial locations on the film, the composition can be directly related to these other properties. To present this large amount of data, ternary diagrams are introduced that efficiently present the interdependence of four variables: elemental composition (accounting for the first three variables, spanning the x, y, and z-axes) and emission wavelength, absorption strength, estimated quantum yield, or refractive index (the color of a datapoint in these axes).

An important step in the research on LSCs made of glass coated with halide thin-films is being able to form solid solutions of two different halide hosts during coating. A solid solution can combine the luminescent properties of its two constituents, potentially yielding desired uniform absorption. In Chapter 4, a single-substrate gradient thin-film library of $NaBr_{0.73}I_{0.27}$ to $NaBr_{0.09}I_{0.91}$, doped with 6.5 % to 16.5 % Eu^{2+} that was not yet explored in literature is therefore presented. This thin-film library is synthesized using combinatorial gradient sputter deposition. The extremes of the presented library, NaBr:Eu^{2+} and NaI:Eu^{2+}, show results that are highly similar to what can be found in literature. These results exemplify that thin-film luminescence is comparable to that observed in bulk powdered phosphors. The library itself shows that the desired solid solution of its local constituents has indeed formed. The gradient film closely follows Vegard's law, shown by X-ray diffractograms. When scanning over the film, and therefore over the composition gradient, the emission from the library fluently moves from 428 nm, corresponding to the side most resembling NaBr:Eu^{2+}, to 439 nm, corresponding to the side most resembling NaI:Eu^{2+}. Therefore, a luminescent thin-film library synthesized with a single sputtering step is now able to provide information on a large range of hosts and dopant concentrations.

Chapter 5 continues with the use of the gradient deposition and xy-scanning methodology. Here, this methodology is utilized to synthesize chemically stable, scratch-resistant, non-hygroscopic and scatter-free materials that are suitable as luminescent thin-films for window applications, in the form of SiAlONs doped

with Eu^{2+}. This amorphous SiAlON family of materials is explored for Si:Al ratios, ranging from 0.062:1 to 3.4:1, and a Eu doping concentrations, ranging from 4.8 at.% to 26 at.%. This single-substrate library covers many compositions that have not been studied before in literature. The gradient library shows a strong redshift from 500 nm to 550 nm as the Si:Al ratio moves to high Al content. These shifts to red can be explained by a decrease in centroid energy caused by the substitution of Si by Al in the second coordination sphere surrounding the emitting Eu^{2+}. An increase in Eu concentration also causes a shift of the emission to red. This shift can in turn be explained by the reabsorption of high energy (low wavelength) light by the emitting Eu^{2+}, in much the same way that reabsorption observed in LSCs operates. The real part of the index of refraction of 1.63 ± 0.03 is typical for oxygen-rich oxynitrides and goes paired with a high absorption coefficient of $1294 \pm 8\,\mathrm{cm}^{-1}\,\mathrm{at.\%}^{-1}$. This high absorption becomes especially clear when viewing a transmission spectrum of the film. A film of only ~ 500 nm in thickness with modest Eu concentrations of ~ 10 at.% already displays a reduced transmission of ~ 50 %.

Whereas Chapter 5 focuses on the discovery and charting of new materials coated on glass, Chapter 6 focuses on a material that is already known in the luminescence community: $AlN:Eu^{3+},O^{2-}$. $AlN:Eu^{3+},O^{2-}$ is interesting for LSC applications because of its non-overlapping absorption and emission spectrum. Therefore, scaling up a window with $AlN:Eu^{3+},O^{2-}$ coating shall exhibit no performance loss due to parasitic self-absorption. Furthermore, $AlN:Eu^{3+},O^{2-}$ only strongly absorbs UV light, making it transparent in the visible spectrum. The parameters necessary to simulate an LSC were, however, unknown. These parameters are absorption strength, refractive index, and the influence of a change in dopant concentration on the quantum yield. The goals of this chapter are therefore threefold: (1) to show what the effects of a change in Eu^{3+} concentration are on the luminescence of $AlN:Eu^{3+},O^{2-}$; (2) to demonstrate how the parameters affecting light absorption, emission and transport can be extracted from a combinatorially sputtered gradient material library; and (3) to model, simulate, and optimize the performance of an $AlN:Eu^{3+},O^{2-}$ thin-film LSC up to 5 µm in thickness using the extracted parameters. $AlN:Eu^{3+},O^{2-}$ strongly absorbs UV light until 450 nm through two allowed charge-transfer type excitations, and a cross-bandgap excitation. It emits this absorbed light without self-absorption as

several f-f emissions, most prominently as red emission at 622 nm $\left({}^5D_0 \rightarrow {}^7F_2\right)$. AlN:$Eu^{3+}$,$O^{2-}$ shows a peak solar absorption of 499 cm^{-1} at.%$^{-1}$ at 350 nm and has an estimated quantum yield that does not exceed 50 %, even at only 1 % Eu doping. With the knowledge of how AlN:Eu^{3+},O^{2-} behaves at different dopant concentrations, its performance as thin-film LSC is modeled. From this modeling it becomes clear that AlN:Eu^{3+},O^{2-} will not become a high-performance LSC. Even at a thickness of 5 µm, only 7 % of the incoming UV light can be converted to red light concentrated at the perimeter of an optimized thin-film AlN:Eu^{3+},O^{2-} LSC. The remaining 93 % of UV light is lost due to reflection at the surface of the LSC (13 %), transmission through the LSC (48 %), host absorption (8.7 %), non-radiative decay (22 %), or escape through the escape cone of the LSC (1.2 %). This chapter demonstrates that it is now possible to individually measure all parameters necessary to simulate and optimize a thin-film-based LSC.

The family of halides doped with divalent Tm are often suggested as LSC-material, due to their absorption of the entire visible spectrum followed by near infrared emission that is not absorbed by the material itself. However, no comprehensive evaluation of their performance as LSC existed. Therefore, simulations of not only the materials' optical efficiency, but also the aesthetic appeal as LSC are carried out in Chapter 7. In Chapter 7, we make fruitful use of the techniques presented in Chapters 5 and 6 and apply them to sputtered thin-films of NaI, $CaBr_2$, CaI_2 doped with Tm^{2+}. This chapter shows that halides doped with Tm^{2+} have a high visible light absorption of maximally 752 cm^{-1} at.%$^{-1}$ in the case of NaI:Tm^{2+}. LSCs based on Tm^{2+} can display excellent color rendering indices of up to 99 %, and neutral color temperatures, between 4500 K and 6000 K, when using the AM1.5g solar spectrum as a reference light source. A 10 µm thick film of NaI:Tm^{2+}, simulated with experimentally determined optical constants, would be able to achieve optical efficiencies of 0.71 % out of a maximally achievable 3.5 % when still transmitting 80 % of the visible spectrum. The low photoluminescent quantum yields of these Tm-doped halides are the main bottleneck that impedes achieving the highest possible optical efficiency.

Significance for Science and Society

For science, the significance of the work presented in this thesis can be found in the high-throughput of materials. In the field of luminescence, while much work is being done on trying to model and predict the behavior of systems using

either density functional theory (DFT), or using empirical means, most research is still based on traditional guided trial-and-error, where one starts with a known structure or composition and slowly moves away from that established material. For both these approaches, the developed methodology described in this thesis can be of great use.

In the case of trial-and-error, the methods presented in the second part of this thesis are directly applicable (and already used). On a single substrate a large quantity of different hosts can be made. The desired property is mapped across the substrate, either using transmission, emission, or decay scans, and from those scans, a direction is determined that subsequent samples or libraries should move to. This process can then be repeated until an optimum of the desired property is reached. Such a process could, for instance, be an extension of what is presented in Chapter 5. In Chapter 5, we explored a large quantity of SiAlON:Eu^{2+} compositions. The gradient sputtering and characterization technique would make it possible to optimize for emission at a certain wavelength. In terms of application, this technique can be applied to the discovery and optimization of LSC materials, as has been presented in Chapters 6 and 7. Also in all other branches of applied luminescence, this search-and-optimize technique can be applied, such as finding materials for white light emitting diodes, afterglow phosphors, and up-/downconversion materials.

In the case of theoretical modeling, the methods presented in this thesis can help in accumulating the required input data. The current status of theoretical models is that experimental data is used as input, and based on those experimental results, a model is derived. These model calculations are typically adjusted afterwards to match the limited set of available experimental data. This data should consist of detailed descriptions of the size of the bandgap, the present optical transitions, and the local crystal structure. The presented gradient technique makes such large quantities of data now available to refine these models, and improve their predictive capabilities. This is shown in Chapter 6 for AlN:Eu^{3+},O^{2-} for the construction of vacuum-referred binding energy (VRBE) diagrams. For these diagrams, the exciton energy and charge transfer transitions of e.g. the valence band to Eu^{3+} are needed to correctly position all divalent rare-earths. If the same system would also be doped with Ce^{3+}, with all five f→d excitation bands resolved, it would become possible to also position all trivalent rare-earths. This can be done with a gradient sputtered solid solution, which would yield the

VRBE diagrams for the many compositions present on a single substrate. Therefore, with only two substrates used, the positions of the f-levels of all rare-earths could be resolved for an entire phase diagram.

For society, the need for efficient building-integrated photovoltaics comes from the desire to continue our standard of living, while at the same time meeting the goals as stated by the Paris agreement to prevent the exhaust of greenhouse gases. To reduce the exhaust of greenhouse gases, the European Union has instated the "Energy Performance of Buildings Directive". This directive requires all new buildings to have a very low net energy consumption by the end of 2020, with preferably renewable energy being the source for the small amount of energy that is still needed. Realizing such nearly zero-energy buildings (nZEBs) is possible. On the consumption end, nZEBs can be realized through energy conservation, for instance by applying high-performing insulation, both as part of the walls and of the windows. On the production end, instead of consuming energy from an off-site generator, the required energy can also be generated on-site. On-site energy generation can be achieved through geo-thermal heat pumps, solar thermal collectors, small wind turbines, and of course, photovoltaics. Most of these methods require large space to function. In urban environments this space is limited to just the roof of a building. This limitation directly puts a cap on the amount of energy that can be generated, especially in high rise office buildings. This limitation can be overcome by seamlessly integrating electricity-generating PV into the building envelope, using building-integrated photovoltaics (BIPV), such as the LSC, which brings us back to this research. As shown in Chapter 2, current LSC solutions in the form of non-toxic quantum dots would already be viable for small-scale energy production and for acquiring expertise in how such LSCs can be incorporated in buildings. The rest of the research presented in this thesis gives a toolbox to accelerate the discovery of LSC materials, and to model how efficient such materials can be.

Samenvatting en Conclusies

Resultaten van dit Proefschrift

De samenstelling van het wereldwijde elektriciteitslandschap wordt verwacht in een versneld tempo te verschuiven naar duurzame elektriciteit. Deze toename van duurzame energie wordt toegeschreven aan zowel een toename in regelgeving die duurzame energie vereist, als aan de steeds hogere rendementen van duurzame energiebronnen. Fotovoltaïsche (PV) cellen gemaakt van Silicium naderen de Shockley-Queisser limiet, en in onderzoek naar tandem PV wordt elk jaar een steeds hoger rendement gerapporteerd. Deze hoge efficienties zijn alleen niet genoeg om aan de elektriciteitsbehoefte van stedelijke gebieden te voorzien. Conventionele PV kan namelijk alleen worden geïnstalleerd op daken of op muren, waardoor de ruimte gebruikt door vensterglas onbenut blijft. Om over deze beperking van ruimte heen te komen, is het mogelijk om PV verder te integreren in vensterglas doormiddel van zogenaamde in het gebouw geïntegreerde PV (GiPV). Dunne films die vensterglas bedekken, waarbij de films gedoteerd zijn met luminescente centra, zijn een noviteit om binnenkomend zonlicht om te zetten naar elektriciteit. In dergelijke ramen, die luminescente zonneconcentratoren (Engels: *Luminescent Solar Concentator* [LSC]) worden genoemd, zet de luminescente deklaag het invallende zonlicht op het raamoppervlak om naar een langere golflengte, waarna dit omgezette licht isotroop in de ruit wordt uitgezonden. 75 tot 80 % van dit omgezette licht blijft daardoor in het glas zitten. Door totale interne reflectie wordt dit opgesloten licht naar de rand van het raam geleid, waar fotovoltaïsche cellen zijn geplaatst. Door de concentratie van het invallende zonlicht van het oppervlakte van het raam naar de rand kan er dus elektriciteit worden opgewekt.

In het eerste deel van dit proefschrift wordt een overzicht gegeven van de stand van zaken binnen het LSC-onderzoek, waarbij de nadruk ligt op praktische toepasbaarheid. Dit deel probeert een antwoord te geven wat voor optisch rendement η_{opt}, d.w.z. de verhouding tussen de fotonen die op de LSC vallen en de fotonen die de rand verlaten, kleurweergave-indexen, en gecorreleerde kleurtemperaturen bereikt kunnen worden in ramen van $100 \times 100 \times 0{,}5\,cm^3$, zoals in de huidige gebouwde omgeving te vinden, waarbij 80 % van het binnenkomende zonlicht, gedefinieerd als AM1.5g, wordt doorgelaten. Met Monte Carlo (MC) simulaties waarbij het pad van individuele lichtstralen gevolgd wordt, worden deze rendementen en kleurweergave-indices van veel recent ontwikkelde en 'conventionele' LSC's berekend in Hoofdstuk 2. Hieruit kan worden geconcludeerd dat de traditionele BASF Rood305 kleurstof nog steeds beter presteert dan de meest recente materialen, met $\eta_{opt} = 3{,}5\,\%$. Echter, gezien de heldere roodachtige paarse kleur, is de kleurweergave-index van Rood305 te laag om in de praktijk ingezet te worden.

Als verliezen ten gevolge van de golfgeleider geen probleem zijn, dan kan een $100 \times 100 \times 0{,}5\,cm^3$ LSC op basis van niet-giftige $CuInS_2/ZnS$ kern/omhulsel kwantumpunten (Engels: quantum dots) een optisch rendement van meer dan 2,8 % behalen, met daarbij nog aanvaardbare kunstmatige kleurenblindheid. De kleurweergave-index is gemiddeld 98, waar de minimale eis voor Europese kantoren 80 is.

LSC's gebaseerd op materialen die met zeldzame aarden zijn gedoteerd hebben ook redelijke rendementen. $CsPbCl_3:Yb^{3+}$ heeft $\eta_{opt} = 1{,}5\,\%$, maar heeft een lage kleurweergave-index van 72. Halogeniden gedoteerd met Tm^{2+} zijn ook een mogelijk materiaal voor LSC gebruik. Deze halogeniden absorberen het hele zichtbare spectrum, waardoor ze $\eta_{opt} = 4{,}5\,\%$ zouden kunnen bereiken, met daarbij kleurweergave-indices van meer dan 91. Hierbij moet vooropgesteld worden dat een hoog kwantumrendement behaald kan worden.

Een nadeel van het berekenen van LSC's met behulp van MC is dat MC een statistische benadering is. Naarmate de gesimuleerde LSC groter wordt of meer absorberend, zal de duur van de simulatie drastisch toenemen. Daarom wordt een alternatief model voor de standaard MC-benadering, het meer-generatie lichttransportmodel (MGLT), gepresenteerd in Hoofdstuk 3. Dit model berekent efficiënt het lichttransport door een LSC bestaande uit één plaat. Het MGLT-model doet dit door de absorptie, emissie en reabsorptie in de ontsnappingskegel van

de hele LSC in één enkele stap, een 'generatie' genoemd, te berekenen. Aan het einde van een generatie evalueert het model welke fractie van het invallende licht nog binnen de LSC blijft, welke fractie door de voor- en achterkant van de LSC is ontsnapt en waar precies, en welke fractie heeft bijgedragen aan nuttig transport naar de rand van de LSC. De prestaties en resultaten van het MGLT-model zijn vergeleken met de eerdergenoemde MC-simulaties. De resultaten van deze benchmarks laten zien dat de resultaten van MC en MGLT bijna perfect overlappen, wat de juistheid van het MGLT-model bewijst. Het MGLT-model kan de efficiëntie van een LSC in typisch twee tot drie generaties berekenen, ongeacht de hoeveelheid absorptie of de grootte van de LSC. Dit leidt tot een constante simulatieduur, waardoor het model ideaal is om de optimale LSC-absorptie en -grootte te vinden voor vooraf bepaalde beperkingen, wat het onderscheidt van de statistische MC-benadering. De optimalisatie van de zelfabsorberende BASF Lumogen F Rood305 kleurstof met een kwantumrendement van bijna eenheid toont bovendien voor het eerst aan dat, bij voldoende absorptie, de reabsorptie van luminescentie in de ontsnappingskegel van de LSC kan leiden tot een verhoging van het optisch rendement. Bij alle gesimuleerde kwantumrendementen van een $100 \times 100 \times 0{,}5\,\mathrm{cm}^3$ Rood305 LSC ligt een lokaal optimum voor de Napieriaanse absorptie rond $10\,\mathrm{cm}^{-1}$. In Hoofdstuk 3 wordt echter aangetoond dat als het kwantumrendement van de zelfabsorberende Rood305 kleurstof boven de 98 % komt te liggen, er zich een tweede optimum vormt bij absorptiecoëfficiënten groter dan $1 \cdot 10^3\,\mathrm{cm}^{-1}$. Dit tweede optimum is ten gevolge van de reabsorptie van licht dat normaal gesproken via de ontsnappingskegel uit de LSC ontsnapt. De opsluitingsefficiëntie wordt hierdoor effectief verhoogd. Dit versterkende reabsorptie-effect toont aan dat zelfabsorptie niet noodzakelijkerwijs nadelig is voor de algemene prestaties van een LSC, wanneer het kwantumrendement nadert tot één.

In het tweede deel van dit proefschrift verschuift de focus naar de combinatorische synthese en karakterisering van luminescente dunne films met hoge doorvoersnelheden. Combinatorische synthese en karakterisering met hoge doorvoersnelheden wordt niet vaak gebruikt op het gebied van luminescente materialen, voornamelijk door het ontbreken van gedetailleerde karakteriseringsmethoden. Voor LSC-onderzoek kan de hoge doorvoersnelheidssynthese van materialen cruciaal zijn voor de ontdekking en optimalisatie van ideale materialen. Technieken

die geautomatiseerde detailanalyses uitvoeren op de syntheseproducten zijn echter nog niet beschikbaar. Daarom wordt in dit tweede deel de combinatorische synthese van luminescente materialen door middel van combinatorische reactieve sputterdepositie en geautomatiseerde analyse van de syntheseproducten gepresenteerd.

De techniek om deze luminescente combinatorisch gedeponeerde materiaalbibliotheken te analyseren werkt door middel van het verenigen van lokale samenstellingsmetingen via energiedispersieve röntgenspectroscopie (EDS), met lokale luminescentie- en transmissiemetingen, welke automatisch in kaart gebracht zijn met een xy-translatie platform. De luminescente eigenschappen: lokale excitatie, emissie en verval van de luminescentiebibliotheek worden in kaart gebracht met een spotgrootte met een diameter van $\sim 10\,\mu m$ to $100\,\mu m$ in diameter. Deze techniek wordt voor het eerst gepresenteerd in Hoofdstuk 4. Deze gradiëntbibliotheken kunnen verlopen van $0{,}15\,\text{at.\%}\,\text{mm}^{-1}$ bevatten. Dit geringe verloop betekent dat een enkele gemeten plek in principe als een homogene samenstelling beschouwd kan worden. Dezelfde opstelling is in Hoofdstuk 5 en Hoofdstuk 6 uitgebreid om ook de transmissie en de nevel van een dunne film lokaal in kaart te brengen. De lokale brekingsindex, extinctiecoëfficiënt en filmdikte kunnen automatisch opgelost worden door de gemeten transmissie te laten passen met de dunnefilmvergelijkingen. Aangezien de EDS-metingen en de lokale luminescentie- en transmissiemetingen dezelfde film beschrijven, kan de samenstelling direct worden gerelateerd aan deze andere eigenschappen, waardoor de ruimtelijke positie op de film buiten beschouwing kan blijven. Om deze grote hoeveelheid gegevens te presenteren, worden ternaire diagrammen geïntroduceerd die de onderlinge afhankelijkheid van vier variabelen, elementaire samenstelling (die de x, y en z-assen opspannen) en de emissiegolflengte, de absorptiesterkte, het geschatte kwantumrendement, of de brekingsindex (die de kleur van een datapunt in deze assen zijn) efficiënt weergeven.

Een belangrijke stap in het onderzoek naar LSC's van glas bedekt met dunne halogeniden films, is het kunnen vormen van vaste oplossingen van twee verschillende halogeniden tijdens het bedekken. Een vaste oplossing kan namelijk de luminescente eigenschappen van de twee bestanddelen combineren en zo de gewenste uniforme absorptie opleveren. Daarom wordt in Hoofdstuk 4 is een dunne filmbibliotheek op een enkel substraat bestaande uit een verloop van $NaBr_{0.73}I_{0.27}$ naar $NaBr_{0.09}I_{0.91}$, gedoteerd met 6,5 % naar 16,5 % Eu^{2+} die nog

niet in de literatuur was onderzocht, gepresenteerd. Deze dunne filmbibliotheek werd gesynthetiseerd met behulp van combinatorische gradiënt sputterdepositie. De uitersten van de gepresenteerde bibliotheek, NaBr:Eu^{2+} en NaI:Eu^{2+}, laten resultaten zien die zeer vergelijkbaar zijn met wat er in de literatuur te vinden is. Hieruit blijkt dat de luminescentie uit een dunne film vergelijkbaar is met die waargenomen in grootschalige poedervormige fosforen. De bibliotheek toont dat de gewenste vaste oplossing van de lokale bestanddelen zich heeft gevormd. Dit wordt bevestigd aan de hand van lokale röntgendiffractogrammen, die zich overeenkomstig de wet van Vegard gedragen. Bij het scannen over de film, en dus over de compositiegradiënt, veranderd de emissie van de bibliotheek vloeiend van 428 nm, wat overeenkomt met de kant die het meest lijkt op NaBr:Eu^{2+}, naar 439 nm, wat overeenkomt met de kant die het meest lijkt op NaI:Eu^{2+}. Concluderend is het vanaf nu dus mogelijk om met een luminescente dunne filmbibliotheek, die gesynthetiseerd is door middel van een enkele sputterdepositiestap, informatie te vergaren van een groot scala aan gastroosters en doteringsconcentraties.

Hoofdstuk 5 gaat door met het gebruik van de gradiëntdepositie- en scanningsmethodologie. Deze methodologie wordt hier gebruikt om chemisch stabiele, krasbestendige, niet-hygroscopische en strooivrije materialen te synthetiseren die geschikt zijn als luminescente dunne films voor raamtoepassingen, in de vorm van SiAlON's gedoteerd met Eu^{2+}. Deze amorfe SiAlON-familie van materialen wordt onderzocht voor Si:Al-verhoudingen van 0,062:1 tot 3,4:1, en een Eu-dopingconcentratie van 4,8 at.% tot 26 at.%. Deze bibliotheek gedeponeerd op een enkel substrat omvat veel composities die niet eerder in de literatuur zijn bestudeerd. De gradiëntbibliotheek laat een sterke roodverschuiving zien van 500 nm naar 550 nm, wanneer de Si:Al-verhouding naar een hoog Al-gehalte gaat. Deze verschuivingen naar rood kunnen verklaard worden door een afname van de zwaartepuntsenergie, veroorzaakt door de vervanging van Si door Al in de tweede coördinatieschil rond het emitterende Eu^{2+}. Een toename van de Eu-concentratie veroorzaakt tevens een verschuiving van de emissie naar rood. Deze verschuiving kan op zijn beurt verklaard worden door de reabsorptie van licht met hoge energie (lage golflengte) door het emitterende Eu^{2+}, in vrijwel dezelfde zin als men roodverschuiving door reabsorptie waargenomen in LSC's verklaart. Het reële deel van de brekingsindex in deze materialen bedraagd $1{,}63 \pm 0{,}03$, kenmerkend voor zuurstofrijke oxinitriden. Dit materiaal vertoont ook een hoge

absorptiecoëfficiënt van $1294 \pm 8\,\mathrm{cm}^{-1}\,\mathrm{at.\%}^{-1}$. Deze hoge absorptie wordt vooral inzichtelijk doormiddel van de transmissiespectra van de film. Een film van slechts $\sim 500\,\mathrm{nm}$ dikte, met een bescheiden Eu-concentratie van $\sim 10\,\mathrm{at.\%}$ toont al een verminderde transmissie $\sim 50\,\%$.

Waar Hoofdstuk 5 zich richtte op het ontdekken en het in kaart brengen van nieuwe materialen als deklaag op glas, richt Hoofdstuk 6 zich op een materiaal dat al bekend is in de luminescentiegemeenschap: AlN:Eu^{3+},O^{2-}. AlN:Eu^{3+},O^{2-} is interessant voor LSC-toepassingen vanwege het niet-overlappende absorptie- en emissiespectrum. Het opschalen van een raam met een AlN:Eu^{3+},O^{2-} deklaag zal daardoor geen rendementsverliezen vertonen als gevolg van parasitaire zelfabsorptie. Bovendien vertoont AlN:Eu^{3+},O^{2-} alleen sterke absorptie van UV-licht, waardoor het doorzichtig is in het zichtbare spectrum. Het was echter onbekend hoe AlN:Eu^{3+},O^{2-} zou presteren als een LSC, omdat, afgezien van de emissiegolflengte, de parameters die nodig zijn om een LSC te simuleren: absorptiesterkte, brekingsindex, en de invloed van een verandering in doteringsconcentratie op het kwantumrendement, onbekend waren. De doelstellingen van dit hoofdstuk zijn dan ook drieledig: (1) het laten zien wat de effecten zijn van een verandering in Eu^{3+} concentratie op de luminescentie van AlN:Eu^{3+},O^{2-}; (2) om aan te tonen hoe de parameters die van invloed zijn op de lichtabsorptie, de emissie en het lichttransport kunnen worden onttrokken aan een combinatorisch gesputterde materiaalbibliotheek; en (3) om de prestaties van een AlN:Eu^{3+},O^{2-} dunne film LSC met een maximale dikte van 5 µm in te modelleren, te simuleren en te optimaliseren met behulp van de onttrokken parameters. AlN:Eu^{3+},O^{2-} absorbeert UV-licht tot 450 nm door middel van twee toegestane ladingsoverdrachtsexcitaties, en een excitatie over de verboden zone. AlN:Eu^{3+},O^{2-} straalt dit geabsorbeerde licht uit zonder zelfabsorptie als verschillende f-f emissies, het meest prominent als rode emissie op 622 nm wegens een $\left({}^5\mathrm{D}_0 \rightarrow {}^7\mathrm{F}_2\right)$ overgang. AlN:Eu^{3+},O^{2-} toont maximale zonlichtabsorptie van $499\,\mathrm{cm}^{-1}\,\mathrm{at.\%}^{-1}$ bij 350 nm en heeft een geschat kwantumrendement die niet hoger is dan 50 %, zelfs niet op slechts 1 at.% Eu-dotering. Met de kennis van hoe AlN:Eu^{3+},O^{2-} zich gedraagt bij verschillende doteringsconcentraties, wordt de prestatie als dunne film LSC gemodelleerd. Uit deze modellering wordt duidelijk dat AlN:Eu^{3+},O^{2-} geen LSC met hoog rendement zal worden. Zelfs bij een dikte van 5 µm, kan slechts 7 percent van het inkomende UV licht worden omgezet naar rood licht, wat op zijn beurt weer geconcentreerd aan de omtrek van een geoptimaliseerde dunne

film LSC. Het resterende UV-licht gaat verloren door reflectie aan het oppervlak van de LSC (13 %), transmissie door de LSC (48 %), absorptie door het gastrooster (8,7 %), stralingsloos verval (22 %), of door ontsnapping via de ontsnappingskegel van de LSC (1,2 %). Dit hoofdstuk toont aan dat het nu mogelijk is om alle parameters individueel te meten die nodig zijn om een LSC gebaseerd op de dunne-filmtechniek te simuleren en te optimaliseren.

De familie van halogeniden gedoteerd met tweewaardig Tm wordt vaak gesuggereerd als LSC-materiaal, vanwege hun absorptie van het gehele zichtbare spectrum, welke wordt gevolgd door nabij-infrarood-emissie. Deze eigenschap zorgt dat het materiaal zijn eigen emissie niet weer zelf absorbeert. Tot nog toe was er echter geen alomvattende evaluatie van hun prestaties als LSC-materiaal. Daarom worden in Hoofdstuk 7 simulaties uitgevoerd van niet alleen de optische efficiëntie van het materiaal, maar ook de esthetische uitstraling als LSC. In Hoofdstuk 7 maken we gebruik van de technieken uit Hoofdstuken 5 en 6 en passen die toe op dunne films van NaI, $CaBr_2$, CaI_2 gedoteerd met Tm^{2+}. Dit hoofdstuk toont aan dat halogeniden gedoteerd met Tm^{2+} een hoge absorptie van zichtbaar licht hebben van maximaal 752 cm^{-1} at.$\%^{-1}$ in het geval van NaI:Tm^{2+}. LSCs op basis van Tm^{2+} kunnen uitstekende kleurweergave-indices tot 99 % hebben, en neutrale kleurtemperaturen, tussen 4500 K en 6000 K, waarbij het AM1.5g zonnespectrum als referentie-lichtbron is gebruikt. Een 10 µm dikke film van NaI:Tm^{2+}, gesimuleerd met experimenteel bepaalde optische constanten, zou een optisch rendement van 0,71 % van de maximaal haalbare 3,5 % kunnen bereiken, waarbij een begrenzing is gezet op dat de LSC nog steeds 80 % van het zichtbare spectrum moet doorlaten. De lage fotoluminescente kwantumopbrengst is het belangrijkste knelpunt dat het bereiken van de hoogst mogelijke optische efficiëntie in de weg staat.

Belang voor de Wetenschap en de Samenleving

Voor de wetenschap is het belang van het in dit proefschrift gepresenteerde werk de behaalde resultaten voor het met hoge doorvoer synthetiseren en karakteriseren van materialen. Op het gebied van luminescentie, waar veel werk wordt verricht om te proberen het gedrag van systemen te modelleren en te voorspellen met behulp van ofwel de dichtheidsfunctionaaltheorie (DFT), of door gebruik te maken van empirische modellen, is het meeste onderzoek nog steeds gebaseerd op met een vooropgesteld plan, ouderwets proberen, waarbij men begint met een

bekende structuur of samenstelling en zich langzaam verwijdert van een bekend materiaal. Voor beide benaderingen kan de ontwikkelde methodologie die in dit proefschrift wordt beschreven van groot nut zijn.

Ten behoeve van de probeer-methodiek zijn de methoden die in het tweede deel van dit proefschrift worden gepresenteerd direct toepasbaar (en al gebruikt). Op één enkel substraat kan een grote hoeveelheid verschillende gastroosters worden gesynthetiseerd. De gewenste eigenschap kan dan in kaart worden gebracht, met behulp van ofwel transmissie-, emissie- of vervalscans, en uit die scans kan een richting worden bepaald waarheen volgende monsters of bibliotheken moeten bewegen. Dit proces kan dan herhaald worden tot een optimum van de gewenste eigenschap bereikt is. Zo'n proces kan bijvoorbeeld een uitbreiding zijn van wat in Hoofdstuk 5 wordt gepresenteerd. In Hoofdstuk 5 hebben we een grote hoeveelheid SiAlON:Eu^{2+} composities onderzocht. De gradiëntsputter- en karakteriseringstechniek zou het mogelijk maken om te optimaliseren voor emissie op een bepaalde golflengte. Qua toepassing kan deze techniek worden toegepast voor de ontdekking en optimalisatie van LSC-materialen, zoals gepresenteerd in Hoofdstuken 6 en 7. Ook in alle andere takken van toegepaste luminescentie kan deze zoek- en optimalisatietechniek worden toegepast, zoals voor het vinden van materialen voor licht emitterende diodes met wit licht, nagloei fosforen, en omhoog/neerconversie materialen.

In het geval van theoretische modellering kunnen de in dit proefschrift gepresenteerde methoden helpen bij het verzamelen van de benodigde invoergegevens. De huidige status van theoretische modellen is dat een model wordt opgesteld voor een nieuw materiaal, op basis van experimentele gegevens van andere materialen. Deze modelberekeningen worden dan meestal achteraf nogmaals aangepast om met de gemeten experimentele data van dit nieuwe materiaal overeen te komen, omdat de set data waarop het initiële model gebaseerd was te beperkt is. Deze gegevens moeten bestaan uit gedetailleerde beschrijvingen van de grootte van de bandkloof, de huidige optische overgangen en de lokale kristalstructuur. De gepresenteerde gradiënttechniek maakt zulke grote hoeveelheden data nu beschikbaar om deze modellen te verfijnen, en hun voorspellende mogelijkheden te verbeteren. Een voorbeeld hiervan is het gebruik van de technieken voor de constructie van diagrammen van bindingsenergieën in relatie tot het vacuümniveau (VRBE), zoals ook gepresenteerd in Hoofdstuk 6 voor AlN:Eu^{3+},O^{2-}. Voor dit type diagram zijn de excitonenergie en ladingsoverdrachtsovergangen van

bijv. de valentieband naar Eu^{3+} nodig om alle tweewaardige zeldzame aarden correct te plaatsen. Als hetzelfde systeem ook gedoteerd zou worden met Ce^{3+}, waarbij alle vijf f→d excitatiebanden individueel zichtbaar zijn, wordt het mogelijk om ook alle driewaardige zeldzame aardmetalen te positioneren. De hiervoor beschreven metingen kunnen gedaan worden aan een gradiënt gesputterde vaste oplossing, wat de VRBE diagrammen zou opleveren voor de vele composities die aanwezig zijn op een enkel substraat. Met slechts twee substraten kunnen dan de posities van de f-niveaus van alle zeldzame aardmetalen dus voor een volledig fasendiagram worden opgelost.

Voor de samenleving komt de behoefte aan een efficiënte GiPV voort uit de wens om onze levensstandaard voort te zetten, met daarbij steeds meer stroomverbruikende apparaten, maar om tegelijkertijd te voldoen aan de doelstellingen uit het akkoord van Parijs om de uitstoot van broeikasgassen die de klimaatverandering veroorzaken te verminderen. Om de uitstoot van broeikasgassen te verminderen, heeft de Europese Unie de 'Richtlijn Energieprestaties van Gebouwen' in het leven geroepen. Deze richtlijn vereist dat alle nieuwe gebouwen tegen eind 2020 een zeer laag netto-energieverbruik hebben, met bij voorkeur hernieuwbare energie als bron voor de kleine hoeveelheid energie die nog nodig is. Het realiseren van dergelijke bijna-energieneutrale gebouwen (nZEB's) is mogelijk. Aan de consumptiekant kunnen nZEB's worden gerealiseerd door energiebesparing, bijvoorbeeld door toepassing van hoogwaardige isolatie, zowel in muren als in ramen. Aan de productiezijde kan, in plaats van energie van een generator elders te gebruiken, de benodigde energie ook ter plaatse worden opgewekt. De energieopwekking ter plaatse kan worden gerealiseerd door middel van geothermische warmtepompen, zonnecollectoren, kleine windturbines en natuurlijk door middel van fotovoltaïsche energie. De meeste van deze methoden vereisen veel ruimte om te kunnen functioneren. In een stedelijke omgeving is deze ruimte beperkt tot het dak van een gebouw. Deze beperking legt direct een limiet op de hoeveelheid energie die kan worden opgewekt, vooral in hoge kantoorgebouwen. Deze beperking kan worden overwonnen door naadloos elektriciteitsproducerende PV te integreren in de gebouwschil, met behulp van GiPV, zoals de LSC, wat ons terugbrengt naar dit onderzoek. Zoals in Hoofdstuk 2 wordt aangetoond, zouden de huidige LSC-oplossingen zoals niet-giftige kwantumpunten al levensvatbaar zijn voor kleinschalige energieproductie en voor het verwerven van expertise in gebouwintegratie. De rest van het onderzoek in dit

proefschrift geeft een gereedschapskist om de ontdekking van LSC-materialen te versnellen en om te modelleren hoe efficiënt dergelijke materialen kunnen zijn.

Acknowledgments

Even though I would like to claim that the small forest worth of pages that came before this chapter was all solely my own work, I, as all scientists, stand on the shoulders of giants. Some of those giants I happen to know a bit more personally than others. Those are the people you will find mentioned and thanked in this section.

First, I would like to thank my promotor and daily supervisor, Erik van der Kolk. Erik, over the past years there was never a dull moment. Even before my PhD started, you moved heaven and earth to arrange that my PhD proposal would be granted. Without you, I would probably not have been able to write this very chapter, or any of the chapters before that. You have a management style that gives people as much freedom as they can handle and I'm very happy with that. Your door is always open and any idea can be discussed. These discussions almost never concluded with 'that's impossible' or 'let's focus on something else', but rather with 'what will you need for that?'

Of course, thanks go to my second promotor, Pieter Dorenbos. Pieter, thank you for educating me in the ways of luminescence through your VRBE schemes, and for letting me educate the Bachelor students during our quantum mechanics course. I won't miss spending a full day every week grading a seemingly never-ending pile of exam sheets, but I will miss being able to assist in designing those very exams.

In this list of educated people, Johan de Haas shouldn't be omitted. From the angry look you always get when you enter his office, you would never say that underneath this glare rests a vast quantity of knowledge and endless patience. Johan, thank you for that patience and for letting me break stuff, "because that's how you learn things". Without your help, all setups described and built in the

previous chapters would have probably never come into being.

During the first years of my PhD, I shared the office with Weronika, Roy, and Hongde. Thank you all for the great times in the office! Roy, thank you for discussing luminescence with me, and making me understand the VRBE model better. Hongde and Weronika, it was great to go flying with you! Though I think I'll stay with commercial flying for the time being. So, sorry Weronika, I won't be joining for aerobatics anytime soon. As the years progressed, slowly new colleagues trickled in. Tianshuai, Maarten, and Giacomo, thank you for continuing the nice times in the office, be it with eating pancakes, movie nights, or not finishing last at the department's pub quizzes. In these last few months, Max, and Vasya joined us. Vasya, good luck with carrying on the halide work. I'm sure that with enough persistence a halide:Tm^{2+} demonstrator LSC can become a reality! Max, I very much enjoyed visiting AJA in Boston together. I now cannot hear anyone say 'mark' without a beautiful Boston accent.

Over the years, I've trained many students, but more so, I would say they trained me. Most of the time, it wasn't me teaching you, but us finding out how anything works together. Suzanne, Friso, Troy, Boris, Sita, Terra, Karima: thank you for being part of the lab and being patient with me as I developed my didactic skills. Special mention goes to Thomas: thank you for the beautiful work on AlN:Eu^{3+}! I think we made it a very solid article! Special mention also goes to Sadiq. I like to think you enjoyed it here so much that you decided to take a job at PHYSEE just to spend more time in our lab. Thank you for all your hard work on SiAlON. With you we made our first real combinatorial library, and I hope many more are still to come!

Speaking of PHYSEE, I would also like to thank Willem, Ferdinand, Ana, Joe and Nina; as well as all the students who did a project co-supervised by PHYSEE: Georgios, Margriet, Caspar, Sicco, Sander, David, and Douwe. It was great having the opportunity to see a start-up grow from a little room next to the DEMO space, to a scale-up with over 30 people employed in a beautiful office. Thank you for the discussions, and of course for providing us with lunch every month!

Apart from Johan, I would also like to thank other technicians who helped me through the years. Kees Goubitz, thank you for introducing me to all things XRD. Adrie Laan, thank you for explaining the SEM/EDX to me, it proved invaluable for developing the 'xy-scanner method'. Rudi Santbergen, thank you for letting us use your transmission setup to verify our measurements. Jan Huizenga, thanks

for having a look whenever we had problems with our electronics!

Next to all these people I shared a lab space with, people with whom I shared a coffee table also deserve thanks. Bert, Beien, Minh, Yuan, Jarno, Pieter Vassier, and Marlies, thank you for the discussions on things having to do with, but also many things other than science.

Apart from all the science, I have a lot of people to thank for trying to improve life for everyone both inside as well as outside the lab. Thank you, Hanna for letting me join the PhD Council of Applied Sciences. I learned so much about TU Delft. I was quite staggered by how involved the organization of a university is, and how much still goes on 'behind-the-scenes'. On that same note, thanks go to my fellow members of the PhD Council, with the members of Team Graduate School in particular, as well as Prof. dr. Laurens Siebbeles and Ans van Schaik. It was great discussing all that can be improved about the Graduate School experience with you, and seeing our ideas implemented!

Inspired by the Applied Sciences PhD Council, I, together with Remco, Beien, Hanan, Maxim, and Giacomo, decided to found the RST PhD Community. I like to think we made a difference for the people in our department. Thank you for hosting all these events together! And of course, thanks go to Prof. dr. ir. Jan Leen Kloosterman and Yvonne Weijgertse for giving us the chance (and budget) to make it all possible. I hope that even when I conclude my time at RST, the PhD Community keeps trying to foster a sense of, well, community within RST.

The people in the security lodge did not only guard me from influences from outside, but they were also guarding my sanity. Whether they were happy with that last task is still a matter of debate, but they still made sure I got home to catch some rest. I will never forget the moment I arrived at the RID on the weekend to an exuberant Danny: "Gefeliciteerd, meneer Merkx! U heeft eindelijk 24 uurs toegang! Ik ben zo blij voor u!"

If we talk about keeping sanity, I cannot forgo mentioning our stellar secretary Trudy, as well as her partner-in-crime Kathalijne. Thank you so much for celebrating all the highs, and talking about all the lows over brownies (and cups of very homeopathic tea in the case of Kathalijne) and during afternoon strolls around the reactor.

No acknowledgements chapter is complete without mentioning the support I received from home. Pap, mam, Anne en Emma: bedankt voor alles! Speciaal voor Anne, nadat ze gedurende een spannend potje "Wie is de Mol," toen ik de

regels toch een beetje anders interpreteerde, uitriep: “Ik kan soms niet geloven dat jij een PhD doet!”, hier toch uiteindelijk het bewijs! More thanks than could ever be written also go to my Lion. Anna, thank you to the moon and back for supporting me over the past four years. Most of my writing happened while on my way to you, be it by plane, train or bus. Thank you for making this thesis readable. I think no one has read what has been written in this thesis as thoroughly as you have. Without my trusty LionSpellCheck™, any message I would’ve liked to get across would be obscured by a forest of grammatical errors. While I now can’t write any longer while on my way to you, living together with you has been incredible, and I hope it will continue this way for a long time to come.

And finally, I would, of course, like to thank you, dear reader, for having picked up my thesis and considering it worth a read. I hope you enjoyed it, or are going to enjoy it, if you skipped immediately to this section.

Publications

Refereed Journal Papers

E.P.J. Merkx, M.P. Plokker, and E. van der Kolk, "The Potential of Transparent Sputtered NaI:Tm^{2+}, $CaBr_2$:Tm^{2+}, and CaI_2:Tm^{2+} Thin-Films as Luminescent Solar Concentrators," Solar Energy Materials & Solar Cells, *under revision*.

D. de Vries, S. van Overbeek, **E.P.J. Merkx**, and E. van der Kolk, "Sm^{2+} doped SiAlO sputter deposited coating for self-absorption and scatter-free luminescent solar concentrator applications," Journal of Luminescence, **225**, 117321 (2020).

E.P.J. Merkx, T.G. Lensvelt, and E. van der Kolk, "Modelling and optimization of UV absorbing photovoltaic windows using a thin film AlN:Eu^{3+} luminescence library," Solar Energy Materials & Solar Cells **200**, 110032 (2019).

E.P.J. Merkx*, S. van Overbeek*, and E. van der Kolk, "Functionalizing window coatings with luminescence centers by combinatorial sputtering of scatter-free amorphous SiAlON:Eu^{2+} thin film composition libraries," Journal of Luminescence **208**, 51–56 (2019).

E.P.J. Merkx and E. van der Kolk, "Method for the Detailed Characterization of Cosputtered Inorganic Luminescent Material Libraries," ACS Combinatorial Science **20**, 595–601 (2018).

Authors with * contributed equally to an article.

E.P.J. Merkx, O.M. ten Kate, and E. van der Kolk, "Rapid optimization of large-scale luminescent solar concentrators: evaluation for adoption in the built environment," Optics Express **25**, A547–A563 (2017).

V. Singh, B.H. Schneider, S.J. Bosman, **E.P.J. Merkx**, and G.A. Steele, "Molybdenum-rhenium alloy based high-*Q* superconducting microwave resonators," Applied Physics Letters **105**, 222601 (2014).

Conference Contributions

E.P.J. Merkx and E. van der Kolk, "Optimizing Tm^{2+}-doped thin film luminescent solar concentrators ," OSA Advanced Photonics Congress, Burlingame, USA (July 2019).

S. van Overbeek, **E.P.J. Merkx**, D. de Vries, and E. van der Kolk, "Optimization of SiAlON Based Electricity Generating Window Coatings Utilizing a Combinatorial Reactive Sputtering Approach," 62^{nd} Annual SVC Technical Conference, Long Beach, USA (April 2019).

E.P.J. Merkx, T.G. Lensvelt, and E. van der Kolk, "Optimization and Expected Performance of AlN:Eu^{3+} Luminescent Solar Concentrators," RST Science Day, Delft, the Netherlands (April 2019).

E.P.J. Merkx and E. van der Kolk, "Luminescence Libraries: a Strategy for Thousands of Samples on a Single Substrate," Physics@Veldhoven, Veldhoven, the Netherlands (January 2018).

E. van der Kolk and **E.P.J. Merkx**, "Tm^{2+} based Luminescent Solar Concentrators," International Conference on Luminescence 2017, João Pessoa, Brazil (August 2017).

E.P.J. Merkx and E. van der Kolk, "Combinatorial synthesis and luminescence mapping of thin films with a composition gradient," International Conference on Luminescence 2017, João Pessoa, Brazil (August 2017).

E.P.J. Merkx and E. van der Kolk, "Rapid Optimization of LSCs: Evaluation for the Built Environment," NanoFront Winter Retreat, Couchevel, France (May 2017).

E.P.J. Merkx, M. de Jong, O.M. ten Kate, F.L. Grapperhaus, W. Kesteloo, and E. van der Kolk, "Luminescent Solar Concentrators based on Thin-Film Tm^{2+} doped Halides: "The PowerWindow"," RST Science Day, Delft, the Netherlands (May 2017).

E.P.J. Merkx, O.M. ten Kate, and E. van der Kolk, "Rapid Optimization of LSCs: Evaluation for the Built Environment," RST Science Day, Delft, the Netherlands (May 2017).

E.P.J. Merkx, O.M. ten Kate, and E. van der Kolk, "Rapid Optimization of LSCs: Evaluation for the Built Environment," SundayNL, Veldhoven, the Netherlands (November 2016).

E.P.J. Merkx, M. de Jong, O.M. ten Kate. E. van der Kolk, and K.W. Krämer, "Efficient Tm^{2+} Doped Halide Luminescent Solar Concentrators," EU PVSEC, Munich, Germany (September 2016).

E.P.J. Merkx, "Efficient Tm^{2+} Doped Halide Luminescent Solar Concentrators," Dutch Ceramic Society Student Speech Contest, Almelo, the Netherlands (March 2016).

E.P.J. Merkx and E. van der Kolk, "Towards Efficient Rare Earth Doped Luminescent Solar Concentrators," Luminescent Solar Concentrators for Greenhouses, Bleiswijk, the Netherlands (April 2016).

Other Publications

Book chapter: **E.P.J. Merkx** and E. van der Kolk, "Luminescent Solar Concentrators," in *Indoor Photovoltaics*, edited by M. Freunek. (Wiley-Scrivener, 2020) Chap. 6.

Popular scientific article: **Evert Merkx**, "Combinatorial Optimization of Luminescent Ceramics for Luminescent Solar Concentrators," KGK **4**, 8–11 (2018).

About the Author

Evert Pieter Jan Merkx was born in Oostvoorne, the Netherlands on September 24th, 1992. After graduating secondary school (VWO with the exact sciences track and International Baccalaureate) at the Jacob van Liesveldt in Hellevoetsluis, he went on to study Applied Physics at Delft University of Technology. During his Master's education, he completed two research internships. One research internship was completed in the Molecular Electronic Devices group of Delft University of Technology, supervised by Dr. V. Singh and Dr. G.A. Steele. The other research internship was in the Microstructured Surfaces Team of the Fraunhofer Institute for Solar Energy in Freiburg i. Br., Germany, supervised by Dr.-Ing. H. Hauser. Evert graduated in 2015 with a Master's thesis on rare-earth-doped luminescent solar concentrators, at the Fundamental Aspects of Materials and Energy group of Delft University of Technology, supervised by Dr. E. van der Kolk. During his Master's studies, as part of the Casimir pre-PhD track, Evert wrote a PhD proposal on thin-film luminescent solar concentrators. Based on this proposal Evert was awarded a research grant by the Casimir Research school, funded by NanoFront. This grant would make the first two years of his PhD possible. In 2016, Evert started his PhD at the Luminescence Materials group, with Dr. E. van der Kolk and Prof. dr. P. Dorenbos as his promotors. The results of this PhD project are presented in this thesis.

Evert is involved in both his own research, as well as in the well-being of his fellow researchers. Next to his PhD research, Evert joined the PhD Council of Applied Sciences to represent the PhDs at RST and was among the founding members of the RST PhD Community. In November 2019, Evert was awarded an Open Mind grant by NWO to research how the techniques described in this thesis can be applied to luminescent materials for horticultural applications.